

Discrete Dynamics in Nature and Society

# Modelling, Control Methods and Applications of Chaotic Oscillators

Lead Guest Editor: Sundarapandian Vaidyanathan

Guest Editors: Aceng Sambas, Chang-Hua Lien, and Mustafa Mamat





---

# **Modelling, Control Methods and Applications of Chaotic Oscillators**



Discrete Dynamics in Nature and Society

---

## **Modelling, Control Methods and Applications of Chaotic Oscillators**

Lead Guest Editor: Sundarapandian Vaidyanathan

Guest Editors: Aceng Sambas, Chang-Hua Lien,  
and Mustafa Mamat




---




Copyright © 2023 Hindawi Limited. All rights reserved.

This is a special issue published in "Discrete Dynamics in Nature and Society." All articles are open access articles distributed under the Creative Commons Attribution License, which permits unrestricted use, distribution, and reproduction in any medium, provided the original work is properly cited.




# Chief Editor

Paolo Renna , Italy

## Associate Editors

Cengiz Çinar, Turkey  
Seenith Sivasundaram, USA  
J. R. Torregrosa , Spain  
Guang Zhang , China  
Lu Zhen , China

## Academic Editors

Fahad Al Basir , India  
Akbar Ali , Saudi Arabia  
Douglas R. Anderson , USA  
Viktor Avrutin , Germany  
Stefan Balint , Romania  
Kamel Barkaoui, France  
Abdellatif Ben Makhlof , Saudi Arabia  
Gabriele Bonanno , Italy  
Florentino Borondo , Spain  
Filippo Cacace , Italy  
Jose Luis Calvo-Rolle , Spain  
Pasquale Candito , Italy  
Giulio E. Cantarella , Italy  
Antonia Chinni , Italy  
Carmen Coll , Spain  
Giancarlo Consolo, Italy  
Alessandro Coppola, Italy  
Anibal Coronel , Chile  
Binxiang Dai , China  
Manuel De la Sen , Spain  
Luisa Di Paola, Italy  
Xiaohua Ding, China  
Tien Van Do , Hungary  
Marcio Eisencraft , Brazil  
Hassan A. El-Morshedy , Egypt  
Elmetwally Elabbasy, Egypt  
Daniele Fournier-Prunaret , France  
Genni Fragnelli , Italy  
Marek Galewski , Poland  
Caristi Giuseppe , Italy  
Gisèle R Goldstein, USA  
Vladimir Gontar, Israel  
Pilar R. Gordoá , Spain  
Luca Guerrini , Italy  
Juan L. G. Guirao , Spain  
Chengming Huang , China




Giuseppe Izzo, Italy  
Sarangapani Jagannathan , USA  
Ya Jia , China  
Emilio Jiménez Macías , Spain  
Nikos I. Karachalios , Greece  
Polinapiliñho F. Katina , USA  
Eric R. Kaufmann , USA  
Mehmet emir Koksál, Turkey  
Nickolai Kosmatov , USA  
Mustafa R. S. Kulenovic , USA  
Kousuke Kuto, Japan  
Junqing Li, China  
Li Li , China  
Wei Li, China  
Ricardo López-Ruiz , Spain  
Rodica Luca , Romania  
A. E. Matouk , Saudi Arabia  
Rigoberto Medina , Chile  
Driss Mehdi , France  
Vicenc Méndez , Spain  
Dorota Mozyrska , Poland  
Jesus Manuel Munoz-Pacheco , Mexico  
Yukihiko Nakata , Japan  
Luca Pancioni , Italy  
Garyfalos Papashinopoulos, Greece  
Ewa Pawluszewicz , Poland  
Alfred Peris , Spain  
Adrian Petrusel , Romania  
Andrew Pickering , Spain  
Tiago Pinto, Spain  
Chuanxi Qian, USA  
Youssef N. Raffoul , USA  
Maria Alessandra Ragusa, Italy  
Aura Reggiani , Italy  
Marko Robnik , Slovenia  
Silvia Romanelli, Italy  
Priyan S, Uzbekistan  
Mouquan SHEN, China  
Christos J. Schinas , Greece  
Mijanur Rahaman Seikh, India  
Tapan Senapati , China  
Kamal Shah, Saudi Arabia  
Leonid Shaikhnet , Israel  
Thanin Sitthiwiratttham , Thailand  
Charalampos Skokos , South Africa





Piergiulio Tempesta , Spain  
Tetsuji Tokihiro , Japan  
Fabio Tramontana , Italy  
Sundarapandian Vaidyanathan , India  
Cruz Vargas-De-León , Mexico  
Hector Vazquez-Leal , Mexico  
Francisco R. Villatoro , Spain  
Hubertus Von Bremen, USA  
Junwei Wang , China  
Kang-Jia Wang , China  
Rui Wang , China  
Xiaoquan Wang, China  
Chun Wei, China  
Zeshui Xu , China  
Bo Yang, USA  
Zaoli Yang , China  
Chunrui Zhang , China  
Haoran Zhang, Sweden  
Ying Zhang , USA  
Zhengqiu Zhang , China  
Yong Zhou , China  
Zuonong Zhu, China  
Mingcheng Zuo, China

# Contents





## **Modelling, Control Methods and Applications of Chaotic Oscillators**

Sundarapandian Vaidyanathan , Aceng Sambas , Chang-Hua Lien , and Mustafa Mamat  
Editorial (3 pages), Article ID 9802412, Volume 2023 (2023)






## **A New Hyperchaotic Two-Scroll System: Bifurcation Study, Multistability, Circuit Simulation, and FPGA Realization**

Sundarapandian Vaidyanathan , Aceng Sambas, Esteban Tlelo-Cuautle , Ciro Fabian Bermudez-Marquez, Khaled Benkouider, and Samy Abdelwahab Safaan  
Research Article (17 pages), Article ID 6604684, Volume 2022 (2022)





## **Complex Dynamics and Effects of Memristive Load Using Current-Mode-Controlled in Buck Converter**

Alain Soup Tewa Kammogne , Edwige Mache Kengne, Sundarapandian Vaidyanathan , Hilaire Bertrand Fotsin , and Thomas Tatietsé Tamo   
Research Article (13 pages), Article ID 7068949, Volume 2022 (2022)



## **Adaptive Finite-Time Sliding Mode Backstepping Controller for Double-Integrator Systems with Mismatched Uncertainties and External Disturbances**

Pooyan Alinaghi Hosseinabadi , Ali Soltani Sharif Abadi , Hemanshu Pota , Sundarapandian Vaidyanathan , and Saad Mekhilef   
Research Article (10 pages), Article ID 3758220, Volume 2022 (2022)




## **Analytic Solution for the Strongly Nonlinear Multi-Order Fractional Version of a BVP Occurring in Chemical Reactor Theory**

Vedat Suat Erturk , A.K. Alomari , Pushpendra Kumar , and Marina Murillo-Arcila   
Research Article (9 pages), Article ID 8655340, Volume 2022 (2022)


## **Asymptotic Behavior of Weak Solutions of Nonisothermal Flow of Herschel–Bulkley Fluid to Free Boundary**

Fares Yazid, Abdelkader Saadallah, Djamel Ouchenane, Nadhir Chougui, Mohamed Abdalla , and Ahmed Himadan   
Research Article (13 pages), Article ID 5610938, Volume 2022 (2022)



## **Dynamical Behaviour and Chaotic Phenomena of HIV Infection through Fractional Calculus**

Rashid Jan , Amin Khan, Salah Boulaaras , and Sulima Ahmed Zubair   
Research Article (19 pages), Article ID 5937420, Volume 2022 (2022)


## **Fully Integrated Chen Chaotic Oscillation System**

Ziyi Ouyang, Jie Jin , Fei Yu , Long Chen, and Lei Ding  
Research Article (7 pages), Article ID 8613090, Volume 2022 (2022)

## **On the Limit Cycles for a Class of Perturbed Fifth-Order Autonomous Differential Equations**


Nabil Sellami, Romaissa Mellal, Bahri Belkacem Cherif , and Sahar Ahmed Idris   
Research Article (18 pages), Article ID 6996805, Volume 2021 (2021)

**Fifteen Limit Cycles Bifurcating from a Perturbed Cubic Center**

Amor Menaceur, Mufda Alrawashdeh, Sahar Ahmed Idris , and Hala Abd-Elmageed

Research Article (9 pages), Article ID 8178729, Volume 2021 (2021)

**Modeling and Dynamical Analysis of Multi-Area Network with a Third-Order Chaotic Power System**

Lixin Yang , Jie Gao, and Jie Ma

Research Article (10 pages), Article ID 8421754, Volume 2021 (2021)



## Editorial

# Modelling, Control Methods and Applications of Chaotic Oscillators

**Sundarapandian Vaidyanathan** <sup>1</sup>, **Aceng Sambas** <sup>2,3</sup>, **Chang-Hua Lien** <sup>4</sup>,  
**and Mustafa Mamat**<sup>2</sup>

<sup>1</sup>Centre for Control Systems, Vel Tech University, 400 Feet Outer Ring Road, Chennai 600062, India

<sup>2</sup>Faculty of Informatics and Computing, Universiti Sultan Zainal Abidin, Gong Badak 21300, Terengganu, Malaysia

<sup>3</sup>Department of Mechanical Engineering, Universitas Muhammadiyah Tasikmalaya, Jawa Barat 46196, Indonesia

<sup>4</sup>Department of Marine Engineering, National Kaohsiung University of Science and Technology, Kaohsiung 81157, Taiwan

Correspondence should be addressed to Sundarapandian Vaidyanathan; [sundarcontrol@gmail.com](mailto:sundarcontrol@gmail.com)

Received 25 March 2023; Accepted 25 March 2023; Published 2 May 2023

Copyright © 2023 Sundarapandian Vaidyanathan et al. This is an open access article distributed under the Creative Commons Attribution License, which permits unrestricted use, distribution, and reproduction in any medium, provided the original work is properly cited.

Nonlinear oscillations have been observed in numerous areas of science as well as engineering [1–4]. Some typical oscillations relate to nonlinear pendulums, population models, business cycles, and jerk systems [5]. Since the discovery of chaotic oscillations in a nonlinear weather model by Lorenz in 1963, chaotic oscillators, their modelling, and control have received much attention in the literature [1]. Chaotic systems and chaotic maps are widely applied in engineering domains such as mechanical oscillations [6, 7], robotics [8–10], nanosystem [11], lasers [12–14], nuclear reactor [15], neural networks [16], encryption [17, 18], cryptosystems [19], and communication devices [20].

This special issue focused on the modelling, control methods and various applications of chaotic oscillators in nature and society. This special issue contains ten articles, the contents of which are summarized as follows.

Vaidyanathan et al. [21] proposed a new four-dimensional two-scroll hyperchaotic system having only two quadratic nonlinearities in their research article and elucidated a detailed bifurcation study of the proposed two-scroll hyperchaotic system. The swift advancement of various areas of chaos theory has paved way into the modelling and engineering applications of chaotic and hyperchaotic systems in various fields. The authors also present the construction of an electronic circuit for the new system using MultiSim (Version 14). With the application of the

Forward Euler Method and Trapezoidal method, the authors have dealt with the implementation of the new two-scroll hyperchaotic system using the model of a field-programmable gate array (FPGA). Details have been provided of the hardware resources used for an FPGA Basys 3 Xilinx Artix-7 XC7A35T-ICPG236C.

Kammogne et al. [22] discussed the complex dynamics and properties of memristive load using current-mode-controlled in buck converter in their research article. It is well-known that electronic power converters exhibit some complex features that can be influenced by the structure parameters, load, and pulse period of the converter. In this article, the authors investigate the complex dynamic phenomena occurring in the dc/dc buck converter, where the main part of this study is consecrated to the nonlinear dynamics when the converter load is memristive. The dynamics analysis of the buck converter with memristive load is carried out with signal plots, bifurcation tools, and Lyapunov diagrams which demonstrate the rich and striking behaviors of the nonlinear dynamical system such as periodic orbits, period-doubling bifurcation, quasiperiodicity, chaos, and pinched hysteresis loops of the memristive load. Finally, the MATLAB simulation results of the buck converter with memristive load are shown to be in good agreement with the analog results obtained with PSIM.

Hosseiniabadi et al. [23] proposed a new adaptive finite-time sliding mode backstepping (AFSMBS) control scheme

in order to control a type of high-order double-integrator systems with mismatched disturbances and uncertainties. The authors incorporate a robust sliding mode control, adaptive control method, backstepping control method, and finite-time stability notion to provide a better tracking performance over applying the techniques separately and to employ their advantages together. Finally, the authors describe simulation results for an example of a remotely operated vehicle (ROV) with three degrees of freedom to demonstrate the efficacy of the suggested control approach in their research article.

Erturk et al. [24] investigated the finding of an analytic solution for the strongly nonlinear multi-order fractional version of a Boundary Value Problem (BVP) associated with a chemical reactor. Using the generalized differential transform technique, the authors describe the procedure for the construction of an approximate analytic solution of the fractional form of a strongly nonlinear BVP with multi-fractional Caputo derivatives occurring in chemical reactor theory. The proposed method is very powerful and can be successfully applied to deal with various kinds of fractional nonlinear boundary value problems.

Yazid et al. [25] studied the asymptotic behavior of weak solutions of non-isothermal flow of Herschel–Bulkley fluid in a thin layer in associated with a nonlinear stationary, nonisothermal, and incompressible model. After formulating the problem statement and variational formulation, the authors derive the estimates for the velocity field and the pressure independently of the parameter. Finally, the authors present a specific Reynolds equation associated with variational inequalities.

Jan et al. [26] investigated the dynamics of HIV via fractional calculus in Atangana–Baleanu framework to understand and formulate the intricate phenomena of this viral infection. The authors present a novel numerical technique for the chaotic and dynamic behaviour of the proposed model. The authors also demonstrate the effect of fractional order on the proposed system of HIV infection. Using numerical simulations, the authors highlight most critical input parameters and propose control intervention to the policy makers. The stability result and the convergence condition for the proposed numerical scheme are also discussed by the authors.

Ouyang et al. [27] designed and verified a fully integrated Chen chaotic oscillation system using OAs and multipliers. A unique feature of the proposed model is that the designed Chen chaotic oscillation system is integrated in a single chip with the advantages of smaller chip area, lower supply voltage, and power consumption. Furthermore, the fully integrated Chen chaotic system is verified with Cadence IC Tools.

Sellami et al. [28] investigated the limit cycles of a fifth-order ordinary differential equation (ODE) by using the averaging theory of the first order and detail sufficient conditions for the existence of limit cycles of the ODE.

Menaceur et al. [29] investigated the bifurcation of limit cycles from the period annulus surrounding the origin of a class of cubic polynomial differential systems by using the averaging theory of first order. In the literature of ordinary

differential equations, it is well-known that limit cycles can be yielded by perturbing a system which has a centre in a suitable manner so that limit cycles bifurcate in the perturbed system.

Yang et al. [30] dealt with the multiarea power network model and specifically used the adaptive control method to analyze the cluster synchronization of a multiarea power network model consisting of a third-order chaotic power system. With a mixture of analytical considerations and numerical simulations on a small-scale multiarea power network model, the authors study on the cluster synchronous performance of the proposed system.

## Data Availability

No data were used to support this study.

## Conflicts of Interest

The editors declare that they have no conflicts of interest.

## Acknowledgments

The editorial team would like to express their appreciation and sincere gratitude to all authors for their valuable contributions in our special issue. In addition, the editors would like to thank the Editorial Board of the Journal, Discrete Dynamics in Nature and Society, for their valuable help and kind support regarding this special issue.

Sundarapandian Vaidyanathan  
Aceng Sambas  
Chang-Hua Lien  
Mustafa Mamat

## References

- [1] R. L. Devaney, *An Introduction to Chaotic Dynamical Systems*, CRC Press, Boca Raton, FL, USA, 3rd edition, 2021.
- [2] A. P. Kuznetsov, Y. V. Sedova, and N. V. Stankevich, “Coupled systems with quasi-periodic and chaotic dynamics,” *Chaos, Solitons & Fractals*, vol. 169, Article ID 113278, 2023.
- [3] H. G. Damghani, F. Nazarimehr, S. Safari, and J. C. Sprott, “Chaotic oscillators with two types of semi-fractal equilibrium points: bifurcations, multistability, and fractal basins of attraction,” *Communications in Nonlinear Science and Numerical Simulation*, vol. 120, Article ID 107143, 2023.
- [4] F. Wang, J. M. Wang, and P. P. Wang, “Chaotic vibration of a two-dimensional wave equation with nonlinear boundary condition,” *Journal of Mathematical Analysis and Applications*, vol. 525, no. 2, Article ID 127143, 2023.
- [5] S. Vaidyanathan and C. H. Lien, *Applications of Sliding Mode Control in Science and Engineering*, Springer, Berlin, Germany, 2017.
- [6] P. Djourwe, J. Y. Effa, and S. G. Nana Engo, “Hidden attractors and metamorphoses of basin boundaries in optomechanics,” *Nonlinear Dynamics*, vol. 111, no. 6, pp. 5905–5917, 2023.
- [7] D. S. Shchapin, A. A. Emelianova, and V. I. Nekorkin, “A chaotic oscillation generator based on mixed dynamics of adaptively coupled Kuramoto oscillators,” *Chaos, Solitons & Fractals*, vol. 166, Article ID 112989, 2023.

- [8] E. Petavratzis, C. Volos, and I. Stouboulos, "Experimental study of terrain coverage of an autonomous chaotic mobile robot," *Integration*, vol. 90, pp. 104–114, 2023.
- [9] Y. Yang, S. Qin, and S. Liao, "Ultra-chaos of a mobile robot: a higher disorder than normal-chaos," *Chaos, Solitons & Fractals*, vol. 167, Article ID 113037, 2023.
- [10] C. Ban, G. Cai, W. Wei, and S. Peng, "Dynamic response and chaotic behavior of a controllable flexible robot," *Nonlinear Dynamics*, vol. 109, no. 2, pp. 547–562, 2022.
- [11] M. Raab, J. Zeininger, Y. Suchorski, K. Tokuda, and G. Ruppachter, "Emergence of chaos in a compartmentalized catalytic reaction nanosystem," *Nature Communications*, vol. 14, no. 1, p. 736, 2023.
- [12] L. Lombardi, G. Aromataris, and V. Annovazzi-Lodi, "Network authentication by close-loop synchronized chaotic lasers," *Optical and Quantum Electronics*, vol. 55, no. 4, p. 326, 2023.
- [13] C. Kai, P. Li, Y. Yang, B. Wang, K. Alan Shore, and Y. Wang, "Forecasting the chaotic dynamics of external cavity semiconductor lasers," *Optics Letters*, vol. 48, no. 5, pp. 1236–1239, 2023.
- [14] Q. Cai, P. Li, Y. Shi et al., "Tbps parallel random number generation based on a single quarter-wavelength-shifted dfb laser," *Optics & Laser Technology*, vol. 162, Article ID 109273, 2023.
- [15] G. Ablay, "New 4D and 3D models of chaotic systems developed from the dynamic behavior of nuclear reactors," *Chaos*, vol. 32, no. 11, Article ID 113108, 2022.
- [16] L. Xiao, L. Li, P. Cao, and Y. He, "A fixed-time robust controller based on zeroing neural network for generalized projective synchronization of chaotic systems," *Chaos, Solitons & Fractals*, vol. 169, Article ID 113279, 2023.
- [17] S. Zhou, X. Wang, and Y. Zhang, "Novel image encryption scheme based on chaotic signals with finite-precision error," *Information Sciences*, vol. 621, pp. 782–798, 2023.
- [18] S. Zhu, X. Deng, W. Zhang, and C. Zhu, "Secure image encryption scheme based on a new robust chaotic map and strong S-box," *Mathematics and Computers in Simulation*, vol. 207, pp. 322–346, 2023.
- [19] D. Chatterjee, B. G. Banik, and A. Banik, "Attack resistant chaos-based cryptosystem by modified baker map and logistic map," *International Journal of Information and Computer Security*, vol. 20, no. 1/2, pp. 48–83, 2023.
- [20] L. Lin, Q. Li, and X. Xi, "Asynchronous secure communication scheme using a new modulation of message on optical chaos," *Optical and Quantum Electronics*, vol. 55, no. 1, p. 15, 2023.
- [21] S. Vaidyanathan, A. Sambas, E. Tlelo-Cuatle, C. F. Bermudez-Marquez, K. Benkouider, and S. A. Safaan, "A new hyperchaotic two-scroll system: bifurcation study, multistability, circuit simulation, and FPGA realization," *Discrete Dynamics in Nature and Society*, vol. 2022, Article ID 6604684, 17 pages, 2022.
- [22] A. S. T. Kammogne, E. M. Kengne, S. Vaidyanathan, H. B. Fotsin, and T. T. Tamo, "Complex dynamics and effects of memristive load using current-mode-controlled in buck converter," *Discrete Dynamics in Nature and Society*, vol. 2022, Article ID 7068949, 13 pages, 2022.
- [23] P. Alinaghi Hosseinabadi, A. Soltani Sharif Abadi, H. Pota, S. Vaidyanathan, and S. Mekhilef, "Adaptive finite-time sliding mode backstepping controller for double-integrator systems with mismatched uncertainties and external disturbances," *Discrete Dynamics in Nature and Society*, vol. 2022, Article ID 3758220, 10 pages, 2022.
- [24] V. S. Erturk, A. K. Alomari, P. Kumar, and M. Murillo-Arcila, "Analytic solution for the strongly nonlinear multi-order fractional version of a BVP occurring in chemical reactor theory," *Discrete Dynamics in Nature and Society*, vol. 2022, Article ID 8655340, 9 pages, 2022.
- [25] F. Yazid, A. Saadallah, D. Ouchenane, N. Chougui, M. Abdalla, and A. Himadan, "Asymptotic behavior of weak solutions of nonisothermal flow of Herschel-Bulkley fluid to free boundary," *Discrete Dynamics in Nature and Society*, vol. 2022, Article ID 5610938, 13 pages, 2022.
- [26] R. Jan, A. Khan, S. Boulaaras, and S. Ahmed Zubair, "Dynamical behaviour and chaotic phenomena of HIV infection through fractional calculus," *Discrete Dynamics in Nature and Society*, vol. 2022, Article ID 5937420, 19 pages, 2022.
- [27] Z. Ouyang, J. Jin, F. Yu, L. Chen, and L. Ding, "Fully integrated Chen chaotic oscillation system," *Discrete Dynamics in Nature and Society*, vol. 2022, Article ID 8613090, 7 pages, 2022.
- [28] N. Sellami, R. Mellal, B. B. Cherif, and S. A. Idris, "On the limit cycles for a class of perturbed fifth-order autonomous differential equations," *Discrete Dynamics in Nature and Society*, vol. 2021, Article ID 6996805, 18 pages, 2021.
- [29] A. Menaceur, M. Alrawashdeh, S. Ahmed Idris, and H. Abd-Elmageed, "Fifteen limit cycles bifurcating from a perturbed cubic center," *Discrete Dynamics in Nature and Society*, vol. 2021, Article ID 8178729, 9 pages, 2021.
- [30] L. Yang, J. Gao, and J. Ma, "Modeling and dynamical analysis of multi-area network with a third-order chaotic power system," *Discrete Dynamics in Nature and Society*, vol. 2021, Article ID 8421754, 10 pages, 2021.



## Research Article

# A New Hyperchaotic Two-Scroll System: Bifurcation Study, Multistability, Circuit Simulation, and FPGA Realization

Sundarapandian Vaidyanathan <sup>1</sup>, Aceng Sambas,<sup>2,3</sup> Esteban Tlelo-Cuautle <sup>4</sup>,  
Ciro Fabian Bermudez-Marquez,<sup>4</sup> Khaled Benkouider,<sup>5</sup> and Samy Abdelwahab Safaan<sup>6,7</sup>

<sup>1</sup>Centre for Control Systems, Vel Tech University, 400 Feet Outer Ring Road, Chennai 600062, India

<sup>2</sup>Mechanical Engineering Department, Universitas Muhammadiyah Tasikmalaya, Tasikmalaya, Jawa Barat 46196, Indonesia

<sup>3</sup>Institute of Strategic Industrial Decision Modelling (ISIDM), Universiti Utara Malaysia, Sintok, Kedah 06010, Malaysia

<sup>4</sup>Electronics Department, The National Institute of Astrophysics, Optics and Electronics (INAOE), Tonantzintla, Puebla 72840, Mexico

<sup>5</sup>Non Destructive Testing Laboratory, Automatic Department, Jijel University, BP 98, Jijel 18000, Algeria

<sup>6</sup>Department of Natural and Applied Sciences, Community College of Buraydah, Qassim University, Buraydah 52571, Saudi Arabia

<sup>7</sup>Nile Higher Institute for Commercial Science and Computer Technology, Mansoura 35511, Egypt

Correspondence should be addressed to Sundarapandian Vaidyanathan; [sundarcontrol@gmail.com](mailto:sundarcontrol@gmail.com)

Received 8 July 2022; Accepted 23 August 2022; Published 22 September 2022

Academic Editor: Abdellatif Ben Makhlouf

Copyright © 2022 Sundarapandian Vaidyanathan et al. This is an open access article distributed under the Creative Commons Attribution License, which permits unrestricted use, distribution, and reproduction in any medium, provided the original work is properly cited.

With the swift advancement of chaos theory, the modeling, chaotic oscillations, and engineering applications of chaotic and hyperchaotic systems are important topics in research. In this research paper, we elucidate our findings of a new four-dimensional two-scroll hyperchaotic system having only two quadratic nonlinearities and carry out a detailed bifurcation study of the proposed dynamical model. Also, an electronic circuit has been constructed for the new system using MultiSim (Version 14). The implementation of the new 4-D hyperchaotic system in a field-programmable gate array (FPGA) is performed herein by applying two numerical methods, *viz.* Forward Euler Method and Trapezoidal Method. The experimental results show a good match with the simulated hyperchaotic attractors. We also provide details of the hardware resources used for an FPGA Basys 3 Xilinx Artix-7 XC7A35T-ICPG236C.

## 1. Introduction

Due to the rapid advancement of chaos theory, chaotic and hyperchaotic systems are applicable in several engineering branches such as memristive circuits [1–4], chemical oscillators [5–7], information sensing systems [8–10], lasers [11, 12], and communication systems [13–16]. Xiu et al. [17] designed a 5-D hyperchaotic system with hardware circuit design developed from a memristive cellular neural network (CNN) and applied it to build a secure communication system. Nazir et al. [18] proposed a secure communication system for encryption based on a 4-D hyperchaotic system and genetic codes. Bian and Yu [19] showed the use of a 6-D

hyperchaotic system to enhance the security of a communication system. Boumaraf and Merazka [20] demonstrated the use of a new 4-D hyperchaotic cryptosystem for encryption applications.

Modeling of two-scroll hyperchaotic systems has attracted good research in the literature [21–23]. This research work reports the findings of a new four-dimensional nonlinear dynamical system having two quadratic nonlinear terms and depicting a two-scroll hyperchaotic attractor. Since the maximal Lyapunov exponent (MLE) of the two-scroll system is  $\tau_{\max} = 2.6174$ , we deduce that the two-scroll system (1) has high complexity. By a rigorous mathematical analysis, it is shown that the proposed mathematical model

has a unique balance point at the origin. This is followed by an extensive bifurcation analysis of the new 4-D two-scroll system reported in this work. We study the changes in the qualitative behavior of the proposed 4-D two-scroll system with respect to changes in the values of the system parameters by means of a bifurcation analysis. Bifurcation analysis for systems exhibiting chaos or hyperchaos is useful to get illuminated on the various qualitative properties like oscillations, quasi-periodicity, chaoticity, and hyperchaoticity when the parameters take various values in specified intervals [24–26]. Our research study also shows that the new hyperchaotic system exhibits multistability, which is a special property of coexistence of attractors for a selected set of values for the parameters but differing sets of values for the initial data of the trajectories [27, 28].

Circuit implementations of chaotic and hyperchaotic systems are of great usability in practice due to direct applications in many engineering disciplines [3, 29, 30]. An electronic model of the proposed hyperchaotic two-scroll system has been envisioned using MultiSim. Embedded and nonembedded implementations of chaotic and hyperchaotic systems are of paramount importance to increase their applications in many scientific and engineering fields since those FPGA designs can be linked directly to the digital world [31–35]. FPGA implementation of the proposed hyperchaotic two-scroll system has also been carried out at the end of this work by applying two numerical methods, *viz.* Forward Euler Method and Trapezoidal Method. Experimental implementation using FPGA facilitates practical applications with the new hyperchaotic model.

## 2. A New Hyperchaotic System with Two-Scroll Attractor

A two-scroll attractor of a new hyperchaotic system is the main contribution of the modelling part of this research paper. Our new system is the following 4-D dynamics given by

$$\dot{z} = f(z), \text{ where } f(z) = \begin{bmatrix} a(z_2 - z_1) - z_3 + z_4 \\ cz_1 - z_2 - z_1z_3 + z_4 \\ -bz_3 + z_1z_2 \\ -dz_2 \end{bmatrix}. \quad (1)$$

In the 4-D dynamics (1),  $z = (z_1, z_2, z_3, z_4)$  and  $a, b, c, d$  are positive system constants. We note that the vector field  $f(z)$  has nine linear terms and two quadratic nonlinear terms.

When we take the constants as  $(a, b, c, d) = (25, 8, 90, 6)$  and the initial data as  $z(0) = (0.8, 0.2, 0.4, 0.6)$ , the Lyapunov characteristic exponents of the model (1) can be estimated using MATLAB for  $T = 1E4$  seconds as follows:

$$\begin{cases} \tau_1 = 2.6174, \\ \tau_2 = 0.2743, \\ \tau_3 = 0, \\ \tau_4 = -36.8194. \end{cases} \quad (2)$$

We note that the sum of the Lyapunov characteristic exponents of the model (1) is a negative quantity, *viz.*

$$\tau_1 + \tau_2 + \tau_3 + \tau_4 = -33.9277. \quad (3)$$

This calculation demonstrates that the 4-D system stated in the equation (1) has a dissipative hyperchaotic attractor with two positive Lyapunov characteristic exponents.

If  $V(t)$  denotes a volume element of the flow of the 4-D hyperchaotic system (1), then the divergence of the flow of  $V$  is calculated as follows:

$$\nabla \cdot V = \frac{\partial f_1}{\partial z_1} + \frac{\partial f_2}{\partial z_2} + \frac{\partial f_3}{\partial z_3} + \frac{\partial f_4}{\partial z_4} = -a - b - 1. \quad (4)$$

This also shows that 4-D hyperchaotic system (1) is dissipative for all positive values of the system constants  $a$  and  $b$ . Since the maximal Lyapunov exponent (MLE) of the two-scroll system is  $\tau_{\max} = 2.6174$ , we deduce that the two-scroll system (1) has high complexity.

Figure 1 shows various MATLAB signal portraits of the 4-D hyperchaotic two-scroll dynamics (1) for the initial data  $z(0) = (0.8, 0.2, 0.4, 0.6)$  and parameter data  $(a, b, c, d) = (25, 8, 90, 6)$ .

The Kaplan–Yorke dimension of the 4-D hyperchaotic two-scroll dynamics (1) can be found as

$$D_{KY} = 3 + \frac{\tau_1 + \tau_2 + \tau_3}{|\tau_4|} = 3.0785. \quad (5)$$

The balance points (or equilibrium points) of system (1) are the roots of the system:

$$f(z) = 0. \quad (6)$$

Thus, we proceed to find the roots of the following nonlinear system:

$$a(z_2 - z_1) - z_3 + z_4 = 0, \quad (7a)$$

$$cz_1 - z_2 - z_1z_3 + z_4 = 0, \quad (7b)$$

$$-bz_3 + z_1z_2 = 0, \quad (7c)$$

$$-dz_2 = 0. \quad (7d)$$

Let us assume that  $a > 0, b > 0, c > 0$ , and  $d > 0$ .

From (7d),  $-dz_2 = 0$  or  $z_2 = 0$ .

When we substitute  $z_2 = 0$  in (7c), we get  $-bz_3 = 0$  or  $z_3 = 0$ .

Furthermore, substitution of  $z_2 = z_3 = 0$  into equations (7a) and (7b) lead to the following:

$$-az_1 + z_4 = 0, \quad (8a)$$

$$cz_1 + z_4 = 0. \quad (8b)$$

Subtracting (8a) from (8b), we get

$$(c + a)z_1 = 0. \quad (9)$$

Since  $c$  and  $a$  are positive constants,  $c + a > 0$ .

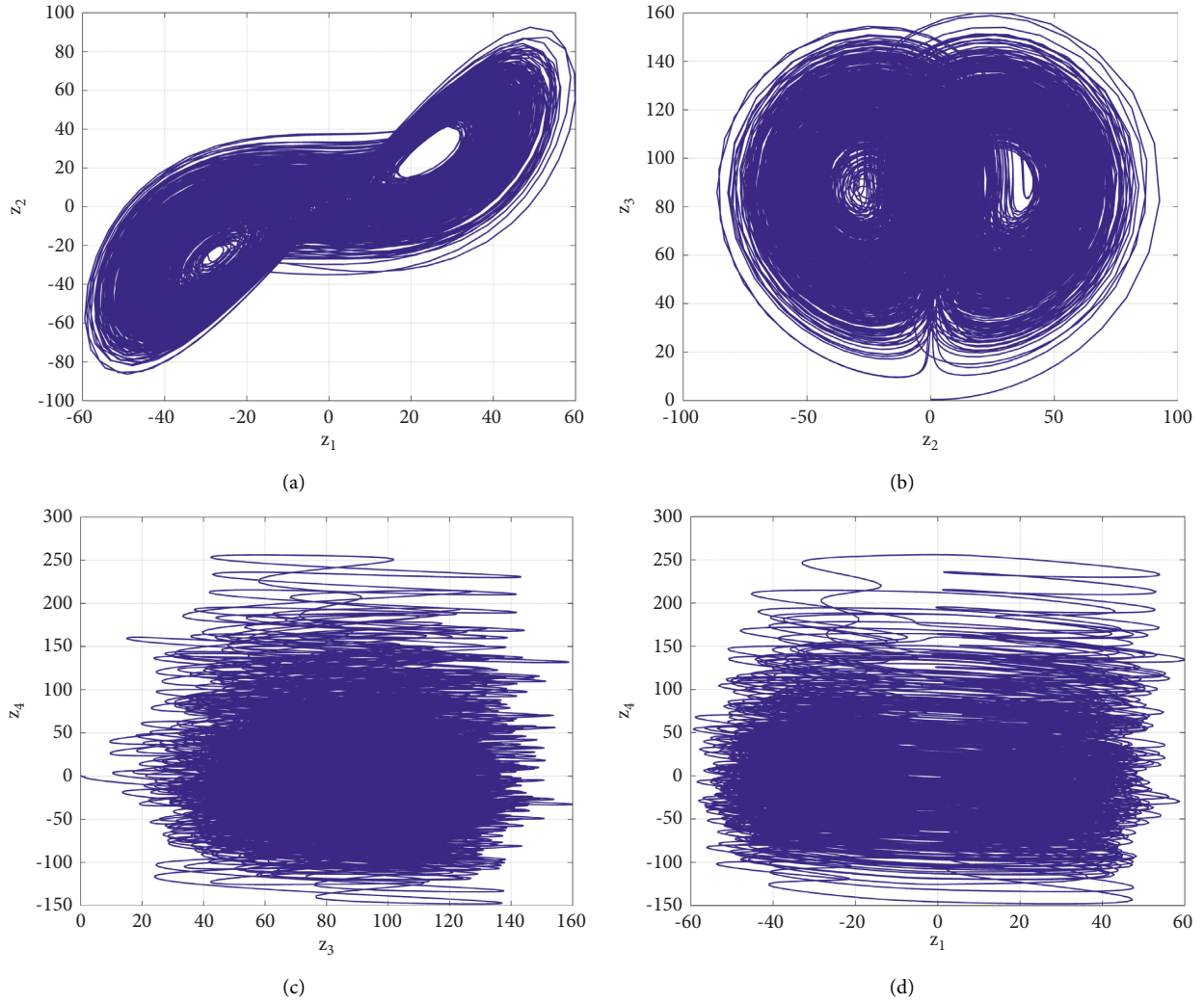


FIGURE 1: Various MATLAB signal portraits of the 4-D hyperchaotic two-scroll dynamics (1).

From (9), we get  $z_1 = 0$ .

Substituting  $z_1 = 0$  into (8a) or (8b), we get  $z_4 = 0$ .

As a result of this calculation, we conclude that  $Z_0 = 0$  is the only balance point for the 4-D two-scroll hyperchaotic system (1). The stability nature of  $Z_0 = 0$  is found by calculating the eigenvalues of the Jacobian matrix  $A = Df(0)$ .

We take the constants for the hyperchaos case as  $(a, b, c, d) = (25, 8, 90, 6)$ .

For these values, we calculate the system Jacobian matrix as

$$A = Df(0) = \begin{bmatrix} -25 & 25 & -1 & 1 \\ 90 & -1 & 0 & 1 \\ 0 & 0 & -8 & 0 \\ 0 & -6 & 0 & 0 \end{bmatrix}. \quad (10)$$

With the use of MATLAB, we estimate the eigenvalues of the matrix  $A$  as

$$\begin{cases} \lambda_1 = 0.3121, \\ \lambda_2 = 35.6688, \\ \lambda_3 = -8.0000, \\ \lambda_4 = -61.9809. \end{cases} \quad (11)$$

This pinpoints that the unique balance point  $Z_0 = 0$  of the two-scroll system (1) is a saddle-point, which is unstable. Hence, the model (1) has a self-excited two-scroll hyperchaotic attractor.

### 3. A Bifurcation Study of the Hyperchaotic Two-Scroll Attractor

In this section of the paper, the dynamical behavior of the novel, extremely complex two-scroll hyperchaotic system (1) is examined with  $Z(0) = (0.8, 0.2, 0.4, 0.6)$ .



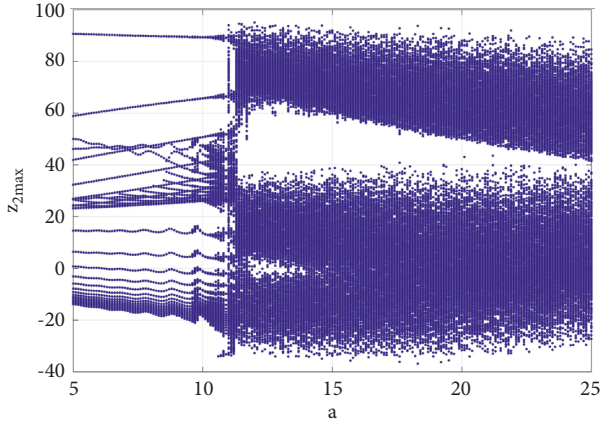


FIGURE 2: Bifurcation diagram for the model (1) when  $a$  varies in  $[5, 25]$  and  $(b, c, d) = (8, 90, 6)$ .

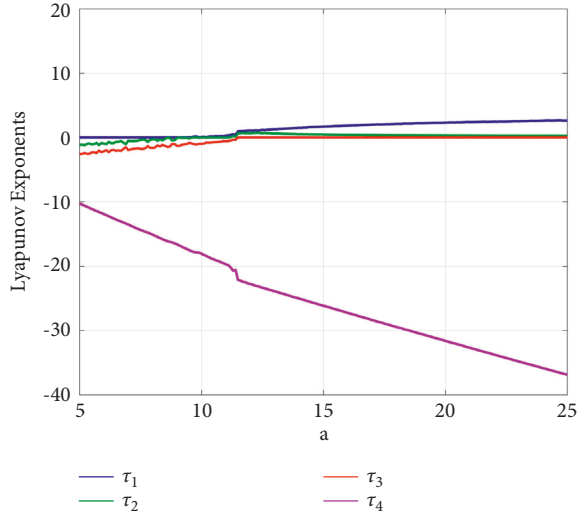


FIGURE 3: Lyapunov exponents for the model (1) when  $a$  varies in  $[5, 25]$  and  $(b, c, d) = (8, 90, 6)$ .

**3.1. Behavior Evolution When  $a$  Changes.** Here, with the values of the constants  $b, c, d$  set to  $b = 8, c = 90$  and  $d = 6$ , the dynamic responses of the 4-D dynamical system (1) are displayed when the value of the constant  $a$  increases in the interval of values  $[5, 25]$ . The outcomes of the simulation show that, depending on the value of parameter  $a$ , system (1) can display a variety of types of behavior such as periodic, chaotic, or hyperchaotic behavior with varying degrees of complexity. Figure 2 displays the bifurcation diagram for system (1). Figure 3 depicts the Lyapunov exponents (LE) spectrum  $(\tau_1, \tau_2, \tau_3, \tau_4)$  for system (1).

From Figures 2 and 3, it can be seen that there are no positive LE value for system (1) in the range of  $5 < a < 9.5$ . Figure 4 shows a periodic response for system (1) when  $a = 6$ . The corresponding LE values of (1) are estimated using MATLAB as follows:

$$\tau_1 = 0, \tau_2 = -0.959, \tau_3 = -2.141, \tau_4 = -11.901. \quad (12)$$

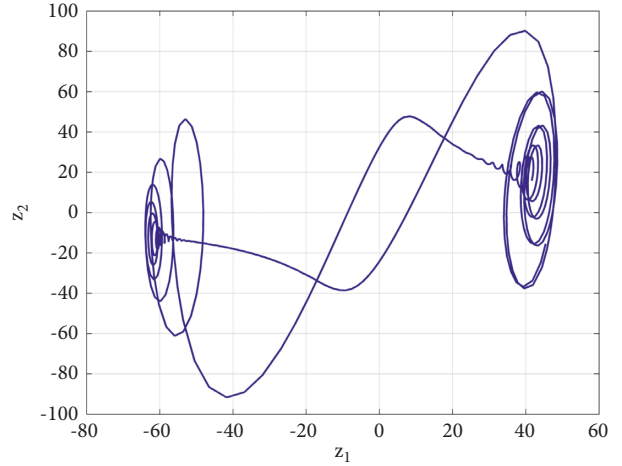


FIGURE 4: A periodic response of the model (1) for  $a = 6$  and  $(b, c, d) = (8, 90, 6)$ .

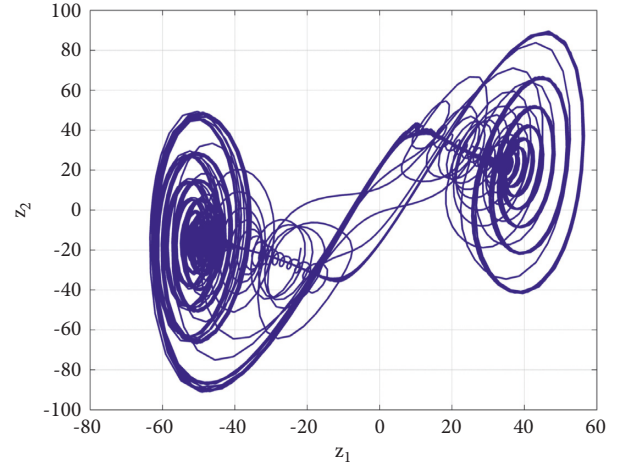


FIGURE 5: A chaotic attractor of the model (1) for  $a = 11$  and  $(b, c, d) = (8, 90, 6)$ .

When  $9.5 < a < 11.4$ ,  $\tau_1$  increases from zero to a positive value while  $\tau_2$  reaches zero. These results indicate that system (1) has a chaotic attractor for this range of parameter  $a$ , as clearly seen in Figure 5, when  $a = 11$ . The corresponding LE values of the new 4-D system are estimated using MATLAB as follows:

$$\tau_1 = 0.296, \tau_2 = 0, \tau_3 = -0.593, \tau_4 = -19.703. \quad (13)$$

Also, when  $a = 11$ , system (1) has a fractional Kaplan–York dimension:

$$D_{KY} = 2 + \frac{\tau_1 + \tau_2}{|\tau_3|} = 2.4992. \quad (14)$$

When  $11.4 < a < 2.5$ , system (1) has two positive LE values, which leads into a hyperchaotic region. Figure 6 presents the hyperchaotic attractor generated by system (1) when  $a = 12$ . The corresponding LE values of (1) are estimated using MATLAB as follows:

$$\tau_1 = 1.065, \tau_2 = 0.691, \tau_3 = 0, \tau_4 = -22.758. \quad (15)$$

Also, when  $a = 12$ , system (1) has a fractional Kaplan–York dimension:

$$D_{KY} = 3 + \frac{\tau_1 + \tau_2 + \tau_3}{|\tau_4|} = 3.0772. \quad (16)$$

From Figure 3, it can be seen that  $\tau_1$  increases with the increase of parameter  $a$ , until it reaches over 2.6 when  $a = 25$ . This causes more disordering in the attractor, as shown in Figure 7. Figures 4–7 portray a 2-D plot of the attractor of the 4-D system (1) in  $(z_1, z_2)$  coordinate plane for different values of the system constant  $a$ , while  $(b, c, d) = (8, 90, 6)$ .

**3.2. Behavior Evolution When  $b$  Changes.** Here, with the values of the constants  $b, c, d$  set to  $a = 25, c = 90$ , and  $d = 6$ , the dynamic responses of the 4-D dynamical system (1) are displayed when the value of the constant  $b$  increases in the interval of values  $[8, 20]$ . The outcomes of the simulation show that, depending on the value of parameter  $b$ , system (1) can display a variety of types of behavior such as periodic, chaotic, or hyperchaotic behavior with varying degrees of complexity. Figure 8 displays the bifurcation diagram for system (1). Figure 9 depicts the LE spectrum  $(\tau_1, \tau_2, \tau_3, \tau_4)$  for system (1).

From Figures 8 and 9, it can be seen that  $\tau_1$  decreases with the increase of the constant  $b$ . When  $8 < b < 14$ , system (1) possesses two positive LE values. Figure 10 shows the hyperchaotic attractor of system (1) when  $b = 10$ . The corresponding LE values of (1) are estimated using MATLAB as follows:

$$\tau_1 = 2.666, \tau_2 = 0.273, \tau_3 = 0, \tau_4 = -38.942. \quad (17)$$

Also, when  $b = 10$ , system (1) has a fractional Kaplan–York dimension:

$$D_{KY} = 3 + \frac{\tau_1 + \tau_2 + \tau_3}{|\tau_4|} = 3.0755. \quad (18)$$

When  $b = 13.8$ , system (1) exhibits a less disordered hyperchaotic attractor shown in Figure 11, when compared with the one in Figure 10. The hyperchaotic attractor exhibited in Figure 11 has  $\tau_1 = 2.442$  and  $D_{KY} = 3.064$ .

When  $14 < b < 15$  the second Lyapunov exponent  $\tau_2$  decreases from a positive value to zero while the first exponent  $\tau_1$  stays still positive. This transition indicates that system (1) has a chaotic response for this range of parameter  $b$ . Figure 12 shows the chaotic attractor of system (1) when  $b = 15$ . This strange attractor is characterized by the following Lyapunov exponents:

$$\tau_1 = 0.061, \tau_2 = 0, \tau_3 = -0.772, \tau_4 = -40.284. \quad (19)$$

Also, when  $b = 10$ , system (1) has a fractional Kaplan–York dimension:

$$D_{KY} = 2 + \frac{\tau_1 + \tau_2}{|\tau_3|} = 2.0790. \quad (20)$$

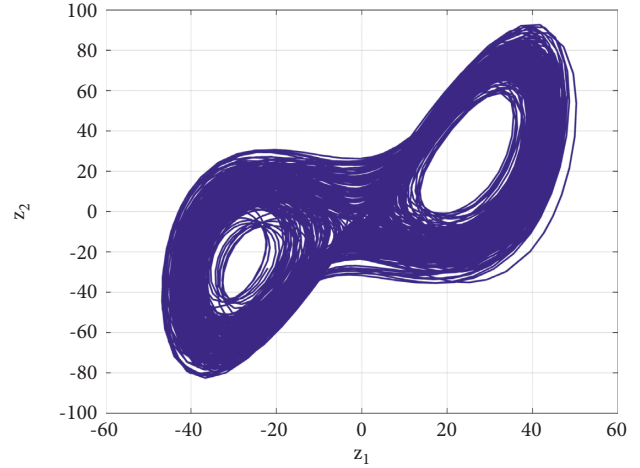


FIGURE 6: A hyperchaotic attractor of model (1) for  $a = 12$  and  $(b, c, d) = (8, 90, 6)$ .

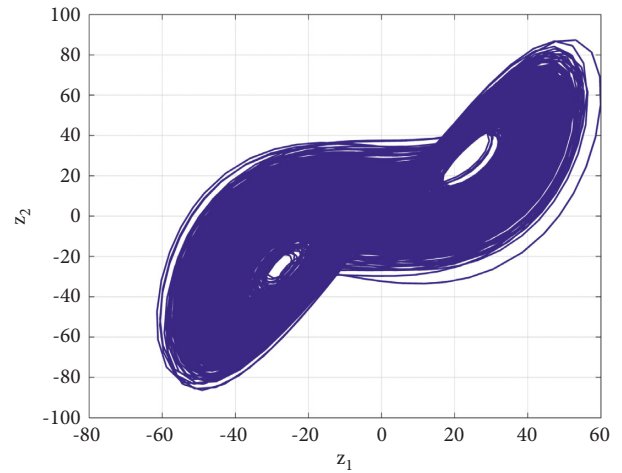


FIGURE 7: A hyperchaotic attractor of the model (1) when  $a = 25$  and  $(b, c, d) = (8, 90, 6)$ .

When  $15 < b < 20$ , there are no positive exponents which mean that system (1) has a periodic response in this region of parameters. The periodic orbit is shown in Figure 13 when  $b = 20$ . The corresponding Lyapunov exponents are calculated and obtained as follows:

$$\tau_1 = 0, \tau_2 = -1.794, \tau_3 = -2.083, \tau_4 = -42.124. \quad (21)$$

Figures 10–12 and 1 portray a 2-D plot of the attractor of the 4-D system (1) in  $(z_1, z_3)$  coordinate plane for different values of the system constant  $b$ , while  $(a, c, d) = (25, 90, 6)$ .

**3.3. Behavior Evolution When  $c$  Changes.** Here, with the values of the constants  $a, b, d$  set to  $a = 25, b = 8$ , and  $d = 6$ , the dynamic responses of system (1) are displayed when the value of the constant  $c$  increases in the interval of values  $[30, 90]$ . The outcomes of the simulation show that, depending on the value of parameter  $c$ , system (1) can display a variety of types of behavior such as periodic, chaotic, or hyperchaotic behavior with varying degrees of

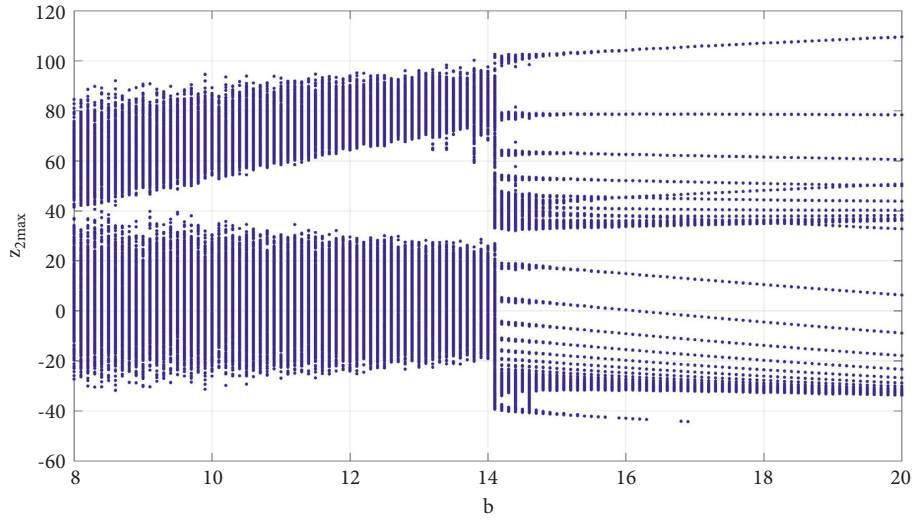


FIGURE 8: Bifurcation diagram for the model (1) when  $b$  varies in  $[8, 20]$  and  $(a, c, d) = (25, 90, 6)$ .

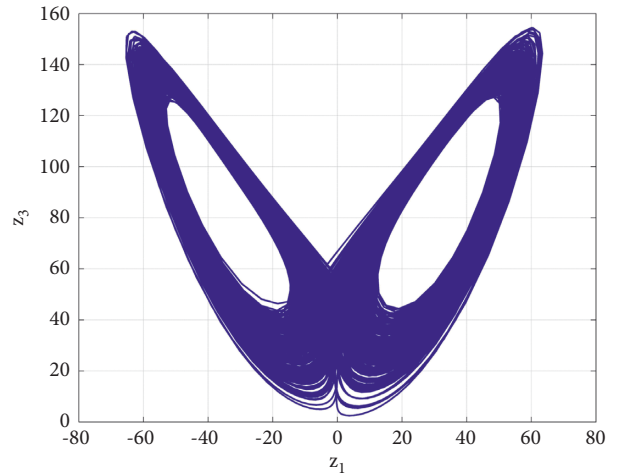
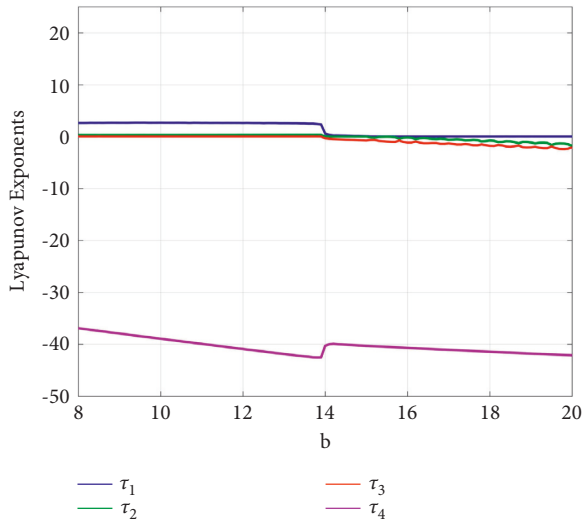


FIGURE 11: A hyperchaotic attractor of the model (1) for  $b = 13.8$  and  $(a, c, d) = (25, 90, 6)$ .

FIGURE 9: Lyapunov exponents for the model (1) when  $b$  varies in  $[8, 20]$  and  $(a, c, d) = (25, 90, 6)$ .

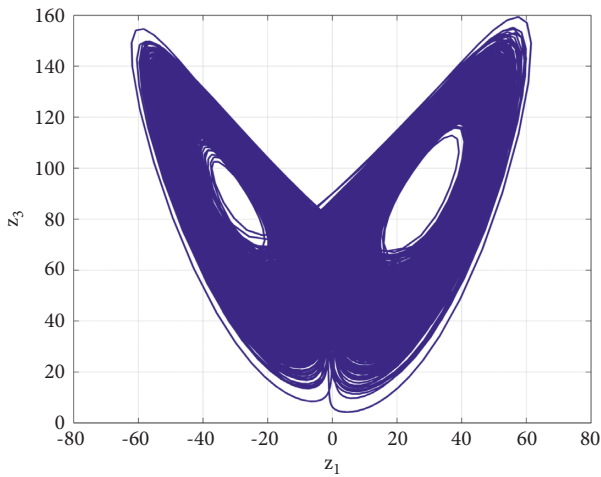


FIGURE 10: A hyperchaotic attractor of the model (1) for  $b = 10$  and  $(a, c, d) = (25, 90, 6)$ .

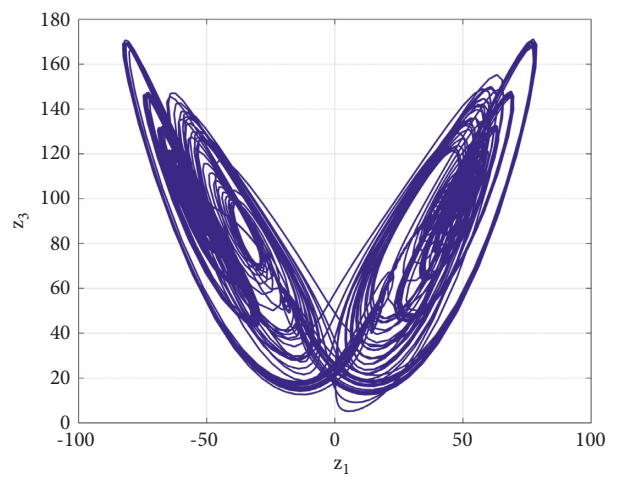


FIGURE 12: A chaotic attractor of the model (1) for  $b = 15$  and  $(a, c, d) = (25, 90, 6)$ .

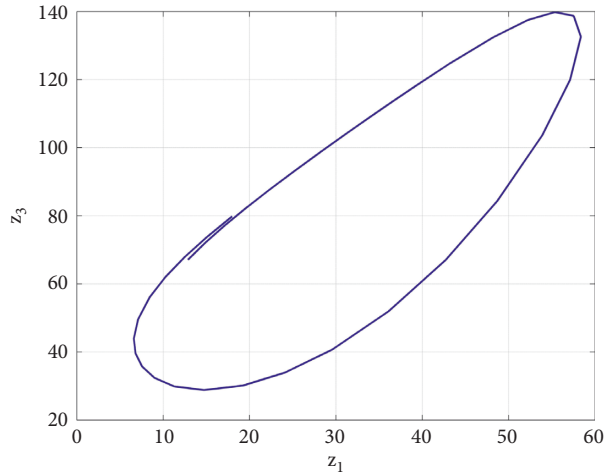


FIGURE 13: A periodic attractor of the model (1) for  $b = 20$  and  $(a, c, d) = (25, 90, 6)$ .

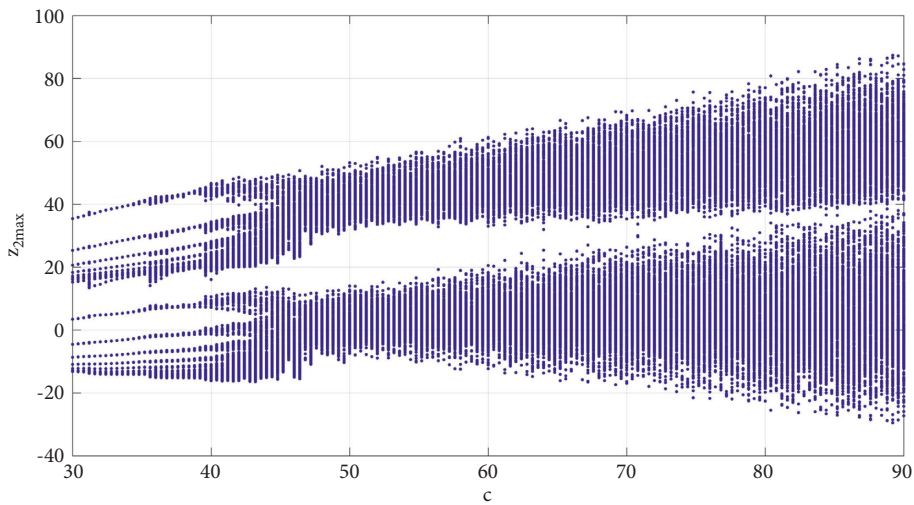


FIGURE 14: Bifurcation diagram for the model (1) when  $c$  varies in  $[30, 90]$  and  $(a, b, d) = (25, 8, 6)$ .

complexity. Figure 14 displays the bifurcation diagram for system (1). Figure 15 depicts the LE spectrum  $(\tau_1, \tau_2, \tau_3, \tau_4)$  for system (1).

From Figures 14 and 15, it can be seen that the first Lyapunov exponent  $\tau_1$  increases with the increase of the constant  $c$ . We define  $A = [30, 30.9] \cup [31.5, 35.1] \cup [37.5, 39]$ . When  $c \in A$ , system (1) does not have any positive LE value. Hence, system (1) has a periodic attractor for the values of  $c$  in this region. Figure 16 shows the periodic attractor of system (1) when  $c = 30.5$ . The corresponding LE values of (1) are estimated using MATLAB as follows:

$$\tau_1 = 0, \tau_2 = -0.222, \tau_3 = -1.035, \tau_4 = -32.744. \quad (22)$$

We define  $B = [30.9, 31.5] \cup [35.1, 37.5] \cup [39, 44.7]$ . When  $c \in B, \tau_1$  increases from zero to a positive value while the second Lyapunov exponent  $\tau_2$  reaches zero. These results indicate that system (1) has a chaotic behavior for this range of the constant  $c \in B$ . Figure 17 shows the chaotic attractor

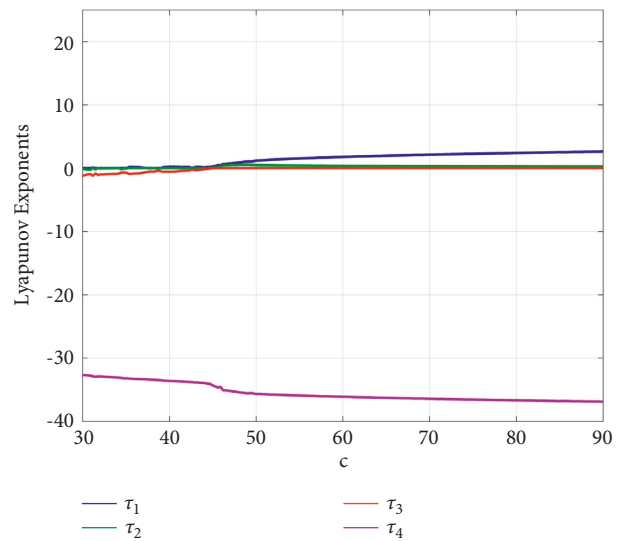


FIGURE 15: Lyapunov exponents for the model (1) when  $c$  varies in  $[30, 90]$  and  $(a, b, d) = (25, 8, 6)$ .



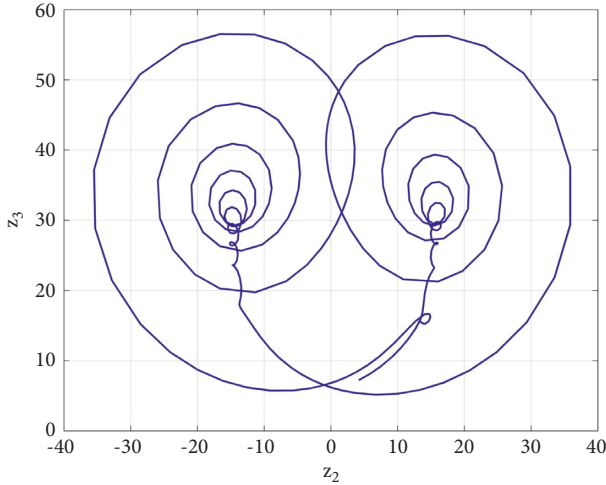


FIGURE 16: A periodic attractor of the 4-D system (1) when  $c = 30.5$  and  $(a, b, d) = (25, 8, 6)$ .

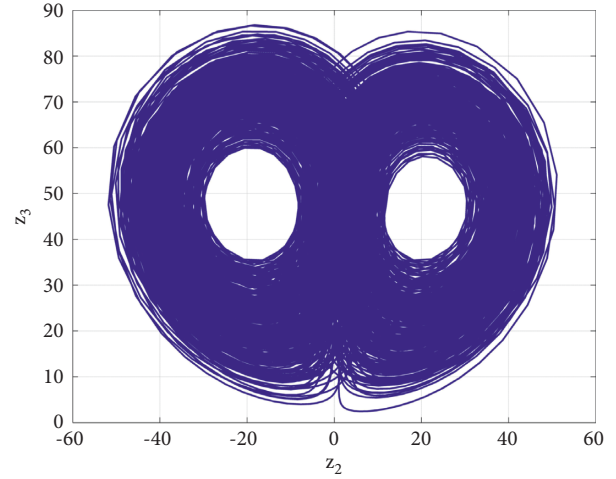


FIGURE 18: A hyperchaotic attractor of the model (1) for  $c = 50$  and  $(a, b, d) = (25, 8, 6)$ .

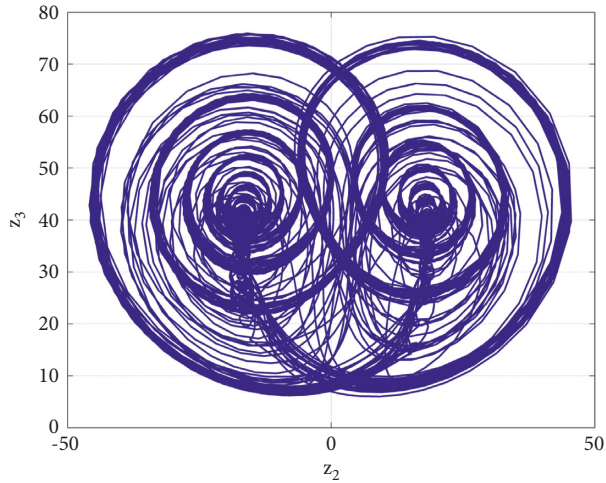


FIGURE 17: A chaotic attractor of the 4-D system (1) when  $c = 40$  and  $(a, b, d) = (25, 8, 6)$ .

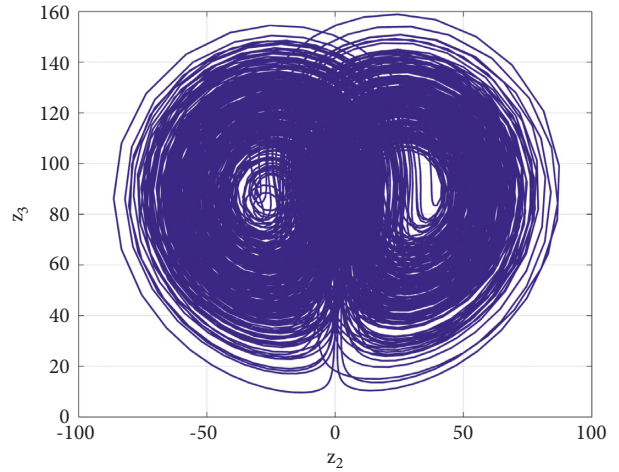


FIGURE 19: A hyperchaotic attractor of the model (1) for  $c = 90$  and  $(a, b, d) = (25, 8, 6)$ .

of system (1) when  $c = 40$ . The corresponding LE values of (1) are estimated using MATLAB as follows:

$$\tau_1 = 0.218, \tau_2 = 0, \tau_3 = -0.601, \tau_4 = -33.618. \quad (23)$$

Also, the Kaplan–Yorke dimension of (1) for  $c = 40$  is obtained as:

$$D_{KY} = 2 + \frac{\tau_1 + \tau_2}{|\tau_3|} = 2.3627. \quad (24)$$

When  $44.7 < c < 90$ , system (1) has two positive LE values, which leads into a wide hyperchaotic region. Figure 18 presents the hyperchaotic attractor exhibited by (1) when  $c = 50$ .

The corresponding LE values of (1) are estimated using MATLAB as follows:

$$\tau_1 = 1.130, \tau_2 = 0.497, \tau_3 = 0, \tau_4 = -35.629. \quad (25)$$

Also, the Kaplan–Yorke dimension of (1) for  $c = 50$  is obtained as:

$$D_{KY} = 3 + \frac{\tau_1 + \tau_2 + \tau_3}{|\tau_4|} = 3.0457. \quad (26)$$

From Figure 15, it can be seen that  $\tau_1$  increases with the increase of the constant  $c$  until it reaches over  $\tau_1 = 2.6$  when  $c = 90$ . This causes a hyperchaotic attractor in which the trajectory is highly disordered, as seen in Figure 19.

Figures 16–19 portray a 2-D plot of the attractor of system (1) in  $(z_2, z_3)$  coordinate plane for different values of the constant  $c$ , while  $(a, b, d) = (25, 8, 6)$ .

**3.4. Behavior Evolution When  $d$  Changes.** Here, with the values of the constants  $a, b, c$  set to  $a = 25, b = 8$ , and  $c = 90$ , the dynamic responses of system (1) are displayed when the value of the constant  $d$  increases in the range of values  $[5, 1100]$ . The outcomes of the simulation show that,

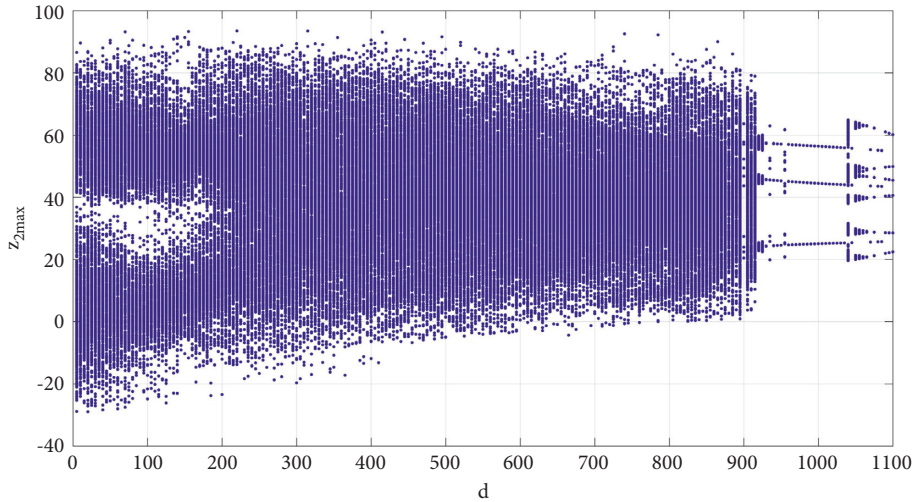


FIGURE 20: Bifurcation diagram for the model (1) when  $d$  varies in  $[0, 1100]$  and  $(a, b, c) = (25, 8, 90)$ .

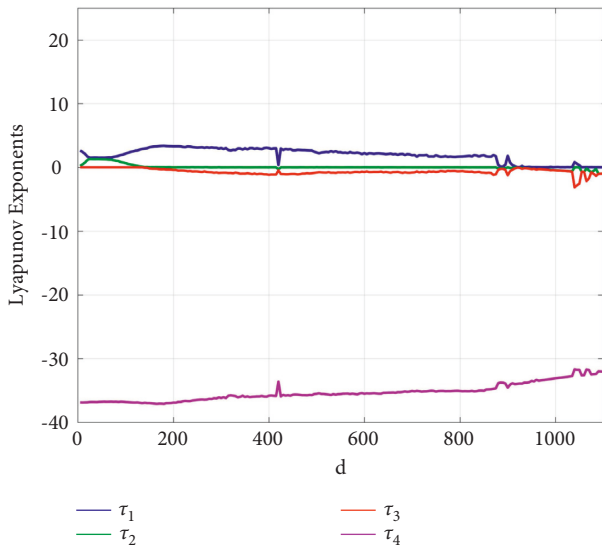


FIGURE 21: Lyapunov exponents for the model (1) when  $d$  varies in  $[0, 1100]$  and  $(a, b, c) = (25, 8, 90)$ .

depending on the value of parameter  $d$ , system (1) can display a variety of types of behavior such as periodic, chaotic, or hyperchaotic behavior with varying degrees of complexity. Figure 20 displays the bifurcation diagram for system (1). Figure 21 depicts the LE spectrum  $(\tau_1, \tau_2, \tau_3, \tau_4)$  for system (1).

When  $5 < d < 140$ , system (1) possesses two positive LE values. Figure 22 shows the hyperchaotic attractor of system (1) when  $d = 40$ . The corresponding LE values of (1) are estimated using MATLAB as follows:

$$\tau_1 = 1.525, \tau_2 = 1.296, \tau_3 = 0, \tau_4 = -36.825. \quad (27)$$

Also, the Kaplan–Yorke dimension of (1) for  $d = 40$  is obtained as:

$$D_{KY} = 3 + \frac{\tau_1 + \tau_2 + \tau_3}{|\tau_4|} = 3.0766. \quad (28)$$

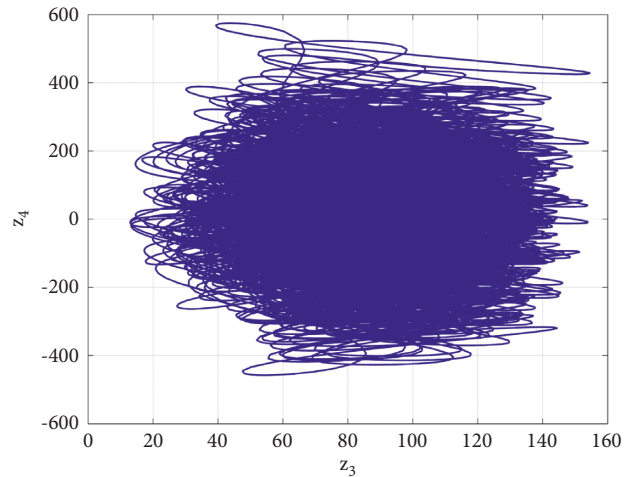


FIGURE 22: A hyperchaotic attractor of the model (1) for  $d = 40$  and  $(a, b, c) = (25, 8, 90)$ .

We define  $C = [140, 875] \cup [1035, 1065]$ . When  $d \in C$ ,  $\tau_2$  decreases from a positive value to zero while  $\tau_1$  stays still positive. This transition indicates that system (1) has a chaotic response for this very wide region. When  $d = 180$ ,  $\tau_1$  reaches its largest value of 3.392.

Figure 23 shows the chaotic attractor of system (1). The corresponding LE values of (1) are estimated using MATLAB as follows:

$$\tau_1 = 3.392, \tau_2 = 0, \tau_3 = -0.316, \tau_4 = -37.089. \quad (29)$$

Also, the Kaplan–Yorke dimension of (1) for  $d = 180$  is obtained as

$$D_{KY} = 3 + \frac{\tau_1 + \tau_2 + \tau_3}{|\tau_4|} = 3.0829. \quad (30)$$

When  $d = 1045$ ,  $\tau_1$  decreases to 0.544 providing less strength to the system’s chaotic dynamics. Figure 24 shows

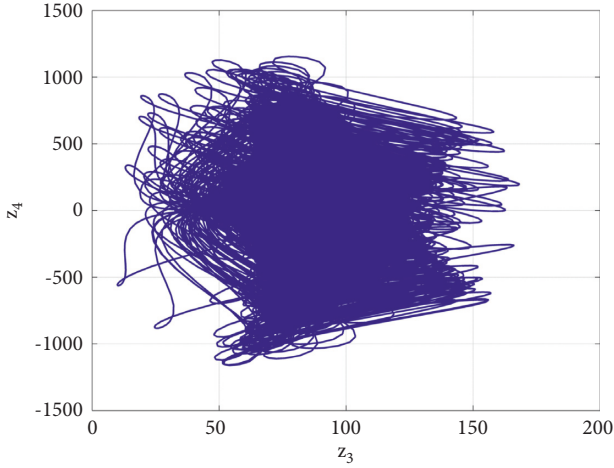


FIGURE 23: A chaotic attractor of the model (1) for  $d = 180$  and  $(a, b, c) = (25, 8, 90)$ .

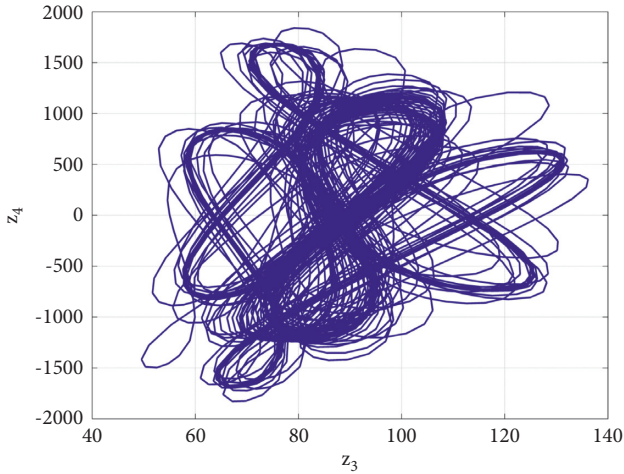


FIGURE 24: A chaotic attractor of the model (1) for  $d = 1045$  and  $(a, b, c) = (25, 8, 90)$ .

the chaotic attractor of system (1). The corresponding LE values of (1) are estimated using MATLAB as follows:

$$\tau_1 = 0.544, \tau_2 = 0, \tau_3 = -2.811, \tau_4 = -31.735. \quad (31)$$

Also, the Kaplan–Yorke dimension of (1) for  $d = 1045$  is obtained as

$$D_{KY} = 2 + \frac{\tau_1 + \tau_2}{|\tau_3|} = 2.1935. \quad (32)$$

We define  $D = [875, 1035] \cup [1065, 1100]$ . When  $d \in D$ , there are no positive LE values which means that system (1) has a periodic response in this region of constants. The periodic orbit is shown in Figure 25 when  $d = 1020$ .

The corresponding LE values of (1) are estimated using MATLAB as follows:

$$\tau_1 = 0, \tau_2 = -0.550, \tau_3 = -0.555, \tau_4 = -32.901. \quad (33)$$

Figures 22–25 portray a 2-D plot of the attractor of the 4-D system (1) in  $(z_3, z_4)$  coordinate plane for different values of the constant  $d$  while  $(a, b, c) = (25, 8, 90)$ .

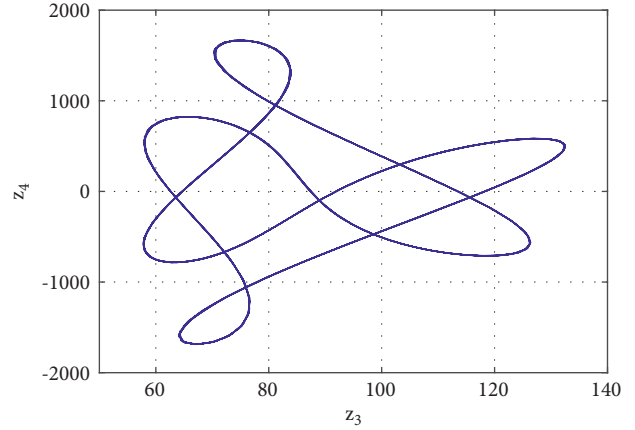


FIGURE 25: A periodic attractor of the model (1) for  $d = 1020$  and  $(a, b, c) = (25, 8, 90)$ .

#### 4. Coexisting Attractors and Multistability for the New System

Multistability, often referred to as coexisting attractors, is a special nonlinear phenomenon wherein two or more distinct attractors evolve simultaneously from various starting points.

Let  $Z_{01}$  and  $Z_{02}$  represent two distinct starting points for the new 4-D system (1), where:

$$Z_0 = (0.5, 0.5, 0.5, 0.5) \text{ (Blue color).}$$

$$W_0 = (-0.5, -0.5, 0.5, -0.5) \text{ (Red color).}$$

First, we fix the system constants as  $a = 25, b = 8, c = 32$ , and  $d = 6$ . As shown in Figure 26, system (1) exhibits two different coexisting attractors. The blue one is a periodic attractor that begins from  $Z_0$  and characterized by the following LE spectrum:

$$\tau_1 = 0, \tau_2 = -0.312, \tau_3 = -0.741, \tau_4 = -32.950. \quad (34)$$

The red one is a chaotic attractor that begins from  $W_0$  and characterized by the following LE spectrum:

$$\tau_1 = 0.041, \tau_2 = 0, \tau_3 = -1.111, \tau_4 = -32.928. \quad (35)$$

Next, we fix the system constants as  $a = 25, b = 14, c = 90$ , and  $d = 6$ . As shown in Figure 27, system (1) exhibits two different coexisting chaotic attractors. The blue chaotic attractor begins from  $Z_0$  and characterized by the following LE spectrum:

$$\tau_1 = 0.322, \tau_2 = 0, \tau_3 = -0.393, \tau_4 = -39.942. \quad (36)$$

The red chaotic attractor begins from  $W_0$  and characterized by the following LE spectrum:

$$\tau_1 = 0.236, \tau_2 = 0, \tau_3 = -0.396, \tau_4 = -39.842. \quad (37)$$

Finally, we fix the system constants as  $a = 25, b = 8, c = 65$ , and  $d = 6$ . As shown in Figure 28, system (1) exhibits two different coexisting hyperchaotic attractors. The blue hyperchaotic attractor begins from  $Z_0$  and characterized by the following LE spectrum:

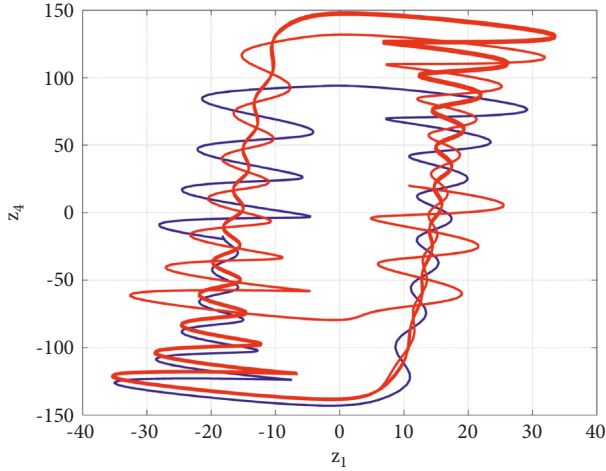


FIGURE 26: The coexistence of one periodic and one chaotic attractor for system (1) projected in the  $(z_1, z_4)$  coordinate plane for the choice of parameters  $(a, b, c, d) = (25, 8, 32, 6)$ .

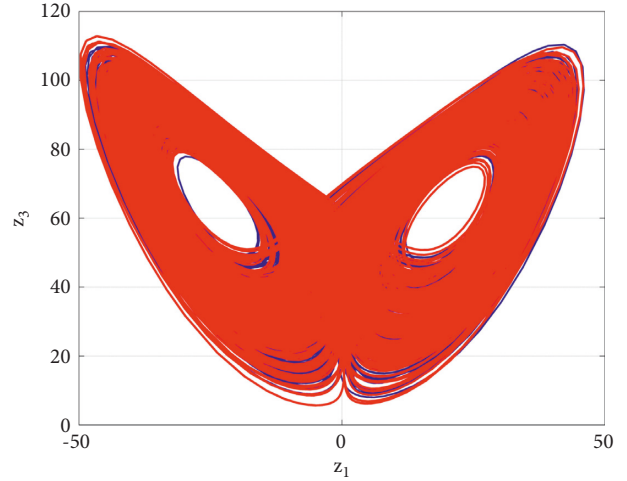


FIGURE 28: The coexistence of hyperchaotic attractors for system (1) projected in the  $(z_1, z_3)$  coordinate plane for the choice of parameters  $(a, b, c, d) = (25, 8, 65, 6)$ .

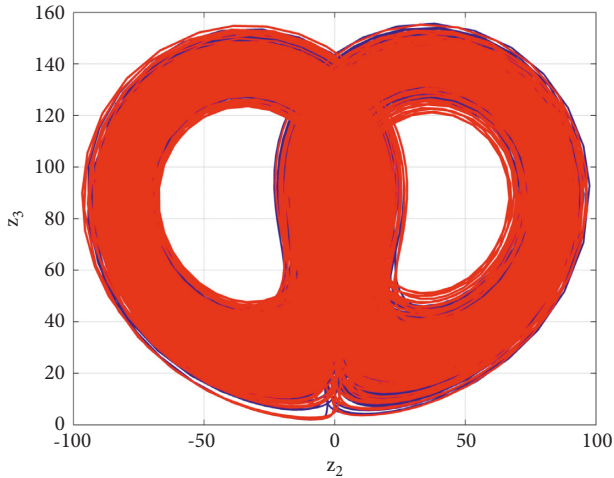


FIGURE 27: The coexistence of chaotic attractors for system (1) projected in the  $(z_2, z_3)$  coordinate plane for the choice of parameters  $(a, b, c, d) = (25, 14, 90, 6)$ .

$$\tau_1 = 1.970, \tau_2 = 0.341, \tau_3 = 0, \tau_4 = -36.313. \quad (38)$$

The red hyperchaotic attractor begins from  $W_0$  and characterized by the following LE spectrum:

$$\tau_1 = 1.958, \tau_2 = 0.339, \tau_3 = 0, \tau_4 = -36.300. \quad (39)$$

### 5. Electronic Circuit Design for the New Hyperchaotic Two-Scroll System

We detail the electronic circuit realization of the proposed two-scroll hyperchaotic model using MultiSim software (Version 14). Figure 29 depicts an analog electronic circuit for the implementation of the proposed hyperchaotic circuit, which includes two analog multipliers (AD63JN), seven

operational amplifiers (TL083CD), seventeen resistors, and four capacitors.

For the circuit design, we rescale the two-scroll model (1) using the following transformation of coordinates:

$$Z_i = \frac{1}{2}z_i, \quad (i = 1, 2, 3, 4). \quad (40)$$

Replacing the old variables with the new variables on the new 4-D hyperchaotic system (1), we obtain the following system:

$$\begin{cases} \dot{Z}_1 = a(Z_2 - Z_1) - Z_3 + Z_4, \\ \dot{Z}_2 = cZ_1 - Z_2 - 2Z_1Z_3 + Z_4, \\ \dot{Z}_3 = -bZ_3 + 2Z_1Z_2, \\ \dot{Z}_4 = -dZ_2. \end{cases} \quad (41)$$

Using Kirchhoff's electrical circuit laws, we derive the circuit model for the rescaled hyperchaotic model (41) as follows:

$$\begin{cases} C_1\dot{Z}_1 = \frac{1}{R_1}Z_2 - \frac{1}{R_2}Z_1 - \frac{1}{R_3}Z_3 + \frac{1}{R_4}Z_4, \\ C_2\dot{Z}_2 = \frac{1}{R_5}Z_1 - \frac{1}{R_6}Z_2 - \frac{1}{10R_7}Z_1Z_3 + \frac{1}{R_8}Z_4, \\ C_3\dot{Z}_3 = -\frac{1}{R_9}Z_3 + \frac{1}{10R_{10}}Z_1Z_2, \\ C_4\dot{Z}_4 = -\frac{1}{R_{11}}Z_2. \end{cases} \quad (42)$$

Here,  $Z_1, Z_2, Z_3, Z_4$  are the voltages across the capacitors,  $C_1, C_2, C_3, C_4$ , respectively. We choose the values of the circuitual elements as follows:



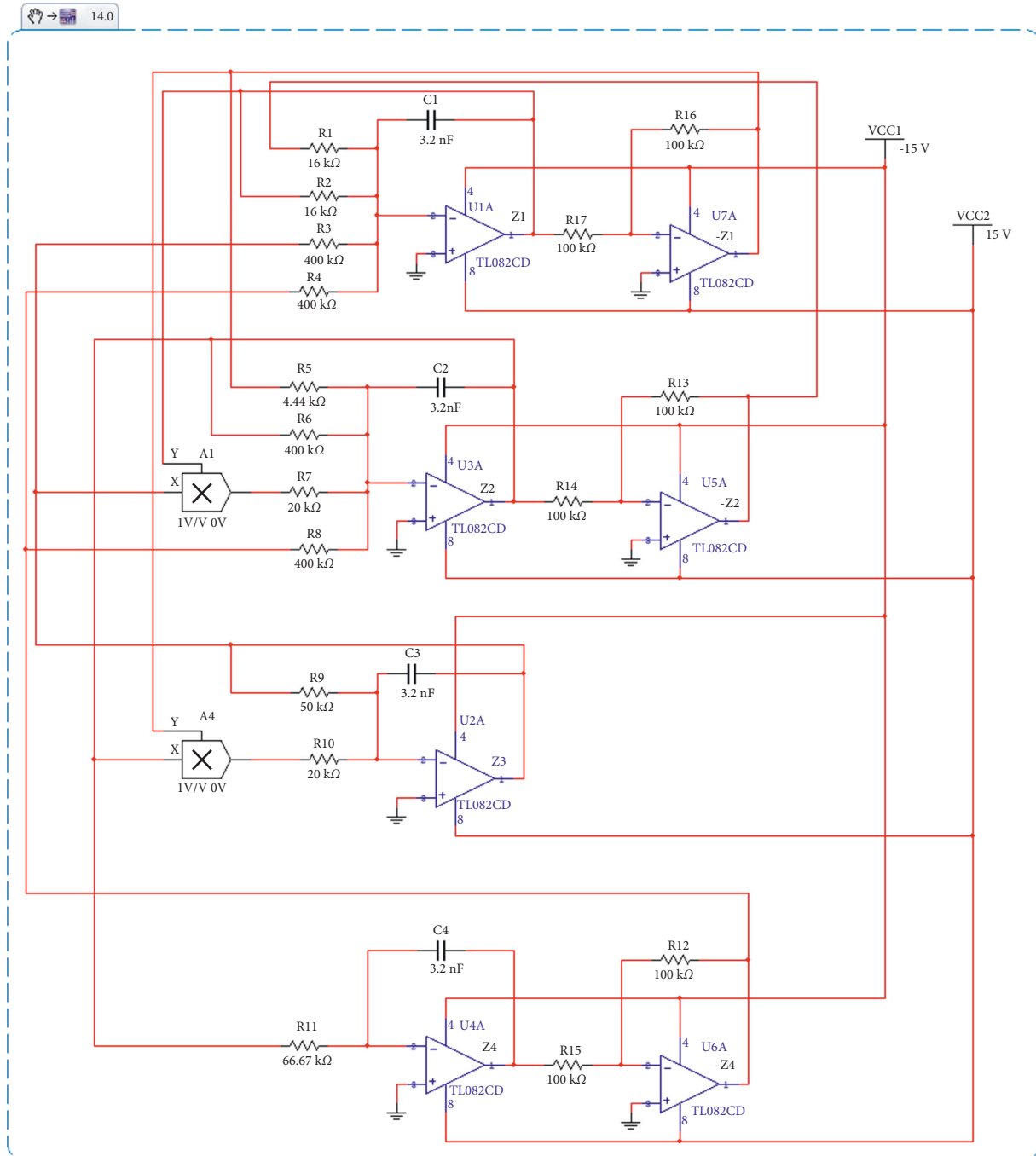


FIGURE 29: The electronic circuit design for the 4-D hyperchaotic system (29).

$$R_1 = R_2 = 16k\Omega, \quad R_3 = R_4 = R_6 = R_8 = 400k\Omega, \quad R_5 = 4.44k\Omega,$$

$$R_7 = R_{10} = 20k\Omega, \quad R_9 = 50k\Omega, \quad R_{11} = 66.67k\Omega,$$

$$R_{12} = R_{13} = R_{14} = R_{15} = R_{16} = R_{17} = 100k\Omega,$$

$$C_1 = C_2 = C_3 = C_4 = 3.2nF.$$

With MultiSim 14.0, we obtain the experiment observations of system (42) in Figures 30–33. It can be seen that the good qualitative agreement between the MATLAB simulations (Figures 1–4) and the MultiSim results

(Figures 30–33) of the hyperchaotic two-scroll system is confirmed.

## 6. FPGA Implementation of the New Two-Scroll Hyperchaotic Model

The use of field-programmable gate arrays (FPGA) has shown advantages in the implementation of chaotic and hyperchaotic systems, as done in [31–34]. One can find guidelines on applying numerical methods that are directly

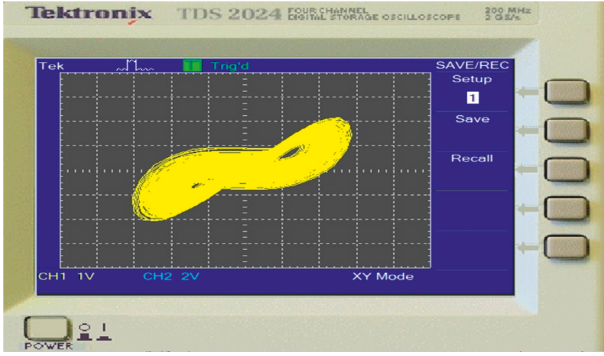


FIGURE 30: Electronic circuit simulation using MultiSim 14.0 for the new hyperchaotic two-scroll circuit (42) in the  $(Z_1, Z_2)$ -coordinate plane.

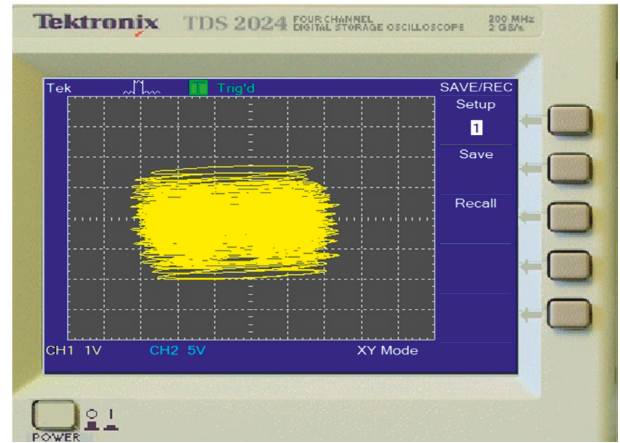


FIGURE 33: Electronic circuit simulation using MultiSim 14.0 for the new hyperchaotic two-scroll circuit (42) in the  $(Z_1, Z_4)$ -coordinate plane.

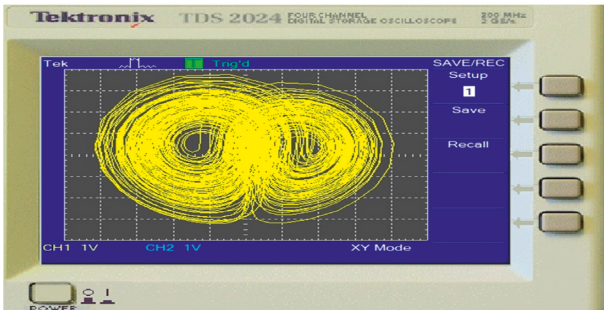


FIGURE 31: Electronic circuit simulation using MultiSim 14.0 for the new hyperchaotic two-scroll circuit (42) in the  $(Z_2, Z_3)$ -coordinate plane.

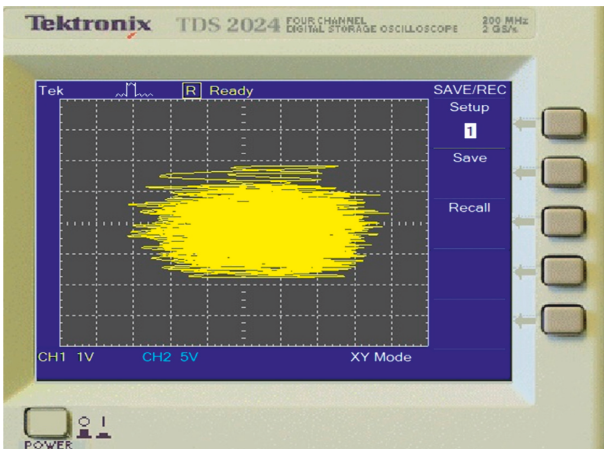


FIGURE 32: Electronic circuit simulation using MultiSim 14.0 for the new hyperchaotic two-scroll circuit (42) in the  $(Z_3, Z_4)$ -coordinate plane.

synthesized into an FPGA [35]. In this work, we show the experimental results of the FPGA implementation of proposed model (1) by applying two common numerical methods. The first one is the forward Euler, whose iterative algorithm is given in equation (30), and the second one is the

implicit algorithm known as trapezoidal method that is given in equation (31).

$$x_{n+1} = x_n + hf(x_n, t_n),$$

$$x_{n+1} = x_n + \frac{h}{2} [f(x_n, t_n) + f(x_{n+1}, t_{n+1})]. \quad (43)$$

It is well-known that a system of ordinary differential equations, as the one associated for the proposed model (1), can be solved by discretizing the equations using a numerical method. In the case of applying the forward Euler, one gets the discrete equations given by equation (44), from which one can clearly see the requirement of arithmetic operations as adders, subtractors, and multipliers. The control of the iterations is performed by designing a state machine control that includes registers, as detailed in [35], where one can see the design of the arithmetic blocks, and a single-constant multiplier block to reduce hardware resources.

$$\begin{cases} z_1[n+1] = z_1[n] + h(a(z_2[n] - z_1[n]) - z_3[n] + z_4[n]), \\ z_2[n+1] = z_2[n] + h(cz_1[n] - z_2[n] - z_1[n]z_3[n] + z_4[n]), \\ z_3[n+1] = z_3[n] + h(-bz_3[n] + z_1[n]z_2[n]), \\ z_4[n+1] = z_4[n] + h(-dz_2[n]). \end{cases} \quad (44)$$

The design of each digital block requires the definition of the number of bits to be processed. In this case, the computer arithmetic is performed by applying fixed-point representation with the format 15.49. The 64 bits are distributed in one bit for the sign, 14 for the integer part, and 49 bit for the fractional part. The bit distribution considers the maximum amplitude values that can appear for each state variable during the processing of the data. For example, from the simulation results of the new 4-D hyperchaotic system (1), the four state variables have amplitudes in the range  $[-199.02, 342.50]$ , but in the discretization process by applying the numerical methods, an analysis of all the internal arithmetic operations, mainly those that result during the

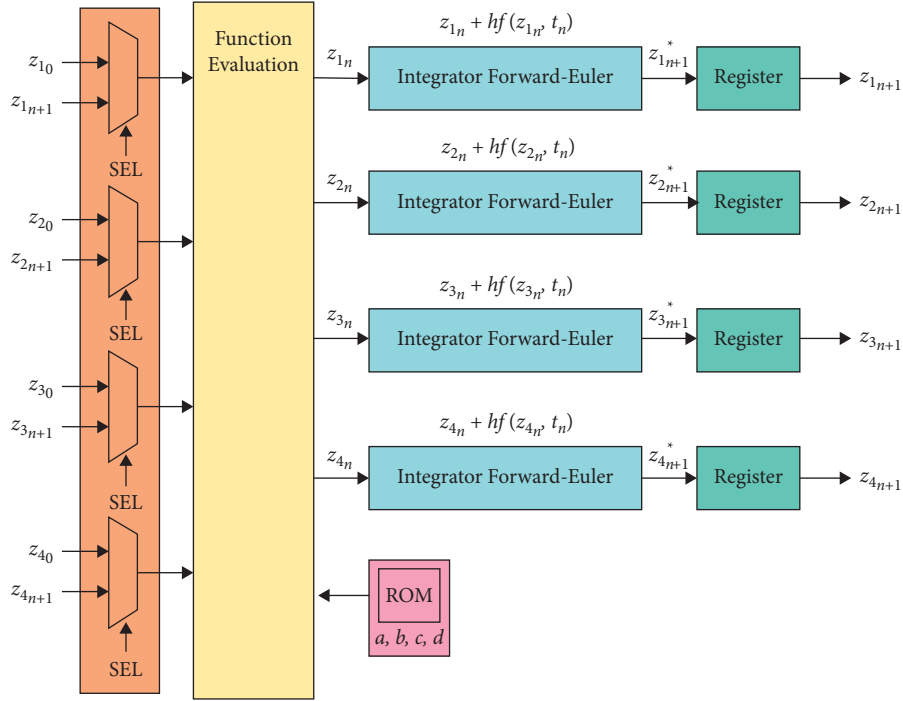


FIGURE 34: Block diagram of the discretization of the proposed model (1) using the forward Euler method.

TABLE 1: Hardware resources for the FPGA design of (1) using the FPGA basys 3 xilinx artix-7 XC7A35T-ICPG236C using two numerical methods with  $h = 0.001$ .

Resources	Forward Euler	Trapezoidal	Available
LUTs	4679	10570	20,800
FF	567	1253	41,600
DSP	45	82	90
Multipliers	10	24	–
Adders	5	18	–
Subtractors	6	12	–
Clock cycles by iteration	2	3	–
Latency (ns)	80	120	–

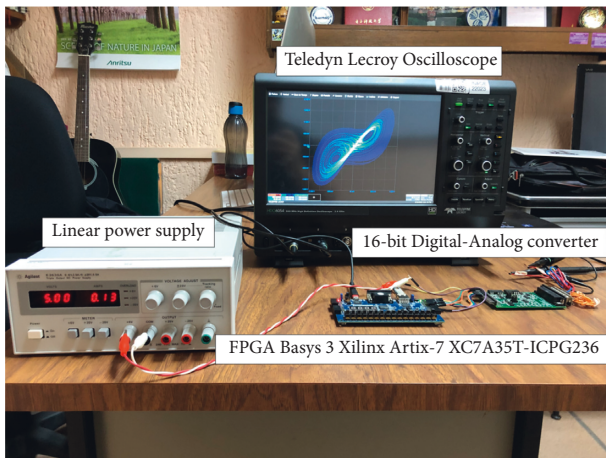


FIGURE 35: Experimental setup to measure the attractors of the proposed model (1) using a FPGA basys 3 xilinx artix-7 XC7A35T-ICPG236, a 16 bit digital-analog converter, a linear power supply and a keysight oscilloscope to visualize the hyperchaotic attractor.

multiplications among state variables, resulted in an absolute range of values in the range  $[-11299.60, 11116.51]$ , thus leading to use the format 15.49.

Figure 34 depicts a block diagram showing the discretization of the proposed model (1) using the forward Euler method given in equation (32). The registers are controlled by a state machine to perform the iteration process. The FPGA implementation is also done in a similar way by applying the trapezoidal method so that the hardware resources for the FPGA design using the FPGA Basys 3 Xilinx Artix-7 XC7A35T-ICPG236C are as summarized in Table 1. One can see the number of lookup tables (LUTs), flip-flops (FF), digital signal processors (DSP), multipliers, adders, and subtractors. We also give the number of clock cycles required by an iteration, and the latency in nano-seconds (ns).

The FPGA experimental setup for the proposed model (1) is shown in Figure 35. Furthermore, the FPGA experimental outputs of (1) are depicted in Figures 36–39.

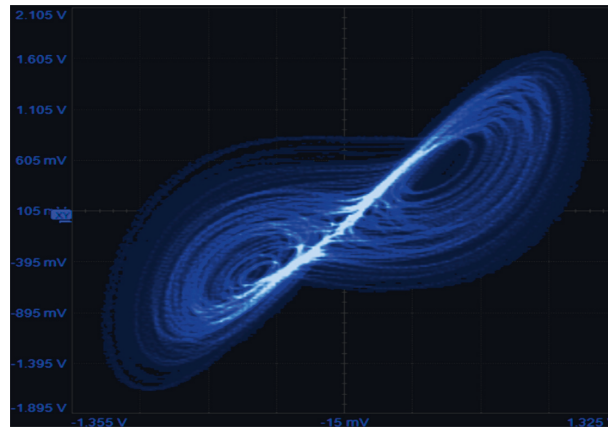


FIGURE 36: Experimental hyperchaotic attractor of the proposed model (1) in the  $(z_1, z_2)$ - plane.

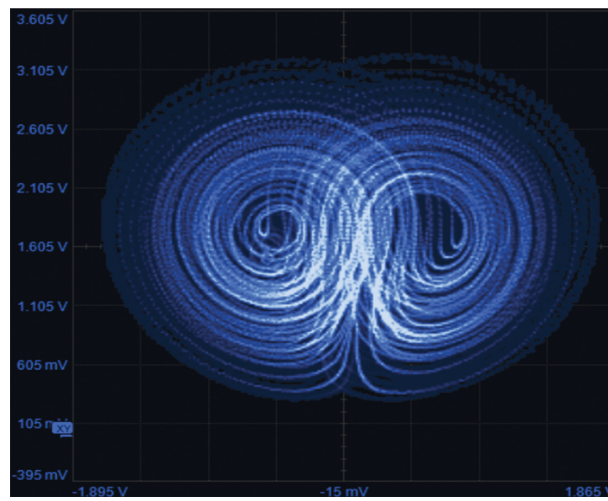


FIGURE 37: Experimental hyperchaotic attractor of the proposed model (1) in the  $(z_2, z_3)$ - plane.

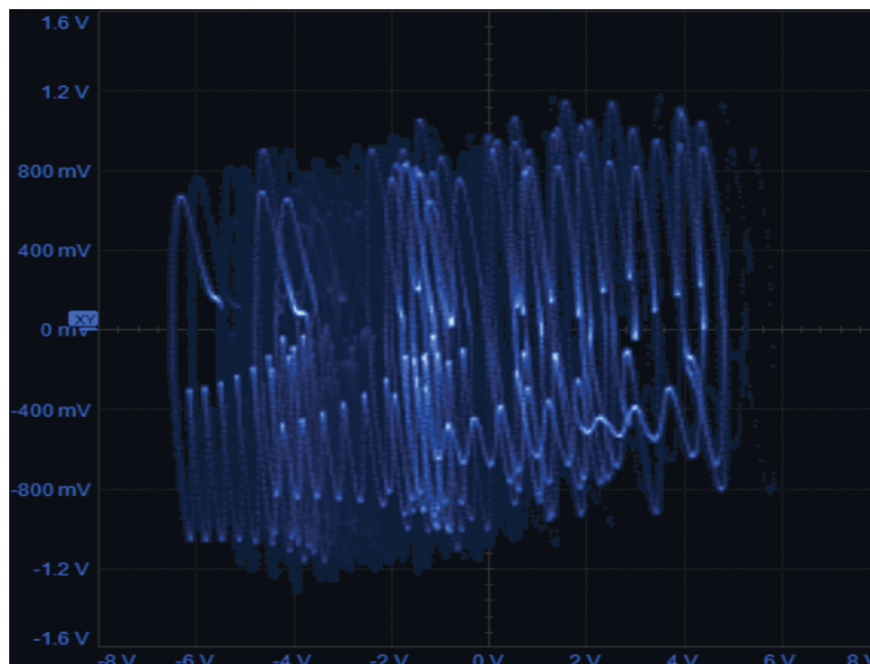


FIGURE 38: Experimental hyperchaotic attractor of the proposed model (1) in the  $(z_3, z_4)$ - plane.



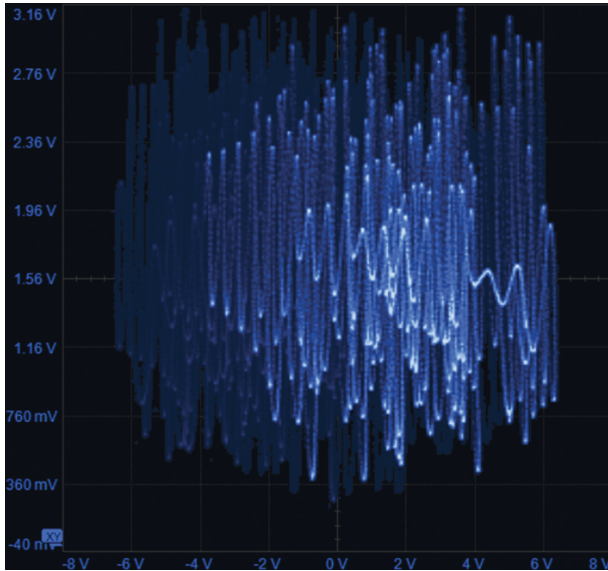


FIGURE 39: Experimental hyperchaotic attractor of the proposed model (1) in the  $(z_1, z_4)$ - plane.

## 7. Conclusions

In this research work, we reported our findings of a new four-dimensional two-scroll hyperchaotic system having only two quadratic nonlinearities. We conducted a detailed dynamic study of the proposed model and noted the co-existence of attractors for fixed parameter values but different initial states. Since the maximal Lyapunov exponent (MLE) of the two-scroll system is  $\tau_{\max} = 2.6174$ , we deduced that the two-scroll system (1) has high complexity. Also, a design for an electronic circuit has been made for the new hyperchaotic system using MultiSim (Version 14). The experimental observation of the hyperchaotic attractors has been shown from the FPGA implementation by applying numerical methods, *viz.* forward Euler method and trapezoidal method. It was observed that the FPGA experimental results using the forward Euler discretization method are in good agreement with the MATLAB simulation results of the proposed hyperchaotic two-scroll system.

## Data Availability

The data used for this research paper are available on request from the corresponding author.

## Conflicts of Interest

The authors declare no conflicts of interest on the publication of this paper.





## References

- [1] Y. Wang, H. Li, G. Yan, and M. Chen, "Predefined-time chaos synchronization of memristor chaotic systems by using simplified control inputs," *Chaos, Solitons & Fractals*, vol. 161, Article ID 112282, 2022.
- [2] Y. Dong, S. Yang, Y. Liang, and G. Wang, "Neuromorphic dynamics near the edge of chaos in memristive neurons," *Chaos, Solitons & Fractals*, vol. 160, Article ID 112241, 2022.
- [3] H. L. Luo, D. W. Ding, Z. L. Yang, and H. Xiao, "Coexisting behaviors of chaotic system with tri-stable locally active memristor and its application in color image encryption," *The European Physical Journal Plus*, vol. 137, no. 5, Article ID 607, 2022.
- [4] X. Wu, S. He, W. Tan, and H. Wang, "From memristor-modeled jerk system to the nonlinear systems with memristor," *Symmetry*, vol. 14, no. 4, Article ID 659, 2022.
- [5] Y. J. F. Kpomahou, A. Adomou, A. E. Yamadjako, and J. Djossou, "Effect of amplitude-modulated force on horse-shoe dynamics in Briggs–Rauscher chemical system modeled by a new parametric oscillator with asymmetric potential," *The European Physical Journal Plus*, vol. 137, no. 6, Article ID 679, 2022.
- [6] A. J. Adéchinan, Y. J. F. Kpomahou, L. A. Hinvi, and C. H. Miwadinou, "Chaos, coexisting attractors and chaos control in a nonlinear dissipative chemical oscillator," *Chinese Journal of Physics*, vol. 77, pp. 2684–2697, 2022.
- [7] S. Liu, Z. Sun, N. Zhao, and W. Xu, "Explosive transition in coupled oscillators through mixed attractive-repulsive interaction," *International Journal of Bifurcation and Chaos*, vol. 32, no. 2, Article ID 2250018, 2022.
- [8] H. Zhang, Z. Qin, Y. Zhang, D. Chen, J. Gen, and H. Qin, "A practical underwater information sensing system based on intermittent chaos under the background of Lévy noise," *EURASIP Journal on Wireless Communications and Networking*, vol. 2022, no. 1, Article ID 41, 2022.
- [9] W. Bao and C. Zhu, "A secure and robust image encryption algorithm based on compressive sensing and DNA coding," *Multimedia Tools and Applications*, vol. 81, no. 11, pp. 15977–15996, 2022.
- [10] H. Zhou, H. Xie, H. Zhang, and H. Zhang, "Parallel remote sensing image encryption algorithm based on chaotic map and DNA encoding," *Journal of Image and Graphics*, vol. 26, no. 5, pp. 1081–1094, 2022.
- [11] X. Gong, H. Wang, Y. Ji, and Y. Zhang, "Optical chaos generation and synchronization in secure communication with electro-optic coupling mutual injection," *Optics Communications*, vol. 521, Article ID 128565, 2022.
- [12] S. Xiang, M. Yang, and J. Wang, "Chaotic optical communications of 12.5-Gbaud OOK and 10-Gbaud QPSK signals based on mutual injection of semiconductor lasers," *Optics Letters*, vol. 47, no. 11, pp. 2818–2821, 2022.
- [13] N. Biswas and R. Mohamed I, "DCSK performance analysis of a chaos-based communication using a newly designed chaotic system," *International Journal of Nonlinear Sciences and Numerical Simulation*, vol. 23, no. 3-4, pp. 579–592, 2022.
- [14] G. Arthi, V. Thanikaiselvan, and R. Amirtharajan, "4D Hyperchaotic map and DNA encoding combined image encryption for secure communication," *Multimedia Tools and Applications*, vol. 81, no. 11, pp. 15859–15878, 2022.
- [15] B. S. Yu, Y. N. Tang, and K. Ji, "Chaotic behaviors of an in-plane tethered satellite system with elasticity," *Acta Astronautica*, vol. 193, pp. 395–405, 2022.
- [16] W. Quan, H. Wang, and Y. Ji, "Three-loop electro-optical phase chaotic secure communication system with time-delay signatures concealment and key space enhancement," *Optics Communications*, vol. 512, Article ID 128065, 2022.
- [17] C. Xiu, J. Fang, and Y. Liu, "Design and circuit implementation of a novel 5D memristive CNN hyperchaotic

- system,” *Chaos, Solitons & Fractals*, vol. 158, Article ID 112040, 2022.
- [18] H. Nazir, I. S. Bajwa, S. Abdullah, R. Kazmi, and M. Samiullah, “A color image encryption scheme combining hyperchaos and genetic codes,” *IEEE Access*, vol. 10, pp. 14480–14495, 2022.
- [19] Y. Y. Bian and W. X. Yu, “A secure communication method based on 6-D hyperchaos and circuit implementation,” *Telecommunication Systems*, vol. 77, no. 4, pp. 731–751, 2021.
- [20] M. Boumaraf and F. Merazka, “Secure speech coding communication using hyperchaotic key generators for AMR-WB codec,” *Multimedia Systems*, vol. 27, no. 2, pp. 247–269, 2021.
- [21] A. Ibraheem, “Switched dual compound–compound anti-synchronization of hyperchaotic dynamical systems,” *International Journal of Algorithms, Computing and Mathematics*, vol. 8, no. 3, Article ID 122, 2022.
- [22] M. Tang, G. Zeng, Y. Yang, and J. Chen, “A hyperchaotic image encryption scheme based on the triple dislocation of the Liu and Lorenz system,” *Optik*, vol. 261, Article ID 169133, 2022.
- [23] S. Li, Y. Wu, and G. Zheng, “Adaptive synchronization for hyperchaotic liu system,” *Frontiers in Physics*, vol. 9, Article ID 812048, 2022.
- [24] Y. Xiao, S. Zhang, and Y. Peng, “Dynamic investigations in a Stackelberg model with differentiated products and bounded rationality,” *Journal of Computational and Applied Mathematics*, vol. 414, Article ID 114409, 2022.
- [25] T. Peixe and A. Rodrigues, “Persistent strange attractors in 3D polymatrix replicators,” *Physica D: Nonlinear Phenomena*, vol. 438, Article ID 133346, 2022.
- [26] B. Zhou, Y. Jin, and H. Xu, “Subharmonic resonance and chaos for a class of vibration isolation system with two pairs of oblique springs,” *Applied Mathematical Modelling*, vol. 108, pp. 427–444, 2022.
- [27] S. Vaidyanathan, K. Benkouider, and A. Sambas, “A new multistable jerk chaotic system, its bifurcation analysis, backstepping control-based synchronization design and circuit simulation,” *Archives of Control Sciences*, vol. 32, no. 1, pp. 123–152, 2022.
- [28] S. S. De Sarkar, A. K. Sharma, and S. Chakraborty, “Chaos, antimonotonicity and coexisting attractors in Van der Pol oscillator based electronic circuit,” *Analog Integrated Circuits and Signal Processing*, vol. 110, no. 2, pp. 211–229, 2022.
- [29] P. Boriskov, “Chaotic LIF oscillator with variable resistance feedback and nonlinear rate coding,” *IEEE Transactions on Circuits and Systems II: Express Briefs*, vol. 69, no. 6, pp. 2982–2986, 2022.
- [30] S. Yan, Z. Song, and W. Shi, “Symmetric coexisting attractors in a novel memristors-based Chua’s chaotic system,” *Journal of Circuits, Systems, and Computers*, vol. 31, no. 07, Article ID 2250120, 2022.
- [31] M. D. Gupta and R. K. Chauhan, “Hardware efficient pseudo-random number generator using chen chaotic system on FPGA,” *Journal of Circuits, Systems, and Computers*, vol. 31, no. 03, Article ID 2250043, 2022.
- [32] W. A. Al-Musawi, W. A. Wali, and M. A. Ali Al-Ibadi, “Field-programmable gate array design of image encryption and decryption using Chua’s chaotic masking,” *International Journal of Electrical and Computer Engineering*, vol. 12, no. 3, pp. 2414–2424, 2022.
- [33] S. Cang, L. Wang, Y. Zhang, Z. Wang, and Z. Chen, “Bifurcation and chaos in a smooth 3D dynamical system extended from Nose-Hoover oscillator,” *Chaos Solitons*, vol. 158, no. 2, Article ID 112016, 2022.
- [34] H. Jia, Z. Chen, W. Shi, and G. Qi, “A new generalized Hamiltonian chaotic system with transient quasi-periodic flows and intermittent chaos,” *International Journal of Bifurcation and Chaos*, vol. 32, no. 2, 2022.
- [35] M. Alcin, M. Tuna, P. Erdogmus, and I. Koyuncu, “FPGA-based dual core TRNG design using Ring and Runge-Kutta-Butcher based on chaotic oscillator,” *Chaos Theory and Applications*, vol. 3, no. 1, pp. 20–28, 2021.

## Research Article

# Complex Dynamics and Effects of Memristive Load Using Current-Mode-Controlled in Buck Converter

**Alain Soup Tewa Kammogne** <sup>1</sup>, **Edwige Mache Kengne**,<sup>1</sup>  
**Sundarapandian Vaidyanathan** <sup>2</sup>, **Hilaire Bertrand Fotsin** <sup>1</sup>,  
**and Thomas Tatietse Tamo** <sup>1</sup>

<sup>1</sup>Laboratory of Condensed Matter, Electronics and Signal Processing (LAMACETS), Department of Physic, Faculty of Sciences, University of Dschang, P.O. Box 67, Dschang, Cameroon

<sup>2</sup>Research and Development Centre, Vel Tech University, Vel Nagar, Avadi, Chennai 600 062, Tamil Nadu, India

Correspondence should be addressed to Alain Soup Tewa Kammogne; kouaneteoua@yahoo.fr

Received 31 March 2022; Revised 13 May 2022; Accepted 24 May 2022; Published 13 July 2022

Academic Editor: Anibal Coronel

Copyright © 2022 Alain Soup Tewa Kammogne et al. This is an open access article distributed under the Creative Commons Attribution License, which permits unrestricted use, distribution, and reproduction in any medium, provided the original work is properly cited.

Electronic power converters are in a state of exhibiting some complex features which can be influenced by the converter's structure parameters and load, as well as its pulse period. In this paper, we propose to investigate these phenomena occurring in the dc/dc buck converter by carrying out the dynamics of the said system when it exhibits the fingerprints of frequency-dependent pinched hysteresis loops. The essential part of this study is consecrated to the nonlinear dynamics when the converter load is memristive. Under two kinds of switch states, the independent nonlinear models and equations are derived which provide a complete dynamics description of the system under investigation. The dynamics analysis is performed by making use of bifurcation tools, phase portraits, and two parameters Lyapunov diagrams showing that the system depicts very rich and striking behaviors such as periodic orbits, period-doubling bifurcation, quasiperiodicity, chaos, and pinched hysteresis loops of the memristive load. Finally, the numerical simulation results are in almost perfect agreement with the analog result obtained with PSIM. The results obtained in this work have not yet been reported in the literature to the best of our knowledge and thus deserve dissemination.

## 1. Introduction

Dc/dc power converters are considered as the most vital empowering devices of electrical and electronic engineering as they act as a buffer between a power source of electronic equipment and a load [1]. These devices are used to convert an unregulated dc voltage to a regulated or variable dc output voltage by stockpiling the input energy momentarily and debit the energy to the output stage to ensure adequate current and voltage regulation. They are also known to have a significant variety of complex nonlinear behaviors such as subharmonic oscillations bifurcation phenomena that can lead to chaotic phenomena, and period-1 oscillations, due to

switching actions and feedback control. We recall that the nonlinear dynamics have been experimentally observed in different types of dc/dc buck converters where there are a series of modulation strategies, such as current-mode control [2, 3], voltage-mode control [4, 5], PWM voltage-current hybrid control [6–10], hysteresis-current or -voltage control [10, 11], one-cycle control [12, 13], and model predictive control [14–16]. Unfortunately, the nonlinear switching of power converters can put their stability at risk and make them prone to exhibit various nonlinear instable phenomena. This can have harmful effects on the converter since stability and efficiency are two fundamental criteria for the design of these converters. It is therefore imperative to

understand and establish the mechanism of formation of various complex phenomena occurring in the buck converters when the circuit parameters, circuits topologies, control schemes, and load change.

Many researchers investigated the dynamic analysis of dc/dc converters according to the system parameters and loads in the literature. Several types of load are reported such as capacitive voltage load [17–19], the linear load [20–24], and the constant current load [25, 26]. The complete dynamic of the dc/dc converter is determined by the type of the load which leads to various complex phenomena with respect to different switching modes. For the sake of brevity, we mention the chaos issue, quasiperiodicity, and some stringent behavior such as the coexistence of attractors and pulse bursting, etc (the reader is referring to References [17, 19, 27] and the references therein). Other important characteristics such as chaos transition in buck-boost [28] and hidden attractors in multilevel dc/dc converters have been investigated by Zhusubaliyev and Wang [29], respectively. The dynamic modeling and analysis of the bidirectional dc/dc boost-buck converter for renewable energy applications were presented by Spier et al. [30], while Kamal and coworkers developed a buck-boost converter small signal model: dynamic analysis under system uncertainties [31]. Recently, the study of complex dynamics in dc/dc boost converter with dspace-based real-time controller is presented by Ghosh et al. [32]. Another relevant work is proposed by Mandal et al. in which the modeling and analysis of complex dynamics for dspace controlled closed-loop dc/dc boost converter is investigated. Despite extensive investigations on the complex behavior of the basic dc/dc topology converters over the past decade [33], such phenomena in the resonant dc/dc converters with memristive load issues remain largely unexplored in the buck converter which still remains challenging and thus deserves more dissemination.

Motivated by the pioneer works of Zhang and Bao dealing with the dynamical behaviors and circuit experiments of the switching dc/dc boost converter have been efficiently studied [34]. In addition, the dynamical effects of memristive load on peak current mode buck-boosts switching converter have been considered [35] which shows that the memristors can be applied to create very complex dynamics (rich texts are provided in References [36, 37]). Due to various applications of this device, it is very important to demonstrate that the current-mode-controlled buck converter with memristance load has a large impact on the exhibited nonlinear dynamics such as chaotic and subharmonic oscillations. We then investigate in this paper the nonlinear dynamical behaviors, i.e., chaotic and subharmonic oscillations, of the dc/dc buck converter with memristance load by numerical simulations and PSIM circuit analysis.

The rest of the paper is organized as follows. In Section 2, the circuit topology and fundamental operating principle of the current-mode-controlled dc/dc buck converter are introduced, respectively. Section 3 presents the system equations and their dimensionless forms based on the

schematic of the buck converter with memristance load. We discuss the equilibrium points of these dimensionless circuit systems and their stability in Section 4. Section 5 is devoted to the forming mechanism of the chaotic and subharmonic dynamics through numerical simulations. Furthermore, the PSIM circuit topology is designed and the results are in perfect agreement with the numerical plots in Section 6. Finally, some conclusions are drawn in Section 7.

## 2. Background and System Description

In this section, we present a basic knowledge on the dc/dc buck converter with a memristive load. Before designing and analyzing the circuit system, it is necessary to mention that, so far, various dc/dc power converters with resistance load have been predominantly studied, with different types of converters such as boost, buck-boost, and buck converters. The single-stage buck converter presents some specific design details on the dynamics which is highly interesting to investigate in behavior when the load is memristive, as presented in Figure 1.

## 3. dc/dc Single-Stage Buck Converter

A single dc/dc buck power converter under investigation is presented in Figure 1. The inductor and capacitor stand as energy storage elements, two semiconductors such as diode and the switch ensures two conduction modes of the circuit, the current-mode-controlled feedback loop consists of a comparator  $U$  and an RS trigger, and the load which can be regarded as a memristive load. Let us denote the reference current as  $I_{ref}$  and the current through inductor  $L$  by  $I$ . The fundamental operation of a buck converter consists of two distinct states (i.e., ON-state and OFF-state), which can be described as in (Table 1).

In summary, the states of the buck converter are controlled by the switch  $S$ . As long as the switch  $S$  is neither on nor off, both ON-state and OFF-state occur in a switching period. From the circuit of Figure 1, it is not obvious to obtain the link between the switching period  $T_s$  and the pulse period  $T$  of the clock; their ratio depends strongly on the dynamical behaviors of the buck converter. This measuring element remains fixed or variable when the buck converter is periodic or quasiperiodic, respectively.

*3.1. Modeling of the Memristor.* Memristor is commonly known as the fourth key circuit element, first introduced by Chua in 1971 [38]. In exact terms, memristor has an elegant effect to memorize the past quantity of electric charge. The current-voltage ( $i, v$ ) is known as a fingerprint of a memristor i.e., it displays a pinched hysteresis loop whose shape varies with frequency. The fundamental mathematical expressions describing the memristor are defined as follows:  $v_M = M(\sigma)i_M$  or  $i_M = W(\varphi)v_M$  where  $M(\sigma)$  and  $W(\varphi)$  denote the memristor controlled by charge  $\sigma$  and flux  $\varphi$ , respectively, which satisfies the following relations:



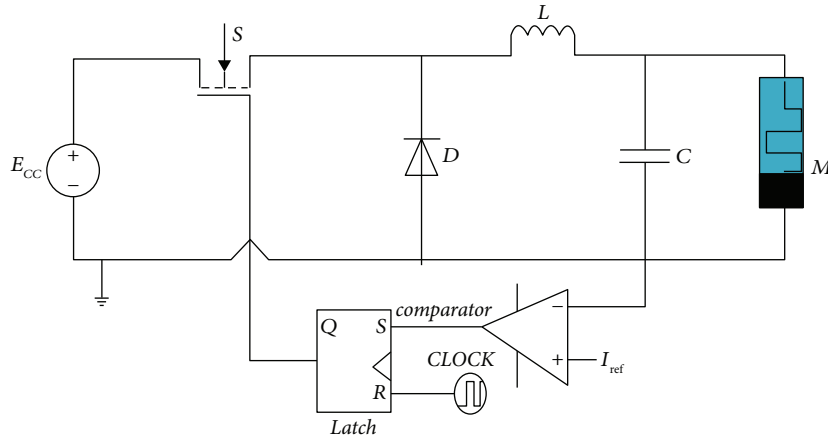


FIGURE 1: A novel circuit system having a dc/dc buck converter and a memristance load.

TABLE 1: Operation principle of the buck converter.

Switch	Initial value of $i_L$	Current variation	Buck state
ON	$i_L(0) = I_{\min}$	$i_L$ increasing and reaches $I_{\text{ref}}$	ON-state
OFF	$i_L(T_S/2) = I_{\text{ref}}$	$i_L$ pass through the diode $D$ and the capacitor $C$	OFF-state

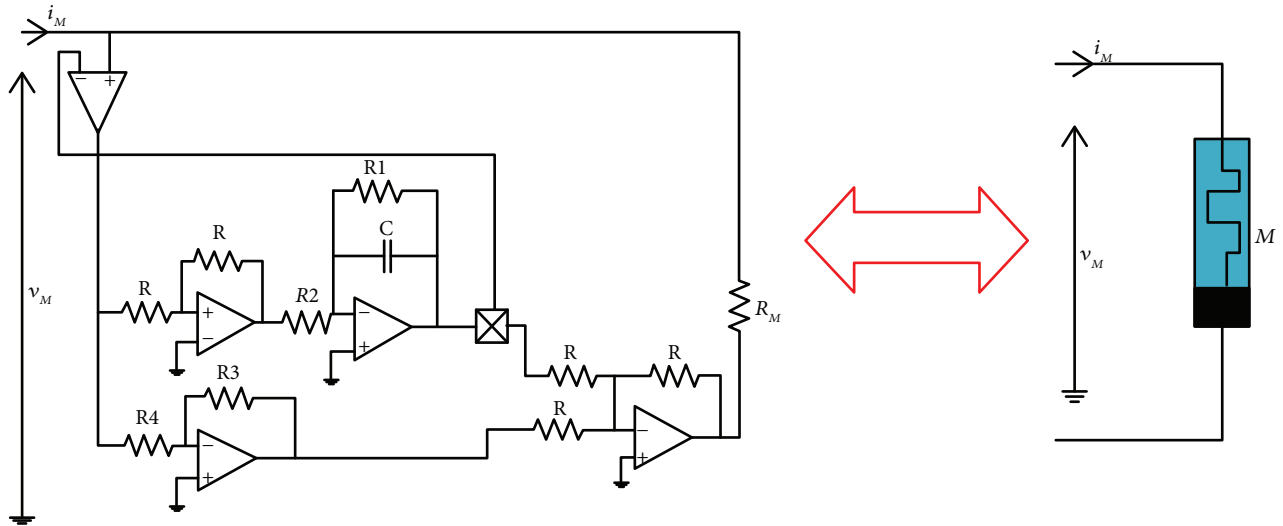


FIGURE 2: Memristive load emulator circuit. Electro-symbol of a memristor.

$$\begin{cases} \frac{dq}{dt} = h(i_M, \sigma, z), \\ \frac{d\varphi}{dt} = k(v_M, \varphi, z), \end{cases} \quad (1)$$

where  $h(i_M, \sigma, z)$  and  $k(v_M, \varphi, z)$  denote the internal state functions of a memristor.

Using Kirchhoff laws and some techniques for circuits analysis, we derive the following equations from Figure 2;

$$\begin{cases} i_M = \left[ \left( \frac{1}{R_M} - \frac{R_3}{R_4 R_M} \right) + \frac{1}{R_M} \varphi \right] v_M, \\ \frac{d\varphi}{dt} = \frac{v_M}{R_2 C} - \frac{\varphi}{R_1 C}. \end{cases} \quad (2)$$

Letting  $v_M = v_c$ ,  $(1/R_2 C) = \alpha m$ ,  $(1/R_1 C) = \alpha n$ ,  $p = (R_3/R_4 R_M) - (1/R_M)$ ,  $r = (1/R_M)$ , equation (2) becomes

$$\begin{cases} i_M = (r\varphi - p)v_M, \\ \frac{d\varphi}{dt} = \alpha(mv_M - n\varphi), \end{cases} \quad (3)$$

where  $i_M$  is the current passing through the memristive emulator (emulator refers to the electronic circuit that imitates the behavior of a complex phenomenon) load where the simplified electro-symbol is represented in Figure 2. The circuit parameters of the memristive load emulator are recorded in Table 2. Taking the input voltage of the terminal of the memristor load emulator as  $v_M = 4 \sin(5000\pi t)V$  and  $f$  chosen as 200 Hz. The loci in the  $v_M - i_M$  phase plane and the memductance curves are plotted in Figures 3(a)–3(d).

TABLE 2: Parameter values.

Circuit component	Values
CLOCK frequency $f$	5000 Hz
Inductance $L$	0.6 mH
Capacitance $C$	200 $\mu$ F
DC source V-I	12 V
Resistance $R_3$	30 k $\Omega$
Resistance $R$	10 $\Omega$
Reference current $I_{\text{ref}}$	0.6 A
Resistance $R_1$	5 k $\Omega$
Resistance $R_2$	10 k $\Omega$
Resistance $R_M$	1 $\Omega$
Resistance $R_4$	10 k $\Omega$

From these figures, we observe the zero-crossing property of the memristor which stipulates that the output  $i_M$  is always equal to the input  $v_{\text{in}}$  at zero. This important feature shows the existence of memristive fingerprint. We recall that, in the past few years, various memristor emulators implemented by already-existing electronic components have been reported in the literature [4, 39]. Most of the hardware topologies mainly include multiplier-based memristor equivalent circuits [40] and op-amps. Many researchers used different memristive loads to capture some special dynamical behaviors in memristive systems [41] and the references therein. Compared with other memristor emulators reported previously, the memristor emulator shown in Figure 2 presents an important feature. The hysteresis curve is located in the quadrants (1 and 3); instead, in references [35, 38], the same curve is located in the quadrants (2 and 4) which corresponds respectively to the active and passive zone of the operation of the memristor. As an active device (as in our case), it provides energy to the system and also allows for chaotic oscillations. However, as a passive device, it consumes energy in the system and obtaining oscillations can only be possible when exploiting a nonlinearity of the system, not of the memristor.

*Remark 1.* We note that the hysteresis loop falls into the second and the fourth quadrants. The memristor is a passive component and then efficiently stores information because the value of its electrical resistance changes permanently when a current is applied. A memristor can also have a high resistance value and a low resistance value. For instance, for a very high resistance value, it is observed that the resulting characteristic is located in the first and fourth quadrants, and for a low resistance value, it can be observed in the second and the third quadrants [42].

*Remark 2.* In real applications, there is no resistive load in nature because the linear component does not exist in real life. Since the load can reveal a plethora of complex behaviors, it seems interesting to investigate the case that the load is characterized by the hysteresis phenomenon such as memristor. We recall that the intrinsic nature of the memristor modifies the current-voltage characteristic of the converter and has a considerable impact on the dynamics of the buck converter.

*3.2. System Description.* We recall that the analysis of the dynamics is strongly determined by the state of the switch. We then propose to obtain the mathematical model from Figure 1 based on the electrical circuit analysis.

*Case 1.* Switch  $D$  is ON

When the switch  $S$  is ON, there are two independent loops denoted by red dashed lines in Figure 4. According to Kirchhoff's law, we have

$$L \frac{di_L}{dt} = E - v_c, \quad (4)$$

$$C \frac{dv_c}{dt} = i_L - (r\varphi - p)v_c,$$

where  $v_c$  denotes the voltage across the flux contused memristor. If we consider the expression  $(d\varphi/dt) = \alpha(mv_c - n\varphi)$  as the memristor's internal state of function, we derive the following equations:

$$\begin{aligned} L \frac{di_L}{dt} &= E - v_c, \\ C \frac{dv_c}{dt} &= i_L - (r\varphi - p)v_c, \\ \frac{d\varphi}{dt} &= \alpha(mv_c - n\varphi). \end{aligned} \quad (5)$$

Equation (4) is the state of equation when the circuit of Figure 2 is in the ON-state. This state will be sustained until  $i$  reaches  $i_{\text{ref}}$ .

*Case 1.* Switch  $S$  is OFF

When the switch  $S$  is OFF, the diode  $D$  conducts. Also, another two independent loops denoted by red dashed line are shown in Figure 4. Combining these two loop equations, we obtain

$$\begin{aligned} L \frac{di_L}{dt} &= -v_c, \\ C \frac{dv_c}{dt} &= i_L - (r\varphi - p)v_c, \\ \frac{d\varphi}{dt} &= \alpha(mv_c - n\varphi). \end{aligned} \quad (6)$$

These two system equations can be summarized into the following system of equations as follows:

$$\begin{aligned} \frac{di_L}{dt} &= -a_1(E(1-u) - v_c), \\ \frac{dv_c}{dt} &= a_2(i_L - (r\varphi - p)v_c), \\ \frac{d\varphi}{dt} &= \alpha(mv_c - n\varphi), \end{aligned} \quad (7)$$

where  $u = \begin{cases} 1, & \text{for turn-off} \\ 0, & \text{for turn-on} \end{cases}$ .

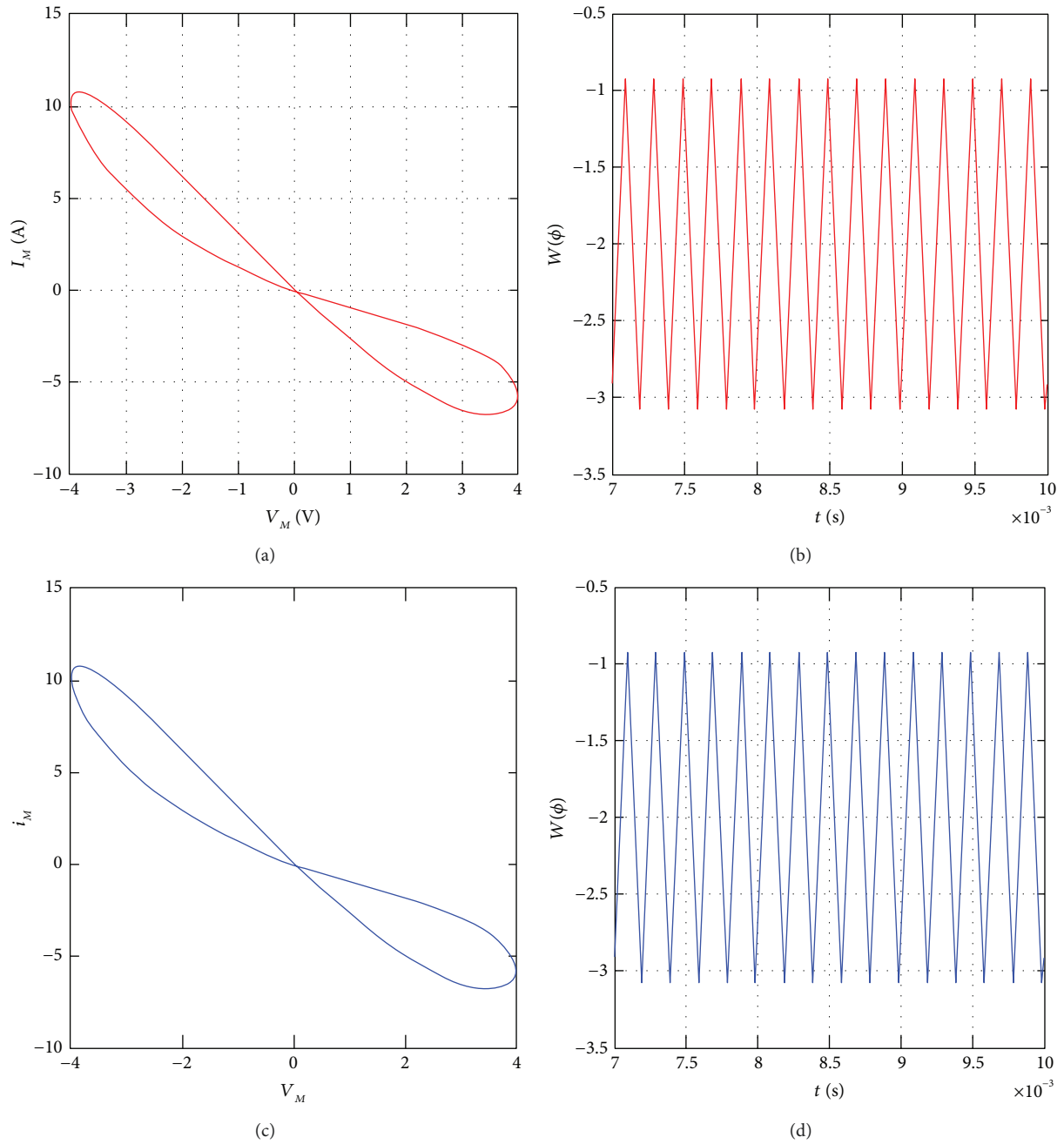


FIGURE 3: Numerical and analog simulation of the pinched hysteresis loops and memductance curves of the memristive load. (a, c) PSIM circuit simulations; (b, d) Fortran numerical simulations; (a, b) pinched hysteresis loops in the  $(v_M - i_M)$  plane; (c, d) memductance curves versus time.

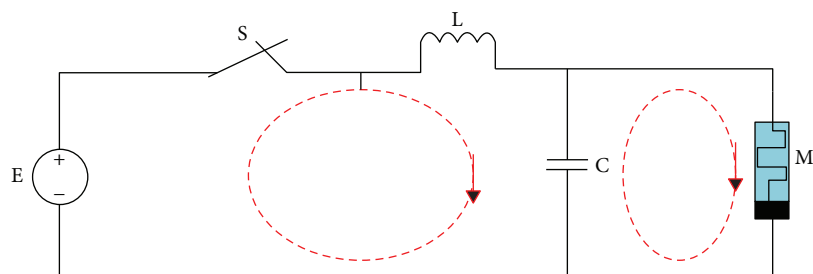


FIGURE 4: Electrical circuit of a switch ON buck chopper.

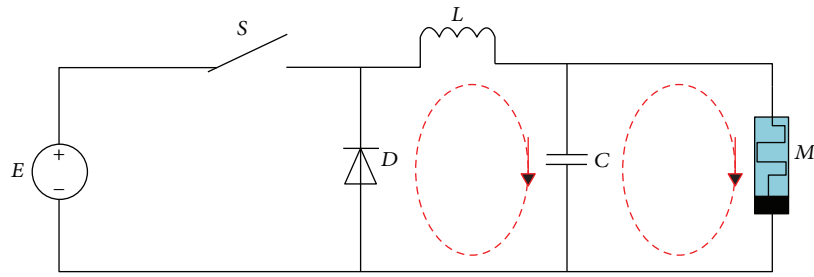


FIGURE 5: Electrical circuit of a switch OFF buck chopper.

TABLE 3: Nature of the roots of the characteristic equation computed for various values of E.

Values of the bifurcation parameter (E)	Eigenvalues at $(\lambda_1, \lambda_2, \lambda_3)$ nontrivial fixed $O_0(((mr/n)E - p)E, E, (m/n)E)$	Eigenvalues at $(\lambda_1, \lambda_2, \lambda_3)$ the origin $O_1(0, 0, 0)$
$E = 0$	$-2.000 \times 10^4; 0.9082 \times 10^4; 0.0918 \times 10^4$ (unstable)	$-2.000 \times 10^4; 0.9082 \times 10^4, 0.0918 \times 10^4$ ; (unstable)
$E = 5$	$(-1.0968 \pm 1.3254i) \times 10^4; -1.0563 \times 10^4$ (stable)	$-2.000 \times 10^4, 0.9082 \times 10^4; 0.0918 \times 10^4$ (unstable)
$E = 8$	$(-1.4861 \pm 1.9474i) \times 10^4, -0.0278 \times 10^4$ ; (stable)	$-2.000 \times 10^4; 0.9082 \times 10^4; 0.0918 \times 10^4$ (unstable)
$E = 12$	$(-1.9917 \pm 2.4597i) \times 10^4, -0.0166 \times 10^4$ ; (stable)	$-2.000 \times 10^4; 0.9082 \times 10^4; 0.0918 \times 10^4$ (unstable)

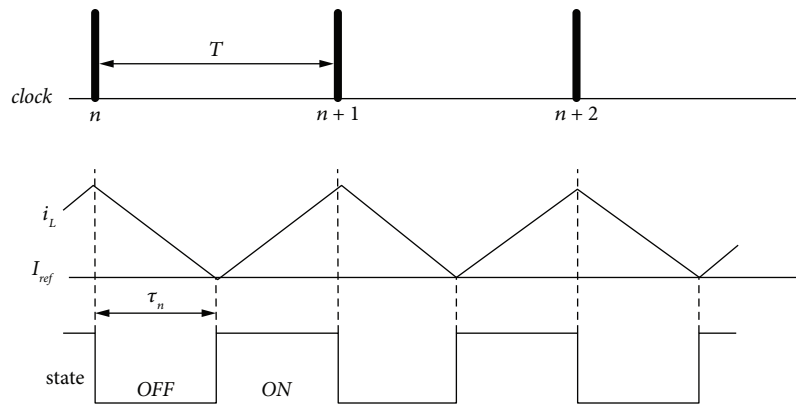


FIGURE 6: Operation waveforms  $i_L$  operating in CCM.

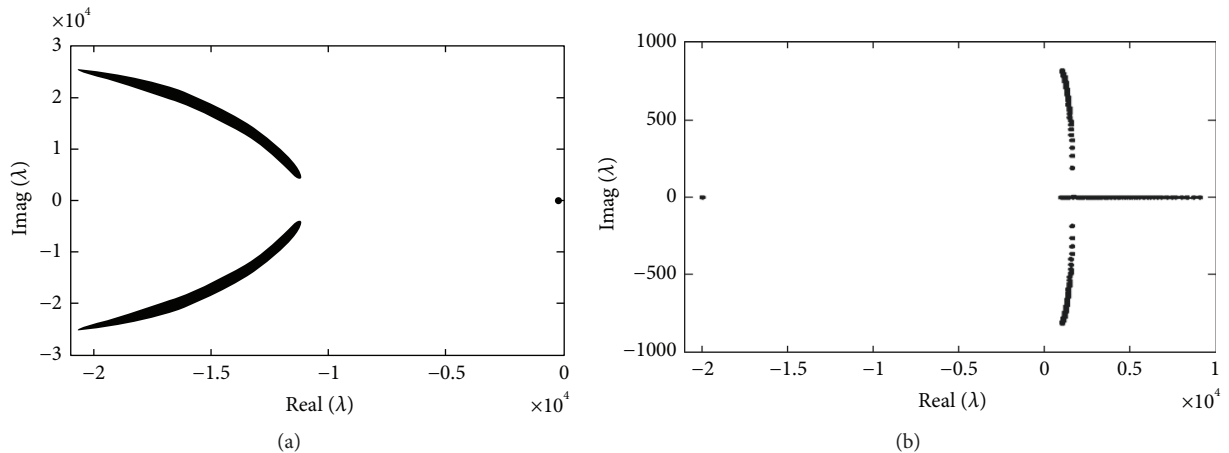


FIGURE 7: Stability analysis for  $u = 0$  (a) and  $u = 1$  (b), stability curves (a, b) plotted with the set of parameters as follows:  $n = 2; m = 1; p = 2; r = 1; \alpha = 10000; L = 0.6 \text{ mH}; E \in [9.5 \text{ V}, 12.5 \text{ V}]$  and  $C \in [200 \mu\text{F}, 1 \text{ mF}]$ .

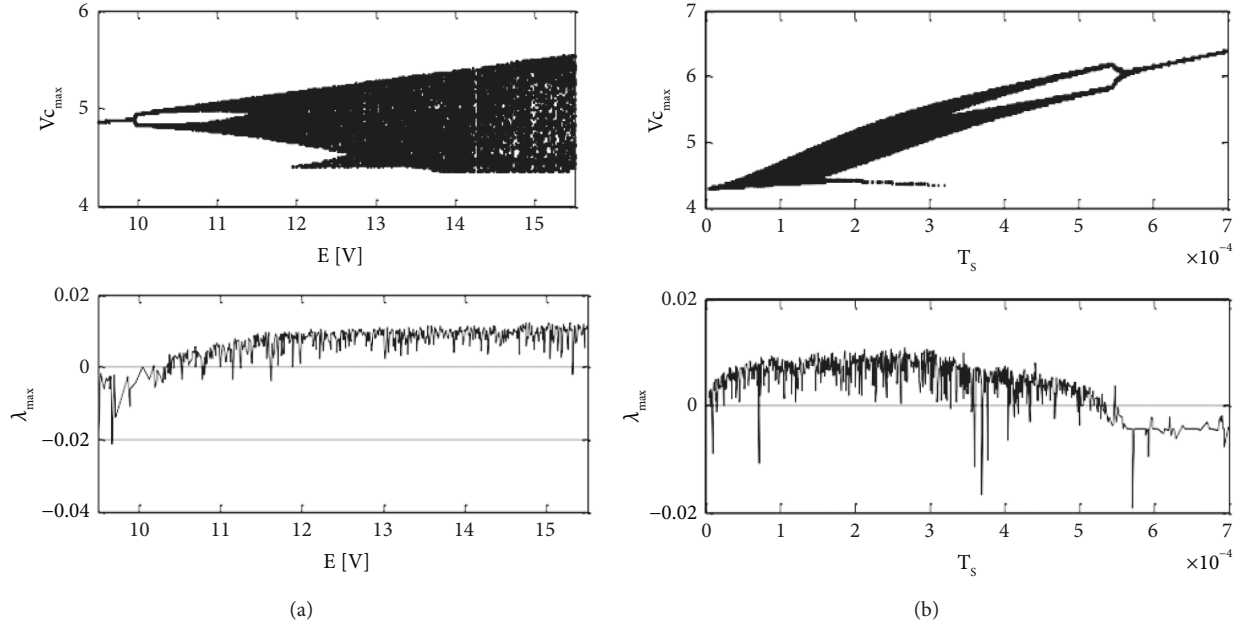


FIGURE 8: Bifurcation diagram versus  $E$  and  $T_s$ : (a)  $E \in [10; 16]$ ; (b)  $T_s \in [0; 7 \times 10^4]$  and the corresponding graph of maximum Lyapunov exponent. A positive value of Lyapunov exponent indicates chaos while regular oscillations are related to negative values of Lyapunov exponent.

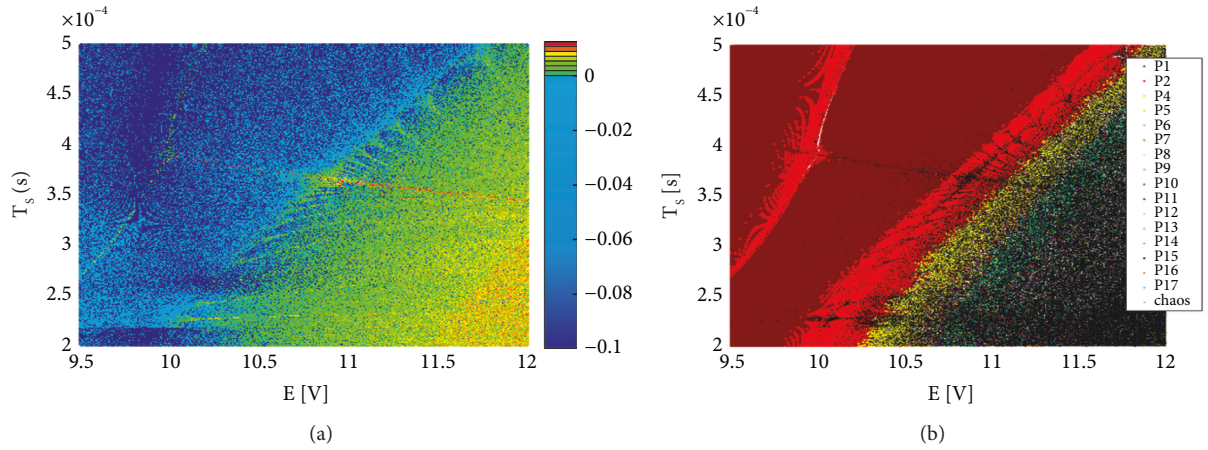


FIGURE 9: Dynamical domain shown in the two parameters space  $(T_s, E)$  is the boundary regions of each dynamical feature in the Buck converter. (a) Periodic oscillations are revealed by red region, while chaotic oscillations are manifested by a continuously changing black region bifurcation diagram and (b) the corresponding two diagram Lyapunov exponents.  $E$  versus parameter  $T_s$ .

There are two states for the continuous mode which are linked. Figure 5 presents the dynamical change of the current  $i_L$  in continuous current mode (CCM).

#### 4. Equilibrium Points and their Stability

Generally, there are equilibrium points in most of the physical systems and it is necessary to investigate the equilibrium points since they affect the system dynamics to a great extent. For equations (5) and (6), we can calculate their equilibrium points by solving the following equation:

$$\begin{pmatrix} \frac{di_L}{dt} & \frac{dv_c}{dt} & \frac{d\phi}{dt} \end{pmatrix} = (0 \ 0 \ 0). \quad (8)$$

By solving (8), the general equilibrium point is given by

$$O_u \left( \left( \frac{mr}{n} E(1-u) - p \right) E(1-u), E(1-u), \frac{m}{n} E(1-u) \right). \quad (9)$$

The Jacobian matrices are

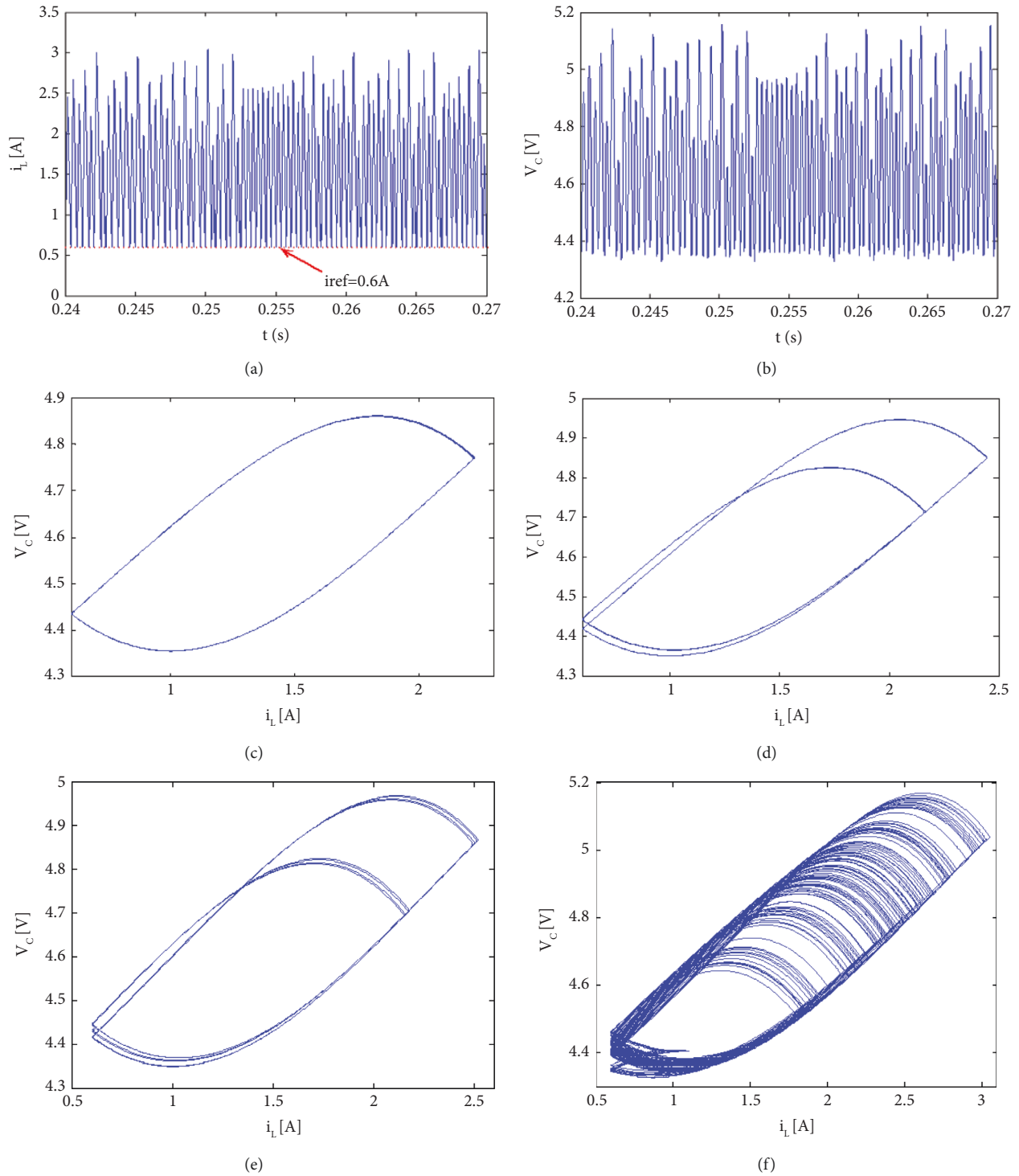


FIGURE 10: MATLAB numerical simulation: the time-domain waveforms and phase portraits of dc/dc single-stage current-mode-controlled buck converter. (a) inductor current with chaotic orbit for  $E = 12$  V; (b) capacitor voltages with chaotic orbit; (c) phase portrait with period-1 orbit for  $E = 9$  V; (d) phase portrait with period-2 orbit for  $E = 9.67$  V; (e) phase portrait with period-4 orbit for  $E = 10.67$  V; (f) phase portrait with chaotic orbit corresponding to (a) and (b).



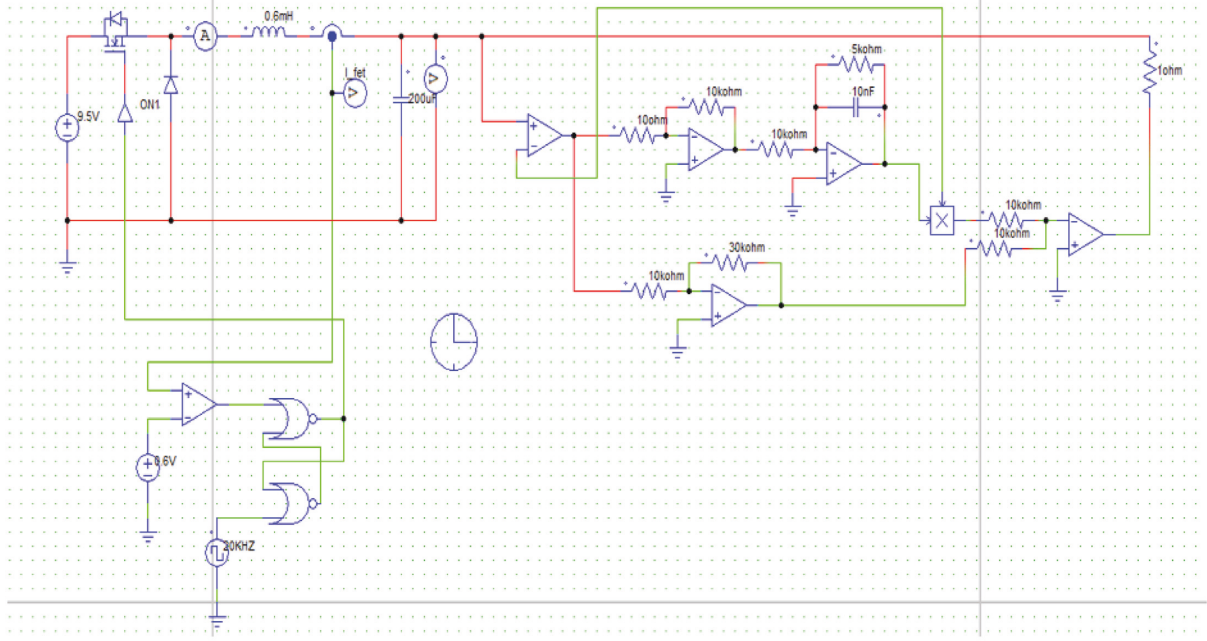


FIGURE 11: Screenshot of PSIM simulation model of the buck converter with memristive load.

$$J_{O_u} = \begin{pmatrix} 0 & -a_1 & 0 \\ a_2 & a_2 p - a_2 r \frac{m}{n} E(1-u) & -a_2 r E(1-u) \\ 0 & \alpha m & -\alpha n \end{pmatrix},$$

$$\text{with } a_1 = \frac{1}{C} e t \text{ and } a_2 = \frac{1}{L}. \quad (10)$$

The eigenvalues are obtained at equilibrium point by solving the expression

$$\det(J_O - \lambda I_3) = 0. \quad (11)$$

The characteristic equation is given by

$$\begin{aligned} \lambda^3 + \left( \alpha n + a_2 r \frac{m}{n} E(1-u) - a_2 p \right) \lambda^2 \\ + (a_1 a_2 + 2 \alpha m a_2 r E(1-u) - \alpha n a_2 p) \lambda \\ + \alpha n a_1 a_2 = 0. \end{aligned} \quad (12)$$

Obviously, equation (12) represents the characteristic equation that can be used to analyze the stability of the system around its equilibrium points. However, the non-trivial fixed points can be found by exploiting numerical methods, in particular, by using the Newton Raphson method. As already pointed out, it can be found that there exists two equilibrium points on the  $(x, y, z)$  plane, that is, for  $u = 0$ , the equilibrium point is,  $O_0(((mr/n)E - p)E, E, (m/n)E)$ , and  $O_1(0, 0, 0)$  for  $u = 1$ . Table 3 shows the roots of the characteristic equation computed for various values of  $E$ . It clearly appears from Table 3 that the system is unstable for some values of  $E$  and the graphical representations are

provided in Figure 6. As the system presents instability, it is necessary to study the dynamic behavior of the system. Note that for a smooth chaotic circuit system with a memristor, the local activity, i.e., the negative resistance region of a memristor is essential for generating chaos, while for a switched chaotic system with a memristor, it might be unnecessary for generating chaos. Figure 7 shows the eigenvalue locus in the complex plan  $(\text{Re}(\lambda), \text{Im}(\lambda))$  with the following parameter values:  $n = 2; m = 1; p = 2; r = 1; \alpha = 10000; L = 0.6 \text{ mH}$ . The intersection of the curve with imaginary axis shows the presence of the Hopf bifurcation in the system.

## 5. Numerical Investigations

**5.1. Bifurcation and Lyapunov Exponent Analysis based on Computer Simulations.** The bifurcation and Lyapunov exponent diagrams are powerful graphical nonlinear analysis tools to locate promising parameter windows that provide a detailed knowledge of the system behavior. There exist several numerical techniques to differentiate these motions, and the bifurcation diagram is one of the most important ones. A bifurcation diagram can be used to exhibit the qualitative changes in features under the variation of one or more parameters on which the system depends. Generally, there exist one or more bifurcation parameters in a chaotic system. To this end, equations (4) and (5) were integrated systematically over grids of equally spaced parameters using a standard Runge–Kutta fourth-order algorithm with a fixed time step  $h = 10^{-6}$ . In order to provide a better performance, Fortran software is exploited to perform this high-resolution computation which is quite demanding. The following initial conditions are considered for the simulations  $x = 1, y = 0, z = 0, t = 0$ . We recall that for a chaotic system, for special parameters, the buck converter may have distinct motions

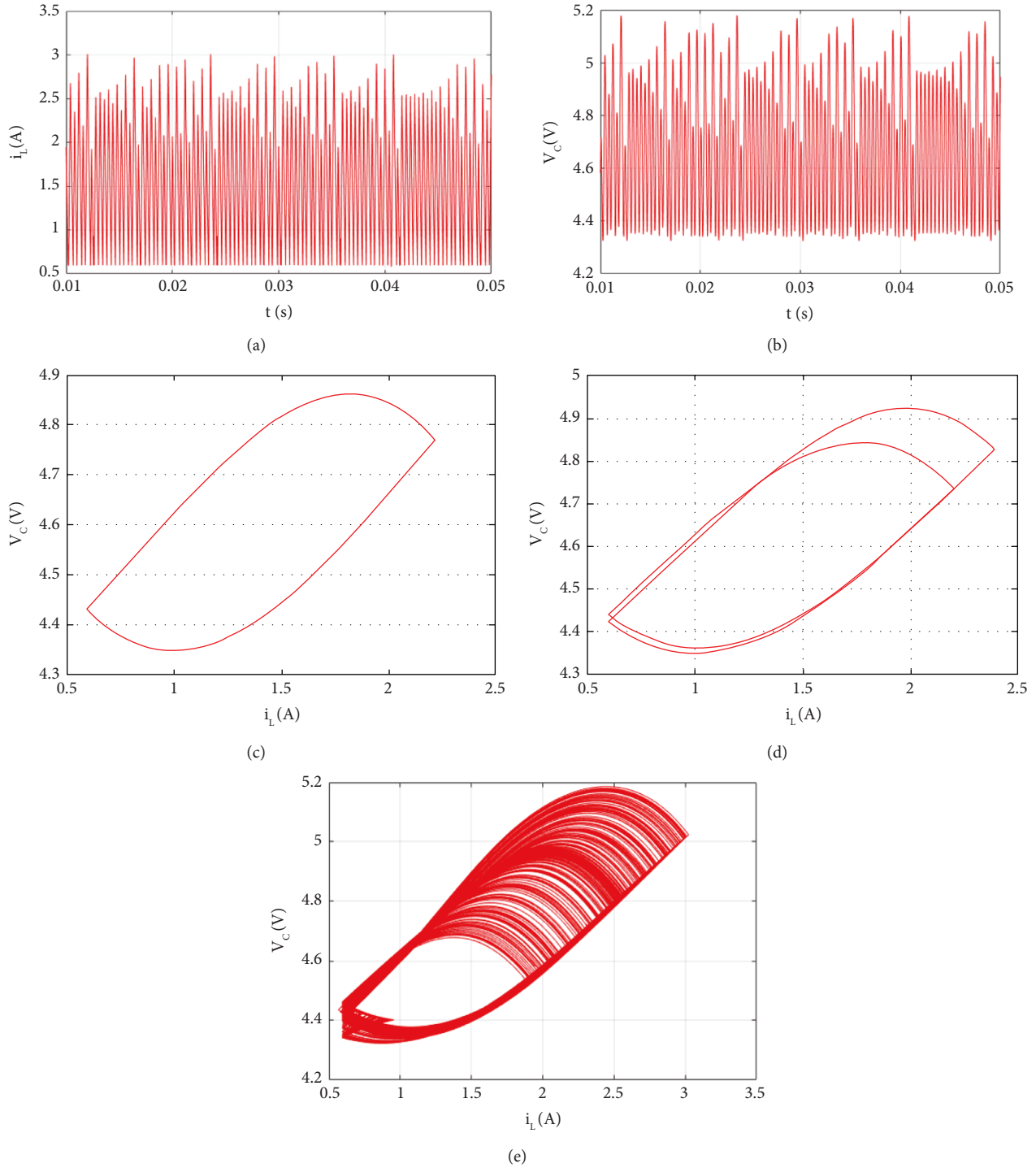


FIGURE 12: Analog simulation PSIM: the time-domain waveforms and phase portraits of dc/dc single-stage current-mode-controlled buck converter. (a) inductor current with chaotic orbit for  $E = 12$  V; (b) capacitor voltages with chaotic orbit; (c) phase portrait with period-1 orbit for  $E = 9$  V; (d) phase portrait with period-2 orbit for  $E = 9.67$  V; (e) phase portrait with chaotic orbit corresponding to (a) versus (b).

such as periodic motion, quasiperiodic motion, sub-harmonic, chaos, and hyper-chaos. Figure 8 presents in two complementary ways (described below) bifurcation diagrams and Lyapunov exponent characterizing the far-

reaching regular organization induced by the set of stable and unstable oscillations of the circuit. These panels' bifurcation and their corresponding Lyapunov exponent are plotted for the values of parameters set as follows:



$$\begin{aligned}
T_s &= 200 \mu\text{s}; m = 1; n = 2; r = 1; p = 2; i_{\text{ref}} = 0.6 \text{ mA}; L \\
&= 0.6 \text{ mH}; C = 200 \mu\text{F}, \\
E &= 12 \text{ V}; m = 1; n = 2; r = 1; p = 2; i_{\text{ref}} = 0.6 \text{ mA}; L \\
&= 0.6 \text{ mH}; C = 200 \mu\text{F}.
\end{aligned} \tag{13}$$

Figures 8(a) and 8(b) show the bifurcation diagrams of the current-mode-controlled buck converter by taking input voltage  $E$  and the  $T_s$  parameter as bifurcation parameters, respectively. From these, we clearly observe that the first period-doubling bifurcations occur at  $E = 10 \text{ V}$  and  $T_s = 5.8 \times 10^{-4}$ , respectively. As the parameter  $E$  increases, forward bifurcation routes with period-doubling and border collision to chaos suddenly appear in the buck converter and globally characterize the routes toward chaos. When parameter  $T_s$  increases, reversed bifurcation routes with period-doubling and chaos appear in the buck converter topology under investigation.

With the aim to have a perfect and complete knowledge of the total dynamics of the system, the standard Lyapunov stability diagrams are plotted to give the zones of chaotic and periodic oscillations according to two parameters of the system. Figures 9(a) and 9(b) represent the bifurcation diagrams with the corresponding Lyapunov exponents when the voltage  $E$  and period  $T_s$  are monitored. One can see that the negative exponents correspond to the periodicity zones of the diagram of bifurcation and the positive exponents correspond to chaos. Figure 9(a) shows a two parameters sweep, obtained by plotting the aforementioned fine parameter grid, the nonzero Lyapunov exponent which stands as a familiar indicator allowing one to discriminate unambiguous chaos (positive exponents) from periodic oscillations (negative exponents). Indeed, the values below zero are the negative values (indicated on the legend by the color blue) of Lyapunov exponent and those above are positive values (on the legend indicated by the color green, red, and yellow) of Lyapunov exponent. A very distinct and complementary representation of the same parameter of bifurcation  $[E, T_s]$  is presented in Figure 9(b), in the form of a bifurcation diagram namely, a diagram obtained by plotting local maxima according to the control parameters. This diagram was drawn using 18 colors; the first 17 colors represent the zones of periodicity (represented by rainbow color) and the last color (black) represents chaos.

The results previously obtained can be proven by the time-domain waveforms and the phase portraits which are particularly important for observing nonlinear phenomena. The current-mode-controlled buck converter can be obtained using Runge–Kutta algorithm via constructing piecewise smooth switching models obtained from Fortran simulation (the time-domain waveforms and the phase portraits of the inductor current versus output voltage). Taking the variation of input voltage  $E$  into consideration, the time-domain inductor current and output voltage waveforms are obtained for  $E = 12 \text{ V}$ . Figures 10(a) and 10(b) present the time evolution of the states ( $i_L$  and  $V_c$ ) and the phase portraits are shown in Figures 10(c)–10(f) which

correspond to period-1 orbit, period-2 orbit, period-4 orbit, and chaotic orbit, respectively.

## 6. PSIM Simulation Results

**6.1. Schematic Circuit.** In this section, the dc/dc converter circuit with a memristance load in PSIM is built to demonstrate the presence of complex phenomena in the system under investigation. Based on Figure 1, the schematic circuit is shown in Figure 11. The schematic circuit consists of the buck circuit (on the left) of the memristor emulator (on the right) and the controlled current source. The experimental values considered are recorded in Table 2. The current sensor ISEN7, which can transform the current signal into a voltage signal, is used to collect the current  $i$  through the inductor  $L$ . The collected voltage signal as the input of comparator  $U$  can be used to compare the reference current  $I_{\text{ref}}$ . Note that the input signal of the comparator  $U$  is in fact a voltage signal; therefore,  $V_2 = 0.6 \text{ V}$  can be regarded as  $I_{\text{ref}} \equiv 0.6 \text{ A}$ .

**6.2. Validation by Circuit Simulations.** PSIM (Power Simulation) software is a useful simulation tool, which can be used to simulate the time sequences and phase portraits of the memristive buck converter. With PSIM Version 9.0 software, the circuit simulation model is built with a relevant frequency and duty cycle of the square-wave voltage source to have these different behaviors. We note that their default values are 5000 Hz and 0.5, respectively. However, we plot the current  $i_M$  at the terminal of the inductor and the voltage  $v_m$  at the terminal of the memristor. The results are reported in Figure 12. Note that the time series, periodic, and chaotic portraits are captured by the virtual oscilloscope in PSIM. With reference to the pictures in Figure 12, it can be seen that the buck converter under consideration experiences the same bifurcation scenarios as predicted in the previous section.

## 7. Conclusion

The nonlinear behavior of current-mode-controlled buck converter memristive load is investigated in this paper. The study of stability allowed us to observe that the system has rich dynamic behavior when some system parameters change. Different tools such as bifurcation diagrams, Lyapunov exponent, phase portraits, and two parameters Lyapunov diagram are considered to provide a systematic total dynamics of the dc/dc buck converter. Peak current-mode controlled single-stage buck converter system with a memristance load goes to chaos via period-doubling and border collision routes. Moreover, it was found that the analog results in PSIM are similar to the numerical results in Fortran. Especially, peak current controlled buck converter exhibits inverse nonlinear behaviors compared with a current-mode-controlled buck converter. More interestingly, one of the key contributions is the finding of various regions in the parameters' space in which the buck converter experiences the unusual phenomenon of competing attractors which is not yet reported in the literature. It should be noted that we only focused on the investigation

of dynamical behaviors with respect to the frequency and the voltage, and it will be necessary to further study the dc/dc converters with a memristance load by considering the system parameters and topological structures in future research studies. It is worth noting here that we have worked with a continuous memristor model on a discrete converter topology, and some recent works present in detail analyzes the discrete memristor model [42, 43]. This issue should be considered in our future directions with the same converter topology with the aim to point out some technical specifications.

## Data Availability

The research data used to support the findings of this study is described and included in the article. Furthermore, some of the data used in the study are also supported by providing references as described in the article.

## Conflicts of Interest

The authors declare that they have no conflicts of interest.

## Acknowledgments

The research proposed here was supported by Sundarapandian Vaidyanathan, who is an academic editor of this journal.

## References

- [1] M. A. Sakka, J. Van Mierlo, and H. Gualous, *Electric Vehicles Modelling and Simulations*, InTech, Rijeka, Croatia, 2011.
- [2] N. Dan, L. Dan, P. Viorel, and I. Corina, "Bifurcation and Chaotic Aspects in Peak Current Controlled Buck-Boost Converters," *WSEAS Transactions on Circuits and Systems*, vol. 7, 2008.
- [3] G. H. Zhou, B. C. Bao, J. P. Xu, and Y. Y. Jin, "Dynamical Analysis and Experimental Verification of valley Current Controlled Buck Converter," *Chinese Physics B*, vol. 19, 2010.
- [4] D. Giaouris, S. Banerjee, B. Zahawi, and V. Pickert, "Stability Analysis of the Continuous-Conduction-Mode Buck Converter Via Filippov's Method," *IEEE Transactions on Circuits and Systems I: Regular Papers*, vol. 55, no. 4, pp. 1084–1096, 2008.
- [5] L. Q. Zheng and Y. Peng, "Chaos control of voltage mode controlled buck-boost converter," *Acta Physica Sinica*, vol. 65, no. 22, 2016.
- [6] M. di Bernardo, F. Garefalo, L. Glielmo, and F. Vasca, "Switchings, bifurcations, and chaos in DC/DC converters," *IEEE Transactions on Circuits and Systems I: Fundamental Theory and Applications*, vol. 45, no. 2, pp. 133–141, 1998.
- [7] H. Li, Z. Li, B. Zhang, Q. Zheng, and W. Halang, "The stability of a chaotic PWM boost converter," *International Journal of Circuit Theory and Applications*, vol. 39, no. 5, pp. 451–460, 2011.
- [8] J. D. Morcillo, D. Burbano, and F. Angulo, "Adaptive Ramp Technique for Controlling Chaos and Subharmonic Oscillations in DC-DC Power Converters," *IEEE Transactions on Power Electronics*, vol. 31, no. 7, pp. 5330–5343, 2016.
- [9] H. Zhang, W. Li, H. Ding, P. Luo, X. Wan, and W. Hu, "Nonlinear Modal Analysis of Transient Behavior in Cascade DC-DC Boost Converters," *International Journal of Bifurcation and Chaos*, vol. 27, no. 9, p. 1750140, 2017.
- [10] L. Corradini, E. Orietti, P. Mattavelli, and S. Saggini, "Digital Hysteretic Voltage-Mode Control for DC-DC Converters Based on Asynchronous Sampling," *IEEE Transactions on Power Electronics*, vol. 24, no. 1, pp. 201–211, 2009.
- [11] R. Gavagsaz-Ghoachani, M. Phattanasak, M. Zandi et al., "Estimation of the bifurcation point of a modulated-hysteresis current-controlled DC-DC boost converter: stability analysis and experimental verification," *IET Power Electronics*, vol. 8, no. 11, pp. 2195–2203, 2015.
- [12] N. Zamani, M. Ataei, and M. Niroomand, "Analysis and control of chaotic behavior in boost converter by ramp compensation based on Lyapunov exponents assignment: theoretical and experimental investigation," *Chaos, Solitons & Fractals*, vol. 81, pp. 20–29, 2015.
- [13] W. Hu, B. Zhang, R. Yang, and D. Qiu, "Dynamic behaviours of constant on-time one-cycle controlled boost converter," *IET Power Electronics*, vol. 11, no. 1, pp. 160–167, 2018.
- [14] P. Karamanakos, T. Geyer, and S. Manias, "Direct Voltage Control of DC-DC Boost Converters Using Enumeration-Based Model Predictive Control," *IEEE Transactions on Power Electronics*, vol. 29, no. 2, pp. 968–978, 2014.
- [15] B. Wang, V. R. K. Kanamarlapudi, L. Xian, X. Peng, K. T. Tan, and P. L. So, "Model Predictive Voltage Control for Single-Inductor Multiple-Output DC-DC Converter With Reduced Cross Regulation," *IEEE Transactions on Industrial Electronics*, vol. 63, no. 7, pp. 4187–4197, 2016.
- [16] Q. Wei, B. Wu, D. Xu, and N. R. Zargari, "Model Predictive Control of Capacitor Voltage Balancing for Cascaded Modular DC-DC Converters," *IEEE Transactions on Power Electronics*, vol. 32, no. 1, pp. 752–761, 2017.
- [17] N. Katayama, S. Tosaka, T. Yamanaka, M. Hayase, K. Dowaki, and S. Kogoshi, "New topology for DC-DC converters used in fuel cell-electric double layer capacitor hybrid power source systems for mobile devices," *IEEE Transactions on Industry Applications*, vol. 52, no. 1, pp. 313–321, 2016.
- [18] B. C. Bao, G. H. Zhou, J. P. Xu, and Z. Liu, "Unified classification of operation-state regions for switching converters with ramp compensation," *IEEE Transactions on Power Electronics*, vol. 26, no. 7, pp. 1968–1975, 2011.
- [19] M. Zhioua, A. El Aroudi, S. Belghith et al., "Modeling, dynamics, bifurcation behavior and stability analysis of a DC-DC boost converter in photovoltaic systems," *International Journal of Bifurcation and Chaos*, vol. 26, no. 10, p. 1650166, 2016.
- [20] S. Banerjee and K. C. Chakrabarty, "Nonlinear modeling and bifurcations in the boost converter," *IEEE Transactions on Power Electronics*, vol. 13, no. 2, pp. 252–260, 1998.
- [21] E. El Aroudi, L. Benadero, E. Toribio, and S. Machiche, "Quasiperiodicity and chaos in the DC-DC buck-boost converter," *International Journal of Bifurcation and Chaos*, vol. 10, no. 02, pp. 359–371, 2000.
- [22] J. P. Wang, B. C. Bao, J. P. Xu, G. H. Zhou, and W. Hu, "Dynamical effects of equivalent series resistance of output capacitor in constant on-time controlled buck converter," *IEEE Transactions on Industrial Electronics*, vol. 60, no. 5, pp. 1759–1768, 2013.
- [23] Y. Wang, R. Yang, B. Zhang, and W. Hu, "Smale Horseshoes and Symbolic Dynamics in the Buck-Boost DC-DC Converter," *IEEE Transactions on Industrial Electronics*, vol. 65, no. 1, pp. 800–809, 2018.
- [24] G. H. Zhou, B. C. Bao, and J. P. Xu, "Complex dynamics and fast-slow scale instability in current-mode controlled buck

- converter with constant current load,” *International Journal of Bifurcation and Chaos*, vol. 23, no. 04, p. 1350062, 2013.
- [25] C. C. Fang, “Saddle-node bifurcation in the buck converter with constant current load,” *Nonlinear Dynamics*, vol. 69, no. 4, pp. 1739–1750, 2012.
- [26] Y. F. Zhou, D. D. Jiang, J. C. Huang, and J. N. Chen, “Impedance characteristic of load in dc-dc converters and its effect on stability,” *Proc CSEE*, vol. 30, pp. 15–21, 2010.
- [27] A. El Aroudi, L. Benadero, E. Toribio, and G. Olivar, “Hopf bifurcation and chaos from torus breakdown in a PWM voltage-controlled DC-DC boost converter,” *IEEE Transactions on Circuits and Systems I: Fundamental Theory and Applications*, vol. 46, no. 11, pp. 1374–1382, 1999.
- [28] Y. Wang, R. Yang, B. Zhang, W. Hu, and W. Hu, “Smale Horseshoes and Symbolic Dynamics in the Buck-Boost DC-DC Converter,” *IEEE Transactions on Industrial Electronics*, vol. 65, no. 1, pp. 800–809, 2018.
- [29] Z. T. Zhusubaliyev and E. Mosekilde, “Multistability and hidden attractors in a multilevel DC/DC converter,” *Mathematics and Computers in Simulation*, vol. 109, pp. 32–45, 2015.
- [30] D. W. Spier, G. G. Oggier, and S. A. O. da Silva, “Dynamic modeling and analysis of the bidirectional DC-DC boost-buck converter for renewable energy applications,” *Sustainable Energy Technologies and Assessments*, vol. 34, pp. 133–145, 2019.
- [31] T. Kamal, U. Arifoğlu, and S. Z. Hassan, “Buck-boost Converter Small Signal Model: Dynamic Analysis under System Uncertainties,” *Journal of Electrical Systems*, vol. 14, no. 2, 2018.
- [32] A. Ghosh, N. Rana, and S. Banerjee, “Study of complex dynamics in DC-DC boost converter with dSPACE-based real time controller,” *International Journal of Power Electronics*, vol. 11, no. 2, pp. 160–178, 2020.
- [33] K. Mandal, S. Banerjee, and C. Chakraborty, “Complex Behavior of Load Resonant DC-DC Converters,” in *Proceedings of the National Conference on Nonlinear Systems and Dynamics (NCNSD 2011)*, Tamil Nadu, India, January 2011.
- [34] R. Zhang, A. Wu, S. Zhang, and S. Cang, “Dynamical Analysis and Circuit Implementation of a DC/DC Single-Stage Boost Converter with Memristance Load,” *Nonlinear Dynamics*, vol. 93, no. 3, pp. 1741–1755, 2018.
- [35] B. Bao, X. Zhang, H. Bao, P. Wu, Z. Wu, and M. Chen, “Dynamical Effects of Memristive Load on Peak Current Mode Buck-Boost Switching Converter,” *Chaos, Solitons & Fractals*, vol. 122, pp. 69–79, 2019.
- [36] D. B. Strukov, G. S. Snider, D. R. Stewart, and R. S. Williams, “The missing memristor found,” *Nature*, vol. 453, no. 7191, pp. 80–83, 2008.
- [37] L. O. Chua and S. M. Sung Mo Kang, “Memristive devices and systems,” *Proceedings of the IEEE*, vol. 64, no. 2, pp. 209–223, 1976.
- [38] L. Chua, “Memristor—the missing circuit element,” *IEEE Transactions on Circuit Theory*, vol. 18, no. 5, pp. 507–519, 1971.
- [39] B. C. Bao, N. Wang, Q. Xu, H. G. Wu, and Y. H. Hu, “A simple third-order memristive band pass filter chaotic circuit,” *IEEE Transactions on Circuits and Systems II: Express Briefs*, vol. 64, no. 8, pp. 977–981, 2017.
- [40] H. Hyongsuk Kim, M. P. Sah, C. Changju Yang, S. Seongik Cho, and L. O. Chua, “Memristor emulator for memristor circuit applications,” *IEEE Transactions on Circuits and Systems I: Regular Papers*, vol. 59, no. 10, pp. 2422–2431, 2012.
- [41] H. G. Wu, B. C. Bao, Z. Liu, Q. Xu, and P. Jiang, “Chaotic and periodic bursting phenomena in a memristive Wien-bridge oscillator,” *Nonlinear Dynamics*, vol. 83, no. 1-2, pp. 893–903, 2015.
- [42] K. Li, H. Bao, H. Li, J. Ma, Z. Hua, and B. C. Bao, “Memristive rulkov neuron model with magnetic induction effects,” *IEEE Transactions on Industrial Informatics*, vol. 18, no. 3, pp. 1726–1736, 2022.
- [43] H. Bao, Z. Hua, H. Li, M. Chen, and B. Bao, “Discrete memristor hyperchaotic maps,” *IEEE Transactions on Circuits and Systems I: Regular Papers*, vol. 68, no. 11, pp. 4534–4544, 2021.

## Research Article

# Adaptive Finite-Time Sliding Mode Backstepping Controller for Double-Integrator Systems with Mismatched Uncertainties and External Disturbances

Pooyan Alinaghi Hosseinabadi <sup>1,2</sup>, Ali Soltani Sharif Abadi <sup>3</sup>, Hemanshu Pota <sup>1</sup>,  
Sundarandian Vaidyanathan <sup>4</sup> and Saad Mekhilef <sup>5,6</sup>

<sup>1</sup>School of Engineering and Information Technology, University of New South Wales, Canberra at ADFA, Kensington, Australia

<sup>2</sup>Distributed Energy Resources Lab (DERlab), College of Engineering and Computer Science, The Australian National University, Canberra, Australia

<sup>3</sup>The Institute of Automatic Control and Robotics, Faculty of Mechatronics, Warsaw University of Technology, Warsaw, Poland

<sup>4</sup>Research and Development Centre, Vel Tech University, 400 Feet Outer Ring Road Avadi, Chennai 600062, Tamil Nadu, India

<sup>5</sup>School of Science, Computing and Engineering Technologies, Swinburne University of Technology, Hawthorn, VIC 3122, Australia

<sup>6</sup>Department of Electrical Engineering, College of Engineering, Universiti Tenaga Nasional, Selangor, Malaysia

Correspondence should be addressed to Pooyan Alinaghi Hosseinabadi; p.alinaghi\_hosseinabadi@adfa.edu.au

Received 3 March 2022; Accepted 27 May 2022; Published 27 June 2022

Academic Editor: Kamal Shah

Copyright © 2022 Pooyan Alinaghi Hosseinabadi et al. This is an open access article distributed under the Creative Commons Attribution License, which permits unrestricted use, distribution, and reproduction in any medium, provided the original work is properly cited.

In this paper, a novel adaptive finite-time sliding mode backstepping (AFSMBS) control scheme is suggested to control a type of high-order double-integrator systems with mismatched disturbances and uncertainties. A robust sliding mode backstepping control method, adaptive control method, and finite-time stability notion are incorporated to provide a better tracking performance over applying them individually and to use their benefits simultaneously. The concept of a sliding mode is used to define a new form of a backstepping controller. The adaptive control method is utilized to adaptively estimate the upper bounds of the disturbances and uncertainties and the estimated data are used in the control law. The notion of the finite-time stability is incorporated with the suggested control scheme to ensure the system's convergence within a finite time. The stability proof is obtained for the closed-loop system in a finite time utilizing the Lyapunov stability theorem. Simulation results are obtained for an example of a remotely operated vehicle (ROV) with three degrees of freedom (3-DOF) to demonstrate the efficacy of the suggested control approach.

## 1. Introduction

Many practical high-order systems are modeled using nonlinear differential equations due to the stochastic noise, uncertainties in the parameters, and variations in the external environment which are unknown beforehand and may occur in the real system [1]. This makes the control of these systems a challenge and as a result, different nonlinear control methods including the nonlinear stability theory [2], backstepping technique [3], Lyapunov function [4], and sliding mode control (SMC) [5–8] have come into existence.

A simple and efficient mathematical framework has been proposed in [9] to tackle nonlinear problems. A novel technique has been suggested in [10] to deal with nonlinear evolutionary issues. A system described as a classical integer-order differential problem has been investigated in [11] to explore the complexities of the human liver.

An effective scheme found in the literature to deal with uncertainties in single or double-integral system is the adaptive control [12, 13] and notable adaptive design methods have been proposed in [14–16] for the control of high-order systems. An adaptive compensation control

method has been proposed in [17] to deal with mismatched disturbances as well as uncertain faults. In addition, the finite-time stability is known for its fast transient performance achievement [18]. Hence, adaptive finite-time control encompasses the merits of both control techniques. It guarantees superior disturbance rejection, robustness properties, and faster convergence rates [19, 20].

The downside to finite-time adaptive control is the complications involved in estimating the upper bound of disturbances and uncertainties [21, 22]. Terminal SMC (TSMC) has been incorporated in [23] due to its robustness to obtain adaptive finite-time convergence, fast convergence, improved transient performance, and higher precision for high-order systems. However, singularity issues were present in the controller [24]. Nonsingular TSMC was applied in [25] to solve the singularity issue; however, finite-time convergence was not achieved and the convergence rate to the equilibrium was slow. An integration of adaptive control with nonsingular TSMC was suggested in [26] to tackle the issue of unknown upper boundaries in adaptive control. The resulting control laws were, however, discontinuous across the terminal sliding mode surface when external disturbances were involved. In [27], finite-time SMC has been incorporated with the adaptive control method to provide the estimated data in the controller. However, undesirable chattering phenomenon exists in the control signal of this control method.

Backstepping is a technique introduced in the 1990s [28] to solve regulation or tracking control problems considering uncertainties in nonlinear feedback systems [29, 30]. The control design process in backstepping begins at the source of the high-order system and backs out to new controllers which stabilize each of the outer subsystems a step at a time till the final control law is obtained [31]. The stability analysis is established by selecting a suitable Lyapunov function [32]. Backstepping is generally used as an alternative to feedback linearization [33]. It provides advantages ranging from transient performance improvement, achieving global stability to achieving a model-free control scheme [34–36]. It has the disadvantage of not being applicable to unparameterized systems or nonlinear systems with structural uncertainties or [32, 37]. It can, however, be combined with different control techniques to solve problems relating to parameter uncertainties, unmodeled dynamics, or external disturbances.

Motivated by the aforementioned discussions, a new and enhanced type of sliding mode backstepping control method is proposed where the concept of sliding mode is utilized to define the backstepping controller. It is assumed that there is no information of the upper bounds of disturbances and uncertainties. So, they are adaptively estimated, and the estimated data are provided in the controller. The system's convergence is ensured within a finite time utilizing the Lyapunov stability theorem and the notion of the finite-time stability. The suggested control method is designed for a type of high-order double-integral systems with mismatched uncertainties and external disturbances. Also, an example of ROV with 3-DOF is provided to apply the proposed controller and test its performance. Simulation results reveal the

validity of the suggested scheme. The novelties of the research can be highlighted as follows:

- (i) A novel incorporation of the robust sliding mode backstepping control method, adaptive control method, and finite-time stability notion is done to provide a superior tracking performance over applying them individually and to use their benefits simultaneously.
- (ii) This proposed controller not only ensures the system's finite-time stability but also does not require any knowledge of the upper bound of disturbances and uncertainties for the controller design.
- (iii) A new form of the candidate Lyapunov function is defined to obtain the finite-time stability proof for the closed-loop system.
- (iv) The proposed control approach is applicable for a wide range of practical applications described by a set of independent double integrator subsystems in the presence of mismatched uncertainties and disturbances.

This article is organized as follows. In Section 2, the system is presented. Mathematical preliminaries and lemmas are given in Section 3. In Section 4, the stability proof is obtained within a finite time utilizing Lyapunov stability theorem. In Section 5, the designed control laws are applied to the ROV with 3-DOF. Section 6 gives the conclusions.

## 2. Problem Statement

Consider the high-order double-integrator system that includes the mismatched uncertainties and external disturbances.

$$\begin{cases} \dot{x}_1 = x_2 + d_1, \\ \dot{x}_2 = f_1(t, x) + g_1(t, x)u_1 + d_2, \\ \dot{x}_3 = x_4 + d_3, \\ \dot{x}_4 = f_2(t, x) + g_2(t, x)u_2 + d_4, \\ \vdots \\ \dot{x}_{2n-1} = x_{2n} + d_{2n-1}, \\ \dot{x}_{2n} = f_n(t, x) + g_n(t, x)u_n + d_{2n}, \end{cases} \quad (1)$$

where  $f_j(t, x), g_j(t, x), j = (1, 2, \dots, n)$  are smooth nonlinear functions;  $g_j^{-1}(t, x)$  is available and nonsingular;  $d_i, i = (1, 2, \dots, 2n)$  is the model of uncertainties and external disturbance; and  $u_j$  is the system's control inputs. The system can be rewritten as follows:

$$\begin{cases} \dot{x}_{2j-1} = x_{2j} + d_{2j-1}, \\ \dot{x}_{2j} = f_j(t, x) + g_j(t, x)u_j + d_{2j}. \end{cases} \quad (2)$$

The external disturbances and uncertainties are given as follows:

$$d_i \leq h_i \text{ where } h_i \leq \hat{h}_i \leq h_i^*. \quad (3)$$

Here,  $h_i$  is the uncertainty upper bound (that is assumed to be unknown);  $\hat{h}_i$  is the estimation of their upper bounds; and  $d_i$  is the Euclidean norm of disturbances and



uncertainties. In the following sections, the finite-time control law is defined utilizing a sliding mode backstepping control scheme. The uncertainty upper bounds are also adaptively estimated and they are utilized in the controller.

*Remark 1.* A wide range of practical applications can be described by a set of independent double integrator subsystems (given by (1)) including the three-link robotic manipulator [38, 39], ship course system [40], two-link robotic manipulator [41], support structure system for offshore wind turbines [42], etc.

### 3. Mathematical Preliminaries and Lemmas

*Definition 1.* Consider a nonlinear system as shown below:

$$\dot{x} = f(t, x), \quad (4)$$

where  $x \in \mathbb{R}^n$  is the vector of the system states;  $f: \mathbb{R}^n \rightarrow \mathbb{R}^n$  is a nonlinear function; and  $t$  is considered on the interval  $[t_0, \infty)$ , where  $t_0 \in \mathbb{R}_+ \cup \{0\}$ . Also, we have  $x(t_0) = x_0$ .

The origin of (4) has global finite-time stability if it has global asymptotic stability and any solution  $x(t, x_0)$  of (4) converges to the origin at some finite time moment for all  $x_0$ ; i.e.,  $\forall t \geq T(x_0): x(t, x_0) = 0$ , where  $T: \mathbb{R}^n \rightarrow \mathbb{R}_{\geq 0}, \forall x_0 \in \mathbb{R}^n$ , is named settling time function, then the origin of (4) has global finite-time stability [43, 44].

*Definition 2.* The signum function is defined as follows:

$$\text{sign}(a) = \begin{cases} 1; a > 0, \\ 0; a = 0, \\ -1; a < 0. \end{cases} \quad (5)$$

We note that  $|a| = \text{asign}(a)$  is always true.

*Definition 3.* The function  $\text{sig}^a(x)$  is given as follows:

$$\text{sig}^a(x) = |x|^a \text{sign}(x) \quad (6)$$

Thus, we have  $x \text{sig}^a(x) = |x|^{a+1}$ .

**Lemma 1.** For each value  $a_1, a_2, \dots, a_n \in \mathbb{R}$  and  $0 < q < 2$ , we have,  $|a_1|^q + |a_2|^q + \dots + |a_n|^q \geq (a_1^2 + a_2^2 + \dots + a_n^2)^{q/2}$  [45].

**Lemma 2.** Assume there exist two real numbers as  $\rho_1 > 0$  and  $0 < \rho_2 < 1$  and a continuously differentiable positive function

$$\dot{V}_1(x) = x_{2j-1}(x_{2j}^* + d_{2j-1}) + \tilde{h}_{2j-1} \dot{\hat{h}}_{2j-1} \Rightarrow \dot{V}_1(x) \leq x_{2j-1}(x_{2j}^* + h_{2j-1}) + \tilde{h}_{2j-1} \dot{\hat{h}}_{2j-1}. \quad (10)$$

Substituting (5) and (6) into (8) yields as follows:

$$\dot{V}_1(x) \leq x_{2j-1}(-\tilde{h}_{2j-1} \text{sig}^{\alpha_{2j-1}}(x_{2j-1}) + h_{2j-1}) + \tilde{h}_{2j-1} r_{2j-1} |x_{2j-1}|^{\alpha_{2j-1}+1}. \quad (11)$$

$V(x): \mathbb{R}^n \rightarrow \mathbb{R}_{\geq 0}$  in such a way that we have  $V(x) = 0$  for  $x(t) = 0$ . If any solution  $x(t)$  of (4) satisfies  $\dot{V}(x) \leq -\rho_1 V^{\rho_2}(x)$ , then the origin of (4) has global finite-time stability and the settling time will be  $T \leq V^{1-\rho_2}(x_0)/\rho_1(1-\rho_2)$  [14, 46].

### 4. AFSMBS Controller

Here, the control goal is to define the finite-time controller for the system given by (2). Then, the stability proof is obtained by defining a candidate Lyapunov function. The backstepping control law is defined using the sliding control concept as follows:

$$\begin{cases} u_j = g^{-1}(-f_j(t, x) - \hat{h}_{2j} \text{sig}^{\alpha_{2j}}(Z_j) + \dot{x}_{2j}^*), \\ x_{2j}^* = -\hat{h}_{2j-1} \text{sig}^{\alpha_{2j-1}}(x_{2j-1}), \end{cases} \quad (7)$$

where we have  $Z_j = x_{2j} - x_{2j}^*$  and  $0 < \alpha_i < 1$ .

$$\begin{cases} \dot{\hat{h}}_{2j-1} = r_{2j-1} |x_{2j-1}|^{\alpha_{2j-1}+1}, \\ \dot{\hat{h}}_{2j} = r_{2j} |Z_j|^{\alpha_{2j}+1}, \end{cases} \quad (8)$$

where we have  $0 < r_i < 1$ .

The block diagram of the proposed AFsmBS approach is shown in Figure 1.

**Theorem 1.** Assume the system given by (2). If the control law (5) and adaptive law (6) are applied to (2), the system's convergence is ensured within a finite time. Also, the uncertainty upper bounds are adaptively estimated within a finite time and the online estimated data are provided in the controller.

*Proof.* The stability proof using the backstepping method consists of two phases as follows.  $\square$

*Phase 1.* To prove the first phase, the candidate Lyapunov function is defined as  $V_1(x) = 1/2 x_{2j-1}^2 + 1/2 \tilde{h}_{2j-1}^2$  where  $\tilde{h}_{2j-1} = \hat{h}_{2j-1} - h_{2j-1}^*$ . Taking its time derivative, we obtain as follows:

$$\begin{aligned} \dot{V}_1(x) &= x_{2j-1} \dot{x}_{2j-1} + \tilde{h}_{2j-1} \dot{\tilde{h}}_{2j-1} \Rightarrow \dot{V}_1(x) \\ &= x_{2j-1} \dot{x}_{2j-1} + \tilde{h}_{2j-1} \dot{\hat{h}}_{2j-1}. \end{aligned} \quad (9)$$

Then, we have as follows:

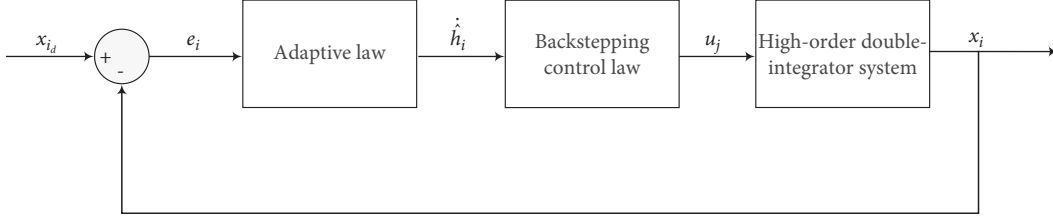


FIGURE 1: Block diagram of the proposed controller.

We obtain as follows:

$$\dot{V}_1(x) \leq |x_{2j-1}| |h_{2j-1} - \hat{h}_{2j-1}| |x_{2j-1}|^{\alpha_{2j-1}+1} + \tilde{h}_{2j-1} r_{2j-1} |x_{2j-1}|^{\alpha_{2j-1}+1}. \quad (12)$$

Adding  $\pm |x_{2j-1}|^{\alpha_{2j-1}+1} h_{2j-1}^*$  to (10) yields as follows:

$$\dot{V}_1(x) \leq |x_{2j-1}| |h_{2j-1} - \hat{h}_{2j-1}| |x_{2j-1}|^{\alpha_{2j-1}+1} + \tilde{h}_{2j-1} r_{2j-1} |x_{2j-1}|^{\alpha_{2j-1}+1} \pm |x_{2j-1}|^{\alpha_{2j-1}+1} h_{2j-1}^*. \quad (13)$$

As a result, we have as follows:

$$\begin{aligned} \dot{V}_1(x) &\leq -|x_{2j-1}| \left( |x_{2j-1}|^{\alpha_{2j-1}} h_{2j-1}^* - h_{2j-1} \right) - \tilde{h}_{2j-1} |x_{2j-1}|^{\alpha_{2j-1}+1} + \tilde{h}_{2j-1} r_{2j-1} |x_{2j-1}|^{\alpha_{2j-1}+1} \\ &\Rightarrow \dot{V}_1(x) \leq -|x_{2j-1}| (\Delta_{1_1}) - \tilde{h}_{2j-1} \left( (1 - r_{2j-1}) |x_{2j-1}|^{\alpha_{2j-1}+1} \right) \\ &\Rightarrow \dot{V}_1(x) \leq -|x_{2j-1}| \Delta_{1_1} - \tilde{h}_{2j-1} \Delta_{1_2} \\ &\Rightarrow \dot{V}_1(x) \leq -\Delta_m \left( |x_{2j-1}| + \tilde{h}_{2j-1} \right), \end{aligned} \quad (14)$$

where  $\Delta_{m_1} = \min(\Delta_{1_1}, \Delta_{1_2})$ , and according to Lemma 1, we obtain as follows:

$$\dot{V}_1(x) \leq -\Delta_{m_1} \left( |x_{2j-1}|^2 + \tilde{h}_{2j-1}^2 \right)^{1/2} \Rightarrow \dot{V}_1(x) \leq -\Delta_{m_1} (2V_1(x))^{1/2}. \quad (15)$$

Choosing  $\rho_{1_1} = \sqrt{2}\Delta_{m_1}$  and  $\rho_{2_1} = 1/2$ , we have,  $\dot{V}_1(x) \leq -\rho_{1_1} V_1^{\rho_{2_1}}(x)$ , and based on Lemma 2, the stability proof of the first phase is guaranteed. Thus, the settling time upper bound  $T_1$  will be  $T_1 \leq V^{1-\rho_{2_1}}(x_0)/\rho_{1_1}(1-\rho_{2_1})$ .

*Phase 2.* To obtain the second phase of the proof, the candidate Lyapunov function is considered as

$V_2(x) = 1/2 Z_j^2 + 1/2 \tilde{h}_{2j}^2$ . Taking its time derivative, we obtain the following:

$$\begin{aligned} \dot{V}_2(x) &= Z_j \dot{Z}_j + \tilde{h}_{2j} \dot{\tilde{h}}_{2j} \Rightarrow \dot{V}_2(x) \\ &= Z_j (\dot{x}_{2j} - \dot{x}_{2j}^*) + \tilde{h}_{2j} \dot{\tilde{h}}_{2j}. \end{aligned} \quad (16)$$

Applying the control law and simplifying it yields the following:

$$\begin{aligned} \dot{V}_2(x) &= Z_j (f_j(t, x) + g_j(t, x)u_j + d_{2j} - \dot{x}_{2j}^*) + \tilde{h}_{2j} \dot{\tilde{h}}_{2j} \\ &\Rightarrow \dot{V}_2(x) \leq -\hat{h}_{2j} |Z_j|^{\alpha_{2j}+1} + h_{2j} |Z_j| + \tilde{h}_{2j} \dot{\tilde{h}}_{2j}. \end{aligned} \quad (17)$$

Adding  $\pm |Z_j|^{\alpha_{2j}+1} h_{2j}^*$  to (15), we yield as follows:

$$\begin{aligned}
 \dot{V}_2(x) &\leq -\tilde{h}_{2j}|Z_j|^{\alpha_{2j}+1} + h_{2j}|Z_j| + \tilde{h}_{2j}\dot{\tilde{h}}_{2j} \pm |Z_j|^{\alpha_{2j}+1} h_{2j}^* \\
 &\Rightarrow \dot{V}_2(x) \leq -|Z_j| \left( |Z_j|^{\alpha_{2j}} h_{2j}^* - h_{2j} \right) - \tilde{h}_{2j}|Z_j|^{\alpha_{2j}+1} + \tilde{h}_{2j} r_{2j} |Z_j|^{\alpha_{2j}+1} \\
 &\Rightarrow \dot{V}_2(x) \leq -|Z_j| \Delta_{2_1} - \tilde{h}_{2j} \left( (1 - r_{2j}) |Z_j|^{\alpha_{2j}+1} \right) \\
 &\Rightarrow \dot{V}_2(x) \leq -|Z_j| \Delta_{2_1} - \tilde{h}_{2j} (\Delta_{2_2}) \\
 &\Rightarrow \dot{V}_2(x) \leq -\Delta_{m_2} \left( |Z_j| + \tilde{h}_{2j} \right),
 \end{aligned} \tag{18}$$

where  $\Delta_{m_2} = \min(\Delta_{2_1}, \Delta_{2_2})$  and according to Lemma 1, we have as follows:

$$\dot{V}_2(x) \leq -\Delta_{m_2} \left( |Z_j|^2 + \tilde{h}_{2j}^2 \right)^{1/2} \Rightarrow \dot{V}_2(x) \leq -\Delta_{m_2} (2V_2(x))^{1/2}. \tag{19}$$

Choosing  $\rho_{1_2} = \sqrt{2}\Delta_{m_2}$ ,  $\rho_{2_2} = 1/2$ , we have  $\dot{V}_2(x) \leq -\rho_{1_2} V_2^{\rho_{2_2}}(x)$  and based on Lemma 2, the stability proof of the second phase is guaranteed. Consequently, the settling time upper bound  $T_2$  is as  $T_2 \leq V_2^{1-\rho_{2_2}}(x_0)/\rho_{1_2} (1 - \rho_{2_2})$ .

As a result, the stability proof of the system (2) is completed and the settling time upper bound will be as  $T = T_1 + T_2$ .

*Remark 2.* The proof shows that in a finite time, we have  $Z_j \rightarrow 0$ . Consequently, in a finite time, we have  $x_{2j} \rightarrow x_{2j}^*$  as well as all the system states reach zero in a finite time and remains zero. Also, the uncertainty upper bounds are estimated in a finite time.

### 5. Application Example

In [47–50], the ROV model with 3-DOF has been presented as follows:

$$\begin{cases} p_1 \ddot{x} + V_x |V| (p_2 |\cos(\phi)| + p_3 |\sin(\phi)|) + p_4 x - p_5 V_{cx} \|V_c\| = T_x, \\ p_1 \ddot{y} + V_y |V| (p_2 |\sin(\phi)| + p_3 |\cos(\phi)|) p_4 y - p_5 V_{cy} \|V_c\| = T_y, \\ p_6 \ddot{\phi} + p_7 \dot{\phi} \dot{\phi} + p_8 \|V_c\|^2 \sin\left(\frac{\phi - \phi_c}{2}\right) + p_9 = M_z, \end{cases} \tag{20}$$

where  $V = [V_x, V_y]^T = [(\dot{x} - V_{cx}), (\dot{y} - V_{cy})]^T$  and  $V_c = [V_{cx}, V_{cy}]^T$  are the vectors of speed in directions  $x, y$  that are constants;  $p_i, i = (1, 2, \dots, 9)$  are constants which are provided in Table 1 with their uncertainties;  $(T_x, T_y, M_z) = (u_1, u_2, u_3)$  are control inputs that need to be

designed;  $\phi_c$  is the current angle between the  $x$  axis and the speed direction.

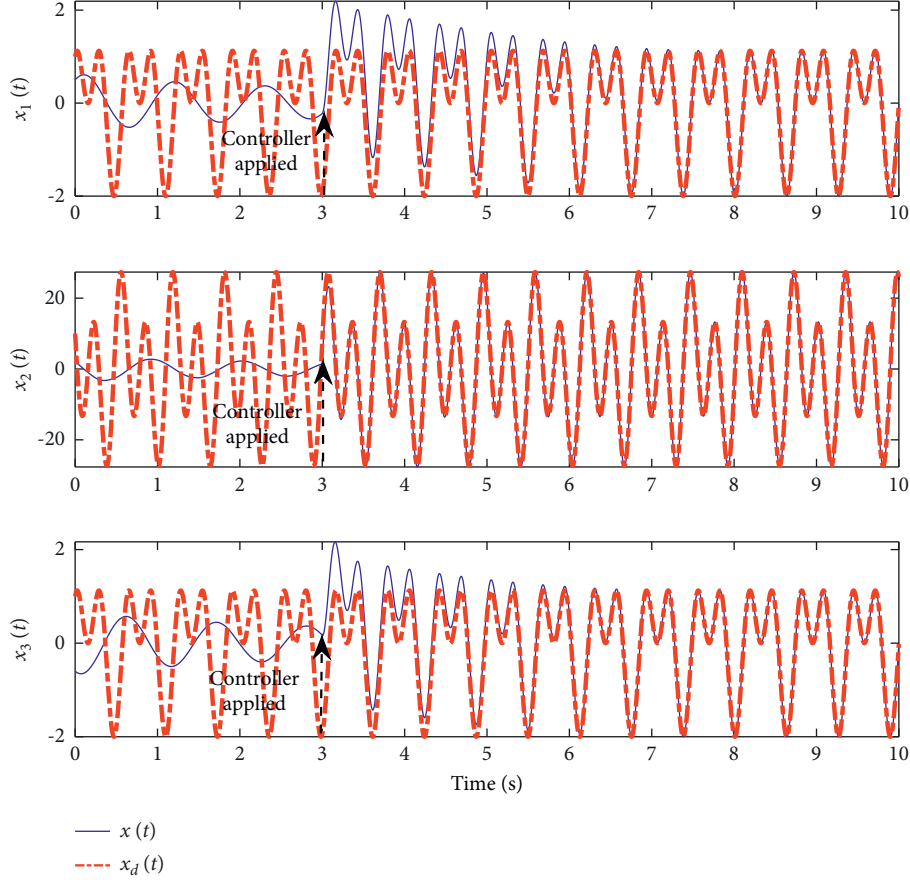
To obtain the system state equations, state variables are defined as follows,  $X = [x_1, x_2, x_3, x_4, x_5, x_6]^T = [x, \dot{x}, y, \dot{y}, \phi, \dot{\phi}]$ . Then, the state equations are rewritten as follows:

$$\begin{cases} \dot{x}_1 = x_2 + d_1, \\ \dot{x}_2 = -p_1^{-1} (V_x \|V\| (p_2 |\cos(x_5)| + p_3 |\sin(x_5)|)) p_4 x_1, \\ \dot{x}_3 = x_4 + d_3, \\ \dot{x}_4 = -p_1^{-1} (V_y \|V\| (p_2 |\sin(x_5)| + p_3 |\cos(x_5)|)) + p_4 x_3 - p_5 V_{cy} \|V_c\| + d_4 + p_1^{-1} u_2, \\ \dot{x}_5 = x_6 + d_5, \\ \dot{x}_6 = -p_6^{-1} (p_7 x_6 |x_6| + p_8 \|V_c\|^2 \sin\left(\frac{x_5 - \phi_c}{2}\right) + d_6 + p_6^{-1} u_3), \end{cases} \tag{21}$$



TABLE 1: System parameters with their uncertainties.

$p_1$	12670	$Kg \pm 10\%$	$p_2$	2667	$Kg \cdot m^{-1} \pm 10\%$	$p_3$	4934	$Kg \cdot m^{-1} \pm 10\%$
$p_4$	417	$N \cdot m^{-1} \pm 5\%$	$p_5$	46912	$Kg \cdot m^{-1} \pm 10\%$	$p_6$	18678	$Kg \cdot m^2 \pm 10\%$
$p_7$	9200	$Kg \cdot m^2 \pm 10\%$	$p_8$	-308.4	$Kg \pm 5\%$	$p_9$	1492	$N \cdot m \pm 5\%$

FIGURE 2: Time responses of  $x_1$ ,  $x_2$ ,  $x_3$  and  $x_{1_d}$ ,  $x_{2_d}$ ,  $x_{3_d}$  using AFSMBS.

where  $\|V_c\| = \sqrt{V_{cx}^2 + V_{cy}^2}$ ,  $\|V\| = \sqrt{V_x^2 + V_y^2}$ , and  $d_j$ ,  $j = (1, 2, \dots, 6)$  is the system uncertainty model.

The control goal is to fulfill a trajectory tracking problem for the ROV; hence, the dynamic error is defined as  $e_j = x_j - x_{j_d}$ . Accordingly, the dynamic error is given as follows:

$$\begin{cases} \dot{e}_1 = e_2 + d_1, \\ \dot{e}_2 = f_1 + d_2 - \dot{x}_{2_d} + p_1^{-1}u_1, \\ \dot{e}_3 = e_4 + d_3, \\ \dot{e}_4 = f_2 + d_4 - \dot{x}_{4_d} + p_1^{-1}u_2, \\ \dot{e}_5 = e_6 + d_5, \\ \dot{e}_6 = f_3 + d_6 - \dot{x}_{6_d} + p_6^{-1}u_3, \end{cases} \quad (22)$$

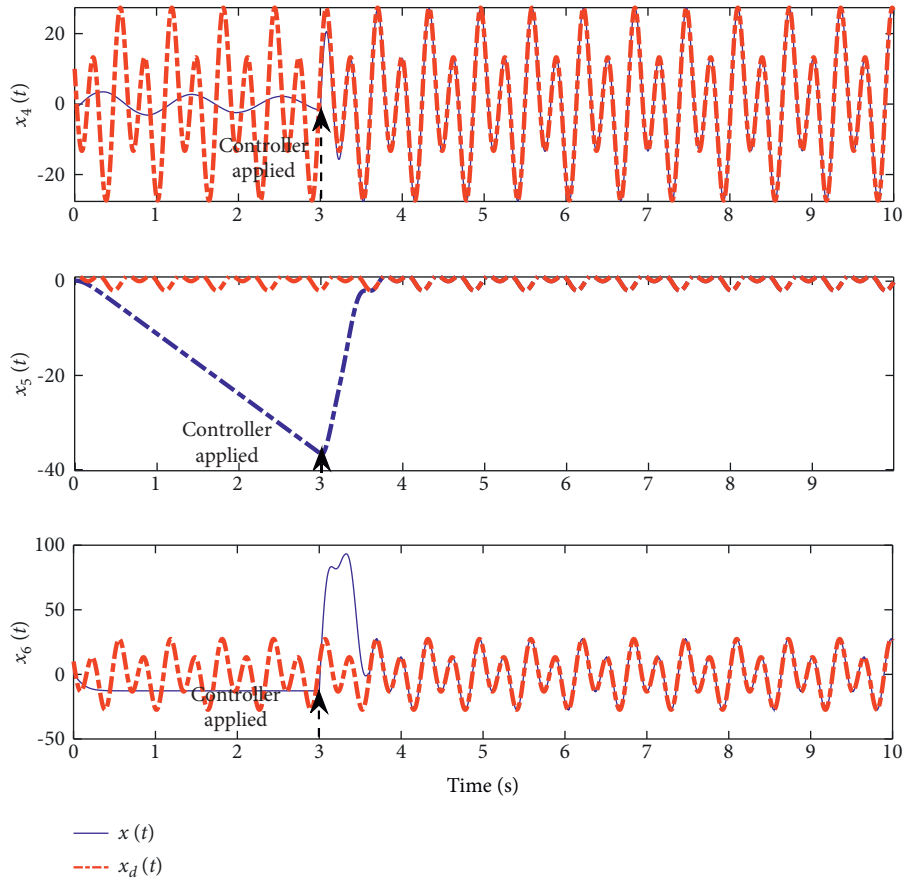
where

$$\begin{cases} f_1 = -P_1^{-1}(V_x \|V\| (p_2 |\cos(x_5)| + p_3 |\sin(x_5)|) + p_4 x_1 - p_5 V_{cx} \|V_c\|), \\ f_2 = -P_1^{-1}(V_y \|V\| (p_2 |\sin(x_5)| + p_3 |\cos(x_5)|) + p_4 x_3 - p_5 V_{cy} \|V_c\|), \\ f_3 = -P_6^{-1} \left( p_7 x_6 |x_6| + p_8 V_c^2 \sin\left(\frac{x_5 - \phi_c}{2}\right) + p_9 \right). \end{cases} \quad (23)$$

The desired trajectory tracking is considered as follows:

$$x_{i_d} = \cos(20t) + \sin(10t). \quad (24)$$

In this section, the designed controller in previous section is applied to the ROV with 3-DOF given by (18). It is to be noted that  $\dot{x}_{2_d}$  given in the control law (5) should track the desired trajectory. To obtain simulation results, the


 FIGURE 3: Time responses of  $x_4$ ,  $x_5$ ,  $x_6$  and  $x_{4_d}$ ,  $x_{5_d}$ ,  $x_{6_d}$  using AFSMBS.

Simulink/MATLAB is utilized with the numerical method of ode4 and the step-size of 0.001. Also, the control input is applied after 3 seconds of start up of the system. In (23), the value of the selected design parameters is given.

$$\alpha_{2j-1} = \alpha_{2j} = \frac{5}{11}, \quad (25)$$

$$r_i = 0.1.$$

Figures 2 to 4 show the simulation results of the AFSMBS method for ROV with 3-DOF. Figures 2 and 3 show the tracking performance before and after applying the controller, where the controller is applied to the system at  $t = 3$  (s). It can be seen that the system states reach the desired trajectories after applying the controller to the system. The efficacy of the controller can be demonstrated by comparing the behavior of the system states before and after applying the controller to the system. The controller effectively drives the system states to their references.

It can be observed from Figure 2 that the states converge to their references after applying the controller as follows. It is to be noted that the controller is applied to the system at  $t = 3$  (s).

- (i)  $x_1 \rightarrow x_{1_d}$  within  $t \approx 2.2$  (s) using AFSMBS
- (ii)  $x_2 \rightarrow x_{2_d}$  within  $t \approx 0.2$  (s) using AFSMBS
- (iii)  $x_3 \rightarrow x_{3_d}$  within  $t \approx 1.7$  (s) using AFSMBS

Figure 3 shows that the states reach their references after applying the controller as follows. Note that the controller is applied to the system at  $t = 3$  (s).

- (i)  $x_4 \rightarrow x_{4_d}$  within  $t \approx 0.3$  (s) using AFSMBS
- (ii)  $x_5 \rightarrow x_{5_d}$  within  $t \approx 0.5$  (s) using AFSMBS
- (iii)  $x_6 \rightarrow x_{6_d}$  within  $t \approx 0.6$  (s) using AFSMBS

Figure 4 shows the control signals  $u_1$ ,  $u_2$ , and  $u_3$  using the AFSMBS controller. It can be seen that the AFSMBS controller is applied to the system at  $t = 3$  (s).

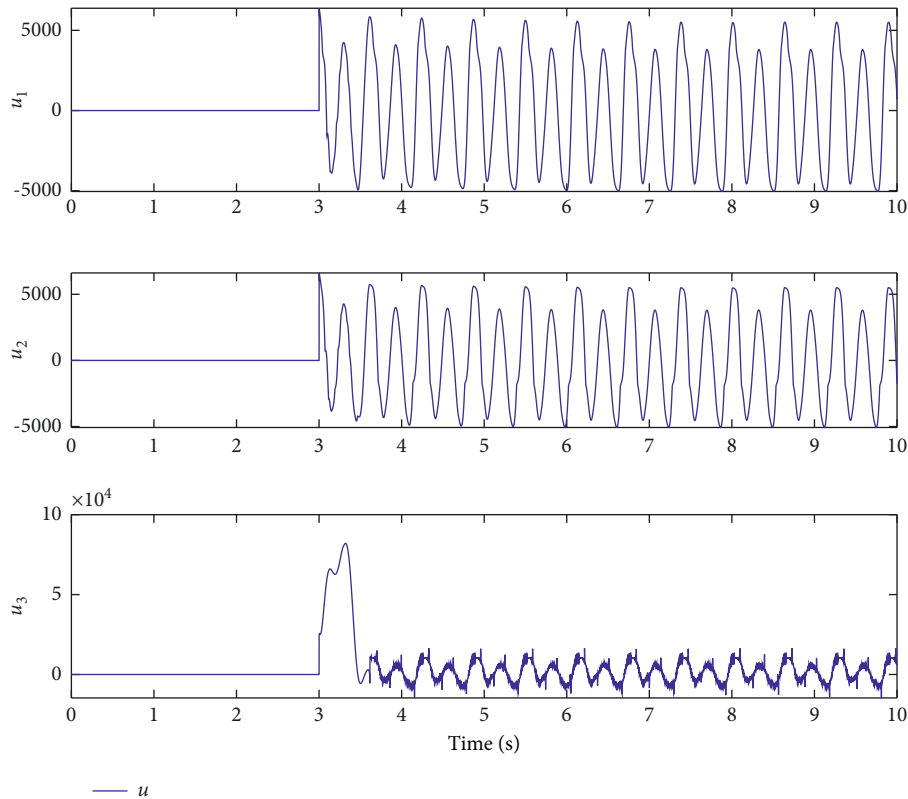


FIGURE 4: Time responses of the control signals  $u_1$ ,  $u_2$ , and  $u_3$  using AFSMBS.

## 6. Conclusion

In this paper, a novel AFSMBS controller is proposed by incorporating the robust sliding mode backstepping control scheme, adaptive control method, and finite-time stability notion for a type of high-order double-integrator systems considering mismatched uncertainties. The backstepping control law is defined utilizing the concept of sliding mode. The upper bound of the uncertainties and external disturbances is adaptively estimated within a finite time and the online estimated data are provided in the controller. The finite-time stability notion is used to guarantee the system's convergence in a finite time. The stability proof is obtained for the closed-loop system in the two phases utilizing a backstepping method and by defining proper candidate Lyapunov functions. The proposed method is applied and simulated for an example of ROV with 3-DOF. The efficacy of the suggested method is demonstrated in the simulation results. For future works, the optimization of the design parameters is recommended.

## Data Availability

No data were used to support this study.

## Conflicts of Interest

The authors declare that they have no conflicts of interest.

## Acknowledgments

This work was supported by the Universiti Tenaga Nasional grant no. IC6-BOLDREFRESH2025 (HCR) under the BOLD2025 Program.

## References

- [1] H. Min, S. Xu, Y. Li, Y. Chu, Y. Wei, and Z. Zhang, "Adaptive Finite-Time Control for Stochastic Nonlinear Systems Subject to Unknown Covariance Noise," *Journal of the Franklin Institute*, vol. 355, no. 5, pp. 2645–2661, 2018.
- [2] A. Isidori, *Nonlinear Control Systems*, Springer Science & Business Media, Berlin, Germany, 2013.
- [3] M. Krstic, I. Kanellakopoulos, and P. V. Kokotovic, *Nonlinear and Adaptive Control Design*, Wiley, Hoboken, NJ, USA, 1995.
- [4] E. D. Sontag, "Input to state stability: basic concepts and results," *Nonlinear and Optimal Control Theory*, vol. 1932, pp. 163–220, 2008.
- [5] P. Alinaghi Hosseinabadi, A. Ordys, A. Soltani Sharif Abadi, S. Mekhilef, and H. R. Pota, "State and disturbance observers-based chattering-free fixed-time sliding mode control for a class of high-order nonlinear systems," *Advanced Control for Applications*, vol. 3, no. 3, e81 pages, 2021.
- [6] P. Alinaghi Hosseinabadi, A. Soltani Sharif Abadi, S. Mekhilef, and H. R. Pota, "Two novel approaches of adaptive finite-time sliding mode control for a class of single-input multiple-output uncertain nonlinear systems," *IET Cyber-Systems and Robotics*, vol. 3, no. 2, pp. 173–183, 2021.
- [7] P. A. Hosseinabadi, A. S. S. Abadi, and S. Mekhilef, "Fuzzy adaptive finite-time sliding mode controller for trajectory

- tracking of ship course systems with mismatched uncertainties,” *International Journal of Automation and Control*, vol. 16, no. 3/4, 255 pages, 2022.
- [8] S. Yu, X. Yu, B. Shirinzadeh, and Z. Man, “Continuous finite-time control for robotic manipulators with terminal sliding mode,” *Automatica*, vol. 41, no. 11, pp. 1957–1964, 2005.
- [9] S. Rashid, R. Ashraf, and F. Jarad, “Strong interaction of Jafari decomposition method with nonlinear fractional-order partial differential equations arising in plasma via the singular and nonsingular kernels,” *AIMS Mathematics*, vol. 7, no. 5, pp. 7936–7963, 2022.
- [10] S. Rashid, R. Ashraf, and E. Bonyah, “On analytical solution of time-fractional biological population model by means of generalized integral transform with their uniqueness and convergence analysis,” *Journal of Function Spaces*, vol. 2022, Article ID 7021288, 2022.
- [11] S. Rashid, F. Jarad, and A. G. Ahmad, “A novel fractal-fractional order model for the understanding of an oscillatory and complex behavior of human liver with non-singular kernel,” *Results in Physics*, vol. 35, Article ID 105292, 2022.
- [12] Y. Hong, H. O. Wang, and L. G. Bushnell, “Adaptive finite-time control of nonlinear systems,” in *Proceedings of the American Control Conference, 2001*, vol. 51, no. 5, pp. 858–862, June 2001.
- [13] M. Sun, J. Chen, and H. Li, “Finite-time adaptive robust control,” in *Proceedings of the 2017 6th Data Driven Control and Learning Systems (DDCLS), May 2017*.
- [14] A. S. S. Abadi, P. A. Hosseinabadi, and S. Mekhilef, “Fuzzy adaptive fixed-time sliding mode control with state observer for a class of high-order mismatched uncertain systems,” *International Journal of Control, Automation and Systems*, vol. 18, no. 10, pp. 2492–2508, 2020.
- [15] Y. Cao, D. Stuart, W. Ren, and Z. Meng, “Distributed containment control for multiple autonomous vehicles with double-integrator dynamics: algorithms and experiments,” *IEEE Transactions on Control Systems Technology*, vol. 19, no. 4, pp. 929–938, 2011.
- [16] W. He, S. Zhang, and S. S. Ge, “Adaptive control of a flexible crane system with the boundary output constraint,” *IEEE Transactions on Industrial Electronics*, vol. 61, no. 8, pp. 4126–4133, 2014.
- [17] X. Yao and Y. Yang, “Adaptive fault compensation and disturbance suppression design for nonlinear systems with an aircraft control application,” *International Journal of Aerospace Engineering*, vol. 2020, pp. 1–16, 2020.
- [18] F. Wang, B. Chen, C. Lin, J. Zhang, and X. Meng, “Adaptive Neural Network Finite-Time Output Feedback Control of Quantized Nonlinear Systems,” *IEEE transactions on cybernetics*, vol. 48, no. 6, pp. 1839–1848, 2017.
- [19] X. Wang, S. Li, and P. Shi, “Distributed finite-time containment control for double-integrator multiagent systems,” *IEEE Transactions on Cybernetics*, vol. 44, no. 9, pp. 1518–1528, 2014.
- [20] B. Huang, A. Li, Y. Guo, C. Wang, and Y. Zhang, “Adaptive backstepping finite-time attitude tracking control of spacecraft without unwinding,” in *Proceedings of the 2017 36th Chinese 2017 Control Conference (CCC)*, July 2017.
- [21] Y. Hong, J. Wang, and D. Cheng, “Adaptive finite-time control of nonlinear systems with parametric uncertainty,” *IEEE Transactions on Automatic Control*, vol. 51, no. 5, pp. 858–862, 2006.
- [22] X.-T. Tran and H.-J. Kang, “A novel adaptive finite-time control method for a class of uncertain nonlinear systems,” *International Journal of Precision Engineering and Manufacturing*, vol. 16, no. 13, pp. 2647–2654, 2015.
- [23] X. Yu and Z. Man, “Model reference adaptive control systems with terminal sliding modes,” *International Journal of Control*, vol. 64, no. 6, pp. 1165–1176, 1996.
- [24] Y. Yang, C. Hua, and X. Guan, “Adaptive fuzzy finite-time coordination control for networked nonlinear bilateral teleoperation system,” *IEEE Transactions on Fuzzy Systems*, vol. 22, no. 3, pp. 631–641, 2014.
- [25] K. Lu, Y. Xia, C. Yu, and H. Liu, “Finite-time tracking control of rigid spacecraft under actuator saturations and faults,” *IEEE Transactions on Automation Science and Engineering*, vol. 13, no. 1, pp. 368–381, 2016.
- [26] M. Zhihong, M. O’day, and X. Yu, “A robust adaptive terminal sliding mode control for rigid robotic manipulators,” *Journal of Intelligent and Robotic Systems*, vol. 24, no. 1, pp. 23–41, 1999.
- [27] P. A. Hosseinabadi and A. S. S. Abadi, “Adaptive terminal sliding mode control of high-order nonlinear systems,” *International Journal of Automation and Control*, vol. 13, no. 6, 668 pages, 2019.
- [28] C. Wang, C. Wen, and Y. Lin, “Decentralized adaptive backstepping control for a class of interconnected nonlinear systems with unknown actuator failures,” *Journal of the Franklin Institute*, vol. 352, no. 3, pp. 835–850, 2015.
- [29] C. Wang and Y. Lin, “Multivariable adaptive backstepping control: a norm estimation approach,” *IEEE Transactions on Automatic Control*, vol. 57, no. 4, pp. 989–995, 2012.
- [30] X. Bu, X. Wu, R. Zhang, Z. Ma, and J. Huang, “Tracking differentiator design for the robust backstepping control of a flexible air-breathing hypersonic vehicle,” *Journal of the Franklin Institute*, vol. 352, no. 4, pp. 1739–1765, 2015.
- [31] F. Chen, R. Jiang, K. Zhang, B. Jiang, and G. Tao, “Robust backstepping sliding-mode control and observer-based fault estimation for a quadrotor UAV,” *IEEE Transactions on Industrial Electronics*, vol. 63, no. 8, pp. 5044–5056, 2016.
- [32] J. Zhang, “Adaptive sliding mode control for re-entry attitude of near space hypersonic vehicle based on backstepping design,” *IEEE/CAA Journal of Automatica Sinica*, vol. 2, no. 1, pp. 94–101, 2015.
- [33] R. Patel and D. Deb, “Adaptive backstepping control of single chamber microbial fuel cell,” in *Proceedings of the 2017 17th International Conference on Control, Automation and Systems (ICCAS)*, October 2017.
- [34] N. Wang and M. J. Er, “Direct adaptive fuzzy tracking control of marine vehicles with fully unknown parametric dynamics and uncertainties,” *IEEE Transactions on Control Systems Technology*, vol. 24, no. 5, pp. 1845–1852, 2016.
- [35] N. Wang, C. Qian, J. C. Sun, and Y. C. Liu, “Adaptive robust finite-time trajectory tracking control of fully actuated marine surface vehicles,” *IEEE Transactions on Control Systems Technology*, vol. 24, no. 4, pp. 1454–1462, 2016.
- [36] Z. Li, C. Y. Su, G. Li, and H. Su, “Fuzzy approximation-based adaptive backstepping control of an exoskeleton for human upper limbs,” *IEEE Transactions on Fuzzy Systems*, vol. 23, no. 3, pp. 555–566, 2015.
- [37] T. Wang, Y. Zhang, J. Qiu, and H. Gao, “Adaptive fuzzy backstepping control for a class of nonlinear systems with sampled and delayed measurements,” *IEEE Transactions on Fuzzy Systems*, vol. 23, no. 2, pp. 302–312, 2015.
- [38] L. Haitao and Z. Tie, “Robot dynamic identification based on the immune clonal selection algorithm,” *Journal of Applied Sciences*, vol. 13, no. 14, pp. 2819–2824, 2013.

- [39] H. Liu, T. Zhang, and X. Tian, "Continuous output-feedback finite-time control for a class of second-order nonlinear systems with disturbances," *International Journal of Robust and Nonlinear Control*, vol. 26, no. 2, pp. 218–234, 2016.
- [40] X. Sun and W. Chen, "Global generalised exponential/finite-time control for course-keeping of ships," *International Journal of Control*, vol. 89, no. 6, pp. 1169–1179, 2016.
- [41] H. Liu and T. Zhang, "Adaptive neural network finite-time control for uncertain robotic manipulators," *Journal of Intelligent and Robotic Systems*, vol. 75, no. 3-4, pp. 363–377, 2014.
- [42] P. Alinaghi Hosseinabadi, A. Soltani Sharif Abadi, S. Mekhilef, and H. R. Pota, "Fixed-time adaptive robust synchronization with a state observer of chaotic support structures for offshore wind turbines," *Journal of Control, Automation and Electrical Systems*, vol. 32, no. 4, pp. 942–955, 2021.
- [43] S. P. Bhat and D. S. Bernstein, "Finite-time stability of continuous autonomous systems," *SIAM Journal on Control and Optimization*, vol. 38, no. 3, pp. 751–766, 2000.
- [44] P. Alinaghi Hosseinabadi, *Finite Time Control of Remotely Operated vehicle/Pooyan Alinaghi Hosseinabadi*, University of Malaya, Kuala Lumpur, Malaysia, 2018.
- [45] S. P. Bhat and D. S. Bernstein, "Continuous finite-time stabilization of the translational and rotational double integrators," *IEEE Transactions on Automatic Control*, vol. 43, no. 5, pp. 678–682, 1998.
- [46] L. Qiao and W. Zhang, "Adaptive non-singular integral terminal sliding mode tracking control for autonomous underwater vehicles," *IET Control Theory & Applications*, vol. 11, no. 8, pp. 1293–1306, 2017.
- [47] P. Alinaghi Hosseinabadi, A. Soltani Sharif Abadi, S. Mekhilef, and H. R. Pota, "Chattering-free trajectory tracking robust predefined-time sliding mode control for a remotely operated vehicle," *Journal of Control, Automation and Electrical Systems*, vol. 31, no. 5, pp. 1177–1195, 2020.
- [48] M. L. Corradini, A. Monteriu, and G. Orlando, "An actuator failure tolerant control scheme for an underwater remotely operated vehicle," *IEEE Transactions on Control Systems Technology*, vol. 19, no. 5, pp. 1036–1046, 2011.
- [49] A. Dyda, D. Oskin, S. Longhi, and A. Monteriu, "A nonlinear system with coupled switching surfaces for remotely operated vehicle control," *IFAC-PapersOnLine*, vol. 49, no. 23, pp. 311–316, 2016.
- [50] T. I. Fossen, "Marine control systems—guidance, navigation, and control of ships, rigs and underwater vehicles," *Marine Cybernetics, Trondheim, Norway, Org. Number NO 985 195 005 MVA*, Springer, New York, NY, USA, 2002.

## Research Article

# Analytic Solution for the Strongly Nonlinear Multi-Order Fractional Version of a BVP Occurring in Chemical Reactor Theory

Vedat Suat Erturk <sup>1</sup>, A.K. Alomari <sup>2</sup>, Pushpendra Kumar <sup>3</sup>,  
and Marina Murillo-Arcila <sup>4</sup>

<sup>1</sup>Department of Mathematics, Faculty of Arts and Sciences, Ondokuz Mayıs University, Samsun 55139, Turkey

<sup>2</sup>Department of Mathematics, Yarmouk University, Irbid 21163, Jordan

<sup>3</sup>Department of Mathematics and Statistics, Central University of Punjab, Bathinda, Punjab 151001, India

<sup>4</sup>Instituto Universitario de Matemática Pura y Aplicada, Universitat Politècnica de València, Valencia 46022, Spain

Correspondence should be addressed to Pushpendra Kumar; [kumarsaraswatpk@gmail.com](mailto:kumarsaraswatpk@gmail.com)

Received 17 April 2022; Revised 8 May 2022; Accepted 31 May 2022; Published 18 June 2022

Academic Editor: Sundarapandian Vaidyanathan

Copyright © 2022 Vedat Suat Erturk et al. This is an open access article distributed under the Creative Commons Attribution License, which permits unrestricted use, distribution, and reproduction in any medium, provided the original work is properly cited.

This study is devoted to constructing an approximate analytic solution of the fractional form of a strongly nonlinear boundary value problem with multi-fractional derivatives that comes in chemical reactor theory. We construct the solution algorithm based on the generalized differential transform technique in four simple steps. The fractional derivative is defined in the sense of Caputo. We also mathematically prove the convergence of the algorithm. The applicability and effectiveness of the given scheme are justified by simulating the equation for given parameter values presented in the system and compared with existing published results in the case of standard derivatives. In addition, residual error computation is used to check the algorithm's correctness. The results are presented in several tables and figures. The goal of this study is to justify the effects and importance of the proposed fractional derivative on the given nonlinear problem. The generalization of the adopted integer-order problem into a fractional-order sense which includes the memory in the system is the main novelty of this research.

## 1. Introduction

Chemical reactors are containers used in chemical engineering to contain chemical processes. Because of their numerous industrial uses, these reactors are crucial. Biological treatment, algae production, and gasoline production are some of the applications for tubular reactors. The mathematical model for an adiabatic tubular chemical reactor that performs an irreversible exothermic chemical reaction is examined in this work. The model may be simplified into the following nonlinear ordinary differential equation for steady-state solutions [1]:

$$\frac{d^2u}{dx^2} - \lambda \frac{du}{dx} + \lambda\mu(\beta - u)\exp(u) = 0, \quad (1)$$

where  $\lambda$ ,  $\mu$ , and  $\beta$  are the Péclet number, Damköhler number, and adiabatic temperature rise, respectively. The relative boundary conditions are given by

$$u'(0) = \lambda u(0), u'(1) = 0. \quad (2)$$

In references [2, 3], the authors investigated the existence of a solution to equations (1) and (2). In [1], the researchers established the existence of numerous solutions. To solve the problem under specific evaluations, certain numerical approaches were used. Green's function, for example, is used to turn the issue into a Hammerstein integral equation in [4]. After that, Adomian's decomposition approach was used to solve the resultant equation. The problem was solved using the Chebyshev finite difference approach in [5]. The authors in [6] used a solution aligned on embedding Green's function inside Krasnoselskii–Mann fixed point iteration method to solve the problem.

In this article, we incorporate fractional order into (1). The following noninteger-order differential equation describes the new equation:



$$\frac{d^q u}{dx^q} - \lambda \frac{d^\gamma u}{dx^\gamma} + \lambda \mu (\beta - u) \exp(u) = 0, \tag{3}$$

where  $d^q/dx^q$  and  $d^\gamma/dx^\gamma$  are the Caputo derivative operators along with fractional orders  $q \in (1, 2]$ ,  $\gamma \in (0, 1]$  subject to the boundary conditions. (1) can be considered as a particular form of (3) by fixing the orders  $q = 2$  and  $\gamma = 1$ . This means the final solution of the fractional-order system must converge to the solution of the integer-order counterpart of the equation. Some recent results on boundary value problems in fractional-order sense can be seen in references [7, 8]. Mostly, the nature of complex dynamics cannot be better stated by integer-order differential equations. In the present case, the fractional-order model may strongly define the nature of the given system. In some circumstances, fractional models yield superior approximation results, according to Abbas et al. [9]. Iyiola et al. [10] have also demonstrated that for cancer tumours, the fractional model delivers a better approximation outcome than the integer-order one. Some recent studies related to the modeling in terms of fractional-order boundary value problems can be learned from references [11, 12]. Recently, a number of nonlinear fractional-order models have been proposed by the researchers to describe the dynamics of various real-life problems like AH1N1/09 influenza [13], childhood diseases [14], human liver dynamics [15], greenhouse gas effects on the population of aquatic animals [16], mosaic diseases in plants [17], maize streak virus [18], and so on.

Fractional calculus has more than three century history and has progressed steadily to the present day. Riemann and Liouville were the first ones who defined the fractional-order differentiation notion in the nineteenth century. Fractional differential equations (FDEs) have been shown to be a valuable tool for representing a wide range of scientific and engineering phenomena. Many FDEs that describe any phenomenon have lack of analytic solutions. As a result of the absence of analytic solutions, a significant variety of techniques for solving FDEs have been devised [19]. FDEs have attracted much more attention as a part of fractional calculus. It is worth noting that a general solution strategy for fractional differential equations is yet to be developed. The majority of problem-solving strategies in this field have been created for certain categories of challenges. For this reason, a single standard technique for solving problems related to fractional calculus has not been found. As a result, identifying compelling and beneficial solution strategies in combination with quick application techniques is valuable and worthy of further investigation [20] (see [21–27] for further information).

Under the best of our investigations, our study introduces the firstly produced numerical solution of (3). For this target, we are directed to find the approximate solution of (3) via generalized differential transform method (GDTM) [28–31].

This paper is organized as follows. In Section 2, a review of the GDTM [28] is given and some important preliminaries are given. In Section 3, the solution procedure is

presented. Convergence theorem of the present solution is proved in Section 4. The solution approximations for equations (2) AND (3) are established in Section 5. Some conclusions are mentioned at the end.

## 2. The Generalized Differential Transform Method

For reader’s facility, this part covers a review of the generalized differential transform [28] as well as some fundamental fractional calculus ideas and terminology.

The generalized differential transform of the  $k$ th derivative of the analytic function  $f(x)$  is given by

$$F_\alpha(k) = \frac{1}{\Gamma(\alpha k + 1)} \left[ (D_{x_0}^\alpha)^k f(x) \right]_{x=x_0}, \tag{4}$$

where  $0 < \alpha \leq 1$ ,  $(D_{x_0}^\alpha)^k = D_{x_0}^\alpha \cdot D_{x_0}^\alpha \dots D_{x_0}^\alpha$ ,  $k$ -times, and  $D_{x_0}^\alpha$  denotes the Caputo fractional differential operator of order  $\alpha$  given by

$$D_a^\alpha f(x) = J_a^{m-\alpha} D^m f(x). \tag{5}$$

Here  $D^m$  is the integer-order differential operator of order  $m$  and  $J^m$  is the Riemann–Liouville integral operator of order  $\mu$  with  $\mu > 0$ , which is given by

$$J_a^\mu f(x) = \frac{1}{\Gamma(\mu)} \int_a^x (x-t)^{\mu-1} f(t) dt, x > 0. \tag{6}$$

The generalized differential inverse transform of  $F_\alpha(k)$  is defined as

$$f(x) = \sum_{k=0}^{\infty} F_\alpha(k) (x - x_0)^{\alpha k}, \tag{7}$$

which practically can be approximated by the following finite series:

$$f(x) \cong \sum_{k=0}^M F_\alpha(k) (x - x_0)^{\alpha k}. \tag{8}$$

Because the initial conditions are represented as integer-order derivatives, the GDTM defines the transformation of the initial conditions as follows:

$$F_\alpha(k) = \begin{cases} \frac{1}{(\alpha k)!} \left. \frac{d^{(\alpha k)} f(x)}{dx^{(\alpha k)}} \right|_{x=x_0}, & \text{if } \alpha k \in \mathbb{Z}^+, \\ 0, & \text{if } \alpha k \notin \mathbb{Z}, \end{cases} \tag{9}$$

$$\text{for } k = 0, 1, \dots, \frac{q}{\alpha} - 1,$$

where  $q$  is the order of considered FDEs.

Putting (4) in (7) yields

$$f(x) = \sum_{k=0}^{\infty} F_\alpha(k) (x - x_0)^{\alpha k}. \tag{10}$$

The idea of a generalized differential transform is obtained from generalized Taylor's formula [28]. It is worth noting that the extended differential transform technique simplifies to the conventional differential transform method when  $\alpha = 1$  [32]. Table 1 lists some of the essential features of GDTM derived from equations (4) and (5).

### 3. Solution Procedure

For solving (2) and (3), we proceed with the following algorithm steps.

- (1) Choose proper value of  $\alpha$  that satisfies  $q/\alpha, \alpha/\alpha \in \mathbb{Z}^+$ .
- (2) Using the generalized differential transform on both sides of equation (3) and the characteristics mentioned in Table 1, we obtain the following recurrence relation:

$$U_\alpha\left(k + \frac{q}{\alpha}\right) = \beta \left[ \lambda \frac{\Gamma(\alpha k + \gamma + 1)}{\Gamma(\alpha k + 1)} U_\alpha\left(k + \frac{\gamma}{\alpha}\right) - \lambda \mu \sum_{m=0}^k W_\alpha(m) [\beta \delta(k - m) - U_\alpha(k - m)] \right], \tag{11}$$

where  $k = 0, 1, 2, \dots$ ,  $\beta = \Gamma(\alpha k + 1)/\Gamma(\alpha k + q + 1)$ , and  $W_\alpha(k)$  is the generalized differential transform of  $e^{u(x)}$  which is given by

$$W_\alpha(j) = \frac{1}{j} \sum_{m=0}^{j-1} (m + 1) U_\alpha(m + 1) W_\alpha(j - m - 1), \tag{12}$$

$$j = \frac{q}{\alpha}, \frac{q}{\alpha} + 1, \dots$$

- (3) The boundary conditions given in (2) for  $x = 0$  are transformed by employing (9) as follows:

$$\begin{aligned} U_\alpha(0) &= A, \\ U_\alpha\left(\frac{1}{\alpha}\right) &= \lambda A, \\ U_\alpha(i) &= 0, \end{aligned} \tag{13}$$

for  $\frac{i}{\alpha} \notin \mathbb{Z}^+$ ,

$$i = 1, \dots, \frac{q}{\alpha} - 1,$$

where  $A = u(0)$  is the initial condition. We can define

$$\begin{aligned} W_\alpha(0) &= e^A, \\ W_\alpha\left(\frac{1}{\alpha}\right) &= \lambda A e^A, \\ W_\alpha(i) &= 0, \end{aligned} \tag{14}$$

$$i = 1, 2, \dots, \frac{1}{\alpha} - 1, \frac{1}{\alpha} - 1, \dots, \frac{q}{\alpha} - 1.$$

The conditions in (2) for  $x = 1$  are transformed by employing (7) as follows:

$$\sum_{k=0}^N (\alpha k) U_\alpha(k) = 0. \tag{15}$$

- (4) Equations (11) and (13) are utilized to find  $U_\alpha(k)$  up to any  $N$ -terms. Then, by using (15), the value of  $A$  is evaluated. Also, the  $N$ th order of approximation is

$$u_N(x) = \sum_{k=0}^N U_\alpha(k) x^{\alpha k}. \tag{16}$$

For simplicity, we can generate the solution for  $q = 1.9$ ,  $\gamma = 0.9$  by assuming  $\alpha = 0.1$ . Then, applying (11) for  $k = 0, 1, 2, \dots, 15$ , we have

$$\begin{aligned} u_{34} &= \sum_{i=0}^{34} U_{0.1}(i) x^{i/10} \\ &= A + \frac{1}{6} A x \lambda (6 + x \lambda (3 + x \lambda)) + \frac{e^A x^{19/10} \lambda (29(A - \beta) + 10x(A(2 + A) - (1 + A)\beta)\lambda) \mu}{29\Gamma(29/10)}. \end{aligned} \tag{17}$$

TABLE 1: Basic properties of GDTM [28].

Original function	Transformed function
$f(x) = g(x) \pm h(x)$	$F_\alpha(k) = G_\alpha(k) \pm H_\alpha(k)$
$f(x) = ag(x)$	$F_\alpha(k) = aG_\alpha(k)$
$f(x) = g(x)h(x)$	$F_\alpha(k) = \sum_{l=0}^k G_\alpha(l)H_\alpha(k-l)$
$f(x) = D_{x_0}^\alpha g(x), 0 < \alpha \leq 1$	$F_\alpha(k) = \Gamma(\alpha(k+1)+1)/\Gamma(\alpha k+1)G_\alpha(k+1)$
$f(x) = (x-x_0)^\gamma$	$F_\alpha(k) = \delta(k-\gamma/\alpha), \delta(k) = \begin{cases} 1, & \text{if } k=0 \\ 0, & \text{if } k \neq 0 \end{cases}$
$f(x) = D_{x_0}^\beta g(x), m-1 < \beta \leq m, m \in \mathbb{Z}^+$	$F_\alpha(k) = \Gamma(\alpha k + \beta + 1)/\Gamma(\alpha k + 1)G_\alpha(k + \beta/\alpha)$
$f(x) = \exp(g(x))$	$F_\alpha(k) = \sum_{i=0}^{k-1} i+1/kG_\alpha(i+1)F_\alpha(k-i-1), \text{ where } F_\alpha(0) = \exp(G_\alpha(0))$

The condition in (15) gives

$$A\lambda + A\lambda^2 + \frac{A\lambda^3}{2} + \frac{19(Ae^A\lambda\mu - e^A\beta\lambda\mu)}{10\Gamma(29/10)} + \frac{29(2Ae^A\lambda^2\mu + A^2e^A\lambda^2\mu - e^A\beta\lambda^2\mu - Ae^A\beta\lambda^2\mu)}{10\Gamma(39/10)} = 0. \tag{18}$$

By fixing the values of  $\lambda, \mu,$  and  $\beta,$  it is easy to solve the equation via the Newton-Raphson method.

$$\sum_{i=0}^{\infty} U_\alpha(i)r^{\alpha i}, \tag{19}$$

where the coefficients are mentioned in (11), has a positive radius of convergence.

### 4. Convergence Analysis

**Lemma 1** (see [33]). *The standard power series  $\sum_{i=0}^{\infty} U_i r^i,$   $r \in \mathbb{R},$  has a radius of convergence  $R$  if and only if the fractional one  $\sum_{i=0}^{\infty} U_\alpha(i)r^{\alpha i}, r \geq 0,$  has a radius of  $R^{1/\mu}.$*

*Proof.* From equation (8), we have

**Theorem 1.** *The fractional power series:*

$$U_\alpha(k) \leq \theta_1 \lambda \mu \sum_{m=0}^{n-q/\alpha} W(m) \left( U_\alpha \left( n-m-\frac{q}{\alpha} \right) - \beta \delta \left( n-m-\frac{q}{\alpha} \right) \right) + \theta_2 \lambda \frac{\Gamma(n\alpha + \gamma + 1)}{\Gamma(n\alpha + 1)} U_\alpha \left( \frac{\gamma}{\alpha} + n - \frac{q}{\alpha} \right), \tag{20}$$

where

$$\theta_1 = \left| \frac{\Gamma((n-q/\alpha)\alpha + 1)}{\Gamma(q + (n-q/\alpha)\alpha + 1)} \right|, \tag{21}$$

$$\theta_2 = \left| \frac{\Gamma((n-q/\alpha)\alpha + \gamma + 1)}{\Gamma(q + (n-q/\alpha)\alpha + 1)} \frac{\Gamma(n\alpha + 1)}{\Gamma(n\alpha + \gamma + 1)} \right|. \tag{22}$$

Now, consider the series

$$z(r) = \sum_{n=0}^{\infty} a_n r^n, \tag{23}$$

for which  $a_0 = |U_\alpha(0)|, a_1 = |U_\alpha(1/\alpha)|,$  and

$$a_n = \left| \theta_1 \lambda \mu \sum_{m=0}^{n-q/\alpha} W(m) \left( U_\alpha \left( n-m-\frac{q}{\alpha} \right) - \beta \delta \left( n-m-\frac{q}{\alpha} \right) \right) + \theta_2 \lambda \frac{\Gamma(n\alpha + \gamma + 1)}{\Gamma(n\alpha + 1)} U_\alpha \left( \frac{\gamma}{\alpha} + n - \frac{q}{\alpha} \right) \right|, \tag{24}$$

TABLE 2: Numerical solutions for  $\mu = 0.7, \lambda = 5, \beta = 0.8$ .

$x$	GDTM	Method in [4]
0.0	0.10164623151473825557	0.10164623106412275851
0.1	0.15160800347538405664	0.15160800244418513970
0.2	0.19969082693869014133	0.19969082598774598630
0.3	0.24564764071345721042	0.24564763919882120986
0.4	0.28919552846307056138	0.28919552652683175159
0.5	0.32997387678814665835	0.32997387500728383184
0.6	0.36746668503341112233	0.36746668342588013969
0.7	0.40086147483935807845	0.40086147462729197629
0.8	0.42879563627198713505	0.42879563852127257524
0.9	0.44890276956983110601	0.44890277089707031201
1.0	0.45700543796118281437	0.45700543763742257810

TABLE 3: GDTM solution and numerical solution with its absolute and residual errors for  $\lambda = 5, \mu = 0.7, \beta = 0.8$ .

$x$	GDTM	Numerical solution	Absolute error	Residual error
0.0	0.1016462307	0.1016462315	$8.085193209 \times 10^{-10}$	$1.665334537 \times 10^{-16}$
0.1	0.1516080019	0.1516080035	$1.624451518 \times 10^{-9}$	$6.106226635 \times 10^{-16}$
0.2	0.199690825	0.1996908269	$1.943355393 \times 10^{-9}$	$4.996003611 \times 10^{-16}$
0.3	0.2456476375	0.2456476407	$3.187346082 \times 10^{-9}$	$5.828670879 \times 10^{-16}$
0.4	0.2891955237	0.2891955285	$4.774220019 \times 10^{-9}$	$1.276756478 \times 10^{-15}$
0.5	0.3299738702	0.3299738768	$6.62490951 \times 10^{-9}$	$8.398837181 \times 10^{-14}$
0.6	0.3674666751	0.367466685	$9.92236443 \times 10^{-9}$	$1.042421705 \times 10^{-11}$
0.7	0.4008614603	0.4008614748	$1.456031457 \times 10^{-8}$	$6.394951235 \times 10^{-10}$
0.8	0.4287956137	0.4287956363	$2.26142593 \times 10^{-8}$	$2.315349923 \times 10^{-8}$
0.9	0.4489027282	0.4489027696	$4.136782861 \times 10^{-8}$	$5.61353519 \times 10^{-7}$
1.0	0.4570053763	0.457005438	$6.16973152 \times 10^{-8}$	$9.929563344 \times 10^{-6}$

for  $n = q/\alpha, q/\alpha + 1, \dots$  and  $a_n = 0$  for  $1 < n < q/\alpha$ .

Then, define

$$\Psi = z(r) = a_0 + a_1 r + \left( \sum_{n=0}^{\infty} a_{n+2} r^n \right) r^2$$

$$= a_0 + a_1 r + r^2 \sum_{n=0}^{\infty} \left\{ \theta_1 \lambda \mu \sum_{m=0}^{n-q/\alpha} W(m) \left( Y \left( n - m - \frac{q}{\alpha} \right) - \beta \delta \left( n - m - \frac{q}{\alpha} \right) \right) + \theta_2 \lambda \frac{\Gamma(n\alpha + \gamma + 1)}{\Gamma(n\alpha + 1)} Y \left( \frac{\gamma}{\alpha} + n - \frac{q}{\alpha} \right) \right\} r^n. \tag{25}$$

Now, we have the function of two variables:

$$\Theta(r, \Psi) = \Psi - a_0 - a_1 r - r^2 (\theta_1 \lambda \mu e^\Psi (\Psi - \beta)r^q + \lambda \theta_2 (D^\gamma \Psi)r^q), \tag{26}$$

which is analytic in the plane  $(r, \Psi)$  with the characteristics  $\Theta(0, a_0) = 0$  and  $\Theta_\Psi(0, a_0) = 1 \neq 0$ . Since  $z(r)$  is an analytic function in a neighborhood of the point  $(0, a_0)$  of the  $(r, \Psi)$ -plane with a positive radius of convergence, then by implicit function theorem, the series in (10) is convergent by Lemma 1.  $\square$

### 5. Numerical Experiments

This section derives the numerical experiments of the given procedure of Section 3 for solving equations (2) and (3). Because the exact solution to the given problem is not known, we instead find the absolute residual error function, which justifies how accurately the numerical solution agrees to the solution of main problems (2) and (3). So, the absolute residual error function is

$$|ER_N(x)| = \left| \frac{d^q u_N(x)}{dx^q} - \lambda \frac{d^\gamma u_N(x)}{dx^\gamma} + \lambda \mu (\beta - u_N(x)) \exp(u_N(x)) \right|, 0 \leq x \leq 1. \tag{27}$$

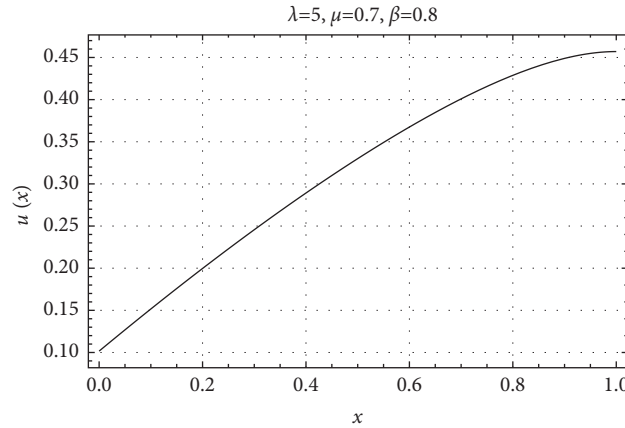


FIGURE 1: Graph of numerical outputs for  $\lambda = 5, \mu = 0.7,$  and  $\beta = 0.8.$

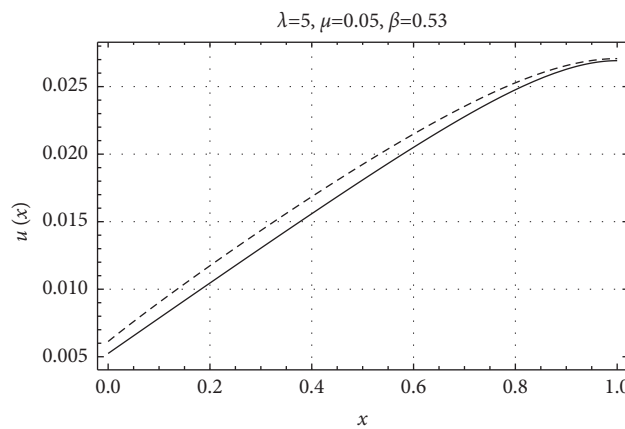


FIGURE 2: GDTM solution:  $q = 1.9$  and  $\gamma = 1$  (line);  $q = 1.9$  and  $\gamma = 0.9$  (dashed).

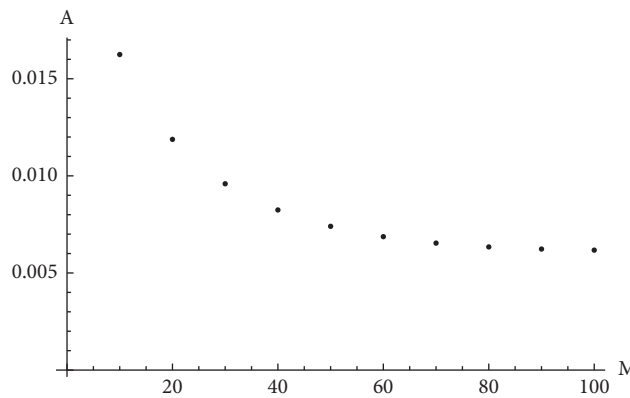


FIGURE 3: Variation of  $A$  with  $N$  for the case  $\lambda = 5, \mu = 0.05, \beta = 0.53.$

Firstly, we start to generate the results for standard fractional derivative  $q = 2, \gamma = 1.$  By fixing  $\alpha = 1, N = 21,$  Table 2 displays our numerical results and matches them with those of the mentioned outputs in [4] for the same iteration number. Numerical solution using default Mathematica package and the GDTM solution and its absolute error and residual error are given in Table 3. Moreover, Figure 1 shows the approximate solutions for  $\mu = 0.7, \lambda = 5,$  and  $\beta = 0.8.$  Figure 1 is in good agreement with Figure 2 given in [5].

Now, we explore the impact of the fractional derivative on the solution of the model. In Figure 3, we show the convergence of obtained missing condition  $A$  with increasing  $N$  when  $q = 1.9$  and  $\gamma = 0.9.$  It is clear that the value of  $A$  starts to be fixed when  $N > 80.$

Tables 4 and 5 introduce the approximate solutions and the residual errors of problems (2) and (3) for different values of  $q, \gamma, \lambda, \mu,$  and  $\beta.$  The residual error indicator demonstrates that the results are accurate for at least  $6 \times 10^{-5}.$

TABLE 4: Numerical outputs for  $\lambda = 5, \mu = 0.05, \beta = 0.53$ .

$x$	$q = 1.9, \gamma = 1.0$		$q = 1.9, \gamma = 0.9$	
	GDTM	Residual error	GDTM	Residual error
0.0	0.00524258	$5.55112 \times 10^{-17}$	0.00612891	$1.69136 \times 10^{-17}$
0.1	0.00785749	$2.77556 \times 10^{-17}$	0.00905165	$9.54098 \times 10^{-18}$
0.2	0.0104581	$1.5786 \times 10^{-16}$	0.0119341	$4.55365 \times 10^{-17}$
0.3	0.013039	$2.43347 \times 10^{-14}$	0.0148969	$1.82536 \times 10^{-15}$
0.4	0.0155894	$4.46358 \times 10^{-12}$	0.0179996	$2.99132 \times 10^{-13}$
0.5	0.0180901	$2.4929 \times 10^{-10}$	0.0212823	$1.55918 \times 10^{-11}$
0.6	0.0205054	$6.57931 \times 10^{-9}$	0.0247751	$3.86786 \times 10^{-10}$
0.7	0.0227707	$1.03475 \times 10^{-7}$	0.0285021	$5.73491 \times 10^{-9}$
0.8	0.024768	$1.11374 \times 10^{-6}$	0.0324832	$5.82065 \times 10^{-8}$
0.9	0.0262822	$8.96982 \times 10^{-6}$	0.0367354	$4.41167 \times 10^{-7}$
1.0	0.0269209	$5.7448 \times 10^{-5}$	0.0412736	$2.64861 \times 10^{-6}$

TABLE 5: Numerical solutions for  $\lambda = 0.05, \mu = 0.5, \beta = 0.6$ .

$x$	$q = 1.9, \gamma = 0.9$		$q = 1.9, \gamma = 1.0$	
	GDTM	Residual error	GDTM	Residual error
0.0	0.233482	$3.46945 \times 10^{-18}$	0.233528	0.
0.1	0.234572	$3.46945 \times 10^{-18}$	0.23462	$3.46945 \times 10^{-18}$
0.2	0.23553	$3.46945 \times 10^{-18}$	0.23558	0.
0.3	0.236365	$5.20417 \times 10^{-18}$	0.236418	$1.73472 \times 10^{-18}$
0.4	0.237083	$5.20417 \times 10^{-18}$	0.237138	$1.73472 \times 10^{-18}$
0.5	0.237686	$1.73472 \times 10^{-18}$	0.237744	0.
0.6	0.238176	0.	0.238236	0.
0.7	0.238556	$5.20417 \times 10^{-18}$	0.238618	0.
0.8	0.238826	$3.46945 \times 10^{-18}$	0.238889	$1.73472 \times 10^{-18}$
0.9	0.238987	$1.73472 \times 10^{-18}$	0.239051	$1.73472 \times 10^{-18}$
1.0	0.239041	$5.20417 \times 10^{-18}$	0.239105	0.

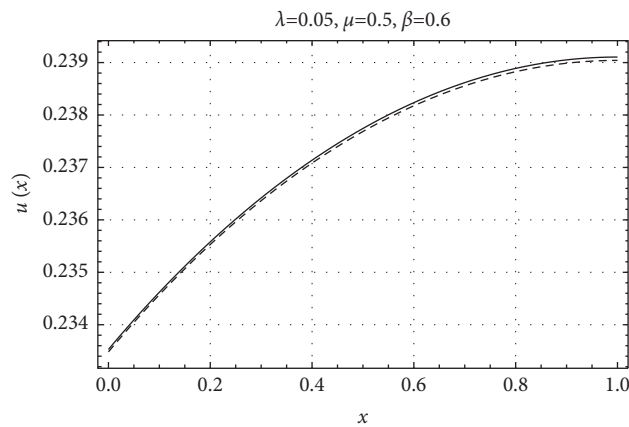


FIGURE 4: GDTM solution:  $q = 1.9$  and  $\gamma = 1$  (line);  $q = 1.9$  and  $\gamma = 0.9$  (dashed).

To study the solution behavior, we plot the present solution for the case of  $\lambda = 5, \mu = 0.05, \beta = 0.53$  when  $q = 1.9, \gamma = 0.9$  and  $q = 1.9, \gamma = 1$  in Figure 2. The solution

for the case of  $\lambda = 0.05, \mu = 0.5, \beta = 0.6$  when  $q = 1.9, \gamma = 0.9$  and  $q = 1.9, \gamma = 1$  is presented in Figure 4. It is clear that the fractional derivatives can change the solution behavior.



## 6. Conclusions

Strongly nonlinear boundary value problem with multi-order fractional derivative that occurred in the chemical reaction theory has been successfully solved via the new algorithm based on GDTM. The constructed solution has been given in terms of convergent infinite series as seen in the provided theorem. The method was easy to apply, and the results have enough good accuracy as shown in the experimental results. The obtained solution was directly generated without any linearization or discretization of the domain. The given method is very powerful and can be easily applied for several kinds of fractional nonlinear boundary value problems in future.

## Data Availability

The data used to support the findings of this study are included within the article.

## Conflicts of Interest

The authors declare that they have no conflicts of interest.

## Acknowledgments

Marina Murillo-Arcila was supported by MCIN/AEI/10.13039/501100011033, Project no. PID2019-105011GB-I00, and by Generalitat Valenciana, Project no. PROMETEU/2021/070.

## References

- [1] R. F. Heinemann and A. B. Poore, "Multiplicity, stability, and oscillatory dynamics of the tubular reactor," *Chemical Engineering Science*, vol. 36, no. 8, pp. 1411–1419, 1981.
- [2] N. Madbouly, "Solutions of Hammerstein Integral Equations Arising from Chemical Reactor Theory," Doctoral Dissertation, University of Strathclyde, Glasgow, Scotland, 1996.
- [3] W. Feng, G. Zhang, and Y. Chai, "Existence of positive solutions for second order differential equations arising from chemical reactor theory," *Discrete and Continuous Dynamical Systems*, pp. 373–381, 2007.
- [4] H. Q. Kafri, S. A. Khuri, and A. Sayfy, "A fixed-point iteration approach for solving a BVP arising in chemical reactor theory," *Chemical Engineering Communications*, vol. 204, no. 2, pp. 198–204, 2017.
- [5] N. Madbouly, D. McGhee, and G. Roach, "Adomian's method for hammerstein integral equations arising from chemical reactor theory," *Applied Mathematics and Computation*, vol. 117, no. 2–3, pp. 241–249, 2001.
- [6] A. Saadatmandi and M. R. Azizi, "Chebyshev finite difference method for a two-point boundary value problems with applications to chemical reactor theory," *Iranian Journal of Mathematical Chemistry*, vol. 3, no. 1, pp. 1–7, 2012.
- [7] V. S. Ertürk, A. Ali, K. Shah, P. Kumar, and T. Abdeljawad, "Existence and stability results for nonlocal boundary value problems of fractional order," *Boundary Value Problems*, vol. 2022, no. 1, p. 25, 2022.
- [8] Z. Bekri, V. S. Ertürk, and P. Kumar, "On the existence and uniqueness of a nonlinear q-difference boundary value problem of fractional order," *International Journal of Modeling, Simulation, and Scientific Computing*, vol. 13, no. 01, Article ID 2250011, 2021.
- [9] S. Abbas, V. S. Ertürk, and S. Momani, "Dynamical analysis of the Irving-Mullineux oscillator equation of fractional order," *Signal Processing*, vol. 102, pp. 171–176, 2014.
- [10] O. S. Iyiola and F. D. Zaman, "A fractional diffusion equation model for cancer tumor," *AIP Advances*, vol. 4, no. 10, Article ID 107121, 2014.
- [11] V. S. Ertürk, A. Ahmadkhanlu, P. Kumar, and V. Govindaraj, "Some novel mathematical analysis on a corneal shape model by using Caputo fractional derivative," *Optik*, vol. 261, Article ID 169086, 2022.
- [12] D. Baleanu, S. Etemad, H. Mohammadi, and S. Rezapour, "A novel modeling of boundary value problems on the glucose graph," *Communications in Nonlinear Science and Numerical Simulation*, vol. 100, Article ID 105844, 2021.
- [13] S. Rezapour and H. Mohammadi, "A study on the AH1N1/09 influenza transmission model with the fractional Caputo-Fabrizio derivative," *Advances in Difference Equations*, vol. 2020, no. 1, p. 488, 2020.
- [14] D. Baleanu, S. M. Atyad, H. Mohammadi, and S. Rezapour, "On modelling of epidemic childhood diseases with the Caputo-Fabrizio derivative by using the Laplace Adomian decomposition method," *Alexandria Engineering Journal*, vol. 59, no. 5, pp. 3029–3039, 2020.
- [15] D. Baleanu, A. Jajarmi, H. Mohammadi, and S. Rezapour, "A new study on the mathematical modelling of human liver with Caputo-Fabrizio fractional derivative," *Chaos, Solitons & Fractals*, vol. 134, Article ID 109705, 2020.
- [16] P. Kumar, V. Govindaraj, V. S. Ertürk, and M. S. Mohamed, "Effects of greenhouse gases and hypoxia on the population of aquatic species: a fractional mathematical model," *Advances in Continuous and Discrete Models*, vol. 2022, no. 1, p. 31, 2022.
- [17] M. Vellappandi, P. Kumar, V. Govindaraj, and W. Albalawi, "An optimal control problem for malaria disease via Caputo fractional derivative," *Alexandria Engineering Journal*, vol. 61, no. 10, pp. 8027–8037, 2022.
- [18] P. Kumar, V. S. Ertürk, M. Vellappandi, H. Trinh, and V. Govindaraj, "A study on the maize streak virus epidemic model by using optimized linearization-based predictor-corrector method in Caputo sense," *Chaos, Solitons & Fractals*, vol. 158, Article ID 112067, 2022.
- [19] A. Çetinkaya and O. Kymaz, "The solution of the time-fractional diffusion equation by the generalized differential transform method," *Mathematical and Computer Modelling*, vol. 57, no. 9–10, pp. 2349–2354, 2013.
- [20] V. S. Ertürk, G. Zaman, B. Alzalg, A. Zeb, and S. Momani, "Comparing two numerical methods for approximating a new giving up smoking model involving fractional order derivatives," *Iranian Journal of Science and Technology Transaction A-Science*, vol. 41, no. 3, pp. 569–575, 2017.
- [21] T. S. Basu and H. Wang, "A fast second-order finite difference method for space-fractional diffusion equations," *International Journal of Numerical Analysis and Modeling*, vol. 9, no. 3, pp. 658–666, 2012.
- [22] A. H. Bhrawy and M. A. Zaky, "Highly accurate numerical schemes for multi-dimensional space variable-order fractional Schrödinger equations," *Computers & Mathematics with Applications*, vol. 73, no. 6, pp. 1100–1117, 2017.
- [23] M. Zayernouri and G. E. Karniadakis, "Exponentially accurate spectral and spectral element methods for fractional ODEs," *Journal of Computational Physics*, vol. 257, no. A, pp. 460–480, 2014.

- [24] M. Dehghan, M. Abbaszadeh, and W. Deng, "Fourth-order numerical method for the space-time tempered fractional diffusion-wave equation," *Applied Mathematics Letters*, vol. 73, pp. 120–127, 2017.
- [25] A. K. Alomari, R. B. AlBadarneh, M. F. A. Al Jamal, and G. A. Drabseh, "Numerical simulation for fractional phi-4 equation using homotopy Sumudu approach," *International Journal of Simulation and Process Modelling*, vol. 16, no. 1, p. 26, 2021 .
- [26] A. K. Alomari, "Homotopy-Sumudu transforms for solving system of fractional partial differential equations," *Advances in Difference Equations*, vol. 2020, no. 1, p. 222, 2020 .
- [27] S. Aljhani, M. S. Md Noorani, and A. K. Alomari, "Numerical solution of fractional-order HIV model using homotopy method," *Discrete Dynamics in Nature and Society*, vol. 202013 pages, Article ID 2149037, 2020.
- [28] Z. Odibat, S. Momani, and V. S. Erturk, "Generalized differential transform method: application to differential equations of fractional order," *Applied Mathematics and Computation*, vol. 197, no. 2, pp. 467–477, 2008.
- [29] J. Liu and G. Hou, "Numerical solutions of the space- and time-fractional coupled Burgers equations by generalized differential transform method," *Applied Mathematics and Computation*, vol. 217, no. 16, pp. 7001–7008, 2011.
- [30] Z. Odibat and S. Momani, "A generalized differential transform method for linear partial differential equations of fractional order," *Applied Mathematics Letters*, vol. 21, no. 2, pp. 194–199, 2008.
- [31] Z. M. Odibat, S. Kumar, N. Shawagfeh, A. Alsaedi, and T. Hayat, "A study on the convergence conditions of generalized differential transform method," *Mathematical Methods in the Applied Sciences*, vol. 40, no. 1, pp. 40–48, 2017.
- [32] J. K. Zhou, *Differential Transformation and its Applications for Electrical Circuits (In Chinese)*, Huazhong University Press, Wuhan, China, 1986.
- [33] A. El-Ajou, O. Arqub, Z. Zhour, and S. Momani, "New results on fractional power series: theories and applications," *Entropy*, vol. 15, no. 12, pp. 5305–5323, 2013.

## Research Article

# Asymptotic Behavior of Weak Solutions of Nonisothermal Flow of Herschel–Bulkley Fluid to Free Boundary

Fares Yazid,<sup>1</sup> Abdelkader Saadallah,<sup>2</sup> Djamel Ouchenane,<sup>1</sup> Nadhir Chougui,<sup>2</sup> Mohamed Abdalla <sup>3,4</sup> and Ahmed Himadan <sup>5,6</sup>

<sup>1</sup>Laboratory of Pure and Applied Mathematics, University of Laghouat, Laghouat, Algeria

<sup>2</sup>Applied Math Lab, Department of Mathematics, Setif 1 University, Sétif 19000, Algeria

<sup>3</sup>Department of Mathematics, Faculty of Science, King Khalid University, Abha 61471, Saudi Arabia

<sup>4</sup>Department of Mathematics, Faculty of Science, South Valley University, Qena 83523, Egypt

<sup>5</sup>Department of Mathematics, College of Sciences and Arts, ArRas, Qassim University, Buraydah, Saudi Arabia

<sup>6</sup>Department of Mathematics, Faculty of Science, Juba University, Juba, Sudan

Correspondence should be addressed to Ahmed Himadan; [ahmedhimadan0@gmail.com](mailto:ahmedhimadan0@gmail.com)

Received 3 March 2022; Accepted 15 April 2022; Published 20 May 2022

Academic Editor: Sundarapandian Vaidyanathan

Copyright © 2022 Fares Yazid et al. This is an open access article distributed under the Creative Commons Attribution License, which permits unrestricted use, distribution, and reproduction in any medium, provided the original work is properly cited.

In this manuscript, the behavior of a Herschel–Bulkley fluid has been discussed in a thin layer in  $\mathbb{R}^3$  associated with a nonlinear stationary, nonisothermal, and incompressible model. Furthermore, the limit problem has been considered, and the studied problem in  $\Omega^\varepsilon$  is transformed into another problem defined in  $\Omega^\varepsilon$  without the parameter  $\Omega^\varepsilon$  ( $\varepsilon$  is the parameter representing the thickness of the layer tend to zero is studied). We also investigated the convergence of the unknowns which are the velocity, pressure, and the temperature of the fluid. In addition, we established the limit problem and the specific Reynolds equation.

## 1. Introduction

In a recent study of problems for the asymptotic behavior for a problem of continuum mechanics in a thin domain  $\Omega^\varepsilon$ , the problem is transformed into an equivalent problem on a domain  $\Omega$  independent of the parameter  $\varepsilon$ . This phenomenon has been presented by many researchers, see, e.g., [1–5]. Specifically, the case of Herschel–Bulkley fluid has been archived in several articles, for instance, [6, 7]. A particularity of Herschel–Bulkley fluid lies in the presence of rigid zones located in the interior of the flow, and as the yield limit increases, the rigid zones become larger and may completely block the flow (see, e.g., [8–10]).

This work is to study the asymptotic behavior for weak solutions of a linked system, including of an incompressible Herschel–Bulkley fluid and the equation of the heat energy, in a three-dimensional bounded domain satisfying Tresca-

type fluid solid boundary conditions. The boundary of this thin domain consists of three parts: the bottom, the lateral part, and the top surface.

The article is organized as follows: in Section 2, we present the mechanical problem of the steady-state flow of Herschel–Bulkley fluid in a three-dimensional thin domain. We also introduce some notations, preliminaries, and some function spaces of our coupled problem.

In Section 3, we use the asymptotic analysis, in which the small parameter  $\varepsilon$  is the height of the domain. We also discuss some estimates, independent on the parameter  $\varepsilon$ , for the velocity, the pressure, and the temperature. Moreover, we give some convergence results. The main results concerning the limit problem with a specific weak form of the Reynolds equation are established in Section 4. Finally, in Section 5, we include some remarks and conclusions on the work.

## 2. Statement of the Problem and Variational Formulation

Here, let  $\omega$  be fixed region in plan  $s = (s_1, s_2) \in \mathbb{R}^2$ . We assume that  $\omega$  has a Lipschitz boundary and is the bottom of the fluid domain. The upper surface  $\Gamma_1^\varepsilon$  is defined by  $s_3 = \varepsilon h(s)$  where  $(0 < \varepsilon < 1)$  is a small parameter that will tend to zero and  $h$  a smooth bounded function such that

$$\left\{ \begin{array}{l} \Sigma_{ij}^\varepsilon = \tilde{\Sigma}_{ij}^\varepsilon - \rho^\varepsilon \delta_{ij}, \\ \tilde{\Sigma}^\varepsilon = g^\varepsilon(T^\varepsilon) \frac{D(w^\varepsilon)}{|D_{II}(w^\varepsilon)|} + \Lambda^\varepsilon(T^\varepsilon) |D(w^\varepsilon)|^{\nu-2} D(w^\varepsilon), \quad \text{if } D(w^\varepsilon) \neq 0, \\ |\tilde{\Sigma}^\varepsilon| \leq g^\varepsilon(T^\varepsilon), \quad \text{if } D(w^\varepsilon) = 0. \end{array} \right. \quad (2)$$

For any tensor  $D = (d_{ij})$ , the notation  $|D|$  represents the matrix norm:  $|D_{II}| = 1/\sqrt{2} (\sum_{i,j=1}^3 d_{ij}d_{ij})^{1/2}$ . Let  $n = (n_1, n_2, n_3)$  the unit outward normal vector on the boundary  $\Gamma^\varepsilon$ . The normal and the tangential velocity on the boundary  $\Omega^\varepsilon$  are  $w_n^\varepsilon = w^\varepsilon \cdot n$ ,  $w_\tau^\varepsilon = w^\varepsilon - w_n^\varepsilon n$ . Also,  $\Sigma^\varepsilon$  is a regular stress tensor field, further let  $\Sigma_n^\varepsilon$  and  $\Sigma_\tau^\varepsilon$  are the normal and tangential components of  $\Sigma^\varepsilon$  on the boundary  $\omega$  by  $\Sigma_n^\varepsilon = (\Sigma^\varepsilon \cdot n) \cdot n$ ,  $\Sigma_\tau^\varepsilon = \Sigma^\varepsilon \cdot n - \Sigma_n^\varepsilon n$ .

**Problem 1.** Find a velocity field  $w^\varepsilon: \Omega^\varepsilon \rightarrow \mathbb{R}^3$ , the pressure  $\rho^\varepsilon$  and a temperature:  $\Omega^\varepsilon \rightarrow \mathbb{R}$  such that

$$\operatorname{div}(\Sigma^\varepsilon) + f^\varepsilon = 0 \text{ in } \Omega^\varepsilon, \quad (3)$$

$$\left\{ \begin{array}{l} \tilde{\Sigma}^\varepsilon = g^\varepsilon(T^\varepsilon) \frac{D(w^\varepsilon)}{|D_{II}(w^\varepsilon)|} + \Lambda^\varepsilon(T^\varepsilon) |D(w^\varepsilon)|^{\nu-2} D(w^\varepsilon) \quad \text{if } D(w^\varepsilon) \neq 0, \\ |\tilde{\Sigma}^\varepsilon| \leq g^\varepsilon(T^\varepsilon) \quad \text{if } D(w^\varepsilon) = 0, \end{array} \right. \quad (4)$$

$$\operatorname{div}(w^\varepsilon) = 0 \text{ in } \Omega^\varepsilon,$$

$$-\operatorname{div} \cdot (K^\varepsilon \nabla T^\varepsilon) = \Lambda^\varepsilon(T^\varepsilon) |D(w^\varepsilon)|^r + \sqrt{2} g^\varepsilon(T^\varepsilon) |D(w^\varepsilon)| - \alpha^\varepsilon T^\varepsilon \text{ in } \Omega, \quad (5)$$

$$w^\varepsilon = 0 \text{ on } \Gamma_1 \cup \Gamma_L,$$

$$w^\varepsilon \times n = 0 \text{ on } \omega, \quad (6)$$

$$\left\{ \begin{array}{l} |\Sigma_\tau^\varepsilon| < k^\varepsilon \Rightarrow w_\tau^\varepsilon = 0 \\ |\Sigma_\tau^\varepsilon| = k^\varepsilon \Rightarrow \exists \lambda \geq 0, w_\tau^\varepsilon = -\lambda \Sigma_\tau^\varepsilon \text{ on } \omega, \\ T^\varepsilon = 0 \text{ on } \Gamma_1 \cup \Gamma_L, \end{array} \right. \quad (7)$$

$$\frac{\partial T^\varepsilon}{\partial n} = 0 \text{ on } \omega. \quad (8)$$

$0 < h_* \leq h(s) \leq h^*$  for all  $(s, 0) \in \omega$  and  $\Gamma_L^\varepsilon$  the lateral surface. We denote by  $\Omega^\varepsilon$  the domain of the following:

$$\Omega^\varepsilon = \{(s, s_3) \in \mathbb{R}^3: (s, 0) \in \omega, 0 < s_3 < \varepsilon h(s)\}. \quad (1)$$

The boundary of  $\Omega^\varepsilon$  is  $\Gamma^\varepsilon$  where  $\Gamma^\varepsilon = \Gamma_1^\varepsilon \cup \Gamma_L^\varepsilon \cup \bar{\omega}$  with  $\Gamma_L^\varepsilon$  is the lateral boundary. We denote by  $\Sigma^\varepsilon$  the deviatoric part and  $\rho^\varepsilon$  the pressure. The fluid is supposed to be viscoplastic, and the relation between  $\Sigma^\varepsilon$  and  $D(w^\varepsilon)$  is given by

where  $\operatorname{div} \Sigma = (\Sigma_{ij,j})$  and  $\operatorname{div} w = w_{i,i}$ . The flow is given by the (3) where the density is assumed equal to one. (4) represents the constitutive law of a Herschel–Bulkley fluid whose the consistency  $\Lambda^\varepsilon$  and the yield limit  $g^\varepsilon$  depend on the temperature,  $1 < \nu < 2$  is the power law exponent of the material. (5) represents the incompressibility condition. Equation (5) represents the energy conservation where the specific heat is assumed equal to one,  $K^\varepsilon > 0$  is the thermal conductivity and the term  $-\alpha^\varepsilon T^\varepsilon$  represents the external heat source with  $\alpha^\varepsilon > 0$ . (5) gives the velocity on  $\Gamma_1 \cup \Gamma_L^\varepsilon$ . As there is no-flux condition across  $\omega$ , then we have equation (6). Condition (7) represents a Tresca thermal friction law on  $\omega$ , where  $k^\varepsilon$  is the friction yields coefficient (8) gives the temperature on  $\Gamma_1 \cup \Gamma_L^\varepsilon$ . (8) is a homogeneous Neumann boundary condition on  $\omega$ :

$$W^{1,\nu}(\Omega^\varepsilon) = \left\{ \vartheta \in L^\nu(\Omega^\varepsilon)^3: \frac{\partial \vartheta_i}{\partial s_j} \in L^\nu(\Omega^\varepsilon) \text{ for } i, j = 1, \dots, 3 \right\},$$

$$V^\varepsilon(\Omega^\varepsilon) = \left\{ \vartheta \in W^{1,\nu}(\Omega^\varepsilon)^3: \vartheta = 0 \text{ on } \Gamma_1 \cup \Gamma_L^\varepsilon, \vartheta \cdot n = 0 \text{ on } \omega \right\},$$

$$V_{\operatorname{div} \cdot}^\varepsilon(\Omega^\varepsilon) = \left\{ \vartheta \in K^\varepsilon: \operatorname{div}(\vartheta) = 0 \right\},$$

$$L_0'(\Omega^\varepsilon) = \left\{ \vartheta \in L^{\nu'}(\Omega^\varepsilon): \int_{\Omega^\varepsilon} \vartheta ds ds_3 = 0 \right\}, \quad (9)$$

and

$$W_{\Gamma_1 \cup \Gamma_L^\varepsilon}^{1,q}(\Omega^\varepsilon) = \left\{ \Phi \in W^{1,q}(\Omega^\varepsilon)^3: \Phi = 0 \text{ on } \Gamma_1 \cup \Gamma_L^\varepsilon \right\}. \quad (10)$$

A formal application of Green's formula, using (3)–(8) leads to the weak formulation: Find a velocity field  $w^\varepsilon \in V_{\operatorname{div} \cdot}^\varepsilon$ ,  $\rho^\varepsilon \in L_0^{\nu'}(\Omega^\varepsilon)$  and  $T^\varepsilon \in W_{\Gamma_1 \cup \Gamma_L^\varepsilon}^{1,q}(\Omega^\varepsilon)$ , ( $1 < q < 3/2$ ) such that

$$\begin{aligned}
 a(w^\varepsilon, \vartheta - w^\varepsilon) - (\rho^\varepsilon, \operatorname{div} \vartheta) + j(T^\varepsilon, \vartheta) - j(T^\varepsilon, w^\varepsilon) &\geq (f^\varepsilon, \vartheta - w^\varepsilon), \forall \vartheta \in V^\varepsilon(\Omega^\varepsilon), \\
 b(T^\varepsilon, \Phi) &= C(w^\varepsilon, T^\varepsilon, \Phi), \forall \Phi \in W_{\Gamma_1^\varepsilon \cup \Gamma_L^\varepsilon}^{1,q}(\Omega^\varepsilon),
 \end{aligned}
 \tag{11}$$

where

$$\begin{aligned}
 a(w^\varepsilon, \vartheta - w^\varepsilon) &= \int_{\Omega^\varepsilon} \Lambda^\varepsilon(T^\varepsilon) |D(w^\varepsilon)|^{\nu-2} D(w^\varepsilon) D(\vartheta) \, ds \, ds_3, \\
 (\rho^\varepsilon, \operatorname{div} \vartheta) &= \int_{\Omega^\varepsilon} \rho^\varepsilon \operatorname{div} \vartheta \, ds \, ds_3, \\
 j(T^\varepsilon, \nu) &= \int_{\bar{\omega}} k^\varepsilon |\nu| \, ds + \sqrt{2} \int_{\Omega^\varepsilon} g^\varepsilon(T^\varepsilon) |D(\nu)| \, ds \, ds_3, \\
 (f^\varepsilon, \nu) &= \int_{\Omega^\varepsilon} f^\varepsilon \nu \, ds \, ds_3 = \sum_{i=1}^3 \int_{\Omega^\varepsilon} f_i^\varepsilon \nu_i \, ds \, ds_3, \\
 b(T^\varepsilon, \Phi) &= \int_{\Omega^\varepsilon} K^\varepsilon \nabla T^\varepsilon \nabla \Phi \, ds \, ds_3, \\
 C(w^\varepsilon, T^\varepsilon, \Phi) &= \int_{\Omega^\varepsilon} \Lambda^\varepsilon(T^\varepsilon) |D(w^\varepsilon)|^\nu \Phi \, ds \, ds_3 \\
 &\quad + \sqrt{2} \int_{\Omega^\varepsilon} g^\varepsilon(T^\varepsilon) |D(w^\varepsilon)| \Phi \, ds \, ds_3 + \int_{\Omega^\varepsilon} \alpha^\varepsilon T^\varepsilon \Phi \, ds \, ds_3.
 \end{aligned}
 \tag{12}$$

It is known that this variational problem has a unique solution, see for more details [10–12].

We assume that there exist  $\Lambda_*, \Lambda^*, g^*, K_\varepsilon^*, K_\varepsilon^*, \alpha_\varepsilon^*, \alpha_\varepsilon^*$  in  $\mathbb{R}$  such that

$$0 \leq \Lambda_* \leq \Lambda^\varepsilon \leq \Lambda^*, \quad 0 \leq g^\varepsilon \leq g^*, \quad f^\varepsilon \in W^{1,\nu'}(\Omega^\varepsilon)^3, \tag{13}$$

and

$$0 \leq K_*^\varepsilon \leq K^\varepsilon \leq K_\varepsilon^*, \quad 0 \leq \alpha_*^\varepsilon \leq \alpha^\varepsilon \leq \alpha_\varepsilon^*. \tag{14}$$

Following some previous results that are useful in the next sections (cf. [13])

$$\|\nabla w^\varepsilon\|_{L^\nu(\Omega^\varepsilon)} \leq C \|D(w^\varepsilon)\|_{L^\nu(\Omega^\varepsilon)}, \quad C \text{ is a positive constant independent of } \varepsilon, \quad 1 < \nu < 2 \text{ (Korn inequality)}, \tag{15}$$

$$\begin{aligned}
 \|w_i^\varepsilon\|_{L^\nu(\Omega^\varepsilon)} &\leq \varepsilon h^* \left\| \frac{\partial w_i^\varepsilon}{\partial \kappa} \right\|_{L^\nu(\Omega^\varepsilon)} \quad \text{for } i = 1, 2; \quad h^* = \max(h(s)), \\
 1 < \nu < 2 &\text{ (Poincaré inequality)},
 \end{aligned}
 \tag{16}$$

$$ab \leq \frac{a^\nu}{\nu} + \frac{b^{\nu'}}{\nu'}, \quad \forall (a, b) \in \mathbb{R}^2, \quad 1 < \nu < 2, \quad \frac{1}{\nu} + \frac{1}{\nu'} = 1 \text{ (Young inequality)}, \tag{17}$$

$$\begin{aligned}
 (a + b)^\rho &\leq (2)^{\rho-1} (a^\rho + b^\rho), \quad \forall (a, b) \in \mathbb{R}_+^{*2}, \quad \forall \rho > 1, \\
 (a + b)^\rho &\leq (a^\rho + b^\rho), \quad \forall (a, b) \in \mathbb{R}_+^{*2}, \quad 0 < \rho < 1.
 \end{aligned}
 \tag{18}$$

### 3. Change of the Domain and Study of Convergence

In this section, we will use the technique of scaling in  $\Omega^\varepsilon$  on the coordinate  $s_3$ , by introducing the change of the variables  $\kappa = s_3/\varepsilon$ . We obtain a fixed domain  $\Omega$  which is independent of  $\varepsilon$ :  $\Omega = \{(s, \kappa) \in \mathbb{R}^3 : (s, 0) \in \bar{\omega}, 0 < \kappa < hs\}$ .

We denote its boundary by  $\Gamma = \bar{\Gamma}_1 \cup \bar{\Gamma}_L \cup \bar{\omega}$ , also we have

$$\begin{aligned}
 \widehat{w}_i^\varepsilon(s, \kappa) &= w_i^\varepsilon(s, s_3), \quad i = 1, 2, \\
 \widehat{w}_3^\varepsilon(s, \kappa) &= \varepsilon^{-1} w_3^\varepsilon(s, s_3), \\
 \widehat{\rho}^\varepsilon(s, \kappa) &= \varepsilon^\nu \rho^\varepsilon(s, s_3).
 \end{aligned}
 \tag{19}$$

Assume that

$$\left. \begin{aligned} \widehat{K}(s, \kappa) &= \varepsilon^{\beta+\nu-2} K^\varepsilon(s, s_3), \widehat{\alpha}(s, \kappa) = \varepsilon^{\beta+\nu} \alpha^\varepsilon(s, s_3), \\ \widehat{\Lambda} &= \Lambda^\varepsilon, \widehat{f}(s, \kappa) = \varepsilon^\nu f^\varepsilon(s, s_3), \widehat{g} = \varepsilon^{\nu-1} g^\varepsilon, \widehat{k} = \varepsilon^{\nu-1} k^\varepsilon, \end{aligned} \right\} \quad (20)$$

with

$$\beta = \frac{3(2-\nu)}{3-\nu}. \quad (21)$$

Let

$$V(\Omega) = \left\{ \widehat{\vartheta} \in (W^{1,\nu}(\Omega))^3 : \widehat{\vartheta} = 0 \text{ on } \Gamma_1 \cup \Gamma_L; \widehat{\vartheta} \cdot n = 0 \text{ on } \omega \right\},$$

$$V_{\text{div}}(\Omega) = \left\{ \widehat{\vartheta} \in K(\Omega) : \text{div} \widehat{\vartheta} = 0 \right\},$$

$$V_\kappa = \left\{ \widehat{\vartheta} \in (L^\nu(\Omega))^2; \frac{\partial \widehat{\vartheta}_i}{\partial \kappa} \in L^\nu(\Omega) : \widehat{\vartheta} = 0 \text{ on } \Gamma_1 \cup \Gamma_L \right\},$$

$$\widetilde{V}_\kappa = \left\{ \widehat{\vartheta} \in V_\kappa : \widehat{\vartheta} \text{ satisfy } (D') \right\},$$

$$\Pi_\kappa = \left\{ \widehat{\vartheta} \in (L^q(\Omega))^2; \frac{\partial \widehat{\vartheta}_i}{\partial \kappa} \in L^q(\Omega) \right\}, \quad (22)$$

where the condition (D') is given by

$$\int_\omega \left( \widehat{\vartheta}_1 \frac{\partial \vartheta}{\partial s_1} + \widehat{\vartheta}_2 \frac{\partial \vartheta}{\partial s_2} \right) ds d\kappa = 0, \quad (23)$$

for all  $\widehat{\vartheta} \in (L^\nu(\Omega))^2$ ,  $\vartheta \in C_0^\infty(\Omega)$ . (D).

By injecting the new data and unknown factors in (19) and (20), we prove that  $(\widehat{w}^\varepsilon, \widehat{\rho}^\varepsilon, \widehat{T}^\varepsilon)$  is a solution of the following problem:

$$\left\{ \begin{aligned} a_0(\widehat{T}^\varepsilon, \widehat{w}^\varepsilon, \widehat{\vartheta} - \widehat{w}^\varepsilon) - (\widehat{\rho}^\varepsilon, \text{div}(\widehat{\vartheta} - \widehat{w}^\varepsilon)) + j_0(\widehat{T}^\varepsilon, \widehat{\vartheta}) - j_0(\widehat{T}^\varepsilon, \widehat{w}^\varepsilon) &\geq (\widehat{f}, \widehat{\vartheta} - \widehat{w}^\varepsilon), \quad \forall \widehat{\vartheta} \in V(\Omega), \\ b_0(\widehat{T}^\varepsilon, \widehat{\Phi}) = C_0(\widehat{w}^\varepsilon, \widehat{T}^\varepsilon, \widehat{\Phi}), & \quad \forall \widehat{\Phi} \in W_{\Gamma_1^i \cup \Gamma_L^i}^{1,q}(\Omega), \end{aligned} \right. \quad (24)$$

where

$$\begin{aligned} a_0(\widehat{T}^\varepsilon, \widehat{w}^\varepsilon, \widehat{\vartheta} - \widehat{w}^\varepsilon) &= \sum_{i,j=1}^2 \int_\Omega \left[ \varepsilon^2 \widehat{\Lambda}(\widehat{T}^\varepsilon) |\bar{D}(\widehat{w}^\varepsilon)|^{\nu-2} \left( \frac{1}{2} \left( \frac{\partial \widehat{w}_i^\varepsilon}{\partial s_j} + \frac{\partial \widehat{w}_j^\varepsilon}{\partial s_i} \right) \right) \right] \frac{\partial(\widehat{\vartheta}_i - \widehat{w}_i^\varepsilon)}{\partial s_j} ds d\kappa \\ &+ \sum_{i=1}^2 \int_\Omega \widehat{\Lambda}(\widehat{T}^\varepsilon) |\bar{D}(\widehat{w}^\varepsilon)|^{\nu-2} \left( \frac{1}{2} \left( \frac{\partial \widehat{w}_i^\varepsilon}{\partial \kappa} + \varepsilon^2 \frac{\partial \widehat{w}_3^\varepsilon}{\partial s_i} \right) \right) \frac{\partial(\widehat{\vartheta}_i - \widehat{w}_i^\varepsilon)}{\partial \kappa} ds d\kappa \\ &+ \int_\Omega \left( \widehat{\Lambda}(\widehat{T}^\varepsilon) |\bar{D}(\widehat{w}^\varepsilon)|^{\nu-2} \varepsilon^2 \frac{\partial \widehat{w}_3^\varepsilon}{\partial \kappa} \right) \frac{\partial(\widehat{\vartheta}_3 - \widehat{w}_3^\varepsilon)}{\partial \kappa} ds d\kappa + \\ &+ \sum_{j=1}^2 \int_\Omega \varepsilon^2 \widehat{\Lambda}(\widehat{T}^\varepsilon) |\bar{D}(\widehat{w}^\varepsilon)|^{\nu-2} \left( \frac{1}{2} \left( \varepsilon^2 \frac{\partial \widehat{w}_3^\varepsilon}{\partial s_j} + \frac{\partial \widehat{w}_j^\varepsilon}{\partial \kappa} \right) \right) \frac{\partial(\widehat{\vartheta}_3 - \widehat{w}_3^\varepsilon)}{\partial s_j} ds d\kappa, \end{aligned}$$



$$\begin{aligned}
 (\hat{\rho}^\varepsilon, \operatorname{div}(\hat{\vartheta} - \hat{w}^\varepsilon)) &= \int_{\Omega^\varepsilon} \hat{\rho}^\varepsilon \operatorname{div}(\hat{\vartheta} - \hat{w}^\varepsilon) ds d\kappa, \\
 j_0(\hat{T}^\varepsilon, \hat{\vartheta}) &= \sqrt{2} \int_{\Omega} \hat{g}(\hat{T}^\varepsilon) |\bar{D}(\hat{\vartheta})| ds d\kappa + \int_{\omega} \hat{k} |\hat{\vartheta}| ds, \\
 (\hat{f}^\varepsilon, \hat{\vartheta} - \hat{w}^\varepsilon) &= \sum_{j=1}^2 \int_{\Omega} \hat{f}_j(\hat{\vartheta}_j - \hat{w}_j^\varepsilon) ds d\kappa + \int_{\Omega} \varepsilon \hat{f}_3(\hat{\vartheta}_3 - \hat{w}_3^\varepsilon) ds d\kappa, \\
 b_0(\hat{T}^\varepsilon, \hat{\Phi}) &= \int_{\Omega} \varepsilon^2 \nabla_\varepsilon \hat{T}^\varepsilon \nabla_\varepsilon \hat{\Phi} ds d\kappa = \sum_{i=1}^2 \int_{\Omega} \varepsilon^2 \hat{K} \frac{\partial \hat{T}^\varepsilon}{\partial s_i} \frac{\partial \hat{\Phi}}{\partial s_i} ds d\kappa + \int_{\Omega} \hat{K} \frac{\partial \hat{T}^\varepsilon}{\partial \kappa} \frac{\partial \hat{\Phi}}{\partial \kappa} ds d\kappa, \\
 C_0(\hat{w}^\varepsilon, \hat{T}^\varepsilon, \hat{\Phi}) &= \int_{\Omega} \varepsilon^\beta \hat{\Lambda}(\hat{T}^\varepsilon) |\bar{D}(\hat{w}^\varepsilon)|^\nu \hat{\Phi} ds d\kappa + \sqrt{2} \int_{\Omega} \varepsilon^\beta \hat{g}(\hat{T}^\varepsilon) |\bar{D}(\hat{w}^\varepsilon)| \hat{\Phi} ds d\kappa - \int_{\Omega} \hat{\alpha} \hat{T}^\varepsilon \hat{\Phi} ds d\kappa, \\
 |\bar{D}(\hat{w}^\varepsilon)| &= \left( \frac{1}{4} \sum_{i,j=1}^2 \varepsilon^2 \left( \frac{\partial \hat{w}_i^\varepsilon}{\partial s_j} + \frac{\partial \hat{w}_j^\varepsilon}{\partial s_i} \right)^2 + \frac{1}{2} \sum_{i=1}^2 \left( \frac{\partial \hat{w}_i^\varepsilon}{\partial \kappa} + \varepsilon^2 \frac{\partial \hat{w}_3^\varepsilon}{\partial s_i} \right)^2 + \varepsilon^2 \left( \frac{\partial \hat{w}_3^\varepsilon}{\partial \kappa} \right)^2 \right)^{1/2}.
 \end{aligned} \tag{25}$$

3.1. A Priori Estimates on the Velocity and the Pressure

**Theorem 1.** For all  $1 < \nu < 2$  and under assumptions (13) and (14) and (20), there exists a constant  $C > 0$  independent of  $\varepsilon$  such that

$$\begin{aligned}
 \sum_{i,j=1}^2 \left\| \varepsilon \frac{\partial \hat{w}_i^\varepsilon}{\partial s_j} \right\|_{L^{\nu'}(\Omega)}^\nu + \sum_{i=1}^2 \left( \left\| \frac{\partial \hat{w}_i^\varepsilon}{\partial \kappa} \right\|_{L^{\nu'}(\Omega)}^\nu + \left\| \varepsilon^2 \frac{\partial \hat{w}_3^\varepsilon}{\partial s_i} \right\|_{L^{\nu'}(\Omega)}^\nu \right) + \left\| \varepsilon \frac{\partial \hat{w}_3^\varepsilon}{\partial \kappa} \right\|_{L^{\nu'}(\Omega)}^\nu &\leq C, \\
 \left\| \frac{\partial \hat{\rho}^\varepsilon}{\partial s_i} \right\|_{W^{-1,\nu'}(\Omega)} &\leq C \quad \text{for } i = 1, 2, \\
 \left\| \frac{\partial \hat{\rho}^\varepsilon}{\partial \kappa} \right\|_{W^{-1,\nu'}(\Omega)} &\leq \varepsilon C.
 \end{aligned} \tag{26}$$

*Proof.* Choosing  $\vartheta = 0$  as test function in inequality (11), we get

$$a(w^\varepsilon, w^\varepsilon) + \sqrt{2} \int_{\Omega^\varepsilon} g^\varepsilon(T^\varepsilon) |D(w^\varepsilon)| ds ds_3 + \int_{\omega} k^\varepsilon |w^\varepsilon| ds \leq (f^\varepsilon, w^\varepsilon), \tag{27}$$

from (16) and (17) we have

$$\begin{aligned}
 (f^\varepsilon, w^\varepsilon) &\leq \varepsilon h^* \|\nabla w^\varepsilon\|_{L^\nu(\Omega^\varepsilon)} \|f^\varepsilon\|_{L^{\nu'}(\Omega^\varepsilon)} \\
 &\leq \frac{1}{2} \Lambda_* C_k \|\nabla w^\varepsilon\|_{L^\nu(\Omega^\varepsilon)}^\nu + \frac{(\varepsilon h^*)^{\nu'}}{\nu' (1/2 \Lambda_* \nu C_k)^{\nu'/\nu}} \|f^\varepsilon\|_{L^{\nu'}(\Omega^\varepsilon)}^{\nu'}.
 \end{aligned} \tag{28}$$

From (27) and (28), we deduce

$$\begin{aligned}
 a(w^\varepsilon, w^\varepsilon) + \sqrt{2} \int_{\Omega^\varepsilon} g^\varepsilon(T^\varepsilon) |D(w^\varepsilon)| ds ds_3 + \int_{\omega} k^\varepsilon |w^\varepsilon| ds \\
 \leq \frac{1}{2} \Lambda_* C_k \|\nabla w^\varepsilon\|_{L^\nu(\Omega^\varepsilon)}^\nu + \frac{(\varepsilon h^*)^{\nu'}}{\nu' (1/2 \Lambda_* \nu C_k)^{\nu'/\nu}} \|f^\varepsilon\|_{L^{\nu'}(\Omega^\varepsilon)}^{\nu'}.
 \end{aligned} \tag{29}$$

We multiply (29) by  $\varepsilon^{\nu-1}$ , we get

$$\begin{aligned}
 \varepsilon^{\nu-1} a(w^\varepsilon, w^\varepsilon) + \sqrt{2} \int_{\Omega^\varepsilon} \hat{g}(\hat{T}) |\bar{D}(\hat{w}^\varepsilon)| ds d\kappa + \int_{\omega} \hat{k} |\hat{w}^\varepsilon| ds \\
 \leq \frac{1}{2} \Lambda_* C_k \varepsilon^{\nu-1} \|\nabla w^\varepsilon\|_{L^\nu(\Omega^\varepsilon)}^\nu + \varepsilon^{\nu-1} \frac{(\varepsilon h^*)^{\nu'}}{\nu' (1/2 \Lambda_* \nu C_k)^{\nu'/\nu}} \|f^\varepsilon\|_{L^{\nu'}(\Omega^\varepsilon)}^{\nu'}.
 \end{aligned} \tag{30}$$

As  $\varepsilon^{\nu'} \|f^\varepsilon\|_{L^{\nu'}(\Omega^\varepsilon)}^{\nu'} = \varepsilon^{1-\nu} \|\hat{f}\|_{L^{\nu'}(\Omega)}$ , we have

$$\begin{aligned} & \varepsilon^{\nu-1} a(w^\varepsilon, w^\varepsilon) + \sqrt{2} \int_{\Omega} \widehat{g}(\widehat{T}^\varepsilon) |\widehat{D}(\widehat{w}^\varepsilon)| ds d\kappa + \int_{\omega} \widehat{k} |\widehat{w}^\varepsilon| ds \\ & \leq \frac{1}{2} \Lambda_* C_k \varepsilon^{\nu-1} \|\nabla w^\varepsilon\|_{L^\nu(\Omega^\varepsilon)}^\nu + \frac{(h^*)^{\nu'}}{\nu' (1/2 \Lambda_* \nu C_k)^{\nu'/\nu}} \|\widehat{f}\|_{L^{\nu'}(\Omega)}. \end{aligned} \quad (31)$$

From Korn's inequality and (15), there exists a constant  $C_k$  independent of  $\varepsilon$ , such that

$$\frac{1}{2} \Lambda_* C_k \varepsilon^{\nu-1} \|\nabla w^\varepsilon\|_{L^\nu(\Omega^\varepsilon)}^\nu + \sqrt{2} \int_{\Omega} \widehat{g}(\widehat{T}^\varepsilon) |\widehat{D}(\widehat{w}^\varepsilon)| ds d\kappa + \int_{\omega} \widehat{k} |\widehat{w}^\varepsilon| ds \leq \frac{(h^*)^{\nu'}}{\nu' (1/2 \Lambda_* \nu C_k)^{\nu'/\nu}} \|\widehat{f}\|_{L^{\nu'}(\Omega)} \quad (32)$$

From (32), we deduce (26), with  $C = (1/2 \Lambda_* C_k)^{-1} (h^*)^{\nu'} / \nu' (1/2 \Lambda_* \nu C_k)^{\nu'/\nu} \|\widehat{f}\|_{L^{\nu'}(\Omega)}$ , and

$$\begin{aligned} \varepsilon^{\nu-1} \|\nabla w^\varepsilon\|_{L^\nu(\Omega^\varepsilon)}^\nu &= \|\nabla \widehat{w}^\varepsilon\|_{L^\nu(\Omega)}^\nu \\ &= \sum_{i,j=1}^2 \left\| \varepsilon \frac{\partial \widehat{w}_i^\varepsilon}{\partial s_j} \right\|_{L^\nu(\Omega)}^\nu + \left\| \varepsilon \frac{\partial \widehat{w}_3^\varepsilon}{\partial \kappa} \right\|_{L^\nu(\Omega)}^\nu + \sum_{i=1}^2 \left( \left\| \frac{\partial \widehat{w}_i^\varepsilon}{\partial \kappa} \right\|_{L^\nu(\Omega)}^\nu + \left\| \varepsilon^2 \frac{\partial \widehat{w}_3^\varepsilon}{\partial s_i} \right\|_{L^\nu(\Omega)}^\nu \right). \end{aligned} \quad (33)$$

We prove (26) and (26) as in [14].  $\square$

**3.2. A Priori Estimates on the Temperature.** In this subsection, we look for a priori estimates on the temperature  $\widehat{T}^\varepsilon$ , for this we need to establish the following result:

**Theorem 2.** *Assume that the assumptions of Theorem 1 are satisfied. Moreover, assume that there exist  $K^*$ ,  $K_*$ , such that*

$$0 < K_* \leq \widehat{K} \leq K^*. \quad (34)$$

Then, there exists a positive constant  $C_1$  independent of  $\varepsilon$ , such that

$$\left\| \frac{\partial \widehat{T}^\varepsilon}{\partial \kappa} \right\|_{W^{1,q}(\Omega)} \leq C_1, \quad (35)$$

$$\sum_{i=1}^2 \left\| \varepsilon \frac{\partial \widehat{T}^\varepsilon}{\partial s_i} \right\|_{W^{1,q}(\Omega)} \leq C_1.$$

*Proof.* Choosing  $\Phi = \vartheta(T^\varepsilon)$  in (24), where  $\vartheta$  is defined by

$$\vartheta(t) = \zeta \operatorname{sign}(t) \int_0^{|t|} \frac{d\tau}{(1+|\tau|)^{\zeta+1}} = \operatorname{sign}(t) \left[ 1 - \frac{1}{(1+|t|)^\zeta} \right], \quad (36)$$

We obtain

$$\zeta K_* \int_{\Omega} \frac{|\nabla \widehat{T}^\varepsilon|^2}{(1+|\widehat{T}^\varepsilon|)^{\zeta+1}} \leq \Lambda^* \varepsilon^{\beta-2} \int_{\Omega} |\widehat{D}(\widehat{w}^\varepsilon)| ds d\kappa + \varepsilon^{\beta-2} \sqrt{2} g^* \int_{\Omega} |\widehat{D}(\widehat{w}^\varepsilon)| ds d\kappa. \quad (37)$$

On the other hand,

$$\int_{\Omega} |\widehat{D}(\widehat{w}^\varepsilon)|^\nu ds d\kappa \leq C(\nu) \left[ \sum_{i,j=1}^2 \left\| \varepsilon \frac{\partial \widehat{w}_i^\varepsilon}{\partial s_j} \right\|_{L^\nu(\Omega)}^\nu + \sum_{i=1}^2 \left( \left\| \frac{\partial \widehat{w}_i^\varepsilon}{\partial \kappa} \right\|_{L^\nu(\Omega)}^\nu + \left\| \varepsilon^2 \frac{\partial \widehat{w}_3^\varepsilon}{\partial s_i} \right\|_{L^\nu(\Omega)}^\nu \right) + \left\| \varepsilon \frac{\partial \widehat{w}_3^\varepsilon}{\partial \kappa} \right\|_{L^\nu(\Omega)}^\nu \right], \quad (38)$$

where  $C(\nu) > 0$  depends only on  $\nu$ .

As  $\nu > 1$  and  $0 < \varepsilon < 1$  then  $\varepsilon^{\nu-1} \leq 1$ , so using this inequality and (26), we deduce

$$\int_{\Omega} \frac{|\nabla \widehat{T}^\varepsilon|^2}{(1+|\widehat{T}^\varepsilon|)^{\zeta+1}} \leq \frac{1}{\zeta K_*} (\Lambda^* C(\nu) C + \sqrt{2} g^* C) \varepsilon^{\beta-2}. \quad (39)$$

Using Holder's inequality with the exponents  $2/q$  and  $2/2 - q$ , for  $q < 3/2$ , we obtain

$$\int_{\Omega} |\nabla_{\varepsilon} \widehat{T}^{\varepsilon}|^q \, dsd\kappa \leq \left( \int_{\Omega} \frac{|\nabla_{\varepsilon} \widehat{T}^{\varepsilon}|^2}{(1 + |\widehat{T}^{\varepsilon}|)^{\zeta+1}} \right)^{q/2} \left( \int_{\Omega} (1 + |\widehat{T}^{\varepsilon}|)^{(\zeta+1)q/2-q} \right)^{2-q/2}, \tag{40}$$

using (39), we get

$$\int_{\Omega} |\nabla_{\varepsilon} \widehat{T}^{\varepsilon}|^q \, dsd\kappa \leq \left( \frac{1}{\zeta K_*} (\Lambda^* C(\nu)C + \sqrt{2} g^* C) \varepsilon^{\beta-2} \right)^{q/2} \left( \int_{\Omega} (1 + |\widehat{T}^{\varepsilon}|)^{q^*} \right)^{2-q/2}, \tag{41}$$

where  $q^* = 3q/3 - q \geq (\zeta + 1)q/2 - q$ .

By (18) and (18), we find

$$\int_{\Omega} |\nabla_{\varepsilon} \widehat{T}^{\varepsilon}|^q \, dsd\kappa \leq \left( \frac{1}{\zeta K_*} (\Lambda^* C(\nu)C + \sqrt{2} g^* C) \varepsilon^{\beta-2} \right)^{q/2} 2^{(q^*-1)2-q/2} \left( |\Omega|^{2-q/2} + \left( \int_{\Omega} |\widehat{T}^{\varepsilon}|^{q^*} \right)^{2-q/2} \right). \tag{42}$$

Now using the Poincaré-Sobolev inequality, we have

$$\begin{aligned} \left( \int_{\Omega} |\widehat{T}^{\varepsilon}|^{q^*} \, dsd\kappa \right)^{1/q^*} &\leq C' \|\nabla_{\varepsilon} \widehat{T}^{\varepsilon}\|_{L^q(\Omega)} \\ &\leq \left( \frac{1}{\zeta K_*} (\Lambda^* C(\nu)C + \sqrt{2} g^* C) \right)^{1/2} \varepsilon^{\beta/2-1} 2^{(q^*-1)2-q/2q} \times C' \left( |\Omega|^{2-q/2q} + \left( \int_{\Omega} |\widehat{T}^{\varepsilon}|^{q^*} \right)^{2-q/2q} \right). \end{aligned} \tag{43}$$

On the other hand, for all  $a > 0, b > 0, c > 0$  and  $0 < s < t$ , we have the implication:

$$\text{If } a^t \leq b + ca^s \text{ then } a \leq \max \left\{ 1, (b + c) \frac{1}{t-s} \right\}. \tag{44}$$

Hence from (43) and (44) and the fact that  $2 - q/2 < 1$ , we deduce

where

$$\xi = \max \left[ 1, \gamma \varepsilon^{(\beta/2-1)(1/q^*-2-q/2q)-1-2-q/2} \right] = \max \left[ 1, \gamma \varepsilon^{3(\beta/2-1)(2-q)} \right], \tag{46}$$

and

$$\begin{aligned} \gamma &= \left[ \left( \frac{1}{\zeta K_*} (\Lambda^* C(\nu)C + \sqrt{2} g^* C) \right)^{1/2} 2^{(q^*-1)2-q/2q} C' (|\Omega|^{2-q/2q} + 1) \right]^{(1/q^*-2-q/2q)^{-1}} \\ &= \left[ \left( \frac{1}{\zeta K_*} (\Lambda^* C(\nu)C + \sqrt{2} g^* C) \right)^{1/22-q/2q} 2^{(q^*-1)2-q/2q} C' (|\Omega|^{2-q/2q} + 1) \right]^6. \end{aligned} \tag{47}$$

As  $\beta = 3(2 - q/3 - q)$ , then  $3(2 - q)(\beta/2 - 1) < 0$ . So for  $\varepsilon \leq \beta^{[1 - 3(2 - q)(\beta/2 - 1)]^{-1}}$ , we obtain

$$\xi = \gamma \varepsilon^{3(\beta/2 - 1)(2 - q)} \geq 1. \quad (48)$$

From (42) and (45), we get

$$\varepsilon^q \int_{\Omega} |\nabla_{\varepsilon} \widehat{T}^{\varepsilon}|^q ds d\kappa \leq \left( \frac{1}{\zeta K_*} (\Lambda^* C(\nu) C + \sqrt{2} g^* C) \right)^{q/2} 2^{(q^* - 1)2 - q/2} (|\Omega|^{2 - q/2} \varepsilon^{\beta/2q} + \gamma \varepsilon^{3(\beta/2 - 1)(2 - q) + \beta/2q}), \quad (49)$$

as  $3(\beta/2 - 1)(2 - q) + (\beta/2)q = 0$  and  $(\beta/2)q > 0$ , we obtain

$$\varepsilon^q \int_{\Omega} |\nabla_{\varepsilon} \widehat{T}^{\varepsilon}|^q ds d\kappa \leq C_1, \quad (50)$$

where

$$C_1 = \left( \frac{1}{\zeta K_*} (\Lambda^* C(\nu) C + \sqrt{2} g^* C) \right)^{q/2} 2^{(q^* - 1)2 - q/2} (|\Omega|^{2 - q/2} + \gamma). \quad (51)$$

where  $C_1$  is a constant independent of  $\varepsilon$ . Thus, we obtain (35) and (35)  $\square$

The following theorem states some immediate estimates of the limit of our initial problem.

**Theorem 3.** *Under the same assumptions as in Theorem 1 and Theorem 2, there exist  $w^* = (w_1^*, w_2^*) \in \widetilde{V}_{\kappa}$ ,  $\rho^* \in L_0^r(\Omega)$  and  $T^* \in \Pi_{\kappa}$  such that*

$$\widehat{w}_i^{\varepsilon} \rightharpoonup w_i^*, \quad i = 1, 2 \quad \text{weakly in } \widetilde{V}_{\kappa}, \quad (52)$$

$$\varepsilon \frac{\partial \widehat{w}_i^{\varepsilon}}{\partial s_j} \rightharpoonup 0, \quad i, j = 1, 2 \quad \text{weakly in } L^r(\Omega), \quad (53)$$

$$\varepsilon \frac{\partial \widehat{w}_3^{\varepsilon}}{\partial \kappa} \rightharpoonup 0, \quad \text{weakly in } L^r(\Omega),$$

$$\varepsilon^2 \frac{\partial \widehat{w}_3^{\varepsilon}}{\partial s_i} \rightharpoonup 0, \quad i = 1, 2 \quad \text{weakly in } L^r(\Omega), \quad (54)$$

$$\varepsilon \widehat{w}_3^{\varepsilon} \rightharpoonup 0, \quad \text{weakly in } L^r(\Omega), \quad (55)$$

$$\widehat{\rho}^{\varepsilon} \rightharpoonup \rho^*, \quad \text{weakly in } L^r(\Omega), \quad \rho^* \text{ depend only of } s, \quad (56)$$

$$\widehat{T}^{\varepsilon} \rightharpoonup T^* \quad \text{weakly in } \Pi_{\kappa}, \quad (57)$$

$$\frac{\partial \widehat{T}^{\varepsilon}}{\partial s_i} \rightharpoonup 0, \quad i = 1, 2 \quad \text{weakly in } L^q(\Omega). \quad (58)$$

*Proof.* The convergence of (52) to (53) is a direct result of inequality (26). Using (26) and (26), we get (56), while (57) and (58) follow from (35).  $\square$

#### 4. Study of the Limit Problem

In this section, we give both the equations satisfied by  $\rho^*$  and  $w^*$  in  $\Omega$  and the inequalities for the trace of the velocity  $w^*(s, 0)$  and the stress  $\partial w^*/\partial \kappa(s, 0)$  on  $\omega$ .

**Theorem 4.** *With the same assumptions of Theorem 3, the solution  $(w^*, \rho^*, T^*)$  satisfies the following relations:*

$$\begin{aligned} & \sum_{i=1}^2 \int_{\Omega} \widehat{\Lambda}(T^*) \left( \frac{1}{2} \right)^{\frac{\nu}{2}} \left( \sum_{i=1}^2 \left( \frac{\partial w_i^*}{\partial \kappa} \right)^2 \right)^{\nu - 2/2} \frac{\partial(w_i^*)}{\partial \kappa} \frac{\partial(\widehat{\vartheta}_i - w_i^*)}{\partial \kappa} ds d\kappa \\ & - \int_{\Omega} \rho^*(s) \left( \frac{\partial \widehat{\vartheta}_1}{\partial s_1} + \frac{\partial \widehat{\vartheta}_2}{\partial s_2} \right) ds d\kappa + \int_{\Omega} \widehat{g}(T^*) \left( \left| \frac{\partial \widehat{\vartheta}}{\partial \kappa} \right| - \left| \frac{\partial w^*}{\partial \kappa} \right| \right) ds d\kappa \end{aligned} \quad (59)$$

$$+ \int_{\omega} \widehat{k}(|\widehat{\vartheta}| - |w^*|) ds \geq \sum_{i=1}^2 \int_{\Omega} \widehat{f}_i(\widehat{\vartheta}_i - w_i^*) ds d\kappa, \quad \forall \widehat{\vartheta} \in W_{\Gamma_1 \cup \Gamma_L},$$

$$\int_{\Omega} \widehat{\Lambda}(T^*) \left( \frac{1}{2} \right)^{\nu/2} \left| \frac{\partial w^*}{\partial \kappa} \right|^{\nu} ds d\kappa + \int_{\Omega} \widehat{g}(T^*) \left| \frac{\partial w^*}{\partial \kappa} \right| ds d\kappa + \int_{\omega} \widehat{k}|w^*| ds = \int_{\Omega} \widehat{f} w^* ds d\kappa, \quad (60)$$

$$\int_{\Omega} \widehat{\Lambda}(T^*) \left( \frac{1}{2} \right)^{\frac{\nu}{2}} \left| \frac{\partial w^*}{\partial \kappa} \right|^{\nu - 2} \frac{\partial w^*}{\partial \kappa} \frac{\partial \widehat{\Phi}}{\partial \kappa} ds d\kappa + \int_{\Omega} \widehat{g}(T^*) \left| \frac{\partial \widehat{\Phi}}{\partial \kappa} \right| ds d\kappa + \int_{\omega} \widehat{k}|\widehat{\Phi}| ds \geq \int_{\Omega} \widehat{f} \widehat{\Phi} ds d\kappa, \quad \forall \widehat{\Phi} \in \Sigma(K), \quad (61)$$

and

$$-\frac{\partial}{\partial \kappa} \left( K \frac{\partial T^*}{\partial \kappa} \right) = -\widehat{\alpha} T^* \text{in} L^q(\Omega), \quad (62)$$

$$\begin{aligned} T^* &= 0 \text{ in } \Gamma_1 \cup \Gamma_L, \\ \frac{\partial T^*}{\partial n} &= 0 \text{ in } \bar{\omega}, \end{aligned} \quad (63)$$

where

$$W_{\Gamma_1 \cup \Gamma_L} = \{ \widehat{\vartheta} = (\widehat{\vartheta}_1, \widehat{\vartheta}_2) \in W^{1,\nu}(\Omega)^2, \widehat{\vartheta} = 0 \text{ on } \Gamma_1 \cup \Gamma_L \}, \quad (64)$$

and

$$\widetilde{\Sigma}(K) = \{ \widehat{\Phi} = (\widehat{\Phi}_1, \widehat{\Phi}_2) \in W^{1,\nu}(\Omega)^2: \widehat{\Phi} \text{ satisfy } (D') \}. \quad (65)$$

The proof of this theorem is based on the following lemma.

**Lemma 1** (Minty). *Let  $E$  be a Banach spaces,  $T: E \rightarrow E'$  a monotone and hemicontinuous operator,  $J: E \rightarrow ]-\infty, +\infty]$  a proper and convex functional. Let  $u \in E$  and  $f \in E'$ . Then the following assertions are equivalent:*

$$\begin{aligned} \langle Tw; v - w \rangle_{E' \times E} + J(v) - J(w) &\geq \langle f; v - w \rangle_{E' \times E}, \quad \forall v \in E, \\ \langle Tv; v - w \rangle_{E' \times E} + J(v) - J(w) &\geq \langle f; v - w \rangle_{E' \times E}, \quad \forall v \in E. \end{aligned} \quad (66)$$

*Proof.* By using Minty's Lemma 1 and the fact that  $\text{div}(\widehat{w}^\varepsilon) = 0$  in  $\Omega$ , then (24) is equivalent to

$$\begin{aligned} a_0(\widehat{T}^\varepsilon, \widehat{\vartheta}, \widehat{\vartheta} - \widehat{w}^\varepsilon) - \sum_{i=1}^2 \left( \widehat{\rho}^\varepsilon, \frac{\partial \widehat{\vartheta}_i}{\partial s_i} \right) - \left( \widehat{\rho}^\varepsilon, \frac{\partial \widehat{\vartheta}_3}{\partial \kappa} \right) + j_0(\widehat{T}^\varepsilon, \widehat{\vartheta}) - j_0(\widehat{T}^\varepsilon, \widehat{w}^\varepsilon) \\ \geq \sum_{i=1}^2 \int_{\Omega} \widehat{f}_i(\widehat{\vartheta}_i - \widehat{w}_i^\varepsilon) \text{d}s \text{d}\kappa + \int_{\Omega} \varepsilon \widehat{f}_3(\widehat{\vartheta}_3 - \widehat{w}_3^\varepsilon) \text{d}s \text{d}\kappa. \end{aligned} \quad (67)$$

From (57), we have  $\widehat{T}^\varepsilon \rightarrow T^*$  almost everywhere. As  $\widehat{\Lambda}$  is continuous function on  $\mathbb{R}$ , then

$$\widehat{\Lambda}(\widehat{T}^\varepsilon) \rightarrow \widehat{\Lambda}(T^*). \quad (68)$$

Using Theorem 4 and the fact  $j_0$  is convex and lower semicontinuous,  $(\liminf j_0(\widehat{T}^\varepsilon, \widehat{w}^\varepsilon) \geq j_0(T^*, w^*))$ , we find

$$\begin{aligned} \sum_{i=1}^2 \int_{\Omega} \frac{1}{2} \widehat{\Lambda}(T^*) \left( \frac{1}{2} \sum_{i=1}^2 \left( \frac{\partial \widehat{\vartheta}_i}{\partial \kappa} \right)^2 \right)^{\nu-2/2} \frac{\partial(\widehat{\vartheta}_i)}{\partial \kappa} \frac{\partial(\widehat{\vartheta}_i - w_i^*)}{\partial \kappa} \text{d}s \text{d}\kappa \\ - \int_{\Omega} \rho^* \left( \frac{\partial \widehat{\vartheta}_1}{\partial s_1} + \frac{\partial \widehat{\vartheta}_2}{\partial s_2} \right) \text{d}s \text{d}\kappa - \int_{\Omega} \rho^* \frac{\partial \widehat{\vartheta}_3}{\partial \kappa} \text{d}s \text{d}\kappa + j_0(T^*, \widehat{\vartheta}) - j_0(T^*, w^*) \\ \geq \sum_{j=1}^2 \int_{\Omega} \widehat{f}_j(\widehat{\vartheta}_j - w_j^*) \text{d}s \text{d}\kappa, \end{aligned} \quad (69)$$

and as  $\int_{\Omega} \rho^* (\partial \widehat{\vartheta}_3 / \partial \kappa) \text{d}s \text{d}\kappa = 0$ , because  $\rho^*$  independent of  $\kappa$ , we get

$$\begin{aligned} \sum_{i=1}^2 \int_{\Omega} \frac{1}{2} \widehat{\Lambda}(T^*) \left( \frac{1}{2} \sum_{i=1}^2 \left( \frac{\partial \widehat{\vartheta}_i}{\partial \kappa} \right)^2 \right)^{\nu-2/2} \frac{\partial(\widehat{\vartheta}_i)}{\partial \kappa} \frac{\partial(\widehat{\vartheta}_i - w_i^*)}{\partial \kappa} \text{d}s \text{d}\kappa \\ - \int_{\Omega} \rho^* \left( \frac{\partial \widehat{\vartheta}_1}{\partial s_1} + \frac{\partial \widehat{\vartheta}_2}{\partial s_2} \right) \text{d}s \text{d}\kappa + j_0(T^*, \widehat{\vartheta}) - j_0(T^*, w^*) \geq \sum_{j=1}^2 \int_{\Omega} \widehat{f}_j(\widehat{\vartheta}_j - w_j^*) \text{d}s \text{d}\kappa. \end{aligned} \quad (70)$$

Using again Minty's lemma for the second time, thus (61) is equivalent to (59). Now, we can choose  $\widehat{\vartheta} = 2w^*$  and  $\widehat{\vartheta} = 0$  respectively in (59), we find (60). For (61), we choose  $\widehat{\Phi} = \widehat{\vartheta} - w^*$  for all  $\widehat{\Phi} \in \Sigma(K)$ . Passing to the limit on  $\varepsilon$  tend to 0 in (24) and using (52)–(54), (57)–(58) we get

$$\int_{\Omega} \widehat{K} \frac{\partial T^*}{\partial \kappa} \frac{\partial \widehat{\Phi}}{\partial \kappa} ds d\kappa = - \int_{\Omega} \widehat{\alpha} T^* \widehat{\Phi} ds d\kappa, \quad \forall \widehat{\Phi} \in W_{\Gamma_1 \cup \Gamma_L}^{1,q}(\Omega), \quad (71)$$

by Green's formula, we obtain

$$\frac{\partial}{\partial \kappa} \left( \widehat{K} \frac{\partial T^*}{\partial \kappa} \right) = \widehat{\alpha} T^* \text{ in } W^{-1,q'}(\Omega). \quad (72)$$

□

$$-\frac{\partial}{\partial \kappa} \left[ \frac{1}{2} \widehat{\Lambda}(T^*) \left( \frac{1}{2} \sum_{i=1}^2 \left( \frac{\partial w_i^*}{\partial \kappa} \right)^2 \right)^{\nu-2/2} \frac{\partial w^*}{\partial \kappa} + \widehat{g}(T^*) \left| \frac{\partial w^* / \partial \kappa}{|\partial w^* / \partial \kappa|} \right| \right] = \widehat{f} - \nabla \rho^*, \text{ in } W^{-1,\nu'}(\Omega)^2. \quad (74)$$

where  $\pi \in L^\infty(\Omega)^2$  and  $\|\pi\|_{\Omega,\infty} \leq 1$ .

*Proof.* If  $\partial w^* / \partial \kappa = 0$ , from (73) we get  $|\widehat{\Sigma}^*| < \widehat{g}(T^*)$ . For all  $\widehat{\Phi} \in \Sigma(K)$ , choosing  $\widehat{\Phi} = \widehat{\Phi}$ , then  $\widehat{\Phi} = -\widehat{\Phi}$  in (61), we obtain

**Theorem 5.** *Let us set*

$$\begin{aligned} \widehat{\Sigma}^* &= \widehat{\Sigma}^* - \nabla \rho^*, \\ \widehat{\Sigma}^* &= \left( \frac{1}{2} \right)^2 \widehat{\Lambda}(T^*) \left| \frac{\partial w^*}{\partial \kappa} \right|^{\nu-2} \frac{\partial w^*}{\partial \kappa} + \widehat{g}(T^*) \pi, \end{aligned} \quad (73)$$

then

$$\left| F \left( \widehat{k} \widehat{\Phi}, \frac{\partial \widehat{\Phi}}{\partial \kappa} \right) \right| \leq \int_{\omega} \widehat{k} |\widehat{\Phi}| ds + \int_{\Omega} \widehat{g}(T^*) \left| \frac{\partial \widehat{\Phi}}{\partial \kappa} \right| ds d\kappa, \quad (75)$$

where

$$F \left( \widehat{k} \widehat{\Phi}, \frac{\partial \widehat{\Phi}}{\partial \kappa} \right) = \int_{\Omega} \widehat{\Lambda}(T^*) \left( \frac{1}{2} \right)^{\nu/2} \left| \frac{\partial w^*}{\partial \kappa} \right|^{\nu-2} \frac{\partial w^*}{\partial \kappa} \frac{\partial \widehat{\Phi}}{\partial \kappa} ds d\kappa - \int_{\Omega} \widehat{f} \widehat{\Phi} ds d\kappa, \quad (76)$$

Now, utilising the Hanh-Banach theorem, then,  $\exists (\chi, \pi) \in L^\infty(\omega)^2 \times L^\infty(\Omega)^2$ , with  $\|\chi\|_{\omega,\infty} \leq 1, \|\pi\|_{\Omega,\infty} \leq 1$ , such that

$$F \left( \widehat{k} \widehat{\Phi}, \frac{\partial \widehat{\Phi}}{\partial \kappa} \right) = - \int_{\omega} \chi \widehat{k} \widehat{\Phi} ds - \int_{\Omega} \pi \widehat{g}(T^*) \frac{\partial \widehat{\Phi}}{\partial \kappa} ds d\kappa. \quad (77)$$

In particular, from (60) and (76), we get

$$\int_{\omega} \widehat{k} |w^*| ds + \int_{\Omega} \widehat{g}(T^*) \left| \frac{\partial w^*}{\partial \kappa} \right| ds d\kappa = \int_{\omega} \chi \widehat{k} w^* ds + \int_{\Omega} \pi \widehat{g}(T^*) \frac{\partial w^*}{\partial \kappa} ds d\kappa. \quad (78)$$

Also, from (76) and (77), we have

$$\int_{\Omega} \widehat{\Lambda}(T^*) \left( \frac{1}{2} \right)^{\nu/2} \left| \frac{\partial w^*}{\partial \kappa} \right|^{\nu-2} \frac{\partial w^*}{\partial \kappa} \frac{\partial \widehat{\Phi}}{\partial \kappa} ds d\kappa + \int_{\omega} \chi \widehat{k} \widehat{\Phi} ds + \int_{\Omega} \pi \widehat{g}(T^*) \frac{\partial \widehat{\Phi}}{\partial \kappa} ds d\kappa - \int_{\Omega} \widehat{f} \widehat{\Phi} ds d\kappa = 0. \quad (79)$$

Next using (78), we have

$$\int_{\omega} \widehat{k} (|w^*| - \chi w^*) ds + \int_{\frac{\partial w^*}{\partial \kappa} \neq 0} \widehat{g}(T^*) \left( \left| \frac{\partial w^*}{\partial \kappa} \right| - \pi \frac{\partial w^*}{\partial \kappa} \right) ds d\kappa = 0. \quad (80)$$

As  $\|\chi\|_{\omega,\infty} \leq 1, \|\pi\|_{\Omega,\infty} \leq 1$ , we deduce



$$\left| \frac{\partial w^*}{\partial \kappa} \right| = \pi \frac{\partial w^*}{\partial \kappa}, \tag{81}$$

$$\tilde{\Sigma}^* = \left( \frac{1}{2} \right)^{\frac{\nu}{2}} \hat{\Lambda}(T^*) \left| \frac{\partial w^*}{\partial \kappa} \right|^{\nu-2} \frac{\partial w^*}{\partial \kappa} + \hat{g}(T^*) \frac{\partial w^* / \partial \kappa}{\left| \frac{\partial w^*}{\partial \kappa} \right|}. \tag{82}$$

$$|w^*| - \chi w^*.$$

Hence, if  $|\partial w^* / \partial \kappa| \neq 0$ , by (73), we obtain

In this case,  $|\tilde{\Sigma}^*| = (1/2)^{\nu/2} \hat{\Lambda}(T^*) |\partial w^* / \partial \kappa|^{\nu-1} + \hat{g}(T^*) > \hat{g}(T^*)$ ; therefore, we can write

$$\left( \frac{1}{2} \right)^{\nu/2} \hat{\Lambda}(T^*) \left| \frac{\partial w^*}{\partial \kappa} \right|^{\nu-2} \frac{\partial w^*}{\partial \kappa} = \begin{cases} 0, & \text{if } |\tilde{\Sigma}^*| \leq \hat{\alpha}, \\ \tilde{\Sigma}^* - \hat{g}(T^*) \frac{\partial w^* / \partial \kappa}{\left| \frac{\partial w^*}{\partial \kappa} \right|}, & \text{if } |\tilde{\Sigma}^*| > \hat{\alpha}, \end{cases} \tag{83}$$

for every  $\hat{\Phi} \in \Sigma(K)$  and from (79), there exist  $p^* \in L^{\nu'}(\Omega)^2$  such that

$$\int_{\Omega} \hat{\Lambda}(T^*) \left( \frac{1}{2} \right)^{\nu/2} \left| \frac{\partial w^*}{\partial \kappa} \right|^{\nu-2} \frac{\partial w^*}{\partial \kappa} \frac{\partial \hat{\Phi}}{\partial \kappa} ds d\kappa + \int_{\omega} \chi \hat{k} \hat{\Phi} ds + \hat{\alpha} \int_{\Omega} \pi \hat{g}(T^*) \frac{\partial \hat{\Phi}}{\partial \kappa} ds d\kappa - \int_{\Omega} \hat{f} \hat{\Phi} ds d\kappa = - \int_{\Omega} \nabla \rho^* \hat{\Phi} ds d\kappa. \tag{84}$$

Using (83) and (84) becomes

and choosing  $\hat{\Phi} \in W_0^{1,\nu}(\Omega)^2$  in (85), we find (74).  $\square$

$$\int_{\Omega} \tilde{\Sigma}^* \frac{\partial \hat{\Phi}}{\partial \kappa} ds d\kappa + \int_{\omega} \chi \hat{k} \hat{\Phi} ds = \int_{\Omega} \hat{f} \hat{\Phi} ds d\kappa - \int_{\Omega} \nabla \rho^* \hat{\Phi} ds d\kappa, \tag{85}$$

The convergence of our problem towards the Reynolds equation given by the following result: Theorem 5.

$$\int_{\omega} \left[ \frac{h^3}{12} \nabla \rho^* + \tilde{F} + \int_0^h \int_0^y \hat{\Lambda}(T^*(s, \zeta)) A^*(s, \zeta) \frac{\partial w^*(s, \xi)}{\partial \xi} d\xi dy - \frac{h}{2} \int_0^h \hat{g}(T^*(s, \zeta)) \left| \frac{\partial u^*}{\partial \kappa} \right|(s, \xi) d\xi \right] \cdot \nabla \vartheta(s) ds = 0, \tag{86}$$

for all  $\vartheta \in W^{1,\nu}(\omega)$  where

**Theorem 6.** The solution  $(w^*, T^*, \rho^*)$  in  $V_{\kappa} \times W^{-1,q}(\Omega) \times L_0^{\nu'}(\omega)$  of equality (86) is unique.

$$\tilde{F}(s) = \int_0^h F(s, y) dy - \frac{h}{2} F(s, h),$$

$$F(s, y) = \int_0^h \int_0^{\xi} \hat{f}(s, t) dt d\xi, \tag{87}$$

*Proof.* Let  $(w^{*,1}, T^{*,1}, \rho^{*,1})$  and  $(w^{*,2}, T^{*,2}, \rho^{*,2})$  be two solutions of (59)–(63) and (86); then  $T^{*,1}$  and  $T^{*,2}$  solve (62)–(63), so  $T = T^{*,1} - T^{*,2}$  satisfies the problem

$$A^*(s, \xi) = \frac{1}{2} \left( \frac{1}{2} \sum_{i=1}^2 \left( \frac{\partial w^*}{\partial \kappa}(s, \xi) \right)^2 \right)^{\nu-2/2}.$$

$$-\frac{\partial}{\partial \kappa} \left( K \frac{\partial T}{\partial \kappa} \right) = -\hat{\alpha} T,$$

$$T = 0 \text{ in } \Gamma_1 \cup \Gamma_L, \tag{88}$$

*Proof.* To prove (86), we integrate twice (74) from 0 to  $\kappa$ , then taking  $\kappa = h$ , we obtain the requested result.  $\square$

$$\frac{\partial T}{\partial \kappa} = 0 \text{ on } \omega.$$

The uniqueness of the limit velocity and pression are given in the following theorem:

so  $T = 0$ , thus  $T^{*,1} = T^{*,2}$ . Taking  $\vartheta = u^{*,2}$  and  $\vartheta = w^{*,1}$  respectively, as test function in (59) we get

$$\begin{aligned} & \sum_{i=1}^2 \int_{\Omega} \widehat{\Lambda}(T^*) \left(\frac{1}{2}\right)^{v/2} \left(\sum_{i=1}^2 \left(\frac{\partial w_i^{*,1}}{\partial \kappa}\right)^2\right)^{v-2/2} \frac{\partial w_i^{*,1}}{\partial \kappa} \frac{\partial}{\partial \kappa} (w_i^{*,1} - w_i^{*,2}) ds d\kappa \\ & \leq {}^2 \sum_{i=1} \int_{\Omega} \widehat{\Lambda}(T^*) \left(\frac{1}{2}\right)^{v/2} \left({}^2 \sum_{i=1} \left(\frac{\partial w_i^{*,2}}{\partial \kappa}\right)^2\right)^{v-2/2} \frac{\partial w_i^{*,2}}{\partial \kappa} \frac{\partial}{\partial \kappa} (w_i^{*,1} - w_i^{*,2}) ds d\kappa. \end{aligned} \tag{89}$$

Observe that for every  $s, y \in \mathbb{R}^n$   
 $(|s|^{v-2}s - |y|^{v-2}y, s - y) \geq (v - 1)(|s| + |y|)^{v-2}|s - y|^2, \quad \forall 1 < v \leq 2,$   
(90)

we obtain

$$\int_{\Omega} \left[ \left| \frac{\partial w^{*,1}}{\partial \kappa} \right| + \left| \frac{\partial w^{*,2}}{\partial \kappa} \right| \right]^{v-2} \left| \frac{\partial w^{*,1}}{\partial \kappa} - \frac{\partial w^{*,2}}{\partial \kappa} \right|^2 ds d\kappa = 0, \tag{91}$$

where  $|\partial w^{*,j}/\partial \kappa| = (\sum_{i=1}^2 (\partial w_i^{*,j}/\partial \kappa)^2)^{1/2}, \quad j = 1, 2$  Using Hölder's inequality, we deduce

$$\int_{\Omega} \left[ \frac{\partial}{\partial \kappa} (w^{*,1} - w^{*,2}) \right]^v ds d\kappa \leq C \left( \int_{\Omega} \left[ \left| \frac{\partial w^{*,1}}{\partial \kappa} \right| + \left| \frac{\partial w^{*,2}}{\partial \kappa} \right| \right]^{v-2} \left| \frac{\partial w^{*,1}}{\partial \kappa} - \frac{\partial w^{*,2}}{\partial \kappa} \right|^2 ds d\kappa \right)^{v/2} \times \left( \int_{\Omega} \left[ \left| \frac{\partial w^{*,1}}{\partial \kappa} \right| + \left| \frac{\partial w^{*,2}}{\partial \kappa} \right| \right]^v ds d\kappa \right)^{2-v/2}. \tag{92}$$

From (91) and (92), we obtain

$$\left\| \frac{\partial}{\partial \kappa} (w^{*,1} - w^{*,2}) \right\|_{L^v(\Omega)} = 0, \tag{93}$$

using Poincaré's inequality, we deduce

$$\|w^{*,1} - w^{*,2}\|_{V_{\kappa}} = 0. \tag{94}$$

Finally, to prove the uniqueness of the pressure, we use (86) with the two pressures  $\rho^{*,1}$  and  $\rho^{*,2}$ , we find

$$\int_{\omega} h^3 / 12 \nabla(\rho^{*,1} - \rho^{*,2}) \nabla \vartheta ds = 0. \tag{95}$$

Taking  $\vartheta = \rho^{*,1} - \rho^{*,2}$ , and by Poincaré's inequality, we deduce  $\|\rho^{*,1} - \rho^{*,2}\|_{L^{v'}(\omega)} = 0$ . So  $\rho^{*,1} = \rho^{*,2}$ . □

### 5. Conclusions

This work studies the asymptotic analysis of an incompressible Herschel–Bulkley fluid in a thin domain with Tresca boundary conditions. The yield stress and the constant viscosity are assumed to vary with respect to the thin layer parameter. Firstly, the problem statement and variational formulation are formulated. We then obtained the estimates for the velocity field and the pressure independently of the parameter. Finally, we gave a specific Reynolds equation associated with variational inequalities and proved the uniqueness [15–23].

### Data Availability

No data were used to support the study.

### Conflicts of Interest

This work does not have any conflicts of interest.

### Acknowledgments

The fifth-named author extends their appreciation to the Deanship of Scientific Research at King Khalid University for funding this work through the Research Groups Program [grant number R.G.P.2/11/43].

### References

- [1] J. Azevedo, M. Bezerra, C. Cuevas, and H. Soto, “Well-posedness and asymptotic behavior for the fractional Keller–Segel system in critical Besov–Herz-type spaces,” *Mathematical Methods in the Applied Sciences*, 2022.
- [2] A. Coronel, F. Huanca, and F. Huanca, “New results for the non-oscillatory asymptotic behavior of high order differential equations of Poincaré type,” *AIMS Mathematics*, vol. 7, no. 4, pp. 6420–6444, 2022.
- [3] B. O. Jacobson and B. J. Hamrock, “Non-Newtonian fluid model incorporated into elastohydrodynamic lubrication of rectangular contacts,” *Journal of Tribology*, vol. 106, no. 2, pp. 275–282, 1984.
- [4] M. A. Ragusa, “On weak solutions of ultraparabolic equations,” *Nonlinear Analysis: Theory, Methods & Applications*, vol. 47, no. 1, pp. 503–511, 2001.
- [5] J. L. Tevaarwerk, *The Shear of Hydrodynamic Oil Films*, Ph.D. Thesis, Cambridge, England, 1976.
- [6] F. Messelmi and B. Merouani, “Flow of Herschel–Bulkley fluid through a two dimensional thin layer,” *Stud. Univ. Babeş–Bolyai Math.* vol. 58, no. 1, pp. 119–130, 2013.
- [7] A. Saadallah, H. Benseridi, and M. Dilmi, “Asymptotic convergence of a generalized non-Newtonian fluid with tresca boundary conditions,” *Acta Mathematica Scientia*, vol. 40, no. 3, pp. 700–712, 2020.
- [8] J. Málek, M. Růžička, and V. V. Shelukhin, “Herschel–bulkley fluids: existence and regularity of steady flows,” *Mathematical Models and Methods in Applied Sciences*, vol. 15, no. 12, pp. 1845–1861, 2005.

- [9] F. Messelmi, "Effects of the yield limit on the behaviour of herschel-bulkley fluid," *Nonlinear Sci. Lett. A*, vol. 2, no. 3, pp. 137–142, 2011.
- [10] F. Messelmi, B. Merouani, and F. Bouzeghaya, "Steady-state thermal herschel-bulkley flow with tresca's friction law," *The Electronic Journal of Differential Equations*, vol. 46, pp. 1–14, 2010.
- [11] A. Massmeyer, E. Di Giuseppe, A. Davaille, T. Rolf, and P. J. Tackley, "Numerical simulation of thermal plumes in a Herschel-Bulkley fluid," *Journal of Non-newtonian Fluid Mechanics*, vol. 195, pp. 32–45, May 2013.
- [12] G. P. Matson and A. J. Hogg, "Two-dimensional dam break flows of Herschel-Bulkley fluids: the approach to the arrested state," *Journal of Non-newtonian Fluid Mechanics*, vol. 142, no. 1-3, pp. 79–94, 2007.
- [13] M. Boukrouche and R. El mir, "Asymptotic analysis of non-Newtonian fluid in a thin domain with Tresca law," *Nonlinear Analysis*, vol. 59, no. 1-2, pp. 85–105, 2004.
- [14] A. Saadallah and H. Benseridi, "Asymptotic analysis of a dynamic flow of the Bingham fluid," *Dynamics of Continuous Discrete and Impulsive Systems: Series B; Applications and Algorithms*, vol. 28, pp. 197–213, 2021.
- [15] M. Boukrouche and G. Łukaszewicz, "Asymptotic analysis of solutions of a thin film lubrication problem with Coulomb fluid-solid interface law," *International Journal of Engineering Science*, vol. 41, no. 6, pp. 521–537, 2003.
- [16] R. Bunoiu and S. Kesavan, "Asymptotic behaviour of a Bingham fluid in thin layers," *Journal of Mathematical Analysis and Applications*, vol. 293, no. 2, pp. 405–418, 2004.
- [17] M. Dilmi, H. Benseridi, and A. Saadallah, "Asymptotic analysis of a bingham fluid in a thin domain with fourier and tresca boundary conditions," *Advances in Applied Mathematics and Mechanics*, vol. 6, no. 6, pp. 797–810, 2014.
- [18] W. H. Herschel and R. Bulkley, "Konsistenzmessungen von Gummi-benzollösungen," *Kolloid Zeitschrift*, vol. 39, no. 4, pp. 291–300, 1926.
- [19] C. Nouar, M. Lebouché, R. Devienne, and C. Riou, "Numerical analysis of the thermal convection for Herschel-Bulkley fluids," *International Journal of Heat and Fluid Flow*, vol. 16, no. 3, pp. 223–232, June 1995.
- [20] C. Nouar, C. Desaubry, and H. Zenaidi, "Numerical and experimental investigation of thermal convection for a thermodependent Herschel-Bulkley fluid in an annular duct with rotating inner cylinder," *European Journal of Mechanics - B: Fluids*, November–December, vol. 17, no. 6, pp. 875–900, 1998.
- [21] S. Poyiadji and K. D. Housiadas, G. C. Georgiou and K. Kaouri, "Asymptotic solutions of weakly compressible Newtonian Poiseuille flows with pressure-dependent viscosity," *European Journal of Mechanics - B: Fluids*, vol. 49, pp. 217–225, 2015.
- [22] Y. Qin, X. Liu, and X. Yang, "Global existence and exponential stability of solutions to the one-dimensional full non-Newtonian fluids," *Nonlinear Analysis: Real World Applications*, vol. 13, no. 2, pp. 607–633, April 2012.
- [23] K. C. Sahu, P. Valluri, P. D. M. Spelt, and O. K. Matar, "Linear instability of pressure-driven channel flow of a Newtonian and a Herschel-Bulkley fluid," *Physics of Fluids*, vol. 19, no. 12, Article ID 122101, 2007.

## Research Article

# Dynamical Behaviour and Chaotic Phenomena of HIV Infection through Fractional Calculus

Rashid Jan <sup>1</sup>, Amin Khan,<sup>1</sup> Salah Boulaaras <sup>2</sup>, and Sulima Ahmed Zubair <sup>2,3</sup>

<sup>1</sup>Department of Mathematics, University of Swabi, Swabi 23430, Pakistan

<sup>2</sup>Department of Mathematics, College of Sciences and Arts, Qassim University, ArRass, Saudi Arabia

<sup>3</sup>Department of Mathematics, College of Science, Juba University, Juba, Sudan

Correspondence should be addressed to Salah Boulaaras; [s.boulaaras@qu.edu.sa](mailto:s.boulaaras@qu.edu.sa)

Received 25 January 2022; Accepted 26 March 2022; Published 30 April 2022

Academic Editor: Sundarapandian Vaidyanathan

Copyright © 2022 Rashid Jan et al. This is an open access article distributed under the Creative Commons Attribution License, which permits unrestricted use, distribution, and reproduction in any medium, provided the original work is properly cited.

The infection of human immunodeficiency virus (HIV) is a serious and potentially incurable infection. There is no cure for HIV and is a public health issue around the world. That is why, it is valuable to investigate the intricate phenomena of HIV infection and provide some control interventions to lessen its economic burden. In this research work, the dynamics of HIV via fractional calculus to conceptualize the intricate phenomena of this viral infection has been formulated and conceptualized. We have shown the rudimentary concept of fractional calculus in Atangana–Baleanu framework. A novel numerical technique is presented for the chaotic and dynamic behaviour of the proposed model. The oscillatory and chaotic phenomena of the system have been shown with the fluctuation of different input factors of the system. Furthermore, we have shown the affect of fractional order on the proposed system of HIV infection. Most critical input parameters are highlighted through numerical simulations and suggested control intervention to the policy makers. Finally, we have shown the stability result and the convergence condition for the proposed numerical scheme.

## 1. Introduction

Mathematics and Biology are extricable linked in different research areas. Genetics, environmental science, population dynamics, medical science, and other fields all benefit from mathematical biology. Mathematics is used to conceptualize, understand, and visualize intricate biological phenomena [1, 2]. It is well known that the development of theoretical principles for biology is referred to theoretical biology while investigation of biological phenomena or processes through mathematical tools is known to be mathematical biology. This implies that mathematics plays an important role to interrogate a biological system. When traditional lab tests are either unfeasible or too difficult to answer a research topic, biologists turn to mathematics to create models that highlight the key factors of transmission process of an infection. Scientists can use these approaches to forecast the likelihood of certain outcomes while simultaneously fine-tuning their research subjects. Different biological events

and processes can be described mathematically in terms of delay, impulsive, stochastic [3], fractional and ordinary differential equations, and so on [4]. In formulating these mathematical models, various assumptions, laws, and axioms that govern these processes are used to demonstrate the complex dynamics of biological events. HIV infection is a serious public health concern worldwide, having claimed about 33 million lives to date, and a slew of mathematical models for the human immune system has been created to depict the complete spectrum of infection. The interaction of human immunodeficiency (HIV) and immune system has been described. HIV has been reported to be an effective agent in achieving immunodeficiency syndrome (AIDS) which impairs the capability of the body to fend against various illnesses. HIV infection is an incurable fatal disease that has killed the lives of about 44,200,000 people. It is reported in 2020 that 37.6 million people are infected by HIV around the world and 1.5 million people are newly infected. However, therapy that works, caring, assessment, as well as

protection of HIV has led to people living longer and healthier lives with HIV. When the HIV virus penetrates a healthy individual's body, it propagates rapidly and causes CD4<sup>+</sup> T-cells destruction that act on the immune system.

The symptoms and signs of HIV infection in its initial phases include the flu, nighttime cravings, coughing, losing weight, a headache, diarrhoea, sunburn, body aches and joint pain, tonsillitis, as well as a dry mouth. The process is still in its initial phases, the virus carries more weight into the bloodstream, and the HIV infection spreads more easily through the body than at other stages. In addition, HIV-infected viruses are spread through body fluids (blood, tears, urine, saliva, and so on) and infect the uninfected person. It is really obvious that CD4<sup>+</sup> T-cells have the fighting ability against infections; additionally, those same CD4<sup>+</sup> T-cells play a significant role as in immune system's modification, so their precession would have a wide range of consequences which can entirely disrupt its immune system's functioning. Because the retention time of such lymphocytes is utilized. Therefore, we define the phase of HIV infection, determining their importance using a mathematical formulation becomes essential. For effective illustration of the interaction of CD4<sup>+</sup> T-cells and HIV-infected viruses, a number of mathematical models were developed.

Several scholars investigated the kinetics of HIV infection using various assumptions. The authors in [5] studied the interaction of CD4<sup>+</sup> T-cells and HIV virus through a mathematical model. Perelson and Nelson [6] also developed a novel model of HIV incorporating the following classes: late infection, constantly infected and non-infected, and the HIV viral particle community. Several recognized characteristics of AIDS were proven their research clinically [6]. Following that, Culshaw and Raun [7] formulated the dynamics of HIV infection and studied HIV dynamics. Bushnaq et al. [8] performed research in which they explored the stability and persistence of HIV/AIDS model, as well as the role of recall throughout the biomechanics with HIV infection, using formalized paraphrasing and fractional differentiation. To highlight the dynamic monitoring behaviours of HIV infection, the authors used a range of methodologies to investigate HIV dynamics [9, 10] while the researchers in [11, 12] computationally interrogated the dynamics of HIV. The main objective of this research work is to formulate the dynamics of HIV infection using a variable term from source rather than a fixed quantity for fresh CD4<sup>+</sup> T-cells. In addition to this, our objective is to visualize the role of input parameters on the output of the system and to investigate the most critical factors of the system for the control of this viral infection.

Non-integer models are famous due to their more valuable, reliable, deeper, and precise knowledge in different areas of science and technology [13, 14]. Due to its inherited characteristics and memory definition, fractional systems [15] perform more accurately. It is also well known that nonlocal behaviour of the system can easily be represented through fractional-calculus [16]. The fraction calculus offered very precise information for such

phenomena, especially for the dynamics of infectious diseases and engineering systems. In fraction calculus, Caputo, Riemann–Liouville, Hilfer, and a few more operations have core laws and have limitations in modeling natural phenomena. Atangana and Baleanu developed a new derivative in 2016 that extended the Mittag–Leffler function to nonlocal and nonsingular cases [16]. This newly developed has been successfully used in different areas of science and engineering [17, 18]. Therefore, the mathematical biologists are interested to investigate the transmission process of different infections through this novel operator to provide accurate results and to conceptualize the contribution of memory in the dynamical behaviour of different diseases. The authors in [19] represented the transmission phenomena of rubella disease through Atangana–Baleanu operators. The transmission phenomena of COVID-19 have been investigated through AB operator in some African countries [20]. This novel operator more accurately represents natural phenomena rather than the previous operators. Thus, we opt to investigate the dynamics of healthy CD4<sup>+</sup> T-cells, infected CD4<sup>+</sup> T-cells, and free viruses of HIV infection through fractional-calculus via Atangana–Baleanu operator.

The research work is structured as follows. The fractional formulation of the HIV infection of CD4<sup>+</sup> T-cells is presented in Section 2 of this article. We introduced a new numerical technique for the analysis of the proposed fractional model in Section 3. In section four, we highlighted the chaotic and oscillatory concepts of the model with fluctuation of different input parameters. Furthermore, the most critical scenario is visualized through these numerical analyses. The proposed numerical scheme's convergence and stability findings have been demonstrated. The last portion of the article contains the entire work's concluding remarks.

## 2. Structure of HIV Dynamics

The most critical necessity for understanding HIV/AIDS infections is to understand the interaction of HIV and CD4<sup>+</sup> T-cells. It is reported that these cells are created throughout the bone marrow and moved to the medulla and then went through special differentiation for maturation into uninfected CD4<sup>+</sup> T-cells. In the human body, the maximal weight is achieved by thymus. The thymus in humans achieves its maximal weight at maturation stage and then gradually grows more complicated. The effect of thymic drainage from adults is small even though the adult thymus is active and its few lymphocytes function as recruits for T-cells and uninfected T-cells. The provided model focuses on CD4<sup>+</sup> T-cells. The number of CD4<sup>+</sup> T-cells that tell us more about the early symptoms can be used to assess the persistence of HIV infection.

The current work is interested to interrogate the oscillatory and path tracking behaviour of the HIV dynamics. These analyses detect the most critical factor and also help the policy makers to identify input factor for the prevention of infection. The assumptions in [11] give the following mathematical descriptions:



$$\begin{aligned} \frac{dT}{dt} &= s - \mu_T T - kVT + rT \left( 1 - \frac{T+I}{T_{\max}} \right), \\ \frac{dI}{dt} &= kVT - \mu_I I, \\ \frac{dV}{dt} &= N\mu_I I - \mu_V V. \end{aligned} \tag{1}$$

Here, the state variables  $T(t)$  and  $I(t)$  indicate the concentration of healthy and infected while  $V(t)$  indicates HIV virus freely available in the blood, respectively. In Table 1, we have shown the initial conditions and all the parameters with description. In the next section, we will extend the model with a fractional framework.

**2.1. HIV Infection’s Fractional Dynamics.** Here, a constant source term  $s$  introduced in [11] is replaced by the variable  $s(V) = s \exp(-\kappa V)$  in the proposed model. The new source term included the model indicating the amount of healthy T-cells generated by thymus as a function of viral load concentration. Because the greater viral load lowers the generation of healthy T lymphocytes, the source term is seen as a variable rather than a constant. Further explanation and detail are given in the research [21–23]. Then, the above system of differential equation (1) in fractional framework with our new assumptions is given by

$$\begin{aligned} {}_0^{ABC}D_t^\ell T &= s \exp(-\kappa V) - \mu_T T + rT \left( 1 - \frac{T+I}{T_{\max}} \right) - kVT, \\ {}_0^{ABC}D_t^\ell I &= kVT - \mu_I I, \\ {}_0^{ABC}D_t^\ell V &= N\mu_I I - \mu_V V - kVT, \end{aligned} \tag{2}$$

where  ${}_0^{ABC}D_t^\ell$  indicates the derivative of Atangana–Baleanu in the Caputo sense of order  $\ell$ . The following portion of the study will go through the rudimentary knowledge of ABC derivative, which will be used to analyze our HIV infection model. This fractional derivative has been recently introduced which is successfully utilized in different research fields.

### 3. Results of Fractional Calculus

Fractional calculus theory is rich in applications and has been applied to many problems in engineering, physics, economics, biology, and many other areas of technology and science. Recent research has shown that they provide more accurate, precise, and reliable results [24, 25]. Here, we introduce the basic idea of fractions for analyzing our system of HIV. In the following, some basic results and concepts of ABC fractional derivative are presented for analysis.

**Definition 1.** Let us take  $f$  such that  $g \in H^1(p, q)$ ,  $p < q$ , then ABC derivative with order  $\zeta$  is given as follows:

$${}_p^{ABC}D_t^\zeta g(t) = \frac{B(\zeta)}{1-\zeta} \int_p^t g'(\zeta) E_\zeta \left[ -\zeta \frac{(t-\xi)^\zeta}{1-\zeta} \right] d\xi, \tag{3}$$

where  $\zeta$  belongs to the closed interval  $[0, 1]$ .

**Definition 2.** Assume  $f(t)$  be any given function, then the integral of the abovementioned operator is indicated by  ${}_p^{ABC}I_t^\zeta g(t)$  and is given by

$${}_p^{ABC}I_t^\zeta g(t) = \frac{1-\zeta}{B(\zeta)} g(t) + \frac{\zeta}{B(\zeta)\Gamma(\zeta)} \int_p^t g(\zeta)(t-\xi)^{\zeta-1} d\xi. \tag{4}$$

Here, as the fractional-order  $\zeta$  approaches to 0, we obtained the initial function.

**Theorem 1** (see [16]). *Let us take  $f$  such that  $f \in C[p, q]$  where  $f$  is continuous, then the following holds true:*

$$\|{}_p^{ABC}D_t^\zeta(g(t))\| < \frac{B(\zeta)}{1-\zeta} \|f(t)\|, \text{ with } \|f(t)\| = \max_{p \leq t \leq q} |g(t)|. \tag{5}$$

Furthermore, it fulfills the following:

$$\|{}_p^{ABC}D_t^\zeta g_1(t) - {}_p^{ABC}D_t^\zeta g_2(t)\| < \varrho_1 \|g_1(t) - g_2(t)\|, \tag{6}$$

which is called Lipschitz condition.

**Theorem 2** (see [16]). *Let us take a fractional system of the form as follows:*

$${}_p^{ABC}D_t^\zeta g(t) = u(t), \tag{7}$$

the above system has the following unique solution:

$$g(t) = \frac{1-\zeta}{B(\zeta)} u(t) + \frac{\zeta}{B(\zeta)\Gamma(\zeta)} \int_p^t u(\zeta)(t-\xi)^{\zeta-1} d\xi. \tag{8}$$

$${}_0^{ABC}D_t^\ell y(t) = \mathcal{K}(t, y(t)). \tag{9}$$

### 4. Numerical Approach for Fractional Derivative

Here is a numerical method that emphasises the fractional model of HIV infection’s oscillatory behaviour and chaos. Numerous numerical techniques have been developed and described to visualize fractional order models. For the fractional dynamics of HIV, we will use a new scheme presented in [26] to describe the solution pathway in (2). To derive the numerical schemes needed for our system (2), we first adopt the following fractional system.

Then, by the theory of fractional calculus, we get

$$y(t) - y(0) = \frac{1-\ell}{ABC(\ell)} \mathcal{K}(t, y(t)) + \frac{\ell}{ABC(\ell)\Gamma(\ell)} \int_0^t (t-\tau)^{\ell-1} \mathcal{K}(\tau, y(\tau)) d\tau. \tag{10}$$



TABLE 1: Description of state-variables and input parameters with corresponding values.

Symbols	Parameter and state-variable interpretation	Values
$V_0$	HIV virus concentration	Assumed
$T_{\max}$	Maximum number of healthy T-cells	$1500 \text{ mm}^{-3}$
$N$	The quantity of virus generated by infected T-cells	Assumed
$\mu_V$	Death rate of HIV virus	$2.4 \text{ day}^{-1}$
$\mu_I$	Death rate of infected T-cells	$0.3 \text{ day}^{-1}$
$\mu_T$	Death rate of healthy T-cells	$0.02 \text{ day}^{-1}$
$r$	Growth rate of healthy T-cells	$3 \text{ day}^{-1}$
$s$	Healthy T-cells supply rate from precursors	$0.1 \text{ mm}^{-3}$
$I_0$	T-cells population with infection	Assumed
$T_0$	T-cells population in healthy form	Assumed
$k$	Infection rate of T-cells by free virus	$2.4 \times 10^{-5} \text{ days}^{-1}$

Here, we take the time  $t = t_n$ , then the above implies that

$$y(t_n) - y(0) = \frac{1 - \ell}{\text{ABC}(\ell)} \mathcal{K}(t_{n-1}, y(t_{n-1})) + \frac{\ell}{\text{ABC}(\ell)\Gamma(\ell)} \int_0^{t_n} (t_n - \tau)^{\ell-1} \mathcal{K}(\tau, y(\tau)) d\tau, \quad (11)$$

and for  $t_{n+1}$ , we get

$$y(t_{n+1}) - y(0) = \frac{1 - \ell}{\text{ABC}(\ell)} \mathcal{K}(t_{n+1}, y(t_{n+1})) + \frac{\ell}{\text{ABC}(\ell)\Gamma(\ell)} \int_0^{t_{n+1}} (t_{n+1} - \tau)^{\ell-1} \mathcal{K}(\tau, y(\tau)) d\tau. \quad (12)$$

From the above, we can find the difference as follows:

$$y(t_{n+1}) - y(t_n) = \frac{1 - \ell}{\text{ABC}(\ell)} [\mathcal{K}(t_n, y(t_n)) - \mathcal{K}(t_{n-1}, y(t_{n-1}))] + \frac{\ell}{\text{ABC}(\ell)\Gamma(\ell)} \int_0^{t_{n+1}} (t_{n+1} - \tau)^{\ell-1} \mathcal{K}(\tau, y(\tau)) d\tau - \int_0^{t_n} (t_n - \tau)^{\ell-1} \mathcal{K}(\tau, y(\tau)) d\tau. \quad (13)$$

This further implies that

$$y(t_{n+1}) - y(t_n) = \frac{1 - \ell}{\text{ABC}(\ell)} [\mathcal{K}(t_n, y(t_n)) - \mathcal{K}(t_{n-1}, y(t_{n-1}))] + B_{\ell,1} - B_{\ell,2}, \quad (14)$$

in which

$$B_{\ell,1} = \frac{\ell}{\text{ABC}(\ell)\Gamma(\ell)} \int_0^{t_{n+1}} (t_{n+1} - \tau)^{\ell-1} \mathcal{K}(\tau, y(\tau)) d\tau. \quad (15)$$

The next step is to get it using an approximation as follows:

$$P(t) \cong \frac{\mathcal{K}(t_n, y_n)}{h} (t - t_{n-1}) - \frac{\mathcal{K}(t_{n-1}, y_{n-1})}{h} (t - t_n). \quad (16)$$

We take  $h = t_m - t_{m-1}$  and obtain the following:

$$\begin{aligned}
 B_{\ell,1} &= \frac{\ell}{\text{ABC}(\ell)\Gamma(\ell)} \int_0^{t_{n+1}} (t_{n+1} - \tau)^{\ell-1} \left[ \frac{\mathcal{K}(t_n, y_n)}{h} (t - t_{n-1}) - \frac{\mathcal{K}(t_{n-1}, y_{n-1})}{h} (t - t_n) \right] d\tau \\
 &= \frac{\ell}{\text{ABC}(\ell)\Gamma(\ell)} \int_0^{t_{n+1}} (t_{n+1} - \tau)^{\ell-1} \left[ \frac{\mathcal{K}(t_n, y_n)}{h} (t - t_{n-1}) - \frac{\mathcal{K}(t_{n-1}, y_{n-1})}{h} (t - t_n) \right] d\tau,
 \end{aligned}
 \tag{17}$$

which implies that

$$B_{\ell,1} = \frac{\ell \mathcal{K}(t_n, y_n)}{\text{ABC}(\ell)\Gamma(\ell)h} \left[ \frac{2ht_{n+1}^\ell}{\ell} - \frac{t_{n+1}^{\ell+1}}{\ell+1} \right] - \frac{\ell \mathcal{K}(t_{n-1}, y_{n-1})}{\text{ABC}(\ell)\Gamma(\ell)h} \left[ \frac{ht_{n+1}^\ell}{\ell} - \frac{t_{n+1}^{\ell+1}}{\ell+1} \right].
 \tag{18}$$

In the same way, we can find

$$B_{\ell,2} = \frac{\ell \mathcal{K}(t_n, y_n)}{\text{ABC}(\ell)\Gamma(\ell)h} \left[ \frac{ht_n^\ell}{\ell} - \frac{t_n^{\ell+1}}{\ell+1} \right] - \frac{\mathcal{K}(t_{n-1}, y_{n-1})}{\text{ABC}(\ell)\Gamma(\ell)h}.
 \tag{19}$$

Next, we have the following:

$$\begin{aligned}
 y(t_{n+1}) - y(t_n) &= \frac{1-\ell}{\text{ABC}(\ell)} [\mathcal{K}(t_n, y(t_n)) - \mathcal{K}(t_{n-1}, y(t_{n-1}))] + \frac{\ell \mathcal{K}(t_n, y_n)}{\text{ABC}(\ell)\Gamma(\ell)h} \left[ \frac{2ht_{n+1}^\ell}{\ell} - \frac{t_{n+1}^{\ell+1}}{\ell+1} \right] \\
 &\quad - \frac{\ell \mathcal{K}(t_{n-1}, y_{n-1})}{\text{ABC}(\ell)\Gamma(\ell)h} \left[ \frac{ht_{n+1}^\ell}{\ell} - \frac{t_{n+1}^{\ell+1}}{\ell+1} \right] - \frac{\ell \mathcal{K}(t_n, y_n)}{\text{ABC}(\ell)\Gamma(\ell)h} \left[ \frac{ht_n^\ell}{\ell} - \frac{t_n^{\ell+1}}{\ell+1} \right] \\
 &\quad + \frac{\mathcal{K}(t_{n-1}, y_{n-1})}{\text{ABC}(\ell)\Gamma(\ell)h}.
 \end{aligned}
 \tag{20}$$

The above gives us

$$\begin{aligned}
 y(t_{n+1}) &= y(t_n) + \mathcal{K}(t_n, y_n) \left[ \frac{1-\ell}{\text{ABC}(\ell)} + \frac{\ell}{\text{ABC}(\ell)h} \left\{ \frac{2ht_{n+1}^\ell}{\ell} - \frac{t_{n+1}^{\ell+1}}{\ell+1} \right\} \right. \\
 &\quad \left. - \frac{\ell}{\text{ABC}(\ell)\Gamma(\ell)h} \left\{ \frac{ht_n^\ell}{\ell} - \frac{t_n^{\ell+1}}{\ell+1} \right\} \right] + \mathcal{K}(t_{n-1}, y_{n-1}) \times, \\
 &\quad \left[ \frac{\ell-1}{\text{ABC}(\ell)} - \frac{\ell}{\text{ABC}(\ell)\Gamma(\ell)h} \left\{ \frac{ht_{n+1}^\ell}{\ell} - \frac{t_{n+1}^{\ell+1}}{\ell+1} + \frac{t_n^{\ell+1}}{h\text{ABC}(\ell)\Gamma(\ell)} \right\} \right].
 \end{aligned}
 \tag{21}$$

The above approach is a two-step Adams–Bashforth method for the ABC fractional derivative; this takes into consideration the kernels nonlinearity, as well as the Atangana–Baleanu operator’s exponential decay law. Furthermore, we will discuss the convergence and stability of the suggested numerical approach in the upcoming part. We

conducted numerous simulations for the better conceptualization of the complicated phenomena of HIV infection. For numerical simulation, the model parameter values and state-variable initial values are shown in Table 1 which is utilized for numerical calculations. Figures 1–4 depict the time series analysis of all the three compartment of the

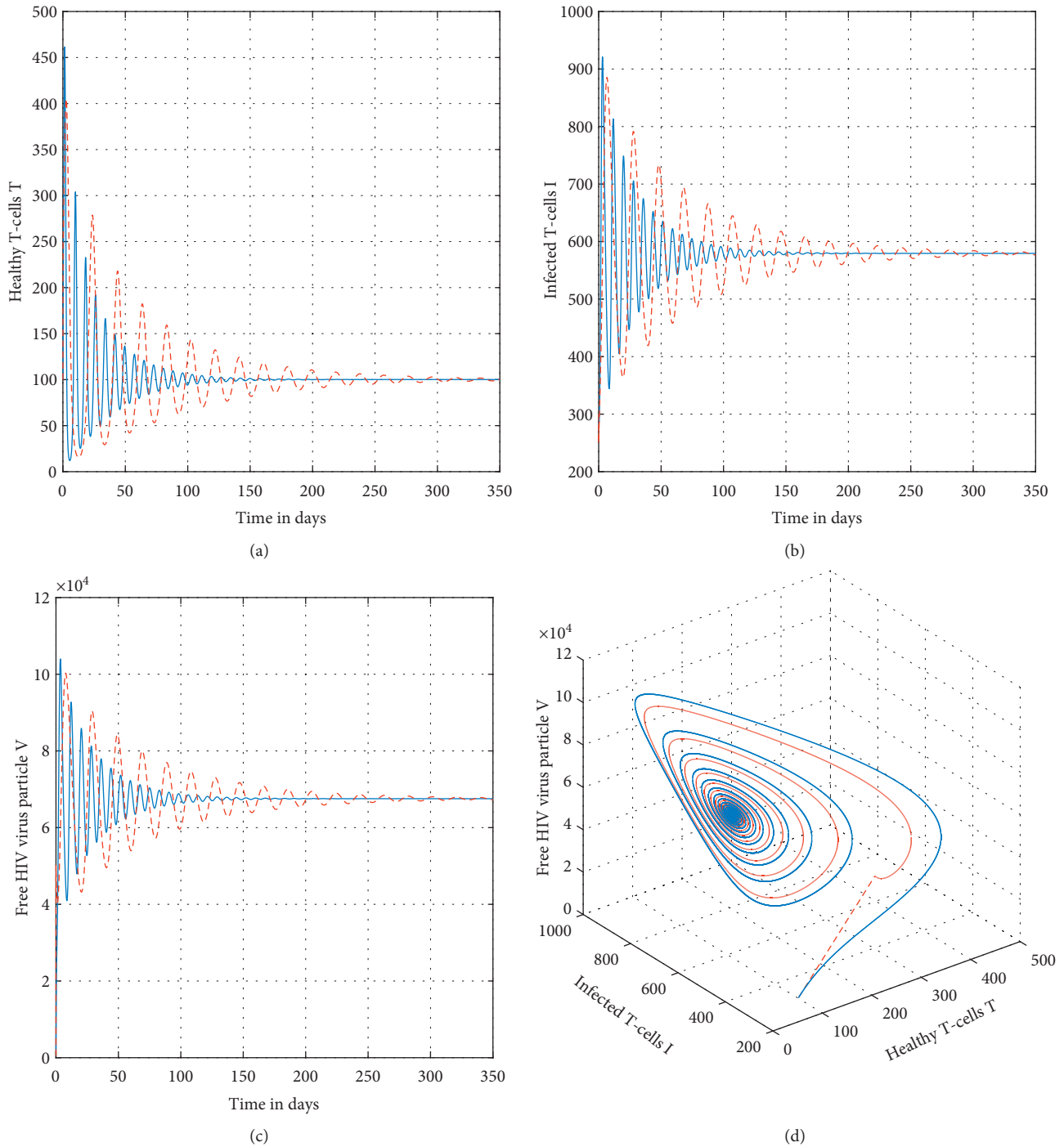


FIGURE 1: Graphical view analysis of the fractional model (2) of HIV by taking the index of memory  $\vartheta = 0.4$ .

proposed system with the variation of the index of memory  $\ell$ , i.e.,  $\ell = 0.4, 0.6, 0.8, 1.0$  to show the dynamical behaviour of HIV infection. It has been observed through numerical outcomes that the parameter  $\ell$  can be used as preventive parameter. Figures 5–8 depict the chaotic behaviour of our system (2) with various values of index of memory  $\ell$ . We noticed that the index of memory  $\ell$  can be also be utilized as chaotic control parameter. Many scientific and engineering applications rely heavily on the chaotic behaviour of the

system. It is well known that there is indeed a strong inclination to conceive and depict chaotic system behaviour. The chaotic modeling validates the feasibility and scalability of the suggested mathematical model, which can then be applied towards the novel chaos systems. We showed that perhaps  $\ell$  had a considerable contribution and may be utilized as an effective parameter for preventative actions. Furthermore, we have shown the impact of several input factors on the dynamics of the system in Figures 9–11.

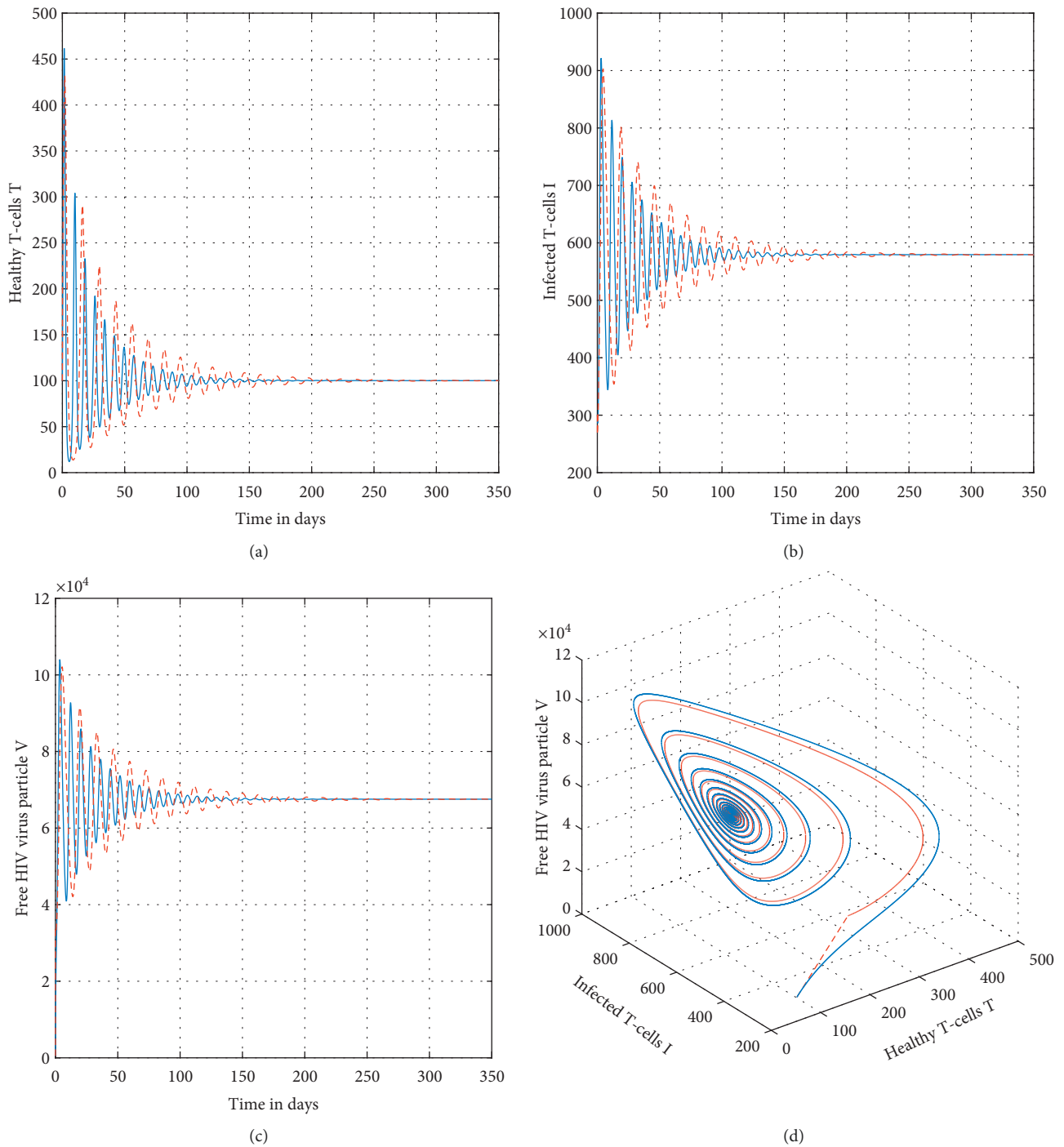


FIGURE 2: Graphical view analysis of the fractional model (2) of HIV by taking the index of memory  $\vartheta = 0.6$ .

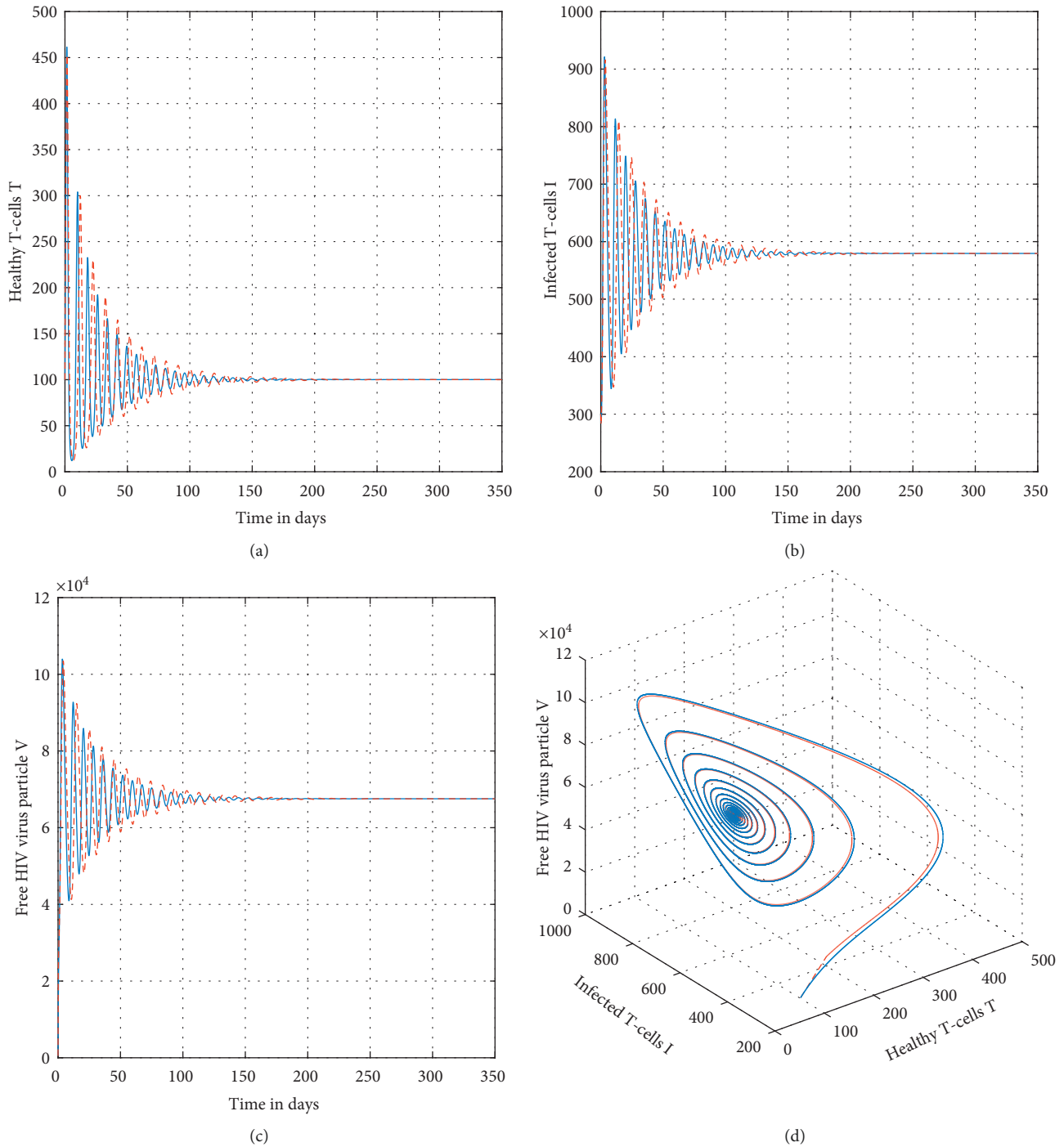


FIGURE 3: Graphical view analysis of the fractional model (2) of HIV by taking the index of memory  $\vartheta = 0.8$ .

Simulations reveal that the suggested numerical scheme is simple to implement and quick to execute. However, more study will be required to investigate the effectiveness of this technique in terms of consistency, accuracy, and computing cost. In the next step, we will discuss convergence and stability result of the above numerical method. The convergence result of the above method has been given as follows.

**Theorem 3.** Assume that  $g$  be a continuous and bounded function and  $x(\tau)$  be the solution of the fractional system as follows:

$${}_{0}^{ABC}D_{\tau}^{\vartheta}x(\tau) = g(\tau, x(\tau)), \tag{22}$$

then the solution of  $x(\tau)$  is as follows:

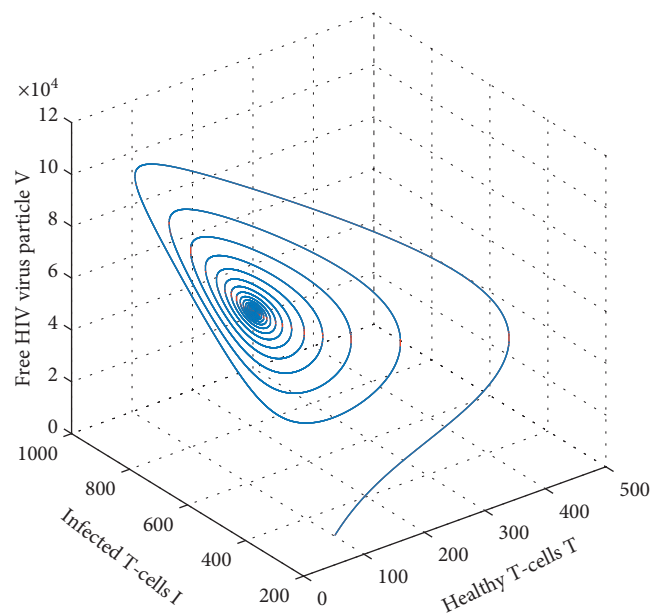
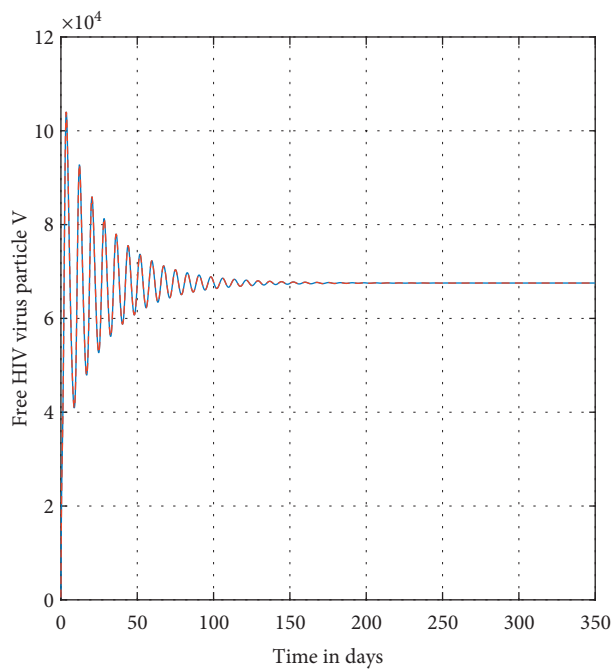
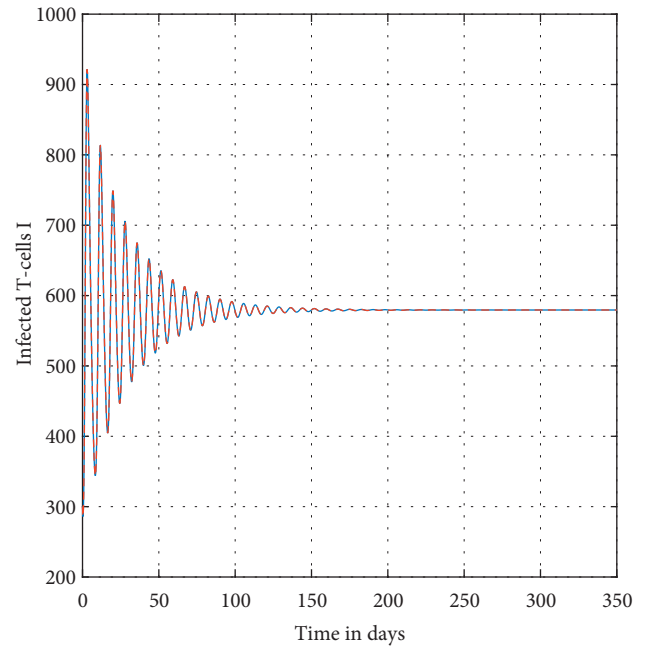
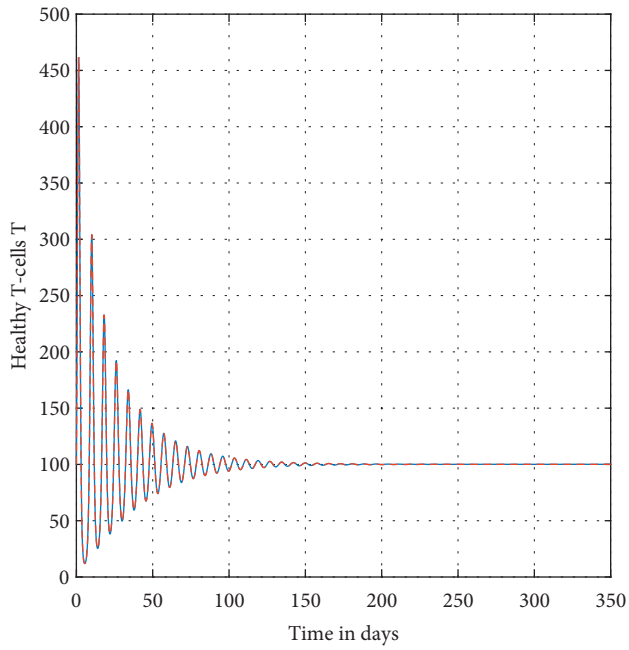


FIGURE 4: Graphical view analysis of the fractional model (2) of HIV by taking the index of memory  $\vartheta = 1.0$ .



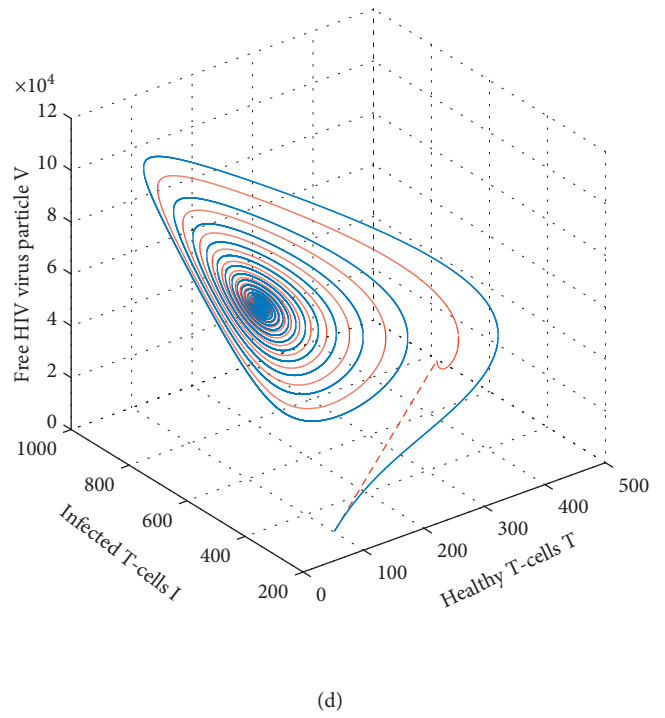
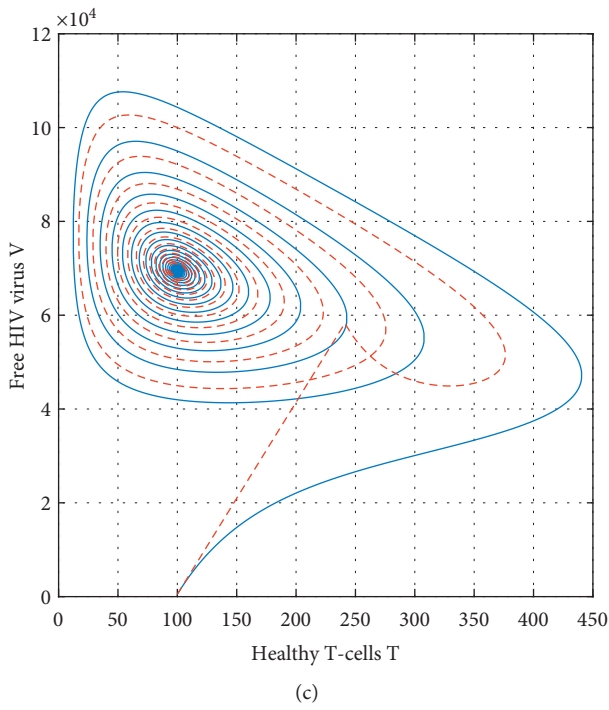
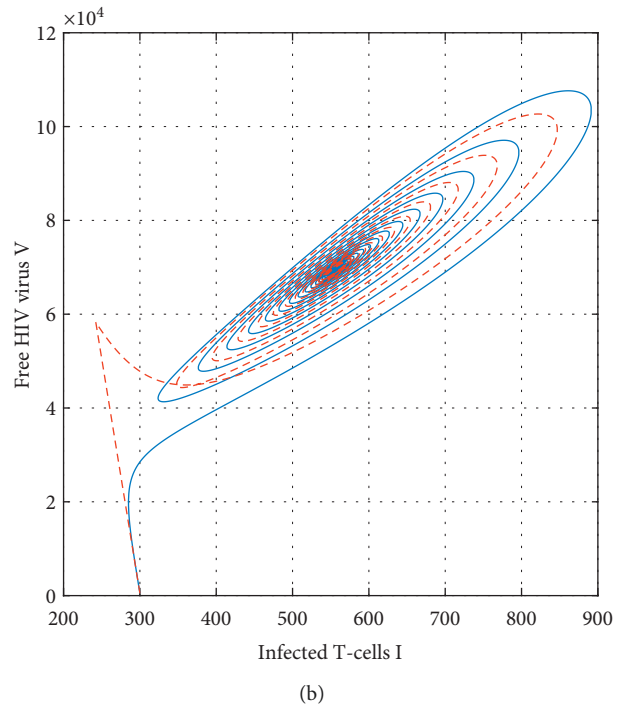
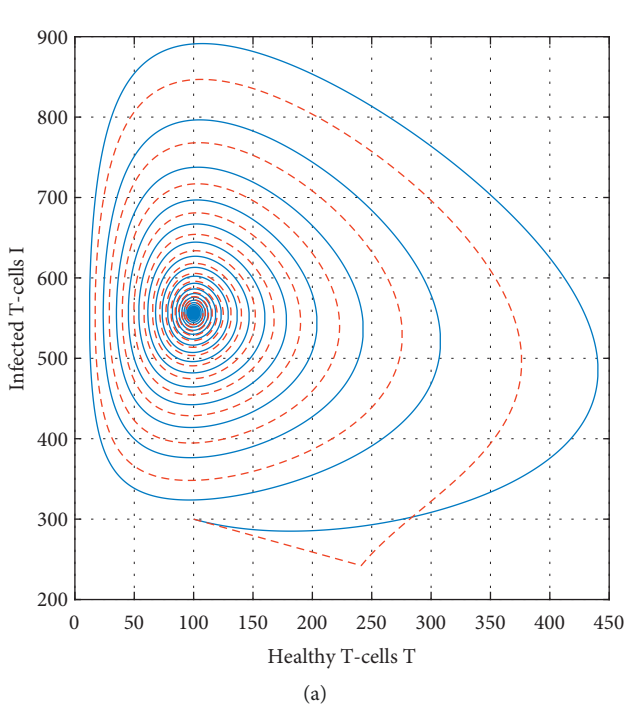


FIGURE 5: Graphical view analysis of the dynamical behaviour of the fractional model (2) to represent its chaotic plot with the index of memory  $\vartheta = 0.35$ .

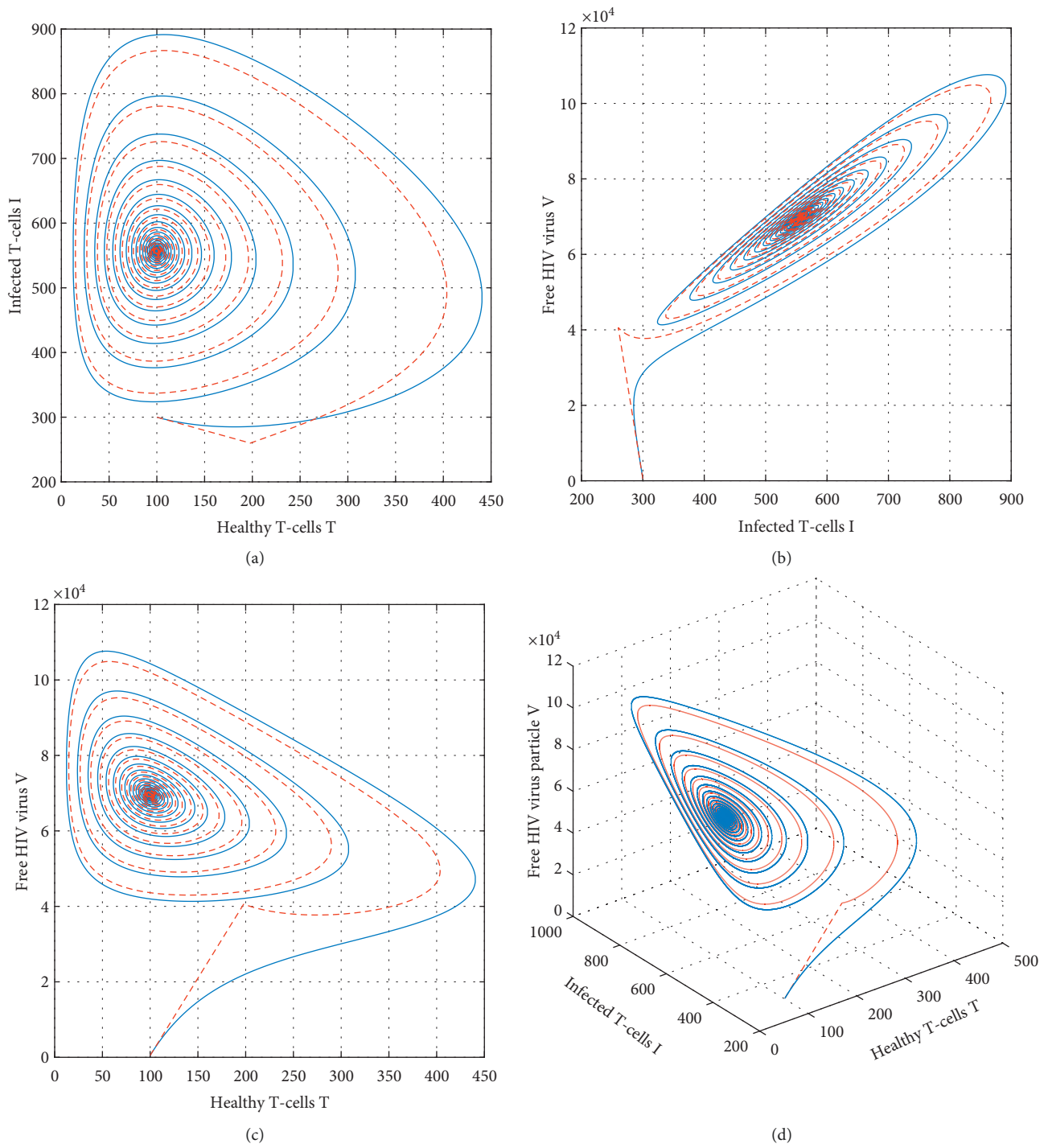


FIGURE 6: Graphical view analysis of the chaotic phenomena of the suggested fractional model (2) of HIV with the index of memory  $\vartheta = 0.55$ .

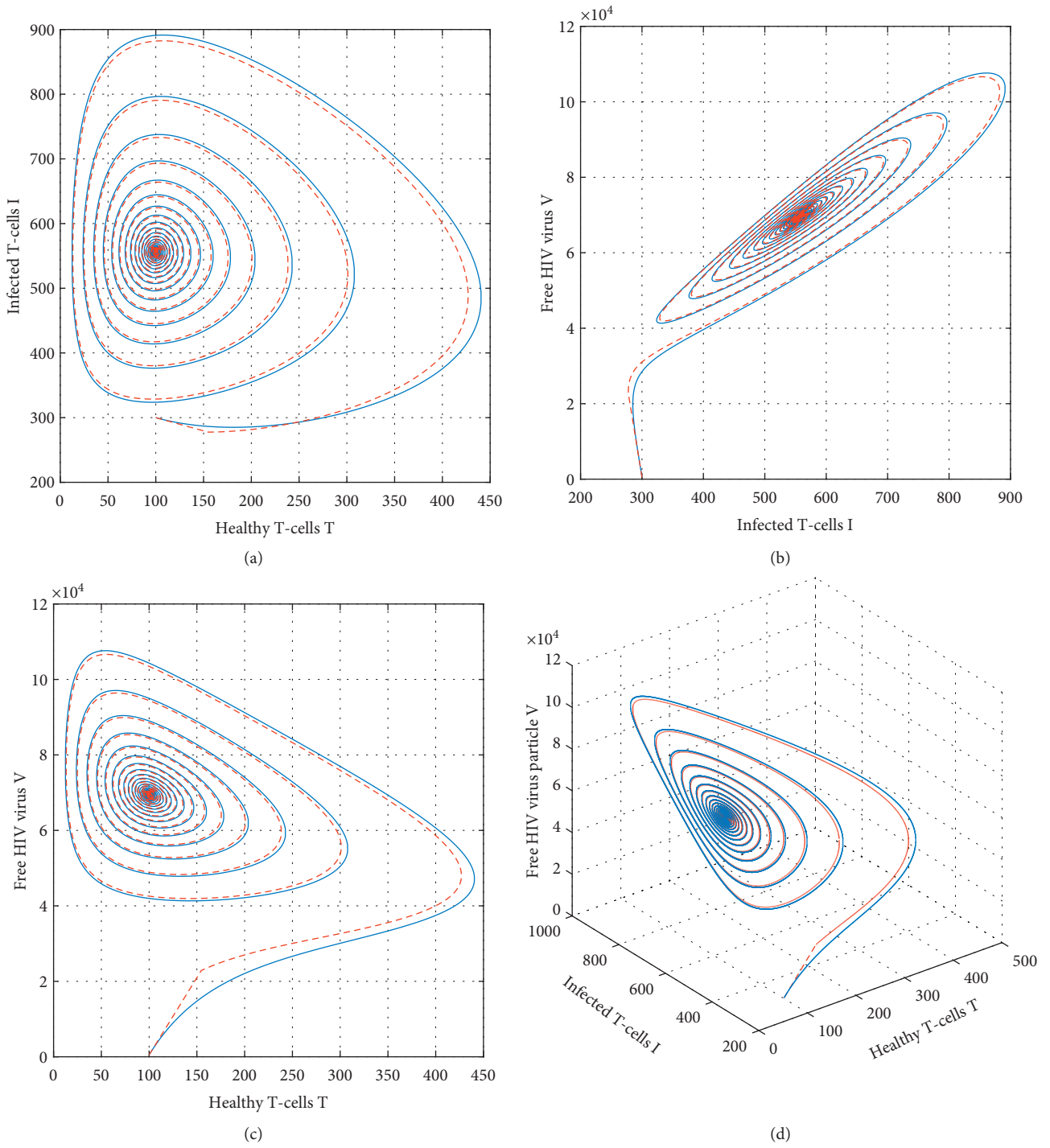


FIGURE 7: Graphical view analysis of the suggested fractional model (2) of HIV to represent its chaotic plot with the index of memory  $\eta = 0.75$ .

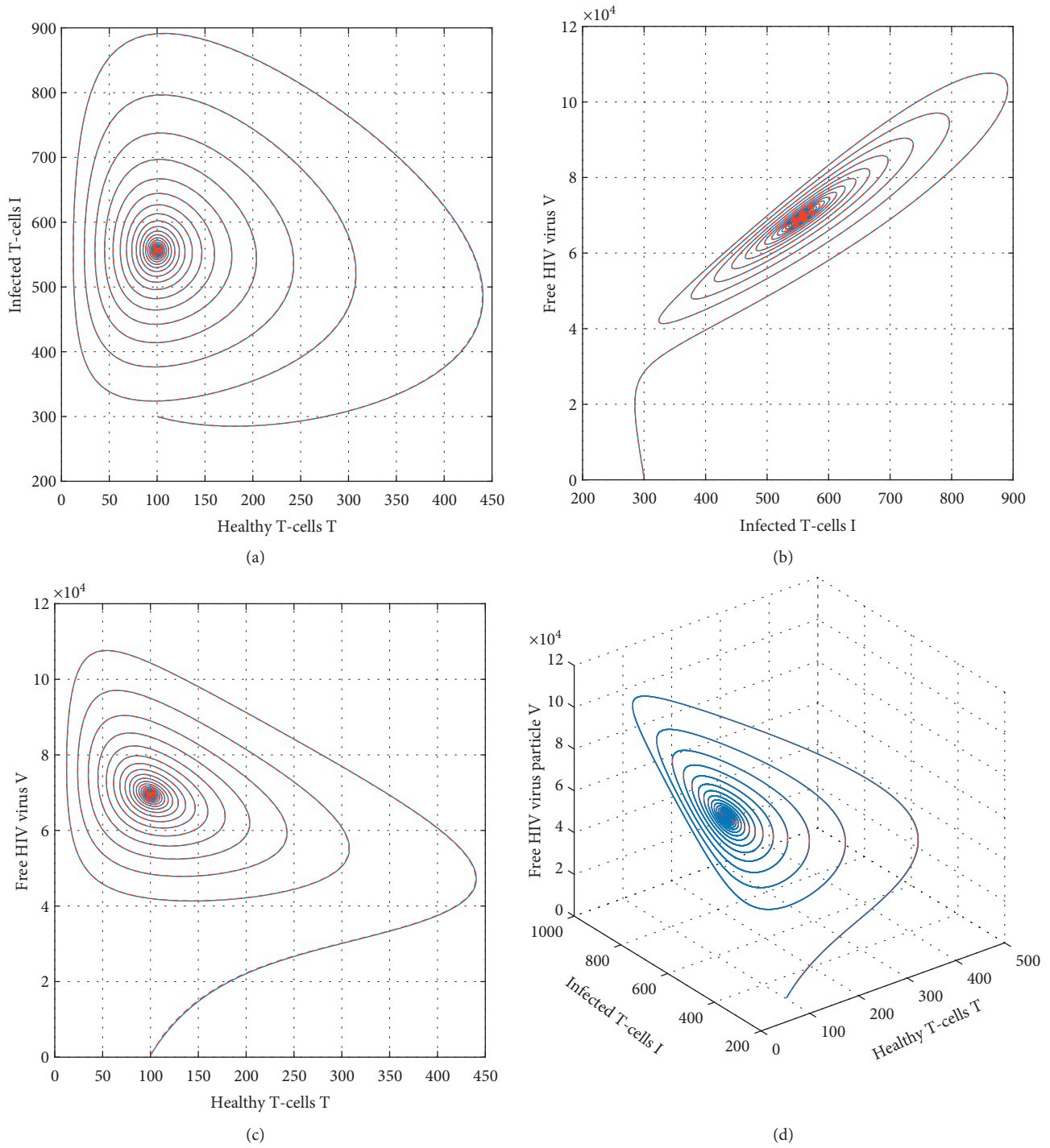


FIGURE 8: Graphical view analysis of the time series of the suggested fractional model (2) of HIV to represent its chaotic plot with the index of memory  $\vartheta = 0.95$ .

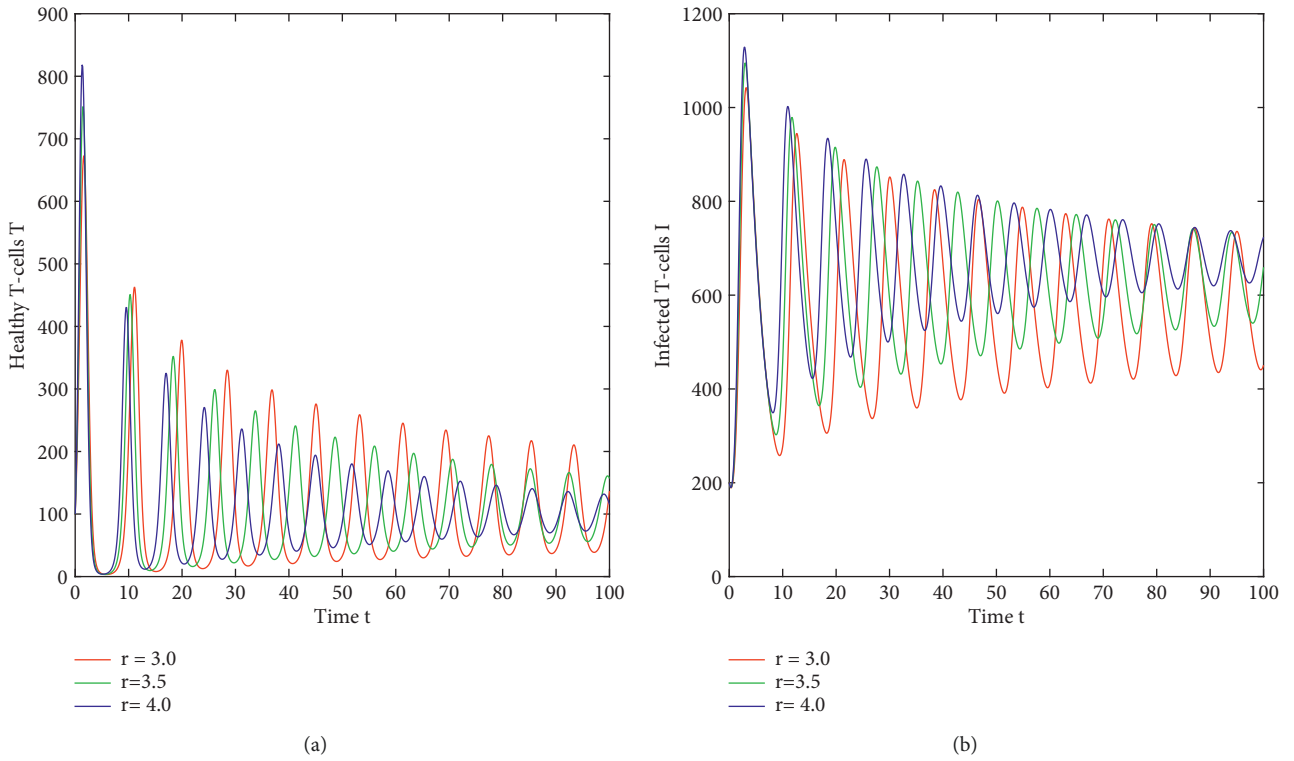


FIGURE 9: Graphical view analysis of the suggested fractional model (2) of HIV with the variation of  $r$ , i.e.,  $r = 3.0, 3.5, 4.0$ .

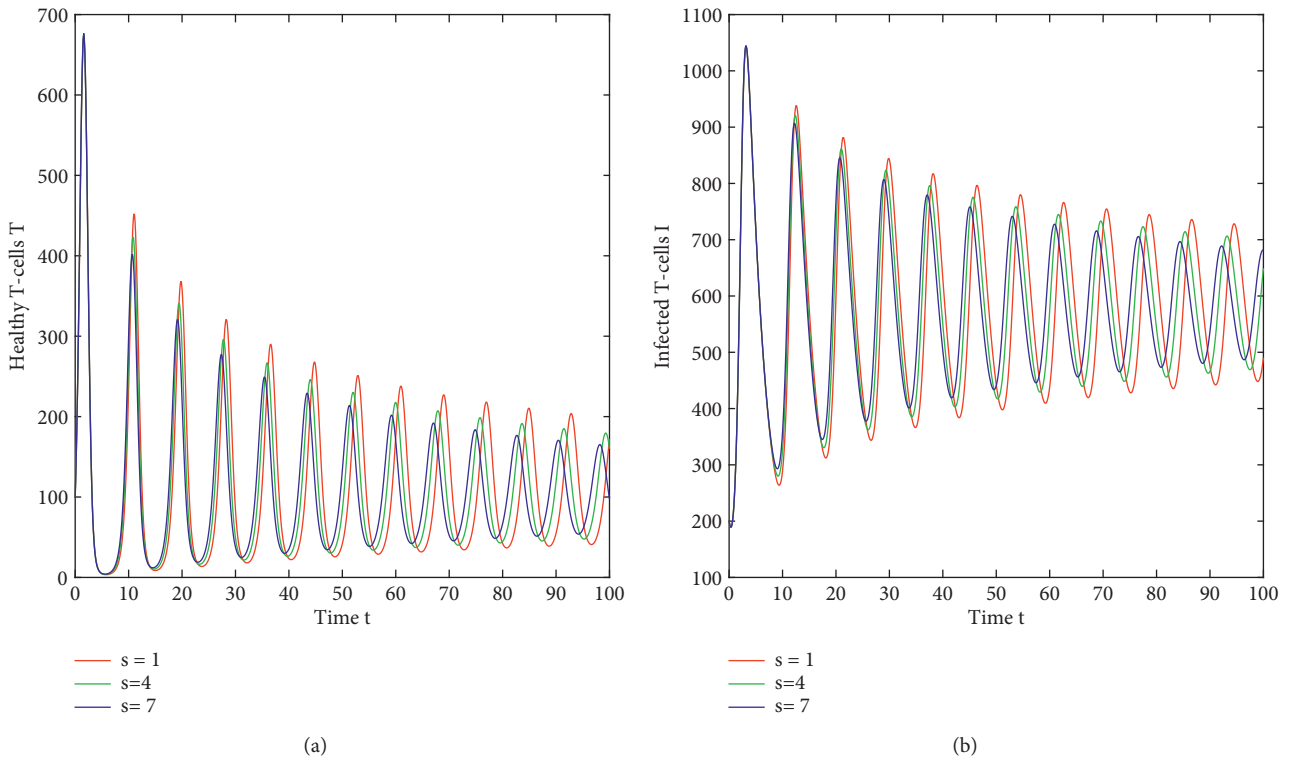


FIGURE 10: Graphical view analysis of the time series of the suggested fractional model (2) of HIV with the variation of  $s$ , i.e.,  $s = 1.0, 4.0, 7.0$ .

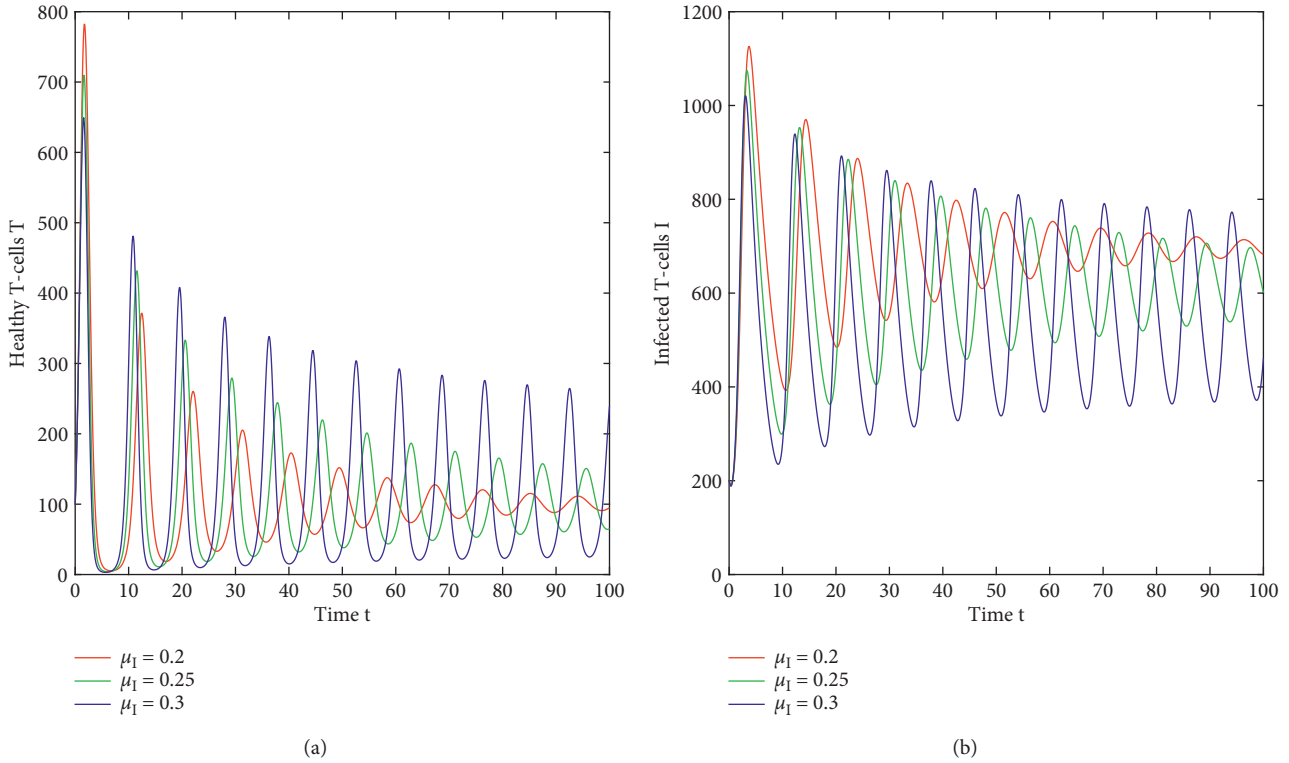


FIGURE 11: Illustration of the time series of the suggested fractional model (2) of HIV with the variation of  $\mu_I$ , i.e.,  $\mu_I = 0.2, 0.25, 0.30$ .

$$\begin{aligned}
 x_{n+1} &= x_n + g(\tau_n, x_n) \\
 &\left[ \frac{1 - \vartheta}{ABC(\vartheta)} + \frac{\vartheta}{ABC(\vartheta)h} \left\{ \frac{2ht_{n+1}^\vartheta}{\vartheta} - \frac{t_{n+1}^{\vartheta+1}}{\vartheta + 1} \right\} - \frac{\vartheta}{h\Gamma(\vartheta)ABC(\vartheta)} \left\{ \frac{ht_n^\vartheta}{\vartheta} - \frac{t_n^{\vartheta+1}}{\vartheta + 1} \right\} \right] \\
 &+ g(\tau_{n-1}, x_{n-1}) \times \left[ \frac{\vartheta - 1}{ABC(\vartheta)} - \frac{\vartheta}{ABC(\vartheta)\Gamma(\vartheta)h} \left[ \frac{2h\tau_{n+1}^\vartheta}{\vartheta} - \frac{\tau_{n+1}^{\vartheta+1}}{\vartheta + 1} + \frac{\tau^{\vartheta+1}}{ABC(\vartheta)h\Gamma(\vartheta)} \right] \right] + H_\vartheta,
 \end{aligned} \tag{23}$$

in which  $\|H_\vartheta\|_\infty < N$ .

*Proof.* To prove the required result, we proceed in the following manner:

$$\begin{aligned}
 x_{n+1} - x_n &= \frac{1 - \vartheta}{ABC(\vartheta)} (g(\tau_n, x_n) - g(\tau_{n-1}, x_{n-1})) + \frac{\vartheta}{\Gamma(\vartheta)ABC(\vartheta)} \\
 &\times \left[ \int_0^{\tau_{n+1}} (\tau_{n+1} - \tau)^{\vartheta-1} g(\tau, x(\tau)) d\tau - \int_0^{\tau_n} (\tau_n - \tau)^{\vartheta-1} g(\tau, x(\tau)) d\tau \right] \\
 &= \frac{1 - \vartheta}{ABC(\vartheta)} (g_n - g_{n-1}) + \frac{\vartheta}{\Gamma(\vartheta)ABC(\vartheta)} \\
 &\left\{ \int_0^{\tau_{n+1}} \frac{\tau - \tau_{n-1}}{\tau_n - \tau_{n-1}} g(\tau_n, x_n) + \frac{\tau - \tau_n}{\tau_{n-1} - \tau_n} g(\tau_{n-1}, x_{n-1}) + \frac{g^{n+1}(\tau)}{(n+1)!} \prod_{i=0}^n (\tau - \tau_i) \right\} (\tau_{n+1} - \tau)^{\vartheta-1} d\tau
 \end{aligned}$$



$$\begin{aligned}
& - \int_0^{\tau_n} \left\{ \frac{\tau - \tau_{n-1}}{\tau_n - \tau_{n-1}} g(\tau_n, x_n) + \frac{\tau - \tau_n}{\tau_{n-1} - \tau_n} f(\tau_{n-1}, y_{n-1}) + \frac{g^n(\tau)}{(n)!} \prod_{i=0}^{n-1} (\tau - \tau_i) \right\} \times (\tau_n - \tau)^{\vartheta-1} d\tau \\
& = \int_0^{\tau_{n+1}} \frac{g^{(n+1)}(\tau)}{(n+1)!} \prod_{i=0}^n (\tau_{n+1} - \tau)^{\vartheta-1} (\tau - \tau_i) d\tau + J(\tau, \vartheta, n) \\
& - \int_0^{\tau_n} \frac{g^{(n)}(\tau)}{(n)!} \prod_{i=0}^n (\tau_n - \tau)^{\vartheta-1} (\tau - \tau_i) d\tau.
\end{aligned} \tag{24}$$

This further gives

$$x_{n+1} - x_n = J(\tau, \vartheta, n) + H_\vartheta(\tau), \tag{25}$$

in which we have

$$\begin{aligned}
J(\tau, \vartheta, n) & = g(\tau_n, x_n) \\
& \left\{ \frac{1 - \vartheta}{ABC(\vartheta)} + \frac{\vartheta}{AB(\vartheta)h} \left[ \frac{2h\tau_{n+1}^\vartheta}{\vartheta} - \frac{\tau_{n+1}^{\vartheta+1}}{\vartheta+1} \right] - \frac{\vartheta}{ABC(\vartheta)h\Gamma(\vartheta)} \left[ \frac{h\tau_n^\vartheta}{\vartheta} - \frac{\tau_n^{\vartheta+1}}{\vartheta+1} \right] \right\} \\
& + g(\tau_{n-1}, x_{n-1}) \left\{ \frac{\vartheta}{ABC(\vartheta)} - \frac{\vartheta}{hABC(\vartheta)\Gamma(\vartheta)} \left( \frac{h\tau_{n+1}^\vartheta}{\vartheta} - \frac{\tau_{n+1}^{\vartheta+1}}{\vartheta+1} + \frac{\tau_n^{\vartheta+1}}{h\Gamma(\vartheta)ABC(\vartheta)} \right) \right\},
\end{aligned} \tag{26}$$

$$H_\vartheta(t) = \int_0^{\tau_{n+1}} \frac{g^{(n+1)}(\tau)}{(n+1)!} \prod_{i=0}^n (\tau_{n+1} - \tau)^{\vartheta-1} (\tau - \tau_i) d\tau - \int_0^{\tau_n} \frac{g^n(\tau)}{(n)!} \prod_{i=0}^{n-1} (\tau - \tau_i) (\tau_n - \tau)^{\vartheta-1} d\tau. \tag{27}$$

Next, we need to prove the following:

$$\begin{aligned}
\|H_\vartheta(\tau)\|_\infty & = \left\| \int_0^{\tau_{n+1}} \frac{g^{(n+1)}(\tau)}{(n+1)!} \prod_{i=0}^n (\tau - \tau_i) (\tau_{n+1} - \tau)^{\vartheta-1} d\tau - \int_0^{\tau_n} \frac{g^n(\tau)}{(n)!} \prod_{i=0}^{n-1} (\tau - \tau_i) (\tau_n - \tau)^{\vartheta-1} d\tau \right\|_\infty \\
& < \left\| \int_0^{\tau_{n+1}} \frac{g^{(n+1)}(\tau)}{(n+1)!} \prod_{i=0}^n (\tau - \tau_i) (\tau_{n+1} - \tau)^{\vartheta-1} d\tau \right\|_\infty + \left\| \int_0^{\tau_n} \frac{g^n(\tau)}{(n)!} \prod_{i=0}^{n-1} (\tau_n - \tau)^{\vartheta-1} (\tau - \tau_i) d\tau \right\|_\infty \\
& < \max_{\tau \in [0, \tau_{n+1}]} \frac{|g^{(n+1)}(\tau)|}{(n+1)!} \left\| \prod_{i=0}^n (\tau - \tau_i) \right\|_\infty \frac{t_{n+1}^\vartheta}{\vartheta} + \max_{\tau \in [0, \tau_{n+1}]} \frac{|g^n(\tau)|}{(n)!} \left\| \prod_{i=0}^{n-1} (\tau - \tau_i) \right\|_\infty \frac{\tau_n^\vartheta}{\vartheta} \\
& < \sup_{\tau \in [0, \tau_{n+1}]} \left\{ \max_{\tau \in [0, \tau_{n+1}]} \frac{|g^{(n+1)}(\tau)|}{(n+1)!}, \max_{\tau \in [0, \tau_{n+1}]} \frac{|g^n(\tau)|}{(n)!} \right\} \left( n! \frac{h^{n+1}}{4\vartheta} \tau^{\vartheta_{n+1}} + (n-1)! \frac{h^n}{4\vartheta} \tau^{\vartheta_n} \right),
\end{aligned} \tag{28}$$

which is the required result.  $\square$

*Atangana–Baleanu fraction framework in Caputo sense is given by*

**Theorem 4.** Assume that  $g$  fulfills Lipschitz condition, then the stability condition for the above numerical scheme in

$$\|g(\tau_n, x_n) - g(\tau_{n-1}, x_{n-1})\|_\infty \longrightarrow 0, \tag{29}$$

as  $n \rightarrow \infty$ .

*Proof.* To prove the required result, we first take

$$\begin{aligned}
 x_{n-1} - x_n &= \frac{1 - \vartheta}{ABC(\vartheta)} [g(\tau_n, x_n) - g(\tau_{n-1}, x_{n-1})] + \frac{\vartheta}{ABC(\vartheta)\Gamma(\vartheta)} \\
 &\times \left[ \int_0^{\tau_{n+1}} g(\tau, x(\tau)) (\tau_{n+1} - \tau)^{\vartheta-1} d\tau - \int_0^{\tau_n} g(\tau, x(\tau)) (\tau_n - \tau)^{\vartheta-1} d\tau \right].
 \end{aligned}
 \tag{30}$$

The following is obtained by taking the norm on both sides:

$$\begin{aligned}
 \|x_{n-1} - x_n\|_\infty &< \left\| \frac{1 - \vartheta}{ABC(\vartheta)} [g(\tau_n, x_n) - g(\tau_{n-1}, x_{n-1})] \right\|_\infty + \frac{\vartheta}{\Gamma(\vartheta)ABC(\vartheta)}, \\
 &\times \left\| \left[ \int_0^{\tau_{n+1}} (\tau_{n+1} - \tau)^{\vartheta-1} g(\tau, x(\tau)) d\tau - \int_0^{\tau_n} (\tau_n - \tau)^{\vartheta-1} g(\tau, x(\tau)) d\tau \right] \right\|_\infty \\
 &< \frac{1 - \vartheta}{ABC(\vartheta)} \|g(\tau_n, x_n) - g(\tau_{n-1}, x_{n-1})\|_\infty \\
 &+ \frac{\vartheta}{ABC(\vartheta)\Gamma(\vartheta)} \left\| \int_0^{\tau_{n+1}} g(\tau, x(\tau)) (\tau_{n+1} - \tau)^{\vartheta-1} d\tau \right\|_\infty \\
 &+ \frac{\vartheta}{ABC(\vartheta)\Gamma(\vartheta)} \left\| \int_0^{\tau_n} g(\tau, x(\tau)) (\tau_n - \tau)^{\vartheta-1} d\tau \right\|_\infty.
 \end{aligned}
 \tag{31}$$

This implies that

$$\begin{aligned}
 \|x_{n+1} - x_n\|_\infty &< \frac{1 - \vartheta}{ABC(\vartheta)} \|g(\tau_n, x_n) - g(\tau_{n-1}, x_{n-1})\|_\infty \\
 &+ \frac{\vartheta}{ABC(\vartheta)\Gamma(\vartheta)} \left\| \int_0^{\tau_{n+1}} (\tau_{n+1} - \tau)^{\vartheta-1} \sum_{i=0}^n \prod_{0 \leq i \leq n} \frac{(\tau - \tau_i)}{(-1)^i h} g(\tau_i, x_i) d\tau \right\|_\infty \\
 &+ \frac{\vartheta}{ABC(\vartheta)\Gamma(\vartheta)} \left\| \int_0^{\tau_n} (\tau_n - \tau)^{\vartheta-1} \sum_{i=0}^{n-1} \prod_{0 \leq i \leq n-1} g(\tau_i, x_i) d\tau \right\|_\infty \\
 &< \frac{1 - \vartheta}{ABC(\vartheta)} \|g(\tau_n, x_n) - g(\tau_{n-1}, x_{n-1})\|_\infty + \|P_n^\vartheta(\tau)\|_\infty + \|H_n^\vartheta(\tau)\|_\infty,
 \end{aligned}
 \tag{32}$$

in which

$$\begin{aligned} \|P_n^\vartheta(\tau)\|_\infty &= \left\| \int_0^{\tau_{n+1}} (\tau_{n+1} - \tau)^{\vartheta-1} \sum_{i=0}^n \frac{(\tau - \tau_i)}{(-1)^i h} g(\tau_i, x_i) d\tau \right\|_\infty \\ &\leq \sum_{i=0}^n \frac{\|g(\tau_i, x_i)\|_\infty}{h} \frac{\tau_{n+1}^\vartheta}{\vartheta} \prod_{i=0}^n |\tau - \tau_i| \end{aligned} \quad (33)$$

$$\begin{aligned} &\leq \sum_{i=0}^n \frac{\|g(\tau_i, x_i)\|_\infty}{h} \frac{\tau_{n+1}^\vartheta}{\vartheta} \frac{n! h^n}{4}, \\ \|H_n^\vartheta(\tau)\|_\infty &\leq \sum_{i=0}^n \frac{\|g(\tau_i, x_i)\|_\infty}{h} \frac{\tau_n^\vartheta}{\vartheta} (n-1)! \frac{h^{n-1}}{4}. \end{aligned} \quad (34)$$

As a result, we obtain

$$\begin{aligned} \|x_{n-1} - x_n\|_\infty &< \frac{1 - \vartheta}{\text{ABC}(\vartheta)} \|g(\tau_n, x_n) - g(\tau_{n-1}, x_{n-1})\|_\infty \\ &+ \sum_{i=0}^n \frac{\|g(\tau_i, x_i)\|_\infty}{4\vartheta} \tau_{n+1}^\vartheta h^{n-1} n! + \sum_{i=0}^{n-1} \frac{\|g(\tau_{i-1}, x_{i-1})\|_\infty}{4\vartheta} \tau_n^\vartheta h^{n-3} (n-1)! \\ &< \frac{Mn!h^n}{4\vartheta} \left\{ \frac{\tau_{n+1}^\vartheta (n+1)}{h} + \frac{\tau_n^\vartheta}{h^2} \right\} + \frac{1 - \vartheta}{\text{ABC}(\vartheta)} \|g(\tau_n, x_n) - g(\tau_{n-1}, x_{n-1})\|_\infty, \end{aligned} \quad (35)$$

which implies that  $|g(\tau_n, x_n) - g(\tau_{n-1}, x_{n-1})|$  goes to zero as  $n$  goes to  $\infty$  and as  $h$  tends to zero, then  $Mn!h^n/4\vartheta$  tends to zero, where  $M = \max_{\tau \in [0, \tau_{n+1}]} |g(\tau, x(\tau))|$ .  $\square$

## 5. Concluding Remarks

HIV/AIDS has a significant impact on economic growth by limiting the availability of human capital. AIDS is killing a high number of people in underdeveloped nations due to a lack of effective prevention, treatment, health care, and nutrition. Therefore, it is significant to interrogate the transmission pathway of HIV to identify the role of different input factors on the output of infection. In this work, we structured the dynamics of  $\text{CD4}^+$  T-cells in HIV infection through fractional calculus. We presented the proposed model through Atangana–Baleanu derivative in the Caputo sense. The rudimentary properties of fractional calculus have been introduced for the examination of the system. We provided a new numerical scheme for addressing the Atangana–Baleanu fractional derivative to conceptualize the dynamics of HIV. The oscillatory and chaotic plots have been presented with the variation of different input parameters. It has been shown that fractional order has an influence on the chaotic behaviour of the suggested model. The memory index  $\ell$  is expected to improve the system and may have been used as a control parameter. We illustrated the impact of input parameters  $r$ ,  $s$ , and  $\mu_I$  on the concentration level of healthy and infected  $\text{CD4}^+$  T-cells. On the basis of our results, the most critical factors of the system are highlighted. We highlighted the influence of different input

parameter on the dynamics of HIV infection. Furthermore, the convergence and stability result of the system have been shown. In future research work, we opt to highlight the influence of time delay on the infection of HIV infection to highlight the importance of time delay for the control and to validate our results through experimental data.

## Data Availability

No data were used to support the study.

## Conflicts of Interest

The authors declare that they have no conflicts of interest.

## References

- [1] L. Wang and M. Y. Li, “Mathematical analysis of the global dynamics of a model for HIV infection of  $\text{CD4}^+$  T cells,” *Mathematical Biosciences*, vol. 200, no. 1, pp. 44–57, 2006.
- [2] S. Qureshi and R. Jan, “Modeling of measles epidemic with optimized fractional order under Caputo differential operator,” *Chaos, Solitons & Fractals*, vol. 145, Article ID 110766, 2021.
- [3] H. C. Tuckwell and E. Le Corfec, “A stochastic model for early HIV-1 population dynamics,” *Journal of Theoretical Biology*, vol. 195, no. 4, pp. 451–463, 1998.
- [4] R. Jan and Y. Xiao, “Effect of partial immunity on transmission dynamics of dengue disease with optimal control,” *Mathematical Methods in the Applied Sciences*, vol. 42, no. 6, pp. 1967–1983, 2019.

- [5] A. S. Perelson, D. E. Kirschner, and R. De Boer, "Dynamics of HIV infection of CD4+ T cells," *Mathematical Biosciences*, vol. 114, no. 1, pp. 81–125, 1993.
- [6] A. S. Perelson and P. W. Nelson, "Mathematical analysis of HIV-1 dynamics in vivo," *SIAM Review*, vol. 41, no. 1, pp. 3–44, 1999.
- [7] R. V. Culshaw and S. Ruan, "A delay-differential equation model of HIV infection of CD4+ T-cells," *Mathematical Biosciences*, vol. 165, no. 1, pp. 27–39, 2000.
- [8] S. A. M. Bushnaq, K. Shah, and G. Zaman, "Existence theory of HIV-1 infection model by using arbitrary order derivative of without singular kernel type," *J. Math. Anal.* vol. 9, no. 1, pp. 16–28, 2018.
- [9] M. Ghoreishi, A. M. Ismail, and A. K. Alomari, "Application of the homotopy analysis method for solving a model for HIV infection of CD4+ T-cells," *Mathematical and Computer Modelling*, vol. 54, no. 11-12, pp. 3007–3015, 2011.
- [10] M. Ongun, "The laplace adomian decomposition method for solving a model for HIV infection of CD4+ 220 T-cells," *Mathematical and Computer Modelling*, vol. 53, no. 5-6, pp. 597–603, 2011.
- [11] H. Vazquez-Leal, L. Hernandez-Martinez, Y. Khan et al., "Multistage HPM applied to path tracking damped oscillations of a model for HIV infection of CD4+ T cells," *British Journal of Mathematics & Computer Science*, vol. 4, no. 8, pp. 1035–1047, 2014.
- [12] A.-H. Abdel-Aty, M. M. A. Khater, H. Dutta, J. Bouslimi, and M. Omri, "Computational solutions of the HIV-1 infection of CD4+T-cells fractional mathematical model that causes acquired immunodeficiency syndrome (AIDS) with the effect of antiviral drug therapy," *Chaos, Solitons & Fractals*, vol. 139, Article ID 110092, 2020.
- [13] S. Arshad, O. Defterli, and D. Baleanu, "A second order accurate approximation for fractional derivatives with singular and non-singular kernel applied to a HIV model," *Applied Mathematics and Computation*, vol. 374, p. 125061, 2020.
- [14] A. Jan, R. Jan, H. Khan, M. S. Zobaer, and R. Shah, "Fractional-order dynamics of Rift Valley fever in ruminant host with vaccination," *Commun. Math. Biol. Neurosci.* vol. 2020, 2020.
- [15] M. Caputo and M. Fabrizio, "A new definition of fractional derivative without singular kernel," *Progr. Fract. Differ. Appl.* vol. 1, no. 2, pp. 1–13, 2015.
- [16] A. Atangana and D. Baleanu, "New Fractional Derivatives with Nonlocal and Non-singular Kernel: Theory and Application to Heat Transfer Model," arXiv preprint arXiv:1602.03408, 2016.
- [17] A. Atangana, "Non validity of index law in fractional calculus: a fractional differential operator with Markovian and non-Markovian properties," *Physica A: Statistical Mechanics and Its Applications*, vol. 505, pp. 688–706, 2018.
- [18] S. Ahmad, A. Ullah, M. Arfan, and K. Shah, "On analysis of the fractional mathematical model of rotavirus epidemic with the effects of breastfeeding and vaccination under Atangana-Baleanu (AB) derivative," *Chaos, Solitons & Fractals*, vol. 140, Article ID 110233, 2020.
- [19] I. Koca, "Analysis of rubella disease model with non-local and non-singular fractional derivatives," *An International Journal of Optimization and Control: Theories & Applications*, vol. 8, no. 1, pp. 17–25, 2018.
- [20] O. T. Kolebaje, O. R. Vincent, U. E. Vincent, and P. V. E. McClintock, "Nonlinear growth and mathematical modelling of COVID-19 in some African countries with the Atangana-Baleanu fractional derivative," *Communications in Nonlinear Science and Numerical Simulation*, vol. 105, Article ID 106076, 2022.
- [21] A. T. Haase, K. Henry, M. Zupancic et al., "Quantitative image analysis of HIV-1 infection in lymphoid tissue," *Science*, vol. 274, no. 5289, pp. 985–989, 1996.
- [22] A. S. Perelson, P. Essunger, Y. Cao et al., "Decay characteristics of HIV-1-infected compartments during combination therapy," *Nature*, vol. 387, no. 6629, pp. 188–191, 1997.
- [23] A. S. Perelson and P. W. Nelson, "Mathematical analysis of HIV-1 dynamics in vivo," *SIAM Review*, vol. 41, no. 1, pp. 3–44, 1999.
- [24] J. F. Gómez-Aguilar, A. Atangana, and V. F. Morales-Delgado, "Electrical circuits RC, LC, and RL described by Atangana-Baleanu fractional derivatives," *International Journal of Circuit Theory and Applications*, vol. 45, no. 11, pp. 1514–1533, 2017.
- [25] K. M. Owolabi, "Modelling and simulation of a dynamical system with the Atangana-Baleanu fractional derivative," *The European Physical Journal Plus*, vol. 133, no. 1, pp. 1–13, 2018.
- [26] A. Atangana and K. M. Owolabi, "New numerical approach for fractional differential equations," *Mathematical Modelling of Natural Phenomena*, vol. 13, no. 1, p. 3, 2018.

## Research Article

# Fully Integrated Chen Chaotic Oscillation System

Ziyi Ouyang,<sup>1</sup> Jie Jin ,<sup>1,2</sup> Fei Yu ,<sup>3</sup> Long Chen,<sup>1</sup> and Lei Ding<sup>2</sup>

<sup>1</sup>School of Information and Electrical Engineering, Hunan University of Science and Technology, Xiangtan 411201, China

<sup>2</sup>College of Information Science and Engineering, Jishou University, Jishou 416000, China

<sup>3</sup>School of Computer and Communication Engineering, Changsha University of Science and Technology, Changsha 410114, China

Correspondence should be addressed to Fei Yu; yufeiyfyf@csust.edu.cn

Received 21 December 2021; Revised 10 January 2022; Accepted 25 January 2022; Published 15 February 2022

Academic Editor: Sundarapandian Vaidyanathan

Copyright © 2022 Ziyi Ouyang et al. This is an open access article distributed under the Creative Commons Attribution License, which permits unrestricted use, distribution, and reproduction in any medium, provided the original work is properly cited.

A fully integrated Chen chaotic oscillation system using operational amplifiers (OAs) and multipliers is designed and verified in this paper. Unlike the conventional breadboard-based Chen chaotic system using off-the-shelf discrete components, the fully integrated Chen chaotic oscillation circuit presented in this paper is realized using GlobalFoundries' 0.18  $\mu\text{m}$  CMOS 1P6M process, and all the circuit components are integrated in a chip. The fully integrated Chen chaotic oscillation system is verified using Cadence IC Design Tools, and the post-layout simulation results indicate that the presented integrated Chen chaotic oscillation system only consumes 148 mW from  $\pm 2.5$  V supply voltage, and its chip area is 6.15 mm<sup>2</sup>.

## 1. Introduction

With the development of nonlinear systems, the research on chaos and chaotic neural networks has grown rapidly in recent years [1–10]. However, the development of chaos and chaotic neural networks mainly focuses on their software algorithm improvement [11–18], the hardware implementation of chaos and chaotic neural networks has fallen far behind their software algorithm. Facing with this issue, the research on hardware circuits implementation of chaos and chaotic neural networks becomes increasing important. Chaos has been investigated widely in the last decades and they become increasing interest subjects because of their great potential applications in many fields such as chaotic signal radar [19], secure communications [20–24], chaos-based analog-to-information conversion and image encryption applications [25]. The double-scroll Chua system is the first physical circuit realization of chaos. Since then, other chaotic and hyperchaotic systems with complex chaotic attractors and nonlinear dynamical characteristics have been realized [26–31], and most of them are validated with commercial available discrete electronic components or

digital signal processing (DSP) and field programmable gate array (FPGA) [32–42].

Most of the reported and physical implemented chaotic systems are realized using off-the-shelf electronic components with breadboards. The breadboard-based chaotic circuits are suitable for theoretically proving the existence and realizability of chaos, they are non-portable and unstable, and far from the practical application of chaos. Unlike the conventional breadboard-based chaotic circuits, the fully integrated chaotic systems are more stable and convenient than their breadboard-based counterparts. Chaotic systems fully integrated on a single chip should be the development direction of chaotic circuits, and the fully integrated chaotic circuits will greatly enhance the practicality of chaos. For example, two CMOS Chua's chaotic circuits were reported in Ref. [43], another 2  $\mu\text{m}$  CMOS process integrated chaotic system with high speed operation was introduced Ref. [44], and an integrated multi-scroll chaotic oscillator generating 3- and 5-scroll attractors was reported in Ref. [45].

Because of its simple circuit structure and easy to be theoretically proven, the famous Chen chaotic system

[46–50] and its deformation circuits are deeply studied in the past decades. Several realization and implementation of Chen chaotic circuits are presented in Ref. [50], however, these circuits are also realized using commercial available discrete electronic components with breadboards. Based on the existing Chen chaotic circuits and systems, a low voltage low power fully integrated classic Chen chaotic oscillation system is realized in this paper. The post-layout simulation results verified that the fully integrated Chen chaotic oscillation system is feasible and achievable. In addition, the main contributions of this work can be summarized below.

- 1) An operational amplifiers (OA) and an analog multiplier with GlobalFoundries' 0.18  $\mu\text{m}$  CMOS 1P6M process are designed in this work.
- 2) Unlike the conventional breadboard-based chaotic circuits, a fully integrated Chen chaotic oscillation system using the designed OA and multiplier is presented.
- 3) The fully integrated Chen chaotic system is verified with Cadence IC Tools. The post-layout simulation results demonstrate that the whole power consumption of the fully integrated Chen chaotic system is about 148 mW, its chip area is only 6.15  $\text{mm}^2$ , and the fully integrated Chen chaotic circuit is a more suitable candidate for practical applications.

## 2. Fully Integrated Chen Chaotic Circuit

The design of fully integrated Chen chaotic circuit is presented in this section. The original Chen chaotic system and its fully integrated circuit is introduced in subsection 2.1, and the implementations of operational amplifier and analog multiplier are introduced in subsection 2.2 and 2.3, respectively.

**2.1. Chen Chaotic System.** The classic dimensionless state equations of the Chen system can be depicted as follow:

$$\begin{cases} \frac{dx}{dt} = a(y - x) \\ \frac{dy}{dt} = (c - a)x - xz + cy, \\ \frac{dz}{dt} = xy - bz \end{cases} \quad (1)$$

where  $a$ ,  $b$  and  $c$  are all constants, and  $a = 35$ ,  $b = 3$ ,  $c = 28$ . When the initial condition is  $(0, 0, 0)$ , the Matlab numerical simulation results of Chen system are presented in Fig 1, and the chaotic attractors are observed as shown in Fig. 1(a)-(c).

Because the supply voltage of the fully integrated Chen chaotic oscillation system are  $\pm 2.5$  V, and the output ranges of state variables  $x$ ,  $y$  and  $z$  in Fig 1 all exceed  $\pm 2.5$  V, state variables compression are necessary. After evenly compressed 40 times of the state variables, the state equations of the Chen system could be expressed as:

$$\begin{cases} \frac{dx}{dt} = 35(y - x), \\ \frac{dy}{dt} = -7x - 40xz + 28y, \\ \frac{dz}{dt} = 40xy - 3z. \end{cases} \quad (2)$$

Let  $\tau = \tau_o \times t$ , and  $\tau_o = 10000$ , and the state equations of the Chen system could be rewritten as:

$$\begin{cases} \frac{dx}{dt} = 100000(3.5y - 3.5x), \\ \frac{dy}{dt} = 100000(-0.7x - 4xz + 2.8y), \\ \frac{dz}{dt} = 100000(4xy - 0.3z). \end{cases} \quad (3)$$

Based on the existing circuit realizations of Chen chaotic systems, a simplified Chen chaotic oscillation circuit suitable for integration is presented in Fig. 2.

Assuming the gains of the multipliers are all  $k$ , and the circuit equation of Fig. 2 could be expressed as:

$$\begin{cases} \frac{dx}{dt} = \frac{1}{R_4 C_1} \left( \frac{R_3 R_6}{R_1 R_5} x + \frac{R_3}{R_2} y \right), \\ \frac{dy}{dt} = \frac{1}{R_{11} C_2} \left( -\frac{R_6 R_{10}}{R_5 R_7} x - \frac{k R_6 R_{10}}{R_5 R_8} xz + \frac{R_{10}}{R_9} y \right), \\ \frac{dz}{dt} = \frac{1}{R_{15} C_3} \left( \frac{k R_{14}}{R_{12}} xy - \frac{R_{14} R_{17}}{R_{13} R_{16}} z \right). \end{cases} \quad (4)$$

**2.2. Implementation of Operational Amplifier.** The designed OA for the integrated Chen chaotic oscillation circuit is shown in Fig. 3. The designed operational amplifier is very simple, and its supply voltages are  $V_{CC} = -V_{SS} = 2.5$  V, and it includes two amplification stages and one bias stage.

The transistors  $M_7$ - $M_{11}$  consist of the differential amplification input stage;  $M_{13}$  is the second common source amplification stage, and  $M_{12}$  is the active load of  $M_{13}$ ; the transistors  $M_1$ - $M_6$  consist of the bias stage of the OA, and the transistor  $M_{14}$  and capacitor  $C$  are used for frequency compensation.

The simulated voltage gain and phase frequency characteristics of the OA are shown in Fig. 4. From the mark  $M_0$ , we can know that the voltage gain of the OA is about 30dB; From the marks  $M_0$  and  $M_1$ , we can calculate that the 3dB bandwidth of the OA is 218.5 kHz; From the marks  $M_2$  and  $M_3$ , we can know that the phase margin of the OA is about  $86.22^\circ$ . The power consumption of the OA is about 5.85 mW.



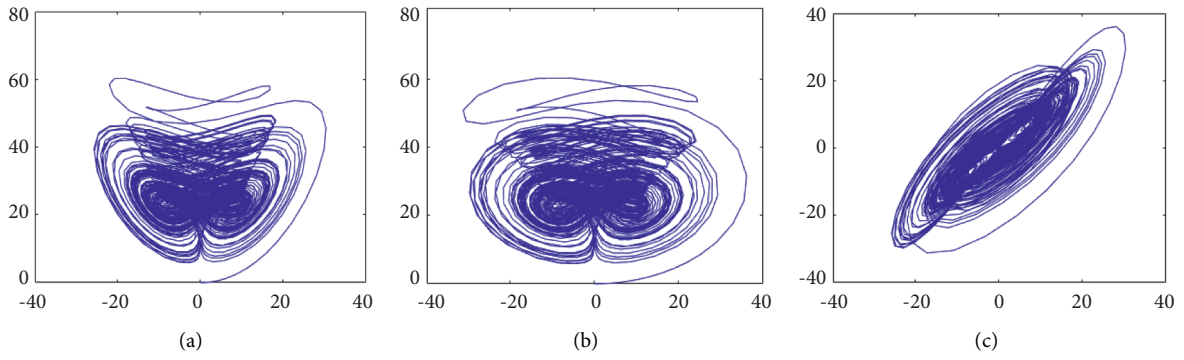


FIGURE 1: Numerically simulated phase portrait of Chen's attractors: (a) x-z plane, (b) z-y plane, and (c) y-x plane.

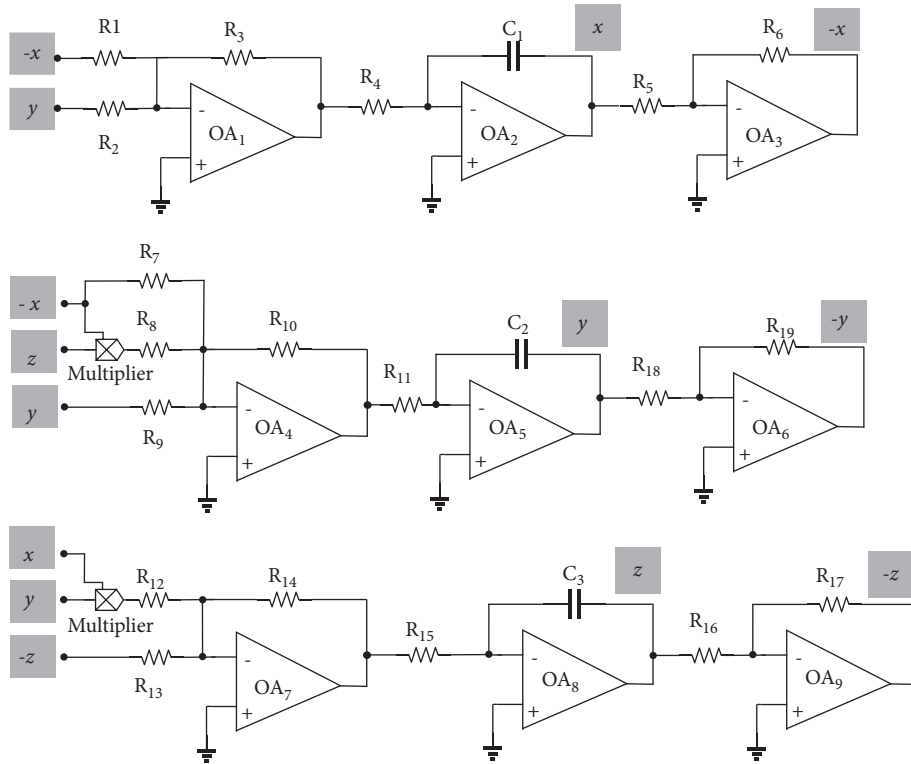


FIGURE 2: The fully integrated Chen chaotic oscillation circuit.

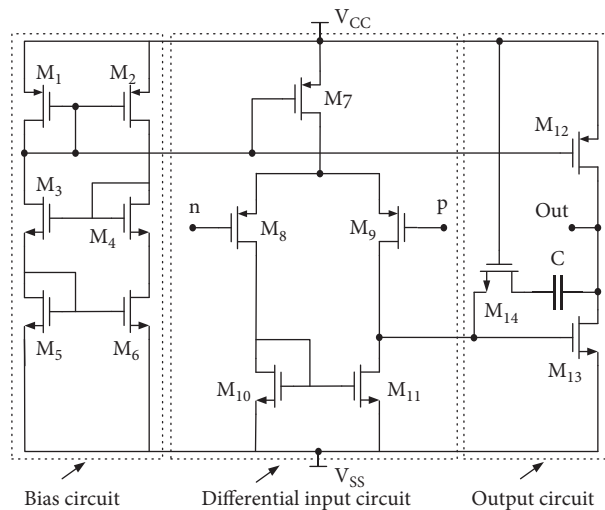


FIGURE 3: The designed OA.

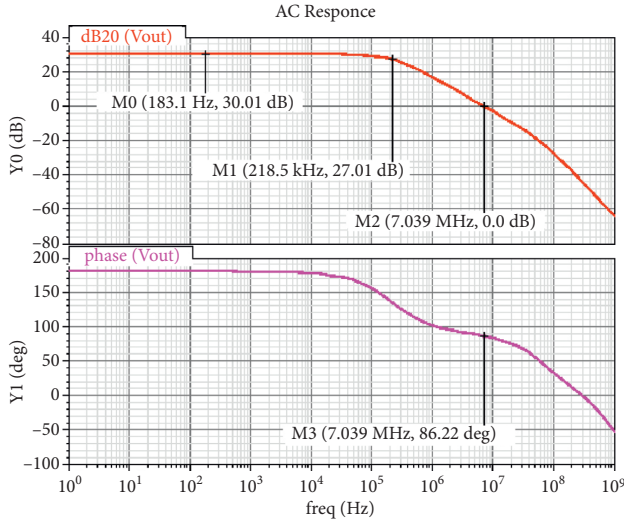


FIGURE 4: Voltage gain and frequency characteristics of the OA.

**2.3. Implementation of Analog Multiplier.** The analog multiplier used in the integrated Chen chaotic oscillation circuit is shown in Fig. 5. The classic Gilbert structure is adopted,  $M_1$  and  $M_2$  consist of the current mirror, and they are the bias stage of the multiplier;  $M_3$  works on its saturation region (also known as amplification region), which can be approximated as a current source to provide bias current for the transconductance stage ( $M_4$  and  $M_5$ );  $M_4$  and  $M_5$  consist of the transconductance stage,  $M_6$ - $M_9$  consist of the Gilbert switch stage [51–53], and  $M_{10}$ - $M_{13}$  consist of the load stage of the analog multiplier. The supply voltages of the multiplier are  $V_{CC} = -V_{SS} = 2.5$  V, and its power consumption is about 47.7 mW.

The transient response of the designed analog multiplier is presented in Fig. 6.  $V_{i1}$  and  $V_{i2}$  are the two input voltages, their input powers are all -10 dBm, and their frequencies are 100 MHz and 10 MHz, respectively.  $V_{out}$  is the output voltage of the analog multiplier. From the above simulation results, it is clear that  $V_{i1}$  is the high frequency carrier,  $V_{i2}$  is the low frequency input signal, and the multiplication is realized in the output voltage  $V_{out}$ . From the marks  $M_0$ - $M_3$  in Fig. 6, peak voltages of  $V_{i1}$  and  $V_{i2}$  are all about 200 mV, and the peak voltage of  $V_{out}$  is about 4mV. According to  $V_{out} = k \times V_{i1} \times V_{i2}$ , it is clear that the parameter  $k$  in equation (4) is about 0.1.

### 3. Post-Layout Simulation Results of the Integrated Chen Chaotic Oscillation Circuit

The presented fully integrated Chen chaotic oscillation circuit in Fig. 2 is simulated and verified using Cadence IC Tools with GlobalFoundries' 0.18  $\mu\text{m}$  CMOS technology. The supply voltages of the fully integrated Chen chaotic circuit are  $\pm 2.5$  V, and its whole static power consumption is about 148mW. Considering equations (3) and (4), the values of circuit elements are selected as  $R_1 = R_2 = 2.85$  k $\Omega$ ,  $R_3 = R_5 = R_6 = R_{10} = R_{14} = R_{16} = R_{17} = R_{18} = R_{19} = 10$  k $\Omega$ ,  $R_4 = R_{11} = R_{15} = 200$  k $\Omega$ ,  $R_8 = R_{12} = 0.25$  k $\Omega$ ,  $R_7 = 14.28$  k $\Omega$ ,  $R_9 = 3.57$  k $\Omega$ ,  $R_{13} = 33.33$  k $\Omega$ ,  $C_1 = C_2 = C_3 = 50$  pF.

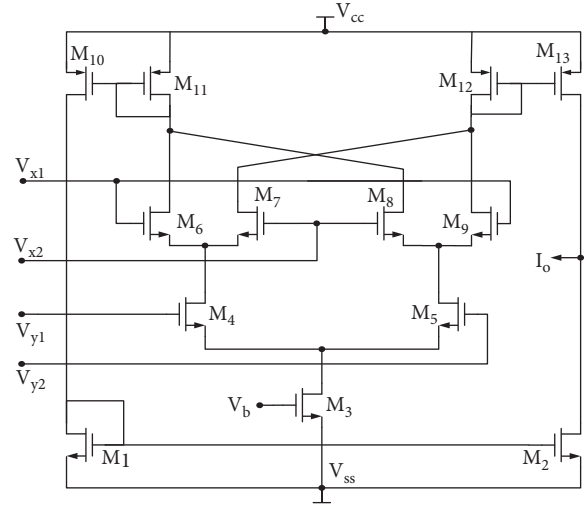


FIGURE 5: The designed analog multiplier.

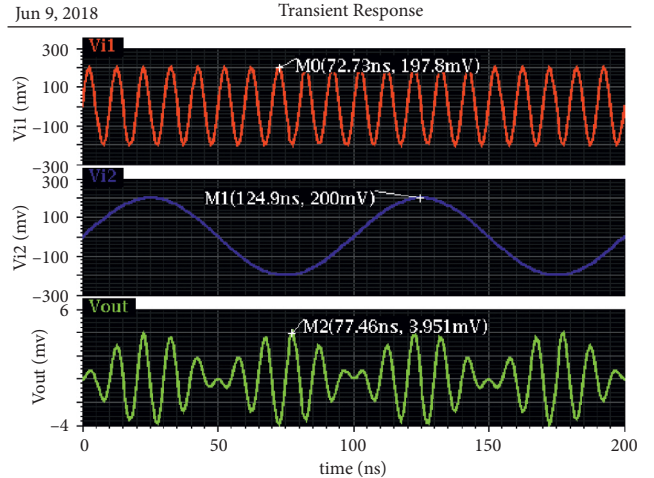


FIGURE 6: The transient response of the analog multiplier.

The chip layout diagram of the Chen Chaotic oscillation system is shown in Fig. 7, and its chip area is 6.15 mm<sup>2</sup> including all the testing pads.

The Mentor Calibre software is used for circuit verification and parasitic extraction. Based on the layout of the Chen chaotic oscillation circuit in Fig. 7, and connecting the extracted parasitics to the original circuit in Fig. 2, the post-layout simulation results of the integrated Chen chaotic oscillation circuit are presented in Figs. 8 and 9.

Fig. 8 is the transient response of the fully integrated Chen chaotic circuit, and various dynamical oscillations can be observed. From Fig.8, it is clear that the peak amplitudes of output voltages  $x$ ,  $y$  and  $z$  are all less than 2 V. Fig. 9 is the phase portraits in  $x$ - $z$ ,  $z$ - $y$  and  $y$ - $x$  planes. By comparing Figs. 1 and Fig. 9, a good qualitative agreement between the post-layout chip circuit simulation and numerical simulation is observed.

There are nine operational amplifiers and two multipliers used in the Chen chaotic oscillation circuit. According to the data sheets of operational amplifier LF347 and multiplier AD633JN in Refs. [51–55], the supply voltage of LF347 is

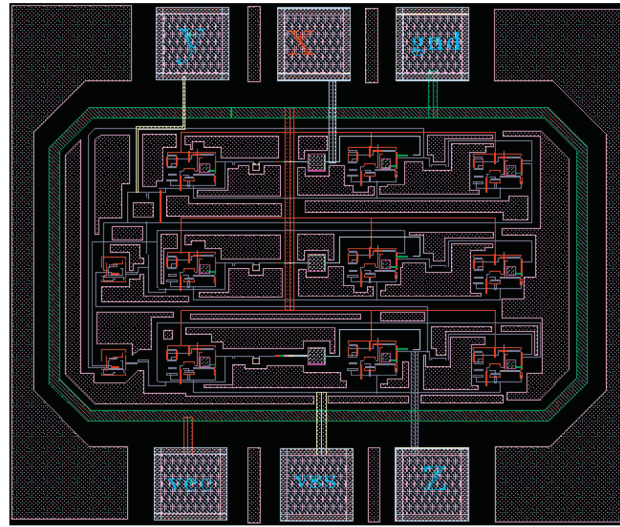


FIGURE 7: Chip layout diagram of the Chen chaotic oscillation circuit.

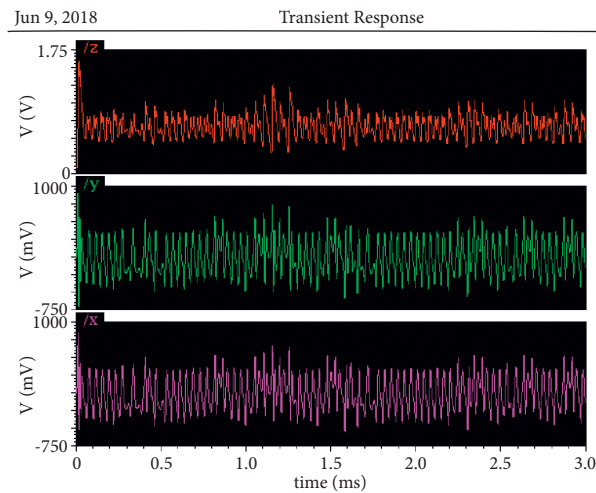


FIGURE 8: Transient response of the Chen chaotic circuit.

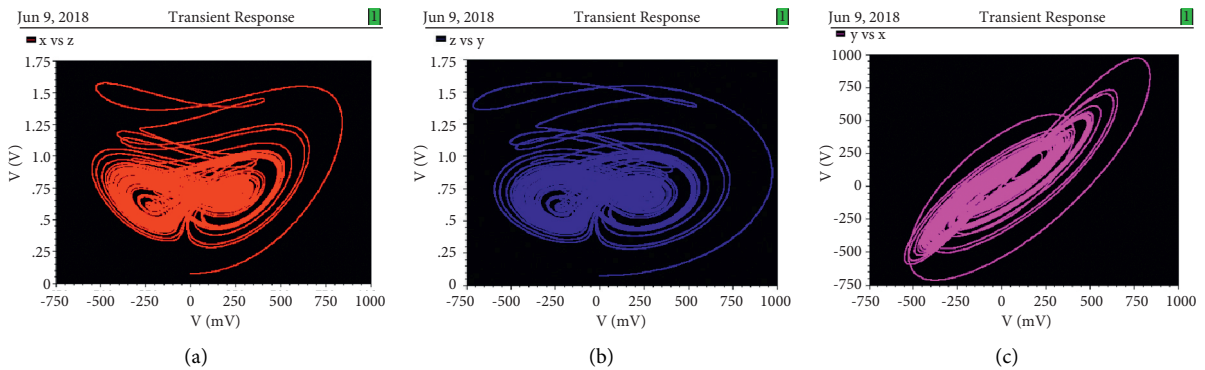


FIGURE 9: Phase portraits of the Chen's attractor in (a) x-z plane, (b) z-y plane, and (c) y-x plane.

$\pm 18$  V, and its power consumption is about 500 mW; the the supply voltage of AD633JN is also  $\pm 18$  V, and its power consumption is also about 500 mW. If the Chen chaotic circuit is realized using commercial available chips LF347

and AD633JN, the whole power consumption is about 5500 mW.

The supply voltage of the fully integrated Chen chaotic oscillation circuit is  $\pm 2.5$  V, the whole power consumption is

about 148 mW, and its chip area is only 6.15 mm<sup>2</sup>. Compared with the conventional realizations using commercial available discrete electronic components with breadboards, the fully integrated Chen chaotic oscillation circuit is a more suitable candidate for practical applications.

#### 4. Conclusion

In this paper, a fully integrated Chen chaotic oscillation system using OAs and multipliers is designed and verified. Unlike the conventional realization using commercial available discrete electronic components with breadboards, the designed Chen chaotic oscillation system is integrated in a single chip. It has the advantages of smaller chip area, lower supply voltage and power consumption. Moreover, it has practical application prospects in demanding portable chaos systems. Besides, it should be further developed from the following objectives to improve the practicability of the fully integrated chaotic circuit. Firstly, other OA and trans-conductance operational amplifier (OTA) with simpler circuit structures and lower power consumption should be designed to further improve the performance of the fully integrated chaotic circuit. In addition, the realization of integrated chaotic circuits with complex chaotic attractors and nonlinear dynamical characteristics is also considered in our future works.

#### Data Availability

All data used to support the findings of this study are available from the corresponding author upon request.

#### Conflicts of Interest

The authors declare that they have no conflicts of interest in this work.

#### Acknowledgments

This work was supported by the National Natural Science Foundation of China (nos. 61905074 and 61966014), the Natural Science Foundation of Hunan Province (nos. 2020JJ4315 and 2020JJ7065), and the Education Department of Hunan Province Youth Project (nos. 20B216 and 21B0345).

#### References

- [1] L. Yang and C. Wang, "Emotion model of associative memory possessing variable learning rates with time delay," *Neurocomputing*, vol. 460, pp. 117–125, 2021.
- [2] F. Yu, L. Liu, L. Xiao, K. Li, and S. Cai, "A robust and fixed-time zeroing neural dynamics for computing time-variant nonlinear equation using a novel nonlinear activation function," *Neurocomputing*, vol. 350, pp. 108–116, 2019.
- [3] Q. Xu, Z. Ju, S. Ding, C. Feng, M. Chen, and B. Bao, "Electromagnetic induction effects on electrical activity within a memristive Wilson neuron model," *Cognitive Neurodynamics*, 2021.
- [4] J. Gong and J. Jin, "A better robustness and fast convergence zeroing neural network for solving dynamic nonlinear equations," *Neural Computing and Applications*, 2021.
- [5] H. Lin, C. Wang, C. Chen et al., "Neural bursting and synchronization emulated by neural networks and circuits," *IEEE Transactions on Circuits and Systems I: Regular Papers*, vol. 68, no. 8, pp. 3397–3410, 2021.
- [6] F. Yu, L. Liu, B. He et al., "Analysis and FPGA realization of a novel 5D hyperchaotic four-wing memristive system, active control synchronization, and secure communication application," *Complexity*, vol. 2019, Article ID 4047957, 2019.
- [7] W. Xie, C. Wang, and H. Lin, "A fractional-order multistable locally active memristor and its chaotic system with transient transition, state jump," *Nonlinear Dynamics*, vol. 104, pp. 4523–4541, 2021.
- [8] H. Lin, C. Wang, Q. Deng, C. Xu, Z. Deng, and C. Zhou, "Review on chaotic dynamics of memristive neuron and neural network," *Nonlinear Dynamics*, vol. 106, no. 1, pp. 959–973, 2021.
- [9] M. Ma, Y. Yang, Z. Qiu et al., "A locally active discrete memristor model and its application in a hyperchaotic map," *Nonlinear Dynamics*, 2022.
- [10] C. Xu, C. Wang, Y. Sun, Q. Hong, Q. Deng, and H. Chen, "Memristor-based neural network circuit with weighted sum simultaneous perturbation training and its applications," *Neurocomputing*, vol. 462, pp. 581–590, 2021.
- [11] J. Jin, L. Zhao, M. Li, F. Yu, and Z. Xi, "Improved zeroing neural networks for finite time solving nonlinear equations," *Neural Computing and Applications*, vol. 32, no. 9, pp. 4151–4160, 2020.
- [12] J. Jin, J. Zhu, and J. Gong, "Novel activation functions-based ZNN models for fixed-time solving dynamic Sylvester equation," *Neural Computing and Applications*, 2022.
- [13] J. Jin, "A robust zeroing neural network for solving dynamic nonlinear equations and its application to kinematic control of mobile manipulator," *Complex and Intelligent Systems*, vol. 7, no. 1, pp. 87–99, 2021.
- [14] F. Yu, L. Liu, H. Shen et al., "Dynamic analysis, circuit design, and synchronization of a novel 6D memristive four-wing hyperchaotic system with multiple coexisting attractors," *Complexity*, vol. 2020, Article ID 5904607, 2020.
- [15] J. Jin and J. Gong, "An interference-tolerant fast convergence zeroing neural network for dynamic matrix inversion and its application to mobile manipulator path tracking," *Alexandria Engineering Journal*, vol. 60, pp. 659–669, 2020.
- [16] F. Yu, L. Liu, S. Qian et al., "Chaos-based application of a novel multistable 5D memristive hyperchaotic system with coexisting multiple attractors," *Complexity*, vol. 2020, Article ID 8034196, 2020.
- [17] J. Jin and J. Gong, "A noise-tolerant fast convergence ZNN for dynamic matrix inversion," *International Journal of Computer Mathematics*, vol. 98, no. 11, pp. 2202–2219, 2021.
- [18] J. Gong and J. Jin, "A faster and better robustness zeroing neural network for solving dynamic Sylvester equation," *Neural Processing Letters*, vol. 53, no. 5, pp. 3591–3606, 2021.
- [19] Z. Liu, X. H. Zhu, W. Hu, and F. Jiang, "Principles of chaotic signal radar," *International Journal of Bifurcation and Chaos*, vol. 17, no. 5, pp. 1735–1739, 2007.
- [20] G. Chen and X. Yu, *Chaos control: Theory and Applications*, Springer, Germany, 2003.
- [21] U. E. Kocamaz, S. Cicek, and Y. Uyaroglu, "Secure communication with chaos and electronic circuit design using passivity based synchronization," *Journal of Circuits, Systems, and Computers*, vol. 27, no. 04, Article ID 1850057, 2018.

- [22] F. Yu, Z. Zhang, L. Liu et al., "Secure communication scheme based on a new 5D multistable four-wing memristive hyperchaotic system with disturbance inputs," *Complexity*, vol. 2020, Article ID 5859273, 16 pages, 2020.
- [23] H. P. Ren, C. Bai, and Z. Z. Huang, "GrebogiC.: secure communication based on hyperchaotic chen system with time-delay," *International Journal of Bifurcation and Chaos*, vol. 27, no. 5, p. 1750076, 2017.
- [24] R. Martínez-Guerra, J. J. Montesinos García, and S. M. Delfín Prieto, "Secure communications via synchronization of liouvillean chaotic systems," *Journal of the Franklin Institute*, vol. 353, no. 17, pp. 4384–4399, 2016.
- [25] F. Yu, X. Kong, and H. Chen, "A 6D fractional-order memristive hopfield neural network and its application in image encryption," *Frontiers in Physics*, 2022.
- [26] A. Ahmadi, X. Wang, F. Nazarimehr, F. E. Alsaadi, F. E. Alsaadi, and V.-T. Pham, "Coexisting infinitely many attractors in a new chaotic system with a curve of equilibria: its extreme multi-stability and Kolmogorov-Sinai entropy computation," *Advances in Mechanical Engineering*, vol. 11, no. 11, p. 168781401988804, 2019.
- [27] Z. Wei, V. T. Pham, A. Khalaf, K. Jacques, and S. Jafari, "A modified multistable chaotic oscillator," *International Journal of Bifurcation and Chaos*, vol. 28, no. 7, p. 1850085, 2018.
- [28] K. Rajagopal, H. Jahanshahi, M. Varan et al., "A hyperchaotic memristor oscillator with fuzzy based chaos control and LQR based chaos synchronization," *AEU - International Journal of Electronics and Communications*, vol. 94, pp. 55–68, 2018.
- [29] X. Ma, J. Mou, J. Liu, C. Ma, F. Yang, and X. Zhao, "A novel simple chaotic circuit based on memristor-memcapacitor," *Nonlinear Dynamics*, vol. 100, no. 3, pp. 2859–2876, 2020.
- [30] C. Ma, J. Mou, P. Li, and T. Liu, "Dynamic analysis of a new two-dimensional map in three forms: integer-order, fractional-order and improper fractional-order," *European Physical Journal - Special Topics*, vol. 203, no. 7, pp. 1945–1957, 2021.
- [31] C. Ma, J. Mou, L. Xiong, S. Banerjee, T. Liu, and X. Han, "Dynamical analysis of a new chaotic system: asymmetric multistability, offset boosting control and circuit realization," *Nonlinear Dynamics*, vol. 103, no. 3, pp. 2867–2880, 2021.
- [32] F. Yu, Z. Zhang, H. Shen, Y. Huang, S. Cai, and S. Du, "FPGA implementation and image encryption application of a new PRNG based on a memristive Hopfield neural network with a special activation gradient," *Chinese Physics B*, vol. 31, no. 2, Article ID 020505, 2022.
- [33] C. Qin, K. Sun, and S. He, "Characteristic analysis of fractional-order memristor-based hypogenetic jerk system and its DSP implementation," *Electronics*, vol. 10, no. 7, p. 841, 2021.
- [34] F. Yu, L. Liu, H. Shen et al., "Multistability analysis, coexisting multiple attractors and FPGA implementation of Yu-Wang four-wing chaotic system," *Mathematical Problems in Engineering*, vol. 2020, Article ID 7530976, 16 pages, 2020.
- [35] H. Lin, C. Wang, F. Yu et al., "An extremely simple multiwing chaotic system: dynamics analysis, encryption application, and hardware implementation," *IEEE Transactions on Industrial Electronics*, vol. 68, no. 12, pp. 12708–12719, 2021.
- [36] F. Yu, H. Shen, L. Liu et al., "CCII and FPGA realization: a multistable modified four-order autonomous Chua's chaotic system with coexisting multiple attractors," *Complexity*, vol. 2020, Article ID 5212601, 17 pages, 2020.
- [37] T. L. Liao, H. C. Chen, C. Y. Peng, and Y. Y. Hou, "Chaos-based secure communications in biomedical information application," *Electronics*, vol. 10, no. 3, Article ID 359, 2021.
- [38] F. Yu, Z. Zhang, H. Shen et al., "Design and FPGA implementation of a pseudo-random number generator based on a Hopfield neural network under electromagnetic radiation," *Frontiers in Physics*, vol. 9, Article ID 690651, 2021.
- [39] F. Yu, H. Shen, Z. Zhang, Y. Huang, S. Cai, and S. Du, "Dynamics analysis, hardware implementation and engineering applications of novel multi-style attractors in a neural network under electromagnetic radiation," *Chaos, Solitons and Fractals*, vol. 152, Article ID 111350, 2021.
- [40] F. Yu, L. Li, B. He et al., "Pseudorandom number generator based on a 5D hyperchaotic four-wing memristive system and its FPGA implementation," *European Physical Journal - Special Topics*, vol. 230, no. 7-8, pp. 1763–1772, 2021.
- [41] F. Yu, H. Shen, Z. Zhang, Y. Huang, S. Cai, and S. Du, "A new multi-scroll Chua's circuit with composite hyperbolic tangent-cubic nonlinearity: complex dynamics, Hardware implementation and Image encryption application," *Integration*, vol. 81, pp. 71–83, 2021.
- [42] X. Chen, S. Qian, F. Yu et al., "Pseudorandom number generator based on three kinds of four-wing memristive hyperchaotic system and its application in image encryption," *Complexity*, vol. 2020, Article ID 8274685, 2020.
- [43] M. Delgado-Restituto, A. Rodríguez-vázquez, R. Lopez-Ahumada, and M. Liñan, "Chaotic synchronization using monolithic Chua oscillators," *International Journal of Electronics*, vol. 79, no. 6, pp. 775–785, 1995.
- [44] C. K. Pham, M. Korehisa, and M. Tanaka, "Chaotic behavior and synchronization phenomena in a novel chaotic transistors circuit," *IEEE Transactions on Circuits and Systems I: Fundamental Theory and Applications*, vol. 43, no. 12, pp. 1006–1011, 1996.
- [45] R. Trejo-Guerra, E. Tlelo-Cuautle, J. M. Jiménez-Fuentes et al., "Integrated circuit generating 3- and 5-scroll attractors," *Communications in Nonlinear Science and Numerical Simulation*, vol. 17, no. 11, pp. 4328–4335, 2012.
- [46] G. Chen and T. Ueta, "Yet another chaotic attractor," *International Journal of Bifurcation and Chaos*, vol. 9, no. 7, pp. 1465–1466, 1999.
- [47] T. Ueta and G. Chen, "Bifurcation analysis of Chen's equation," *International Journal of Bifurcation and Chaos*, vol. 10, no. 08, pp. 1917–1931, 2000.
- [48] T. S. Zhou, G. Chen, and Y. Tang, "Complex dynamical behaviors of the chaotic Chen's system," *International Journal of Bifurcation and Chaos*, vol. 13, no. 9, pp. 2561–2574, 2003.
- [49] F. Yu, S. Qian, X. Chen et al., "A new 4D four-wing memristive hyperchaotic system: dynamical analysis, electronic circuit design, shape synchronization and secure communication," *International Journal of Bifurcation and Chaos*, vol. 30, no. 10, Article ID 2050147, 2020.
- [50] G. Q. Zhong and W. K. S. Tang, "Circuitry implementation and synchronization of Chen's attractor," *International Journal of Bifurcation and Chaos*, vol. 12, no. 06, pp. 1423–1427, 2002.
- [51] J. Jin, "Programmable multi-direction fully integrated chaotic oscillator," *Microelectronics Journal*, vol. 75, no. c, pp. 27–34, 2018.
- [52] J. Jie and C. Li, "Fully integrated memristor and its application on the scroll-controllable hyperchaotic system," *Complexity*, vol. 2019, Article ID 4106398, 8 pages, 2019.
- [53] J. Jin, "Resonant amplifier-based sub-harmonic mixer for zero-IF transceiver applications, Integration," *The VLSI Journal*, vol. 57, no. c, pp. 69–73, 2017.
- [54] <https://www.ti.com/product/LF347>.
- [55] <https://www.analog.com/en/products/ad633.html#product-overview>.



## Research Article

# On the Limit Cycles for a Class of Perturbed Fifth-Order Autonomous Differential Equations

Nabil Sellami,<sup>1</sup> Romaiassa Mellal,<sup>1</sup> Bahri Belkacem Cherif <sup>2,3</sup> and Sahar Ahmed Idris <sup>4,5</sup>

<sup>1</sup>Department of Mathematics, University of Guelma, BO 401, Guelma 24000, Algeria

<sup>2</sup>Department of Mathematics, College of Sciences and Arts in Arrass, Qassim University, Buraydah, Saudi Arabia

<sup>3</sup>Preparatory Institute for Engineering Studies in Sfax, Sfax, Tunisia

<sup>4</sup>College of Industrial Engineering, King Khalid University, Abha, Saudi Arabia

<sup>5</sup>Department of Mathematics, College of Sciences, Juba University, Juba, Sudan

Correspondence should be addressed to Sahar Ahmed Idris; sa6044690@gmail.com

Received 12 September 2021; Accepted 23 November 2021; Published 7 December 2021

Academic Editor: Sundarapandian Vaidyanathan

Copyright © 2021 Nabil Sellami et al. This is an open access article distributed under the Creative Commons Attribution License, which permits unrestricted use, distribution, and reproduction in any medium, provided the original work is properly cited.

We study the limit cycles of the fifth-order differential equation  $\overset{v}{x} - \overset{v}{e}x - d\overset{v}{x} - c\overset{v}{x} - b\overset{v}{x} - ax = \varepsilon F(x, \overset{v}{x}, \overset{v}{x}, \overset{v}{x}, \overset{v}{x})$  with  $a = \lambda\mu\delta$ ,  $b = -(\lambda\mu + \lambda\delta + \mu\delta)$ ,  $c = \lambda + \mu + \delta + \lambda\mu\delta$ ,  $d = -(1 + \lambda\mu + \lambda\delta + \mu\delta)$ ,  $e = \lambda + \mu + \delta$ , where  $\varepsilon$  is a small enough real parameter,  $\lambda$ ,  $\mu$ , and  $\delta$  are real parameters, and  $F \in C^2$  is a nonlinear function. Using the averaging theory of first order, we provide sufficient conditions for the existence of limit cycles of this equation.

## 1. Introduction and Statement of the Main Results

The study of the limit cycles is one of the main topics of the qualitative theory of differential equations and dynamical systems. A limit cycle of a differential equation is an isolated periodic orbit of this equation; it means that there is no periodic orbits in the vicinity of this limit cycle. There are several theories and methods for the study of the existence, uniqueness, or number and stability of limit cycles of differential equations which have been developed in trying to answer Hilbert's sixteenth problem posed in 1900 [1] about the maximum number of limit cycles that a planar polynomial differential system can have.

The averaging theory is one of the most important tools used actually to the study of limit cycles for second and higher order differential equations, you can see in [2–8]. More details on the averaging theory can be found in the books of Sanders and Verhulst [9] and of Verhulst [9].

In [7], the authors studied the limit cycles of the following third-order differential equation

$$\overset{v}{x} - \mu x + \overset{v}{x} - \mu x = \varepsilon F(x, \overset{v}{x}, x, t), \quad (1)$$

with  $\mu \neq 0$ ;  $\varepsilon$  is a small real parameter;  $F \in C^2$  is  $2\pi$ -periodic in  $t$ .

In [5], the authors studied equation (1) with  $F = F(x, \overset{v}{x}, \overset{v}{x})$  which is autonomous. They studied the two cases  $\mu \neq 0$  and  $\mu = 0$ .

In [6], the authors studied the following fourth-order differential equation:

$$\overset{v}{x} - (\lambda + \mu)\overset{v}{x} + (1 + \lambda\mu)x - (\lambda + \mu)\overset{v}{x} + \lambda\mu x = \varepsilon F(x, \overset{v}{x}, x, \overset{v}{x}, t), \quad (2)$$

where  $\lambda$  and  $\mu$  are real,  $\varepsilon$  is a small real parameter, and  $F \in C^2$  is  $2\pi$ -periodic in  $t$ .

In [4], the authors studied equation (2) with  $F = F(x, \overset{v}{x}, \overset{v}{x}, \overset{v}{x})$  which is autonomous.

In this paper, we shall use a result of the averaging theory to study the limit cycles of the following class of fifth-order autonomous ordinary differential equations:

$$\overset{v}{x} - \overset{v}{e}x - d\overset{v}{x} - cx - b\overset{v}{x} - ax = \varepsilon F(x, \overset{v}{x}, \overset{v}{x}, \overset{v}{x}, \overset{v}{x}), \quad (3)$$



where

$$\begin{aligned} a &= \lambda\mu\delta, b = -(\lambda\mu + \lambda\delta + \mu\delta), c = \lambda + \mu + \delta + \lambda\mu\delta, \\ d &= -(1 + \lambda\mu + \lambda\delta + \mu\delta), e = \lambda + \mu + \delta, \end{aligned} \quad (4)$$

where the dot means derivative with respect to an independent variable  $t$ ,  $\varepsilon$  is a small enough parameter, and  $F \in C^2$  is a nonlinear function. Here, the variable  $x$  and the parameters  $\lambda, \mu, \delta$  and  $\varepsilon$  are real.

In [8], the authors studied equation (3) with  $F = F(x, \dot{x}, \ddot{x}, x, t)$  which depends explicitly on the independent variable  $t$ . Here, we study the autonomous case using a different approach. Note that our results are distinct and new.

Now, we state our main results for the limit cycles of equation (3).

For the different values of the parameters  $\lambda, \mu$ , and  $\delta$ , we distinguish the five following cases.

Case 1.  $\lambda\mu\delta \neq 0$  and  $\lambda \neq \mu \neq \delta$ .

Case 2.  $\lambda = 0, \mu\delta \neq 0$ , and  $\mu \neq \delta$ .

Case 3.  $\lambda = 0$  and  $\mu = \delta \neq 0$ .

Case 4.  $\lambda \neq 0$  and  $\mu = \delta \neq 0$ .

Case 5.  $\lambda = \mu = \delta \neq 0$ .

For each one of these cases, we will give a theorem which provides sufficient conditions for the existence of limit cycles of equation (3) and we provide also an application.

There are two other cases ( $\lambda = \mu = 0$  and  $\delta \neq 0$ ) and ( $\lambda = \mu = \delta = 0$ ) that we cannot study because they are too much degenerated for Theorem 6.

when  $\varepsilon \rightarrow 0$ .

Theorem 1 will be proved in Section 3.1.1.

An application of Theorem 1 is the following.

**Corollary 1.** Assume that  $\lambda\mu\delta \neq 0$ ,  $\lambda \neq \mu \neq \delta$ ,  $\lambda\mu + \lambda\delta + \mu\delta \neq 1$ , and

$$F(x, \dot{x}, \ddot{x}, \dot{x}, x) = x^5 - x^4 - \dot{x}^3 - \dot{x}^2 - x - 1. \quad (9)$$

1.1. Case 1:  $\lambda\mu\delta \neq 0$  and  $\lambda \neq \mu \neq \delta$ . In order to state our results for this case, we define the function

$$\mathcal{F}(r_0) = \frac{1}{2\pi} \int_0^{2\pi} \sin \theta F(A_1, A_2, A_3, A_4, A_5) d\theta, \quad (5)$$

where

$$\begin{aligned} A_1 &= \frac{((\lambda\mu\delta - \lambda - \mu - \delta)\cos \theta + (1 - \lambda\mu - \lambda\delta - \mu\delta)\sin \theta)r_0}{(1 + \lambda^2)(1 + \mu^2)(1 + \delta^2)}, \\ A_2 &= \frac{((1 - \lambda\mu - \lambda\delta - \mu\delta)\cos \theta + (\lambda + \mu + \delta - \lambda\mu\delta)\sin \theta)r_0}{(1 + \lambda^2)(1 + \mu^2)(1 + \delta^2)}, \\ A_3 &= \frac{((\lambda + \mu + \delta - \lambda\mu\delta)\cos \theta + (\lambda\mu + \lambda\delta + \mu\delta - 1)\sin \theta)r_0}{(1 + \lambda^2)(1 + \mu^2)(1 + \delta^2)}, \\ A_4 &= \frac{((\lambda\mu + \lambda\delta + \mu\delta - 1)\cos \theta + (\lambda\mu\delta - \lambda - \mu - \delta)\sin \theta)r_0}{(1 + \lambda^2)(1 + \mu^2)(1 + \delta^2)}, \\ A_5 &= \frac{((\lambda\mu\delta - \lambda - \mu - \delta)\cos \theta + (1 - \lambda\mu - \lambda\delta - \mu\delta)\sin \theta)r_0}{(1 + \lambda^2)(1 + \mu^2)(1 + \delta^2)}. \end{aligned} \quad (6)$$

Our main result for this case is the following theorem.

**Theorem 1.** Assume that  $\lambda\mu\delta \neq 0$  and  $\lambda \neq \mu \neq \delta$ . For every positive simple zero  $r_0^*$  of the function  $\mathcal{F}(r_0)$  given by (5) there is a limit cycle  $x(t, \varepsilon)$  of equation (3) tending to the periodic solution

$$x^*(t) = \frac{((\lambda\mu\delta - \lambda - \mu - \delta)\cos t + (1 - \lambda\mu - \lambda\delta - \mu\delta)\sin t)r_0^*}{(1 + \lambda^2)(1 + \mu^2)(1 + \delta^2)}, \quad (7)$$

of

$$\ddot{x} - (\lambda + \mu + \delta)\dot{x} + (1 + \lambda\mu + \lambda\delta + \mu\delta)\dot{x} - (\lambda + \mu + \delta + \lambda\mu\delta)x + (\lambda\mu + \lambda\delta + \mu\delta)\dot{x} - \lambda\mu\delta x = 0, \quad (8)$$

Then, there is a limit cycle  $x_1(t, \varepsilon)$  of equation (3) tending to the periodic solution

$$x_1^*(t) = \frac{2((\lambda\mu\delta - \lambda - \mu - \delta)\cos t + (1 - \lambda\mu - \lambda\delta - \mu\delta)\sin t)}{\sqrt{5(1 + \lambda^2)(1 + \mu^2)(1 + \delta^2)}}, \quad (10)$$

of equation (8) when  $\varepsilon \rightarrow 0$ .

Corollary 1 will be proved in Section 3.1.2.

1.2. Case 2:  $\lambda = 0, \mu \delta \neq 0$ , and  $\mu \neq \delta$ . We define the functions

$$\begin{aligned} \mathcal{F}_1(r_0, Z_0) &= \frac{1}{2\pi_0} \int_0^{2\pi} \sin \theta F(B_1, B_2, B_3, B_4, B_5) d\theta, \\ \mathcal{F}_2(r_0, Z_0) &= \frac{1}{2\pi_0} \int_0^{2\pi} F(B_1, B_2, B_3, B_4, B_5) d\theta, \end{aligned} \tag{11}$$

and

$$\begin{aligned} B_1 &= \frac{((-\mu - \delta)\cos \theta + (1 - \mu\delta)\sin \theta)r_0}{(1 + \mu^2)(1 + \delta^2)} + \frac{Z_0}{\mu\delta}, \\ B_2 &= \frac{((1 - \mu\delta)\cos \theta + (\mu + \delta)\sin \theta)r_0}{(1 + \mu^2)(1 + \delta^2)}, \\ B_3 &= \frac{((\mu + \delta)\cos \theta + (\mu\delta - 1)\sin \theta)r_0}{(1 + \mu^2)(1 + \delta^2)}, \\ B_4 &= \frac{((\mu\delta - 1)\cos \theta - (\mu + \delta)\sin \theta)r_0}{(1 + \mu^2)(1 + \delta^2)}, \\ B_5 &= \frac{(-(\mu + \delta)\cos \theta + (1 - \mu\delta)\sin \theta)r_0}{(1 + \mu^2)(1 + \delta^2)}. \end{aligned} \tag{12}$$

Our main result for this case is the following theorem.

**Theorem 2.** Assume that  $\lambda = 0, \mu\delta \neq 0$ , and  $\mu \neq \delta$ . For every zero  $(r_0^*, Z_0^*)$  of the system  $\mathcal{F}_1(r_0, Z_0) = \mathcal{F}_2(r_0, Z_0) = 0$  where  $\mathcal{F}_1$  and  $\mathcal{F}_2$  are given by (11) such that

$$\det\left(\frac{\partial(\mathcal{F}_1, \mathcal{F}_2)}{\partial(r_0, Z_0)}\right)\Big|_{(r_0, Z_0)=(r_0^*, Z_0^*)} \neq 0, \tag{13}$$

there is a limit cycle  $x(t, \varepsilon)$  of equation (3) tending to the periodic solution

$$x^*(t) = \frac{((-\mu - \delta)\cos t + (1 - \mu\delta)\sin t)r_0^*}{(1 + \mu^2)(1 + \delta^2)} + \frac{Z_0^*}{\mu\delta}, \tag{14}$$

of

$$\overset{\dots}{x} - (\mu + \delta)\overset{\dots}{x} + (1 + \mu\delta)\overset{\dot{}}{x} - (\mu + \delta)\overset{\ddot{}}{x} + \mu\delta\overset{\dot{}}{x} = 0, \tag{15}$$

when  $\varepsilon \rightarrow 0$ .

Theorem 2 will be proved in Section 3.2.1.

An application of Theorem 2 is the following.

**Corollary 2.** Assume that  $\lambda = 0, \mu\delta \neq 0, \mu \neq \delta, \mu\delta \neq 1$ , and  $F(x, \dot{x}, \ddot{x}, \overset{\dot{}}{x}, x) = x^2 - 2x + \dot{x}^2$ , then there is a limit cycle  $x_2(t, \varepsilon)$  of equation (3) tending to the periodic solution

$$x_2^*(t) = \frac{((-\mu - \delta)\cos t + (1 - \mu\delta)\sin t)}{\sqrt{(1 + \mu^2)(1 + \delta^2)}} + 1, \tag{16}$$

of equation (15) when  $\varepsilon \rightarrow 0$ .

Corollary 2 will be proved in Section 3.

1.3. Case 3:  $\lambda = 0$  and  $\mu = \delta \neq 0$ . We define the functions

$$\begin{aligned} \mathcal{F}_1(r_0, Z_0) &= \frac{1}{2\pi_0} \int_0^{2\pi} -\sin \theta F(C_1, C_2, C_3, C_4, C_5) d\theta, \\ \mathcal{F}_2(r_0, Z_0) &= \frac{1}{2\pi_0} \int_0^{2\pi} F(C_1, C_2, C_3, C_4, C_5) d\theta, \end{aligned} \tag{17}$$

where

$$\begin{aligned} C_1 &= \frac{(2\mu \cos \theta + (\mu^2 - 1)\sin \theta)r_0}{(1 + \mu^2)^2} + \frac{Z_0}{\mu^2}, \\ C_2 &= \frac{((\mu^2 - 1)\cos \theta - 2\mu \sin \theta)r_0}{(1 + \mu^2)^2}, \\ C_3 &= \frac{(-2\mu \cos \theta - (\mu^2 - 1)\sin \theta)r_0}{(1 + \mu^2)^2}, \\ C_4 &= \frac{(-(\mu^2 - 1)\cos \theta + 2\mu \sin \theta)r_0}{(1 + \mu^2)^2}, \\ C_5 &= \frac{(2\mu \cos \theta + (\mu^2 - 1)\sin \theta)r_0}{(1 + \mu^2)^2}. \end{aligned} \tag{18}$$

Our main result for this case is the following theorem.

**Theorem 3.** Assume that  $\lambda = 0$  and  $\mu = \delta \neq 0$ . For every zero  $(r_0^*, Z_0^*)$  of the system  $\mathcal{F}_1(r_0, Z_0) = \mathcal{F}_2(r_0, Z_0) = 0$  where  $\mathcal{F}_1$  and  $\mathcal{F}_2$  are given by (17) such that

$$\det\left(\frac{\partial(\mathcal{F}_1, \mathcal{F}_2)}{\partial(r_0, Z_0)}\right)\Big|_{(r_0, Z_0)=(r_0^*, Z_0^*)} \neq 0, \tag{19}$$

there is a limit cycle  $x(t, \varepsilon)$  of equation (3) tending to the periodic solution

$$x^*(t) = \frac{(2\mu \cos t + (\mu^2 - 1)\sin t)r_0^*}{(1 + \mu^2)^2} + \frac{Z_0^*}{\mu^2}, \tag{20}$$

of

$$\overset{\dots}{x} - 2\mu\overset{\dots}{x} + (1 + \mu^2)\overset{\dot{}}{x} - 2\mu\overset{\ddot{}}{x} + \mu^2\overset{\dot{}}{x} = 0, \tag{21}$$

when  $\varepsilon \rightarrow 0$ .

Theorem 3 will be proved in Section 3.3.1.

An application of Theorem 3 is the following.

**Corollary 3.** Assume that  $\lambda = 0, \delta = \mu \neq 0, \mu \neq -1 \pm \sqrt{5}/2$ , and  $F(x, \dot{x}, \ddot{x}, \overset{\dot{}}{x}, x) = x^2 - x\dot{x} - 1$ , then there is a limit cycle  $x_3(t, \varepsilon)$  of equation (3) tending to the periodic solution

$$x_3^*(t) = \frac{(2\mu \cos t + (\mu^2 - 1)\sin t)\sqrt{2}}{1 + \mu^2}, \tag{22}$$

of equation (21) when  $\varepsilon \rightarrow 0$ .

Corollary 3 will be proved in Section 3.3.2.

1.4. Case 4:  $\lambda \neq 0$  and  $\mu = \delta \neq 0$ . We define the function

$$\mathcal{F}(r_0) = \frac{1}{2\pi} \int_0^{2\pi} -\sin \theta F(D_1, D_2, D_3, D_4, D_5) d\theta, \quad (23)$$

where

$$\begin{aligned} D_1 &= \frac{((\lambda + 2\mu - \lambda\mu^2)\cos \theta + (\mu^2 + 2\lambda\mu - 1)\sin \theta)r_0}{(1 + \lambda^2)(1 + \mu^2)^2}, \\ D_2 &= \frac{((\mu^2 + 2\lambda\mu - 1)\cos \theta - (\lambda + 2\mu - \lambda\mu^2)\sin \theta)r_0}{(1 + \lambda^2)(1 + \mu^2)^2}, \\ D_3 &= \frac{(-(\lambda + 2\mu - \lambda\mu^2)\cos \theta - (\mu^2 + 2\lambda\mu - 1)\sin \theta)r_0}{(1 + \lambda^2)(1 + \mu^2)^2}, \\ D_4 &= \frac{(-(\mu^2 + 2\lambda\mu - 1)\cos \theta + (\lambda + 2\mu - \lambda\mu^2)\sin \theta)r_0}{(1 + \lambda^2)(1 + \mu^2)^2}, \\ D_5 &= \frac{((\lambda + 2\mu - \lambda\mu^2)\cos \theta + (\mu^2 + 2\lambda\mu - 1)\sin \theta)r_0}{(1 + \lambda^2)(1 + \mu^2)^2}. \end{aligned} \quad (24)$$

Our main result for this case is the following theorem.

**Theorem 4.** Assume that  $\lambda \neq 0$  and  $\delta = \mu \neq 0$ . For every positive simple zero  $r_0^*$  of the function  $\mathcal{F}(r_0)$  given by (23), there is a limit cycle  $x(t, \varepsilon)$  of equation (3) tending to the periodic solution

$$x^*(t) = \frac{((\lambda + 2\mu - \lambda\mu^2)\cos t + (\mu^2 + 2\lambda\mu - 1)\sin t)r_0^*}{(1 + \lambda^2)(1 + \mu^2)^2}, \quad (25)$$

of

$$\begin{aligned} \ddot{x} - (\lambda + 2\mu)x + (1 + 2\lambda\mu + \mu^2)x - (\lambda + 2\mu + \lambda\mu^2)x \\ + (2\lambda\mu + \mu^2)\dot{x} - \lambda\mu^2x = 0, \end{aligned} \quad (26)$$

when  $\varepsilon \rightarrow 0$ .

Theorem 4 will be proved in Section 3.4.1.

An application of Theorem 4 is the following.

**Corollary 4.** Assume that  $\lambda \neq 0$ ,  $\delta = \mu \neq 0$ ,  $\mu^2 + 2\lambda\mu - 1 \neq 0$ , and  $F(x, \dot{x}, \ddot{x}, \dot{x}, x) = x^3 - x - 1$ , then there is a limit cycle  $x_4(t, \varepsilon)$  of equation (3) tending to the periodic solution

$$x_4^*(t) = \frac{2\sqrt{3}((\lambda + 2\mu - \lambda\mu^2)\cos t + (\mu^2 + 2\lambda\mu - 1)\sin t)}{3\sqrt{1 + \lambda^2}(1 + \mu^2)}, \quad (27)$$

of equation (26) when  $\varepsilon \rightarrow 0$ .

Corollary 4 will be proved in Section 3.4.2.

1.5. Case 5:  $\lambda = \mu = \delta \neq 0$ . In order to state our result for this case, we define the function

$$\mathcal{F}(r_0) = \frac{1}{2\pi} \int_0^{2\pi} \sin \theta F(E_1, E_2, E_3, E_4, E_5) d\theta, \quad (28)$$

where

$$\begin{aligned} E_1 &= \frac{((\lambda^3 - 3\lambda)\cos \theta + (1 - 3\lambda^2)\sin \theta)r_0}{(1 + \lambda^2)^3}, \\ E_2 &= \frac{((1 - 3\lambda^2)\cos \theta - (\lambda^3 - 3\lambda)\sin \theta)r_0}{(1 + \lambda^2)^3}, \\ E_3 &= \frac{(-(\lambda^3 - 3\lambda)\cos \theta - (1 - 3\lambda^2)\sin \theta)r_0}{(1 + \lambda^2)^3}, \\ E_4 &= \frac{(-(1 - 3\lambda^2)\cos \theta + (\lambda^3 - 3\lambda)\sin \theta)r_0}{(1 + \lambda^2)^3}, \\ E_5 &= \frac{((\lambda^3 - 3\lambda)\cos \theta + (1 - 3\lambda^2)\sin \theta)r_0}{(1 + \lambda^2)^3}. \end{aligned} \quad (29)$$

Our main result for this case is the following theorem.

**Theorem 5.** Assume that  $\mu = \delta = \lambda \neq 0$ . For every positive simple zero  $r_0^*$  of the function  $\mathcal{F}(r_0)$  given by (28), there is a limit cycle  $x(t, \varepsilon)$  of equation (3) tending to the periodic solution

$$x^*(t) = \frac{((\lambda^3 - 3\lambda)\cos t + (1 - 3\lambda^2)\sin t)r_0^*}{(1 + \lambda^2)^3}, \quad (30)$$

of

$$\ddot{x} - 3\lambda x + (1 + 3\lambda^2)x - (3\lambda + \lambda^3)\ddot{x} + 3\lambda^2\dot{x} - \lambda^3x = 0, \quad (31)$$

when  $\varepsilon \rightarrow 0$ .

Theorem 5 will be proved in Section 3.5.1.

An application of Theorem 5 is the following.

**Corollary 5.** Assume that  $\mu = \delta = \lambda \neq 0$ ,  $\lambda \neq \pm\sqrt{3}$ ,  $\lambda \neq \pm\sqrt{3}/3$ , and  $F(x, \dot{x}, \ddot{x}, \dot{x}, x) = -\ddot{x}^2x + x^3 + x^2 - \dot{x}\ddot{x} + \dot{x} - 1$ , then there is a limit cycle  $x_5(t, \varepsilon)$  of equation (3) tending to the periodic solution

$$x_5^*(t) = \frac{2\sqrt{3}\sqrt{(3\lambda^2 - 1)\lambda(\lambda^4 - 2\lambda^2 - 3)}((\lambda^3 - 3\lambda)\cos t + (1 - 3\lambda^2)\sin t)}{3(3\lambda^2 - 1)(1 + \lambda^2)^2}, \tag{32}$$

of equation (31) when  $\varepsilon \rightarrow 0$ .

Corollary 5 will be proved in Section 3.5.2.

## 2. The Main Tool (First-Order Averaging Theory)

In this section, we present the basic result from the averaging theory that we need for proving the main results of this article.

We consider the problem of the bifurcation of  $T$ -periodic solutions from the differential system

$$\dot{x}(t) = F_0(x, t) + \varepsilon F_1(x, t) + \varepsilon^2 F_2(x, t, \varepsilon), \tag{33}$$

with  $\varepsilon = 0$  to  $\varepsilon \neq 0$  sufficiently small. The functions  $F_0, F_1: \Omega \times \mathbb{R} \rightarrow \mathbb{R}^n$  and  $F_2: \Omega \times \mathbb{R} \times (-\varepsilon_0, \varepsilon_0) \rightarrow \mathbb{R}^n$  are  $\mathcal{C}^2$  functions,  $T$ -periodic in the variable  $t$ , and  $\Omega$  is an open subset of  $\mathbb{R}^n$ . We suppose that the unperturbed system

$$\dot{x}(t) = F_0(x, t), \tag{34}$$

has a  $k$ -dimensional submanifold  $\mathcal{Z}$  of periodic solutions.

Let  $\mathbf{x}(t, \mathbf{z})$  be the solution of the unperturbed system (34) such that  $\mathbf{x}(0, \mathbf{z}) = \mathbf{z}$ . The linearisation of system (34) along the periodic solution  $\mathbf{x}(t, \mathbf{z})$  is written as

$$\dot{y} = D_x F_0(\mathbf{x}(t, \mathbf{z}), t)y. \tag{35}$$

We denote by  $M_z(t)$  some fundamental matrices of the linear differential system (35) and by  $\xi: \mathbb{R}^k \times \mathbb{R}^{n-k} \rightarrow \mathbb{R}^k$  the projection of  $\mathbb{R}^n$  onto its first  $k$  coordinates; i.e.,  $\xi(x_1, \dots, x_n) = (x_1, \dots, x_k)$ .

**Theorem 6.** Let  $\mathbb{V} \subset \mathbb{R}^k$  be open and bounded and  $\beta_0: Cl(\mathbb{V}) \rightarrow \mathbb{R}^{n-k}$  be a  $\mathcal{C}^2$  function. We assume that

- (i)  $\mathcal{Z} = \{\mathbf{z}_\alpha = (\alpha, \beta_0(\alpha)), \alpha \in Cl(\mathbb{V})\} \subset \Omega$ , and that for each  $\mathbf{z}_\alpha \in \mathcal{Z}$ , the solution  $x(t, \mathbf{z}_\alpha)$  of (34) is  $T$ -periodic.

- (ii) For each  $\mathbf{z}_\alpha \in \mathcal{Z}$ , there is a fundamental matrix  $M_{\mathbf{z}_\alpha}(t)$  of (35) such that the matrix  $M_{\mathbf{z}_\alpha}^{-1}(0) - M_{\mathbf{z}_\alpha}^{-1}(T)$  has in the upper right corner the  $k \times (n - k)$  zero matrix, and in the lower right corner a matrix  $\Delta_\alpha((n - k) \times (n - k))$  with  $\det \Delta_\alpha \neq 0$ . We consider the function  $\mathcal{F}: Cl(\mathbb{V}) \rightarrow \mathbb{R}^k$

$$\mathcal{F}(\alpha) = \xi \left( \frac{1}{T} \int_0^T M_{\mathbf{z}_\alpha}^{-1}(t) F_1(\mathbf{x}(t, \mathbf{z}_\alpha), t) dt \right). \tag{36}$$

If there exists  $a \in \mathbb{V}$  with  $\mathcal{F}(a) = 0$  and  $\det((d\mathcal{F}/d\alpha)(a)) \neq 0$ , then there is a  $T$ -periodic solution  $\varphi(t, \varepsilon)$  of the system (33) such that  $\varphi(0, \varepsilon) \rightarrow z_a$  as  $\varepsilon \rightarrow 0$ .

Theorem 1 goes back to [10] and [11]; for a shorter proof, see [12].

Note that the periodic orbits provided by Theorem 6 are limit cycles.

## 3. Proofs of the Results

### 3.1. Proofs of the Results in Case 1: $\lambda \mu \delta \neq 0$ and $\lambda \neq \mu \neq \delta$

3.1.1. Proof of Theorem 1. We consider equation (3) and put  $y = \dot{x}$ ,  $z = \dot{x}$ ,  $u = \dot{x}$ , and  $v = x$ , then equation (3) can be written as

$$\begin{cases} \dot{x} = y, \\ \dot{y} = z, \\ \dot{z} = u, \\ \dot{u} = v, \\ \dot{v} = ax + by + cz + du + ev + \varepsilon F(x, y, z, u, v). \end{cases} \tag{37}$$

System (37) with  $\varepsilon = 0$  has a unique singular point at the origin and the linear part of this system has the eigenvalues  $\pm i$ ,  $\lambda$ ,  $\mu$ , and  $\delta$ . Using the change of variables

$$\begin{pmatrix} X \\ Y \\ Z \\ U \\ V \end{pmatrix} = \begin{pmatrix} \lambda\mu\delta & -\lambda\mu - \lambda\delta - \mu\delta & \lambda + \mu + \delta & -1 & 0 \\ 0 & -\lambda\mu\delta & \lambda\mu + \lambda\delta + \mu\delta & -\lambda - \mu - \delta & 1 \\ \mu\delta & -\mu - \delta & 1 + \mu\delta & -\mu - \delta & 1 \\ \lambda\delta & -\lambda - \delta & 1 + \lambda\delta & -\lambda - \delta & 1 \\ \lambda\mu & -\lambda - \mu & 1 + \lambda\mu & -\lambda - \mu & 1 \end{pmatrix} \begin{pmatrix} x \\ y \\ z \\ u \\ v \end{pmatrix}, \tag{38}$$

we transform system (37) into the following system:

$$\begin{cases} \dot{X} = -Y, \\ \dot{Y} = X + \varepsilon \tilde{F}(X, Y, Z, U, V), \\ \dot{Z} = \lambda Z + \varepsilon \tilde{F}(X, Y, Z, U, V), \\ \dot{U} = \mu U + \varepsilon \tilde{F}(X, Y, Z, U, V), \\ \dot{V} = \delta V + \varepsilon \tilde{F}(X, Y, Z, U, V), \end{cases} \quad (39)$$

where

$$\tilde{F} = \tilde{F}(X, Y, Z, U, V) = F(a_1, a_2, a_3, a_4, a_5),$$

$$\begin{aligned} a_1 &= \frac{(\lambda\mu\delta - \lambda - \mu - \delta)X}{(\lambda^2 + 1)(\mu^2 + 1)(\delta^2 + 1)} + \frac{(1 - \lambda\mu - \lambda\delta - \mu\delta)Y}{(\lambda^2 + 1)(\mu^2 + 1)(\delta^2 + 1)} + \frac{Z}{(\lambda^2 + 1)(\lambda - \mu)(\lambda - \delta)} - \frac{U}{(\mu^2 + 1)(\lambda - \mu)(\mu - \delta)} + \frac{V}{(\delta^2 + 1)(\lambda - \delta)(\mu - \delta)}, \\ a_2 &= \frac{(1 - \lambda\mu - \lambda\delta - \mu\delta)X}{(\lambda^2 + 1)(\mu^2 + 1)(\delta^2 + 1)} - \frac{(\lambda\mu\delta - \lambda - \mu - \delta)Y}{(\lambda^2 + 1)(\mu^2 + 1)(\delta^2 + 1)} + \frac{\lambda Z}{(\lambda^2 + 1)(\lambda - \mu)(\lambda - \delta)} - \frac{\mu U}{(\mu^2 + 1)(\lambda - \mu)(\mu - \delta)} + \frac{\delta V}{(\delta^2 + 1)(\lambda - \delta)(\mu - \delta)}, \\ a_3 &= -\frac{(\lambda\mu\delta - \lambda - \mu - \delta)X}{(\lambda^2 + 1)(\mu^2 + 1)(\delta^2 + 1)} - \frac{(1 - \lambda\mu - \lambda\delta - \mu\delta)Y}{(\lambda^2 + 1)(\mu^2 + 1)(\delta^2 + 1)} + \frac{\lambda^2 Z}{(\lambda^2 + 1)(\lambda - \mu)(\lambda - \delta)} - \frac{\mu^2 U}{(\mu^2 + 1)(\lambda - \mu)(\mu - \delta)} + \frac{\delta^2 V}{(\delta^2 + 1)(\lambda - \delta)(\mu - \delta)}, \\ a_4 &= -\frac{(1 - \lambda\mu - \lambda\delta - \mu\delta)X}{(\lambda^2 + 1)(\mu^2 + 1)(\delta^2 + 1)} + \frac{(\lambda\mu\delta - \lambda - \mu - \delta)Y}{(\lambda^2 + 1)(\mu^2 + 1)(\delta^2 + 1)} + \frac{\lambda^3 Z}{(\lambda^2 + 1)(\lambda - \mu)(\lambda - \delta)} - \frac{\mu^3 U}{(\mu^2 + 1)(\lambda - \mu)(\mu - \delta)} + \frac{\delta^3 V}{(\delta^2 + 1)(\lambda - \delta)(\mu - \delta)}, \\ a_5 &= \frac{(\lambda\mu\delta - \lambda - \mu - \delta)X}{(\lambda^2 + 1)(\mu^2 + 1)(\delta^2 + 1)} + \frac{(1 - \lambda\mu - \lambda\delta - \mu\delta)Y}{(\lambda^2 + 1)(\mu^2 + 1)(\delta^2 + 1)} + \frac{\lambda^4 Z}{(\lambda^2 + 1)(\lambda - \mu)(\lambda - \delta)} - \frac{\mu^4 U}{(\mu^2 + 1)(\lambda - \mu)(\mu - \delta)} + \frac{\delta^4 V}{(\delta^2 + 1)(\lambda - \delta)(\mu - \delta)}. \end{aligned} \quad (40)$$

Note that the linear part of system (39) is in the real normal Jordan form of the linear part of system (37). We pass now from the Cartesian coordinates  $(X, Y, Z, U, V)$  to the cylindrical ones  $(r, \theta, Z, U, V)$  with  $X = r \cos \theta$ ,  $Y = r \sin \theta$ , and we obtain

$$\begin{cases} \dot{r} = \varepsilon \sin \theta G(r, \theta, Z, U, V), \\ \dot{\theta} = 1 + \frac{\varepsilon}{r} \cos \theta G(r, \theta, Z, U, V), \\ \dot{Z} = \lambda Z + \varepsilon G(r, \theta, Z, U, V), \\ \dot{U} = \mu U + \varepsilon G(r, \theta, Z, U, V), \\ \dot{V} = \delta V + \varepsilon G(r, \theta, Z, U, V), \end{cases} \quad (41)$$

where  $G(r, \theta, Z, U, V) = \tilde{F}(r \cos \theta, r \sin \theta, Z, U, V)$ .

After dividing by  $\dot{\theta}$  and simplifying, we find

$$\begin{cases} \frac{dr}{d\theta} = \varepsilon \sin \theta G(r, \theta, Z, U, V) + o(\varepsilon^2), \\ \frac{dZ}{d\theta} = \lambda Z + \varepsilon \left(1 - \frac{\lambda Z}{r} \cos \theta\right) G(r, \theta, Z, U, V) + o(\varepsilon^2), \\ \frac{dU}{d\theta} = \mu U + \varepsilon \left(1 - \frac{\mu U}{r} \cos \theta\right) G(r, \theta, Z, U, V) + o(\varepsilon^2), \\ \frac{dV}{d\theta} = \delta V + \varepsilon \left(1 - \frac{\delta V}{r} \cos \theta\right) G(r, \theta, Z, U, V) + o(\varepsilon^2). \end{cases} \quad (42)$$

System (42) is now of the same form as system (33) with

$$\mathbf{x} = \begin{pmatrix} r \\ Z \\ U \\ V \end{pmatrix}, \quad t = \theta,$$

$$F_0(\mathbf{x}, \theta) = \begin{pmatrix} 0 \\ \lambda Z \\ \mu U \\ \delta V \end{pmatrix},$$

$$F_1(\mathbf{x}, \theta) = \begin{pmatrix} \sin \theta G(r, \theta, Z, U, V) \\ \left(1 - \frac{\lambda Z}{r} \cos \theta\right) G(r, \theta, Z, U, V) \\ \left(1 - \frac{\mu U}{r} \cos \theta\right) G(r, \theta, Z, U, V) \\ \left(1 - \frac{\delta V}{r} \cos \theta\right) G(r, \theta, Z, U, V) \end{pmatrix}.$$

We shall apply Theorem 6 to system (42). System (42) with  $\varepsilon = 0$  has the  $2\pi$ -periodic solutions

$$\begin{pmatrix} r(\theta) \\ Z(\theta) \\ U(\theta) \\ V(\theta) \end{pmatrix} = \begin{pmatrix} r_0 \\ 0 \\ 0 \\ 0 \end{pmatrix}, \quad \forall r_0 > 0. \tag{44}$$

By the notations of Theorem 6, we have that  $k = 1$  and  $n = 4$ . Let  $r_1 > 0$  and  $r_2 > 0$ ; we take  $\mathbb{V} = ]r_1, r_2[ \subset \mathbb{R}$ ,  $\alpha = r_0 \in [r_1, r_2]$ , and

$$\begin{aligned} \beta_0: [r_1, r_2] &\longrightarrow \mathbb{R}^3, \\ r_0 &\longmapsto \beta_0(r_0) = (0, 0, 0). \end{aligned} \tag{45}$$

We also take

$$\mathcal{X} = \{z_\alpha = (r_0, 0, 0, 0), r_0 \in [r_1, r_2]\}. \tag{46}$$

The fundamental matrix  $M_{z_\alpha}(\theta)$  of the linear system (42) with  $\varepsilon = 0$  with respect to the periodic solution  $z_\alpha = (r_0, 0, 0, 0)$  satisfying that  $M_{z_\alpha}(0)$  is the identity matrix is

$$M_{z_\alpha}(\theta) = \begin{pmatrix} 1 & 0 & 0 & 0 \\ 0 & e^{\lambda\theta} & 0 & 0 \\ 0 & 0 & e^{\mu\theta} & 0 \\ 0 & 0 & 0 & e^{\delta\theta} \end{pmatrix}. \tag{47}$$

We have

$$M_{z_\alpha}^{-1}(0) - M_{z_\alpha}^{-1}(2\pi) = \begin{pmatrix} 0 & 0 & 0 & 0 \\ 0 & 1 - e^{-2\pi\lambda} & 0 & 0 \\ 0 & 0 & 1 - e^{-2\pi\mu} & 0 \\ 0 & 0 & 0 & 1 - e^{-2\pi\delta} \end{pmatrix}, \tag{48}$$

which satisfy the assumption (ii) of Theorem 6. Taking

$$\begin{aligned} \xi: \mathbb{R} \times \mathbb{R}^3 &\longrightarrow \mathbb{R}, \\ (r, Z, U, V) &\longmapsto \xi(r, Z, U, V) = r, \end{aligned} \tag{49}$$

we must compute the function  $\mathcal{F}(\alpha)$  given by (36), and we obtain

$$\begin{aligned} \mathcal{F}(\alpha) &= \mathcal{F}(r_0) = \frac{1}{2\pi} \int_0^{2\pi} \sin \theta G(r_0, \theta, 0, 0, 0) d\theta \\ &= \frac{1}{2\pi} \int_0^{2\pi} \sin \theta F(A_1, A_2, A_3, A_4, A_5) d\theta, \end{aligned} \tag{50}$$

and  $A_1, A_2, A_3, A_4$ , and  $A_5$  are given by (6). Then, by Theorem 6, for every simple zero  $r_0^*$  of the function  $\mathcal{F}(r_0)$ , there exists a limit cycle  $(r, Z, U, V)(\theta, \varepsilon)$  of system (42) such that

$$(r, Z, U, V)(0, \varepsilon) \longrightarrow (r_0^*, 0, 0, 0), \text{ when } \varepsilon \longrightarrow 0. \tag{51}$$

Going back through the change of coordinates, we obtain a limit cycle  $(r, \theta, Z, U, V)(t, \varepsilon)$  of system (41) such that

$$(r, \theta, Z, U, V)(0, \varepsilon) \longrightarrow (r_0^*, 0, 0, 0, 0), \text{ when } \varepsilon \longrightarrow 0. \tag{52}$$

We have a limit cycle  $(X, Y, Z, U, V)(t, \varepsilon)$  of system (39) such that

$$(X, Y, Z, U, V)(0, \varepsilon) \longrightarrow (r_0^*, 0, 0, 0, 0) \text{ when } \varepsilon \longrightarrow 0. \tag{53}$$

Finally, we obtain a limit cycle  $x(t, \varepsilon)$  of equation (3) tending to the periodic solution (7) of equation (8) when  $\varepsilon \longrightarrow 0$ .

Theorem 1 is proved.

*3.1.2. Proof of Corollary 1.* If  $F(x, \dot{x}, \ddot{x}, x) = x^5 - \dot{x}^4 - \ddot{x}^3 - \dot{x}^2 - x - 1$ , then we have

$$\begin{aligned} \mathcal{F}(r_0) &= \frac{r_0(-1 + \lambda\mu + \lambda\delta + \mu\delta)}{16(1 + \lambda^2)^3(1 + \mu^2)^3(1 + \delta^2)^3} \\ &\cdot (-5r_0^2 + 4(1 + \lambda^2)(1 + \mu^2)(1 + \delta^2)) \\ &\cdot (r_0^2 + 2(1 + \lambda^2)(1 + \mu^2)(1 + \delta^2)), \end{aligned} \tag{54}$$

which have the real positive simple zero  $r_0^* = 2\sqrt{5}/5\sqrt{(1 + \lambda^2)(1 + \mu^2)(1 + \delta^2)}$  with

$$\frac{df}{dr_0}(r_0^*) = -\frac{34}{9} \frac{-1 + \lambda\mu + \lambda\delta + \mu\delta}{(1 + \lambda^2)(1 + \mu^2)(1 + \delta^2)} \neq 0. \tag{55}$$



The proof of Corollary 1 follows directly by applying Theorem 1 and (10) is obtained by substituting  $r_0^*$  in (7).

### 3.2. Proofs of the Results in Case 2: $\lambda = 0, \mu \delta \neq 0$ , and $\mu \neq \delta$

3.2.1. Proof of Theorem 2. If  $\lambda = 0$ , equation (3) can be written as

$$\begin{cases} \dot{x} = y, \\ \dot{y} = z, \\ \dot{z} = u, \\ \dot{u} = v, \\ \dot{v} = -\mu\delta y + (\mu + \delta)z - (1 + \mu\delta)u + (\mu + \delta)v + \varepsilon F(x, y, z, u, v). \end{cases} \quad (56)$$

System (56) has a unique singular point at the origin and the eigenvalues of the linear part of this system are  $\pm i, 0, \mu$ , and  $\delta$ . By the linear transformation

$$\begin{pmatrix} X \\ Y \\ Z \\ U \\ V \end{pmatrix} = \begin{pmatrix} 0 & -\mu\delta & \mu + \delta & -1 & 0 \\ 0 & 0 & \mu\delta & -\mu - \delta & 1 \\ \mu\delta & -\mu - \delta & 1 + \mu\delta & -\mu - \delta & 1 \\ 0 & -\delta & 1 & -\delta & 1 \\ 0 & -\mu & 1 & -\mu & 1 \end{pmatrix} \begin{pmatrix} x \\ y \\ z \\ u \\ v \end{pmatrix}, \quad (57)$$

we transform system (56) into the following system:

$$\begin{cases} \dot{X} = -Y, \\ \dot{Y} = X + \varepsilon\tilde{F}(X, Y, Z, U, V), \\ \dot{Z} = \varepsilon\tilde{F}(X, Y, Z, U, V), \\ \dot{U} = \mu U + \varepsilon\tilde{F}(X, Y, Z, U, V), \\ \dot{V} = \delta V + \varepsilon\tilde{F}(X, Y, Z, U, V), \end{cases} \quad (58)$$

where

$$\begin{aligned} \tilde{F} &= \tilde{F}(X, Y, Z, U, V) = F(b_1, b_2, b_3, b_4, b_5), \\ b_1 &= \frac{(-\mu - \delta)X}{(\mu^2 + 1)(\delta^2 + 1)} + \frac{(1 - \mu\delta)Y}{(\mu^2 + 1)(\delta^2 + 1)} + \frac{Z}{\mu\delta} + \frac{U}{\mu(\mu^2 + 1)(\mu - \delta)} - \frac{V}{\delta(\delta^2 + 1)(\mu - \delta)}, \\ b_2 &= \frac{(1 - \mu\delta)X}{(\mu^2 + 1)(\delta^2 + 1)} - \frac{(-\mu - \delta)Y}{(\mu^2 + 1)(\delta^2 + 1)} + \frac{U}{(\mu^2 + 1)(\mu - \delta)} - \frac{V}{(\delta^2 + 1)(\mu - \delta)}, \\ b_3 &= -\frac{(-\mu - \delta)X}{(\mu^2 + 1)(\delta^2 + 1)} - \frac{(1 - \mu\delta)Y}{(\mu^2 + 1)(\delta^2 + 1)} + \frac{\mu U}{(\mu^2 + 1)(\mu - \delta)} - \frac{\delta V}{(\delta^2 + 1)(\mu - \delta)}, \\ b_4 &= \frac{(1 - \mu\delta)X}{(\mu^2 + 1)(\delta^2 + 1)} + \frac{(-\mu - \delta)Y}{(\mu^2 + 1)(\delta^2 + 1)} + \frac{\mu^2 U}{(\mu^2 + 1)(\mu - \delta)} - \frac{\delta^2 V}{(\delta^2 + 1)(\mu - \delta)}, \\ b_5 &= \frac{(-\mu - \delta)X}{(\mu^2 + 1)(\delta^2 + 1)} + \frac{(1 - \mu\delta)Y}{(\mu^2 + 1)(\delta^2 + 1)} + \frac{\mu^3 U}{(\mu^2 + 1)(\mu - \delta)} - \frac{\delta^3 V}{(\delta^2 + 1)(\mu - \delta)}. \end{aligned} \quad (59)$$

Note that the linear part of system (58) is in the real Jordan normal form of the linear part of system (56). We pass now from the Cartesian coordinates  $(X, Y, Z, U, V)$  to the cylindrical ones  $(r, \theta, Z, U, V)$  with  $X = r \cos \theta$ ,  $Y = r \sin \theta$ , and we obtain

$$\begin{cases} \dot{r} = \varepsilon \sin \theta G(r, \theta, Z, U, V), \\ \dot{\theta} = 1 + \frac{\varepsilon}{r} \cos \theta G(r, \theta, Z, U, V), \\ \dot{Z} = \varepsilon G(r, \theta, Z, U, V), \\ \dot{U} = \mu U + \varepsilon G(r, \theta, Z, U, V), \\ \dot{V} = \delta V + \varepsilon G(r, \theta, Z, U, V), \end{cases} \quad (60)$$

where  $G(r, \theta, Z, U, V) = \bar{F}(r \cos \theta, r \sin \theta, Z, U, V)$ .

After dividing by  $\dot{\theta}$  and simplifying, we find

$$\begin{cases} \frac{dr}{d\theta} = \varepsilon \sin \theta G(r, \theta, Z, U, V) + o(\varepsilon^2), \\ \frac{dZ}{d\theta} = \varepsilon G(r, \theta, Z, U, V) + o(\varepsilon^2), \\ \frac{dU}{d\theta} = \mu U + \varepsilon \left(1 - \frac{\mu U}{r} \cos \theta\right) G(r, \theta, Z, U, V) + o(\varepsilon^2), \\ \frac{dV}{d\theta} = \delta V + \varepsilon \left(1 - \frac{\delta V}{r} \cos \theta\right) G(r, \theta, Z, U, V) + o(\varepsilon^2). \end{cases} \quad (61)$$

System (61) is now of the same form as system (33) with

$$\mathbf{x} = \begin{pmatrix} r \\ Z \\ U \\ V \end{pmatrix}, \quad t = \theta,$$

$$F_0(\mathbf{x}, \theta) = \begin{pmatrix} 0 \\ 0 \\ \mu U \\ \delta V \end{pmatrix}, \quad (62)$$

$$F_1(\mathbf{x}, \theta) = \begin{pmatrix} \sin \theta G(r, \theta, Z, U, V) \\ G(r, \theta, Z, U, V) \\ \left(1 - \frac{\mu U}{r} \cos \theta\right) G(r, \theta, Z, U, V) \\ \left(1 - \frac{\delta V}{r} \cos \theta\right) G(r, \theta, Z, U, V) \end{pmatrix}.$$

We shall apply Theorem 6 to system (61). System (61) with  $\varepsilon = 0$  has the  $2\pi$ -periodic solutions

$$\begin{pmatrix} r(\theta) \\ Z(\theta) \\ U(\theta) \\ V(\theta) \end{pmatrix} = \begin{pmatrix} r_0 \\ Z_0 \\ 0 \\ 0 \end{pmatrix}, \quad \forall r_0 > 0, \forall Z_0 \in \mathbb{R}. \quad (63)$$

By the notations of Theorem 6, we have that  $k = 2$  and  $n = 4$ . Let  $R > 0$ ; we take

$$\mathbb{V} = \{(r_0, Z_0) : 0 < r_0^2 + Z_0^2 < R\} \subset \mathbb{R}^2, \quad (64)$$

$\alpha = (r_0, Z_0) \in \mathbb{V}$ , and

$$\begin{aligned} \beta_0 : Cl(\mathbb{V}) &\longrightarrow \mathbb{R}^2, \\ &: (r_0, Z_0) \mapsto \beta_0(r_0, Z_0) = (0, 0). \end{aligned} \quad (65)$$

We also take

$$\mathcal{Z} = \{\mathbf{z}_\alpha = (r_0, Z_0, 0, 0), (r_0, Z_0) \in \mathbb{V}\}. \quad (66)$$

The fundamental matrix  $M_{\mathbf{z}_\alpha}(\theta)$  of the linear system (61) with  $\varepsilon = 0$  with respect to the periodic solution  $\mathbf{z}_\alpha = (r_0, Z_0, 0, 0)$  satisfying that  $M_{\mathbf{z}_\alpha}(0)$  is the identity matrix is

$$M_{\mathbf{z}_\alpha}(\theta) = \begin{pmatrix} 1 & 0 & 0 & 0 \\ 0 & 1 & 0 & 0 \\ 0 & 0 & e^{\mu\theta} & 0 \\ 0 & 0 & 0 & e^{\delta\theta} \end{pmatrix}. \quad (67)$$

We have

$$M_{\mathbf{z}_\alpha}^{-1}(0) - M_{\mathbf{z}_\alpha}^{-1}(2\pi) = \begin{pmatrix} 0 & 0 & 0 & 0 \\ 0 & 0 & 0 & 0 \\ 0 & 0 & 1 - e^{-2\pi\mu} & 0 \\ 0 & 0 & 0 & 1 - e^{-2\pi\delta} \end{pmatrix}, \quad (68)$$

which satisfy the assumption (ii) of Theorem 6. Taking

$$\begin{aligned} \xi: \mathbb{R}^2 \times \mathbb{R}^2 &\longrightarrow \mathbb{R}^2, \\ &: (r, Z, U, V) \mapsto \xi(r, Z, U, V) = (r, Z), \end{aligned} \quad (69)$$

we must compute the function  $\mathcal{F}(\alpha)$  given by (36), and we obtain

$$\begin{aligned} \mathcal{F}(\alpha) = \mathcal{F}(r_0, Z_0) &= \frac{1}{2\pi_0} \begin{pmatrix} \sin \theta G(r_0, \theta, Z_0, 0, 0) \\ G(r_0, \theta, Z_0, 0, 0) \end{pmatrix}, \\ d\theta &= \begin{pmatrix} \mathcal{F}_1(r_0, Z_0) \\ \mathcal{F}_2(r_0, Z_0) \end{pmatrix}, \end{aligned} \quad (70)$$

where

$$\begin{aligned} \mathcal{F}_1(r_0, Z_0) &= \frac{1}{2\pi_0} \int_0^{2\pi} \sin \theta F(B_1, B_2, B_3, B_4, B_5) d\theta, \\ \mathcal{F}_2(r_0, Z_0) &= \frac{1}{2\pi_0} \int_0^{2\pi} F(B_1, B_2, B_3, B_4, B_5) d\theta, \end{aligned} \quad (71)$$

and  $B_1, B_2, B_3, B_4$ , and  $B_5$  are given by (12). Then, by Theorem 6, for every simple zero  $(r_0^*, Z_0^*)$  of the function  $\mathcal{F}(r_0, Z_0)$  there exists a limit cycle  $(r, Z, U, V)(\theta, \varepsilon)$  of system (61) such that

$$(r, Z, U, V)(0, \varepsilon) \longrightarrow (r_0^*, Z_0^*, 0, 0), \text{ when } \varepsilon \longrightarrow 0. \quad (72)$$

Going back through the change of coordinates, we obtain a limit cycle  $(r, \theta, Z, U, V)(t, \varepsilon)$  of system (60) such that

$$(r, \theta, Z, U, V)(0, \varepsilon) \longrightarrow (r_0^*, Z_0^*, 0, 0, 0), \text{ when } \varepsilon \longrightarrow 0. \quad (73)$$

We have a limit cycle  $(X, Y, Z, U, V)(t, \varepsilon)$  of system (58) such that

$$(X, Y, Z, U, V)(0, \varepsilon) \longrightarrow (r_0^*, Z_0^*, 0, 0, 0), \text{ when } \varepsilon \longrightarrow 0. \quad (74)$$

Finally, we obtain a limit cycle  $x(t, \varepsilon)$  of equation (3) tending to the periodic solution (14) of equation (15) when  $\varepsilon \longrightarrow 0$ .

Theorem 2 is proved.

**3.2.2. Proof of Corollary 2.** If  $F(x, \dot{x}, \ddot{x}, \dot{\dot{x}}, \ddot{\dot{x}}) = x^2 - 2x + \dot{x}^2$ , then we have

$$\begin{aligned} \mathcal{F}_1(r_0, Z_0) &= \frac{r_0(\mu\delta - 1)(\mu\delta - Z_0)}{\mu\delta(1 + \mu^2)(1 + \delta^2)}, \\ \mathcal{F}_2(r_0, Z_0) &= \frac{r_0^2\mu^2\delta^2 - Z_0(1 + \mu^2)(1 + \delta^2)(2\mu\delta - Z_0)}{\mu^2\delta^2(1 + \mu^2)(1 + \delta^2)}. \end{aligned} \quad (75)$$

The system  $\mathcal{F}_1(r_0, Z_0) = \mathcal{F}_2(r_0, Z_0) = 0$  has the zero  $(r_0^*, Z_0^*) = (\sqrt{(1 + \mu^2)(1 + \delta^2)}, \mu\delta)$  such that

$$\det\left(\frac{\partial(\mathcal{F}_1, \mathcal{F}_2)}{\partial(r_0, Z_0)}\right)\Big|_{(r_0, Z_0) = (r_0^*, Z_0^*)} = \frac{2(\mu\delta - 1)}{\mu\delta(1 + \mu^2)(1 + \delta^2)} \neq 0. \quad (76)$$

The proof of Corollary 2 follows directly by applying Theorem 2 and (16) is obtained by substituting  $(r_0^*, Z_0^*)$  in (14).

### 3.3. Proofs in Case 3: $\lambda = 0$

**3.3.1. Proof of Theorem 3.** If  $\lambda = 0$ ,  $\mu = \delta \neq 0$ , then equation (3) can be written as

$$\begin{cases} \dot{x} = y, \\ \dot{y} = z, \\ \dot{z} = u, \\ \dot{u} = v, \\ \dot{v} = -\mu^2 y + 2\mu z - (1 + \mu^2)u + 2\mu v + \varepsilon F(x, y, z, u, v). \end{cases} \quad (77)$$

System (77) has a unique singular point at the origin and the eigenvalues of the linear part of this system are  $\pm i, 0$ , and  $\mu$ . By the linear transformation

$$\begin{pmatrix} X \\ Y \\ Z \\ U \\ V \end{pmatrix} = \begin{pmatrix} 0 & \mu^2 & -2\mu & 1 & 0 \\ 0 & 0 & -\mu^2 & 2\mu & -1 \\ \mu^2 & -2\mu & 1 + \mu^2 & -2\mu & 1 \\ 0 & 1 & 0 & 1 & 0 \\ 0 & -\mu & 1 & -\mu & 1 \end{pmatrix} \begin{pmatrix} x \\ y \\ z \\ u \\ v \end{pmatrix}, \quad (78)$$

we transform system (77) into the following system:

$$\begin{cases} \dot{X} = -Y, \\ \dot{Y} = X - \varepsilon \tilde{F}(X, Y, Z, U, V), \\ \dot{Z} = \varepsilon \tilde{F}(X, Y, Z, U, V), \\ \dot{U} = \mu U + V, \\ \dot{V} = \mu V + \varepsilon \tilde{F}(X, Y, Z, U, V), \end{cases} \quad (79)$$

where

$$\begin{aligned} \tilde{F} &= \tilde{F}(X, Y, Z, U, V) = F(c_1, c_2, c_3, c_4, c_5), \\ c_1 &= \frac{2\mu X}{(\mu^2 + 1)^2} + \frac{(\mu^2 - 1)Y}{(\mu^2 + 1)^2} + \frac{Z}{\mu^2 + 1} + \frac{U}{\mu(\mu^2 + 1)} - \frac{(3\mu^2 + 1)V}{\mu^2(\mu^2 + 1)^2}, \\ c_2 &= \frac{(\mu^2 - 1)X}{(\mu^2 + 1)^2} - \frac{2\mu Y}{(\mu^2 + 1)^2} + \frac{U}{\mu^2 + 1} - \frac{2\mu V}{(\mu^2 + 1)^2}, \\ c_3 &= \frac{-2\mu X}{(\mu^2 + 1)^2} - \frac{(\mu^2 - 1)Y}{(\mu^2 + 1)^2} + \frac{\mu U}{\mu^2 + 1} - \frac{(\mu^2 - 1)V}{(\mu^2 + 1)^2}, \\ c_4 &= \frac{-(\mu^2 - 1)X}{(\mu^2 + 1)^2} + \frac{2\mu Y}{(\mu^2 + 1)^2} + \frac{\mu^2 U}{\mu^2 + 1} + \frac{2\mu V}{(\mu^2 + 1)^2}, \\ c_5 &= \frac{2\mu X}{(\mu^2 + 1)^2} + \frac{(\mu^2 - 1)Y}{(\mu^2 + 1)^2} + \frac{\mu^3 U}{\mu^2 + 1} + \frac{\mu^2(\mu^2 + 3)V}{(\mu^2 + 1)^2}. \end{aligned} \quad (80)$$

Note that the linear part of system (81) is in the real Jordan normal form of the linear part of system (77). We pass now from the Cartesian coordinates  $(X, Y, Z, U, V)$  to the cylindrical ones  $(r, \theta, Z, U, V)$  with  $X = r \cos \theta$ ,  $Y = r \sin \theta$ , and we obtain

$$\begin{cases} \dot{r} = -\varepsilon \sin \theta G(r, \theta, Z, U, V), \\ \dot{\theta} = 1 + \frac{\varepsilon}{r} \cos \theta G(r, \theta, Z, U, V), \\ \dot{Z} = \varepsilon G(r, \theta, Z, U, V), \\ \dot{U} = \mu U + V, \\ \dot{V} = \mu V + \varepsilon G(r, \theta, Z, U, V), \end{cases} \quad (81)$$

where  $G(r, \theta, Z, U, V) = \tilde{F}(r \cos \theta, r \sin \theta, Z, U, V)$ .

After dividing by  $\theta$  and simplifying, we find

$$\begin{cases} \frac{dr}{d\theta} = -\varepsilon \sin \theta G(r, \theta, Z, U, V) + o(\varepsilon^2), \\ \frac{dZ}{d\theta} = \varepsilon G(r, \theta, Z, U, V) + o(\varepsilon^2), \\ \frac{dU}{d\theta} = \mu U + V + \varepsilon \frac{\mu U + V}{r} \cos \theta G(r, \theta, Z, U, V) + o(\varepsilon^2), \\ \frac{dV}{d\theta} = \mu V + \varepsilon \left(1 + \frac{\mu V}{r} \cos \theta\right) G(r, \theta, Z, U, V) + o(\varepsilon^2). \end{cases} \quad (82)$$

System (82) is now of the same form as system (33) with

$$\mathbf{x} = \begin{pmatrix} r \\ Z \\ U \\ V \end{pmatrix}, \quad t = \theta, \quad (83)$$

$$F_0(\mathbf{x}, \theta) = \begin{pmatrix} 0 \\ 0 \\ \mu U + V \\ \mu V \end{pmatrix}, \quad (83)$$

$$F_1(\mathbf{x}, \theta) = \begin{pmatrix} -\sin \theta G(r, \theta, Z, U, V) \\ G(r, \theta, Z, U, V) \\ \frac{\mu U + V}{r} \cos \theta G(r, \theta, Z, U, V) \\ \left(1 + \frac{\mu V}{r} \cos \theta\right) G(r, \theta, Z, U, V) \end{pmatrix}.$$

We shall apply Theorem 6 to system (82). System (82) with  $\varepsilon = 0$  has the  $2\pi$ -periodic solutions

$$\begin{pmatrix} r(\theta) \\ Z(\theta) \\ U(\theta) \\ V(\theta) \end{pmatrix} = \begin{pmatrix} r_0 \\ Z_0 \\ 0 \\ 0 \end{pmatrix}, \quad \forall r_0 > 0, \forall Z_0 \in \mathbb{R}. \quad (84)$$

By the notations of Theorem 6, we have that  $k = 2$  and  $n = 4$ . Let  $R > 0$ ; we take

$$\mathbb{V} = \{(r_0, Z_0): 0 < r_0^2 + Z_0^2 < R\} \subset \mathbb{R}^2. \quad (85)$$

$\alpha = (r_0, Z_0) \in \mathbb{V}$  and

$$\begin{aligned} \beta_0: CI(\mathbb{V}) &\longrightarrow \mathbb{R}^2, \\ &: (r_0, Z_0) \mapsto \beta_0(r_0, Z_0) = (0, 0). \end{aligned} \quad (86)$$

We also take

$$\mathcal{Z} = \{z_\alpha = (r_0, Z_0, 0, 0), (r_0, Z_0) \in \mathbb{V}\}. \quad (87)$$

The fundamental matrix  $M_{z_\alpha}(\theta)$  of the linear system (82) with  $\varepsilon = 0$  with respect to the periodic solution  $z_\alpha = (r_0, Z_0, 0, 0)$  satisfying that  $M_{z_\alpha}(0)$  is the identity matrix is

$$M_{z_\alpha}(\theta) = \begin{pmatrix} 1 & 0 & 0 & 0 \\ 0 & 1 & 0 & 0 \\ 0 & 0 & e^{\mu\theta} & \theta e^{\mu\theta} \\ 0 & 0 & 0 & e^{\mu\theta} \end{pmatrix}. \quad (88)$$

We have

$$M_{z_\alpha}^{-1}(0) - M_{z_\alpha}^{-1}(2\pi) = \begin{pmatrix} 0 & 0 & 0 & 0 \\ 0 & 0 & 0 & 0 \\ 0 & 0 & 1 - e^{-2\pi\mu} & 2\pi e^{-2\pi\mu} \\ 0 & 0 & 0 & 1 - e^{-2\pi\mu} \end{pmatrix}, \quad (89)$$

which satisfy the assumption (ii) of Theorem 6. Taking

$$\begin{aligned} \xi: \mathbb{R}^2 \times \mathbb{R}^2 &\longrightarrow \mathbb{R}^2, \\ &: (r, Z, U, V) \mapsto \xi(r, Z, U, V) = (r, Z), \end{aligned} \quad (90)$$

we must compute the function  $\mathcal{F}(\alpha)$  given by (36), and we obtain

$$\begin{aligned} \mathcal{F}(\alpha) &= \mathcal{F}(r_0, Z_0) = \frac{1}{2\pi\theta} \begin{pmatrix} -\sin \theta G(r_0, \theta, Z_0, 0, 0) \\ G(r_0, \theta, Z_0, 0, 0) \end{pmatrix} d\theta \\ &= \begin{pmatrix} \mathcal{F}_1(r_0, Z_0) \\ \mathcal{F}_2(r_0, Z_0) \end{pmatrix}, \end{aligned} \quad (91)$$

where

$$\begin{aligned} \mathcal{F}_1(r_0, Z_0) &= \frac{1}{2\pi\theta} \int_0^{2\pi} -\sin \theta F(C_1, C_2, C_3, C_4, C_5) d\theta, \\ \mathcal{F}_2(r_0, Z_0) &= \frac{1}{2\pi\theta} \int_0^{2\pi} F(C_1, C_2, C_3, C_4, C_5) d\theta, \end{aligned} \quad (92)$$

and  $C_1, C_2, C_3, C_4$ , and  $C_5$  are given by (18). Then, by Theorem 6, for every simple zero  $(r_0^*, Z_0^*)$  of the function  $\mathcal{F}(r_0, Z_0)$ , there exists a limit cycle  $(r, Z, U, V)(\theta, \varepsilon)$  of system (82) such that

$$(r, Z, U, V)(0, \varepsilon) \longrightarrow (r_0^*, Z_0^*, 0, 0), \text{ when } \varepsilon \longrightarrow 0. \quad (93)$$

Going back through the change of coordinates, we obtain a limit cycle  $(r, \theta, Z, U, V)(t, \varepsilon)$  of system (81) such that

$$(r, \theta, Z, U, V)(0, \varepsilon) \longrightarrow (r_0^*, Z_0^*, 0, 0, 0), \text{ when } \varepsilon \longrightarrow 0. \quad (94)$$

We have a limit cycle  $(X, Y, Z, U, V)(t, \varepsilon)$  of system (79) such that

$$(X, Y, Z, U, V)(0, \varepsilon) \longrightarrow (r_0^*, Z_0^*, 0, 0, 0), \text{ when } \varepsilon \longrightarrow 0. \quad (95)$$

Finally, we obtain a limit cycle  $x(t, \varepsilon)$  of equation (3) tending to the periodic solution (20) of equation (21) when  $\varepsilon \longrightarrow 0$ .

Theorem 3 is proved.

3.3.2. *Proof of Corollary 3.* If  $F(x, \dot{x}, \ddot{x}, \dot{x}, x) = x^2 - x\dot{x} - 1$ , then we have

$$\mathcal{F}_1(r_0, Z_0) = \frac{(1 - \mu - \mu^2)r_0 Z_0}{\mu^2(1 + \mu^2)^2}, \quad (96)$$

$$\mathcal{F}_2(r_0, Z_0) = \frac{r_0^2}{2(1 + \mu^2)^2} + \frac{Z_0^2}{\mu^4} + 1.$$

The system  $\mathcal{F}_1(r_0, Z_0) = \mathcal{F}_2(r_0, Z_0) = 0$  has the zero  $(r_0^*, Z_0^*) = (\sqrt{2}(1 + \mu^2), 0)$  such that

$$\det\left(\frac{\partial(\mathcal{F}_1, \mathcal{F}_2)}{\partial(r_0, Z_0)}\right)\Big|_{(r_0, Z_0)=(r_0^*, Z_0^*)} = \frac{2(\mu^2 + \mu - 1)}{\mu^2(1 + \mu^2)^2} \neq 0. \quad (97)$$

The proof of Corollary 3 follows directly by applying Theorem 3 and (22) is obtained by substituting  $(r_0^*, Z_0^*)$  in (20).

3.4. *Proofs in Case 4:  $\lambda \neq 0$  and  $\mu = \delta \neq 0$*

3.4.1. *Proof of Theorem 4.* If  $\lambda \neq 0$  and  $\mu = \delta \neq 0$ , then equation (3) can be written as

$$\begin{cases} \dot{x} = y, \\ \dot{y} = z, \\ \dot{z} = u, \\ \dot{u} = v, \\ \dot{v} = \lambda\mu^2 x - (\mu^2 + 2\lambda\mu)y + (\lambda + 2\mu + \lambda\mu^2)z \\ \quad - (\mu^2 + 2\lambda\mu + 1)u + (\lambda + 2\mu)v + \varepsilon F(x, y, z, u, v). \end{cases} \quad (98)$$

System (98) with  $\varepsilon = 0$  has a unique singular point at the origin and the linear part of this system has the eigenvalues  $\pm i, \lambda$ , and  $\mu$ . Using the change of variables

$$\begin{pmatrix} X \\ Y \\ Z \\ U \\ V \end{pmatrix} = \begin{pmatrix} -\lambda\mu^2 & \mu^2 + 2\lambda\mu & -\lambda - 2\mu & 1 & 0 \\ 0 & \lambda\mu^2 & -\mu^2 - 2\lambda\mu & \lambda + 2\mu & -1 \\ \mu^2 & -2\mu & \mu^2 + 1 & -2\mu & 1 \\ -\lambda & 1 & -\lambda & 1 & 0 \\ \lambda\mu & -\lambda - \mu & 1 + \lambda\mu & -\lambda - \mu & 1 \end{pmatrix} \begin{pmatrix} x \\ y \\ z \\ u \\ v \end{pmatrix}, \tag{99}$$

$$\begin{cases} \dot{X} = -Y, \\ \dot{Y} = X - \varepsilon\tilde{F}(X, Y, Z, U, V), \\ \dot{Z} = \lambda Z + \varepsilon\tilde{F}(X, Y, Z, U, V), \\ \dot{U} = \mu U + V, \\ \dot{V} = \mu V + \varepsilon\tilde{F}(X, Y, Z, U, V), \end{cases} \tag{100}$$

where

we transform the system (98) into the following system:

$$\tilde{F} = \tilde{F}(X, Y, Z, U, V) = F(d_1, d_2, d_3, d_4, d_5),$$

$$d_1 = \frac{(-\lambda\mu^2 + 2\mu + \lambda)X}{(\lambda^2 + 1)(\mu^2 + 1)^2} + \frac{(\mu^2 + 2\lambda\mu - 1)Y}{(\lambda^2 + 1)(\mu^2 + 1)^2} + \frac{Z}{(\lambda^2 + 1)(\lambda - \mu)^2} - \frac{U}{(\mu^2 + 1)(\lambda - \mu)} - \frac{(3\mu^2 - 2\lambda\mu + 1)V}{(\mu^2 + 1)^2(\lambda - \mu)^2},$$

$$d_2 = \frac{(\mu^2 + 2\lambda\mu - 1)X}{(\lambda^2 + 1)(\mu^2 + 1)^2} - \frac{(-\lambda\mu^2 + 2\mu + \lambda)Y}{(\lambda^2 + 1)(\mu^2 + 1)^2} + \frac{\lambda Z}{(\lambda^2 + 1)(\lambda - \mu)^2} - \frac{\mu U}{(\mu^2 + 1)(\lambda - \mu)} - \frac{(2\mu^3 - \lambda\mu^2 + \lambda)V}{(\mu^2 + 1)^2(\lambda - \mu)^2},$$

$$d_3 = \frac{(-\lambda\mu^2 + 2\mu + \lambda)X}{(\lambda^2 + 1)(\mu^2 + 1)^2} - \frac{(\mu^2 + 2\lambda\mu - 1)Y}{(\lambda^2 + 1)(\mu^2 + 1)^2} + \frac{\lambda^2 Z}{(\lambda^2 + 1)(\lambda - \mu)^2} - \frac{\mu^2 U}{(\mu^2 + 1)(\lambda - \mu)} - \frac{\mu(\mu^3 - \mu + 2\lambda)V}{(\mu^2 + 1)^2(\lambda - \mu)^2},$$

$$d_4 = \frac{(\mu^2 + 2\lambda\mu - 1)X}{(\lambda^2 + 1)(\mu^2 + 1)^2} + \frac{(-\lambda\mu^2 + 2\mu + \lambda)Y}{(\lambda^2 + 1)(\mu^2 + 1)^2} + \frac{\lambda^3 Z}{(\lambda^2 + 1)(\lambda - \mu)^2} - \frac{\mu^3 U}{(\mu^2 + 1)(\lambda - \mu)} - \frac{\mu^2(\lambda\mu^2 - 2\mu + 3\lambda)V}{(\mu^2 + 1)^2(\lambda - \mu)^2},$$

$$d_5 = \frac{(-\lambda\mu^2 + 2\mu + \lambda)X}{(\lambda^2 + 1)(\mu^2 + 1)^2} + \frac{(\mu^2 + 2\lambda\mu - 1)Y}{(\lambda^2 + 1)(\mu^2 + 1)^2} + \frac{\lambda^4 Z}{(\lambda^2 + 1)(\lambda - \mu)^2} - \frac{\mu^4 U}{(\mu^2 + 1)(\lambda - \mu)} - \frac{\mu^3(-\mu^3 + 2\lambda\mu^2 - 3\mu + 4\lambda)V}{(\mu^2 + 1)^2(\lambda - \mu)^2}. \tag{101}$$

Note that the linear part of system (100) is in the real normal Jordan form of the linear part of system (98). We pass now from the Cartesian coordinates  $(X, Y, Z, U, V)$  to the cylindrical ones  $(r, \theta, Z, U, V)$  with  $X = r \cos \theta$ ,  $Y = r \sin \theta$ , and we obtain

$$\begin{cases} \dot{r} = -\varepsilon \sin \theta G(r, \theta, Z, U, V), \\ \dot{\theta} = 1 + \frac{\varepsilon}{r} \cos \theta G(r, \theta, Z, U, V), \\ \dot{Z} = \lambda Z + \varepsilon G(r, \theta, Z, U, V), \\ \dot{U} = \mu U + V, \\ \dot{V} = \mu V + \varepsilon G(r, \theta, Z, U, V), \end{cases} \tag{102}$$

where  $G(r, \theta, Z, U, V) = \tilde{F}(r \cos \theta, r \sin \theta, Z, U, V)$ .

After dividing by  $\theta$  and simplifying, we find

$$\begin{cases} \frac{dr}{d\theta} = -\varepsilon \sin \theta G(r, \theta, Z, U, V) + o(\varepsilon^2), \\ \frac{dZ}{d\theta} = \lambda Z + \varepsilon \left( 1 + \frac{\lambda Z}{r} \cos \theta \right) G(r, \theta, Z, U, V) + o(\varepsilon^2), \\ \frac{dU}{d\theta} = \mu U + V + \varepsilon \left( \frac{\mu U + V}{r} \cos \theta \right) G(r, \theta, Z, U, V) + o(\varepsilon^2), \\ \frac{dV}{d\theta} = \mu V + \varepsilon \left( 1 + \frac{\mu V}{r} \cos \theta \right) G(r, \theta, Z, U, V) + o(\varepsilon^2). \end{cases} \tag{103}$$

System (103) is now of the same form as system (33) with

$$\mathbf{x} = \begin{pmatrix} r \\ Z \\ U \\ V \end{pmatrix}, \quad t = \theta,$$

$$F_0(\mathbf{x}, \theta) = \begin{pmatrix} 0 \\ \lambda Z \\ \mu U + V \\ \mu V \end{pmatrix}, \quad (104)$$

$$F_1(\mathbf{x}, \theta) = \begin{pmatrix} -\sin \theta G(r, \theta, Z, U, V) \\ \left(1 + \frac{\lambda Z}{r} \cos \theta\right) G(r, \theta, Z, U, V) \\ \left(\frac{\mu U + V}{r} \cos \theta\right) G(r, \theta, Z, U, V) \\ \left(1 + \frac{\mu V}{r} \cos \theta\right) G(r, \theta, Z, U, V) \end{pmatrix}.$$

We shall apply Theorem 6 to system (103). System (103) with  $\varepsilon = 0$  has the  $2\pi$ -periodic solutions

$$\begin{pmatrix} r(\theta) \\ Z(\theta) \\ U(\theta) \\ V(\theta) \end{pmatrix} = \begin{pmatrix} r_0 \\ 0 \\ 0 \\ 0 \end{pmatrix}, \quad \forall r_0 > 0. \quad (105)$$

By the notations of Theorem 6, we have that  $k = 1$  and  $n = 4$ . Let  $r_1 > 0$  and  $r_2 > 0$ ; we take  $\mathbb{V} = ]r_1, r_2[ \subset \mathbb{R}$ ,  $\alpha = r_0 \in [r_1, r_2]$ , and

$$\begin{aligned} \beta_0: [r_1, r_2] &\longrightarrow \mathbb{R}^3, \\ r_0 &\longmapsto \beta_0(r_0) = (0, 0, 0). \end{aligned} \quad (106)$$

We also take

$$\mathcal{Z} = \{\mathbf{z}_\alpha = (r_0, 0, 0, 0), \quad r_0 \in [r_1, r_2]\}. \quad (107)$$

The fundamental matrix  $M_{\mathbf{z}_\alpha}(\theta)$  of the linear system (103) with  $\varepsilon = 0$  with respect to the periodic solution  $\mathbf{z}_\alpha = (r_0, 0, 0, 0)$  satisfying that  $M_{\mathbf{z}_\alpha}(0)$  is the identity matrix is

$$M_{\mathbf{z}_\alpha}(\theta) = \begin{pmatrix} 1 & 0 & 0 & 0 \\ 0 & e^{\lambda\theta} & 0 & 0 \\ 0 & 0 & e^{\mu\theta} & \theta e^{\mu\theta} \\ 0 & 0 & 0 & e^{\mu\theta} \end{pmatrix}. \quad (108)$$

We have

$$M_{\mathbf{z}_\alpha}^{-1}(0) - M_{\mathbf{z}_\alpha}^{-1}(2\pi) = \begin{pmatrix} 0 & 0 & 0 & 0 \\ 0 & 1 - e^{-2\pi\lambda} & 0 & 0 \\ 0 & 0 & 1 - e^{-2\pi\mu} & 2\pi e^{-2\pi\mu} \\ 0 & 0 & 0 & 1 - e^{-2\pi\mu} \end{pmatrix}, \quad (109)$$

which satisfy the assumption (ii) of Theorem 6. Taking

$$\xi: \mathbb{R} \times \mathbb{R}^3 \longrightarrow \mathbb{R}, \quad (110)$$

$$: (r, Z, U, V) \mapsto \xi(r, Z, U, V) = r,$$

we must compute the function  $\mathcal{F}(\alpha)$  given by (34), and we obtain

$$\mathcal{F}(\alpha) = \frac{1}{2\pi_0} \int_0^{2\pi} -\sin \theta G(r_0, \theta, 0, 0, 0) d\theta, \quad (111)$$

$$\mathcal{F}(r_0) = \frac{1}{2\pi_0} \int_0^{2\pi} -\sin \theta F(D_1, D_2, D_3, D_4, D_5) d\theta,$$

and  $D_1, D_2, D_3, D_4$ , and  $D_5$  are given by (24). Then, by Theorem 6, for every simple zero  $r_0^*$  of the function  $\mathcal{F}(r_0)$ , there exists a limit cycle  $(r, Z, U, V)(\theta, \varepsilon)$  of system (103) such that

$$(r, Z, U, V)(0, \varepsilon) \longrightarrow (r_0^*, 0, 0, 0), \quad \text{when } \varepsilon \longrightarrow 0. \quad (112)$$

Going back through the change of coordinates, we obtain a limit cycle  $(r, \theta, Z, U, V)(t, \varepsilon)$  of system (102) such that

$$(r, \theta, Z, U, V)(0, \varepsilon) \longrightarrow (r_0^*, 0, 0, 0, 0), \quad \text{when } \varepsilon \longrightarrow 0. \quad (113)$$

We have a limit cycle  $(X, Y, Z, U, V)(t, \varepsilon)$  of system such that

$$(X, Y, Z, U, V)(0, \varepsilon) \longrightarrow (r_0^*, 0, 0, 0, 0), \quad \text{when } \varepsilon \longrightarrow 0. \quad (114)$$

Finally, we obtain a limit cycle  $x(t, \varepsilon)$  of equation (3) tending to the periodic solution (25) of equation (26) when  $\varepsilon \longrightarrow 0$ .

Theorem 4 is proved.

**3.4.2. Proof of Corollary 4.** If  $F(x, \dot{x}, \ddot{x}, \overset{\text{t}}{\ddot{x}}, \overset{\text{t}}{\ddot{x}}) = x^3 - x - 1$ , then we have

$$\mathcal{F}(r_0) = \frac{r_0(-1 + 2\lambda\mu + \mu^2) \left(4(1 + \lambda^2)(1 + \mu^2)^2 - 3r_0^2\right)}{8(1 + \lambda^2)^2(1 + \mu^2)^4}, \quad (115)$$

which have the real positive simple zero  $r_0^* = 2\sqrt{3}/3\sqrt{(1 + \lambda^2)(1 + \mu^2)}$  with

$$\frac{df}{dr_0}(r_0^*) = \frac{1 - 2\lambda\mu - \mu^2}{(1 + \lambda^2)(1 + \mu^2)^2} \neq 0. \quad (116)$$



The proof of Corollary 4 follows directly by applying Theorem 4 and (27) is obtained by substituting  $r_0^*$  in (25).

3.5. Proofs in Case 5:  $\lambda = \mu = \delta \neq 0$

3.5.1. Proof of Theorem 5. If  $\lambda = \mu = \delta \neq 0$ , then equation (3) can be written as

$$\begin{cases} \dot{x} = y, \\ \dot{y} = z, \\ \dot{z} = u, \\ \dot{u} = v, \\ \dot{v} = \lambda^3 x - 3\lambda^2 y + (3\lambda + \lambda^3)z - (3\lambda^2 + 1)u + 3\lambda v + \varepsilon F(x, y, z, u, v). \end{cases} \quad (117)$$

System (117) with  $\varepsilon = 0$  has a unique singular point at the origin and the linear part of this system has the eigenvalues  $\pm i$  and  $\lambda$ . Using the change of variables

$$\begin{pmatrix} X \\ Y \\ Z \\ U \\ V \end{pmatrix} = \begin{pmatrix} \lambda^3 & -3\lambda^2 & 3\lambda & -1 & 0 \\ 0 & -\lambda^3 & 3\lambda^2 & -3\lambda & 1 \\ 1 & 0 & 1 & 0 & 0 \\ -\lambda & 1 & -\lambda & 1 & 0 \\ \lambda^2 & -2\lambda & \lambda^2 + 1 & -2\lambda & 1 \end{pmatrix} \begin{pmatrix} x \\ y \\ z \\ u \\ v \end{pmatrix}, \quad (118)$$

we transform system (117) into the following system:

$$\begin{cases} \dot{X} = -Y, \\ \dot{Y} = X + \varepsilon \tilde{F}(X, Y, Z, U, V), \\ \dot{Z} = \lambda Z + U, \\ \dot{U} = \lambda U + V, \\ \dot{V} = \lambda V + \varepsilon \tilde{F}(X, Y, Z, U, V), \end{cases} \quad (119)$$

where

$$\begin{aligned} \tilde{F} &= \tilde{F}(X, Y, Z, U, V) = F(e_1, e_2, e_3, e_4, e_5), \\ e_1 &= \frac{\lambda(\lambda^2 - 3)X + (1 - 3\lambda^2)Y + (\lambda^2 + 1)^2 Z - 2\lambda(\lambda^2 + 1)U + (3\lambda^2 - 1)V}{(\lambda^2 + 1)^3}, \\ e_2 &= \frac{(1 - 3\lambda^2)X - \lambda(\lambda^2 - 3)Y + \lambda(\lambda^2 + 1)^2 Z + (1 - \lambda^4)U + \lambda(\lambda^2 - 3)V}{(\lambda^2 + 1)^3}, \\ e_3 &= \frac{-\lambda(\lambda^2 - 3)X - (1 - 3\lambda^2)Y + \lambda^2(\lambda^2 + 1)^2 Z + 2\lambda(\lambda^2 + 1)U + (1 - 3\lambda^2)V}{(\lambda^2 + 1)^3}, \\ e_4 &= \frac{-(1 - 3\lambda^2)X + \lambda(\lambda^2 - 3)Y + \lambda^3(\lambda^2 + 1)^2 Z + \lambda^2(\lambda^2 + 3)(\lambda^2 + 1)U - \lambda(\lambda^2 - 3)V}{(\lambda^2 + 1)^3}, \\ e_5 &= \frac{\lambda(\lambda^2 - 3)X + (1 - 3\lambda^2)Y + \lambda^4(\lambda^2 + 1)^2 Z + 2\lambda^3(\lambda^2 + 2)(\lambda^2 + 1)U + \lambda^2(3\lambda^2 + \lambda^4 + 6)V}{(\lambda^2 + 1)^3}. \end{aligned} \quad (120)$$

Note that the linear part of system (119) is in the real normal Jordan form of the linear part of system (51). We pass now from the Cartesian coordinates  $(X, Y, Z, U, V)$  to the cylindrical ones  $(r, \theta, Z, U, V)$  with  $X = r \cos \theta$ ,  $Y = r \sin \theta$ , and we obtain

$$\begin{cases} \dot{r} = \varepsilon \sin \theta G(r, \theta, Z, U, V), \\ \dot{\theta} = 1 + \frac{\varepsilon}{r} \cos \theta G(r, \theta, Z, U, V), \\ \dot{Z} = \lambda Z + U, \\ \dot{U} = \lambda U + V, \\ \dot{V} = \lambda V + \varepsilon G(r, \theta, Z, U, V), \end{cases} \quad (121)$$

where  $G(r, \theta, Z, U, V) = \bar{F}(r \cos \theta, r \sin \theta, Z, U, V)$ .

After dividing by  $\dot{\theta}$  and simplifying, we find

$$\begin{cases} \frac{dr}{d\theta} = \varepsilon \sin \theta G(r, \theta, Z, U, V) + o(\varepsilon^2), \\ \frac{dZ}{d\theta} = \lambda Z + U - \varepsilon \left( \frac{\lambda Z + U}{r} \cos \theta \right) G(r, \theta, Z, U, V) + o(\varepsilon^2), \\ \frac{dU}{d\theta} = \lambda U + V - \varepsilon \left( \frac{\lambda U + V}{r} \cos \theta \right) G(r, \theta, Z, U, V) + o(\varepsilon^2), \\ \frac{dV}{d\theta} = \lambda V + \varepsilon \left( 1 - \frac{\lambda V}{r} \cos \theta \right) G(r, \theta, Z, U, V) + o(\varepsilon^2). \end{cases} \quad (122)$$

System (122) is now of the same form as system (33) with

$$\mathbf{x} = \begin{pmatrix} r \\ Z \\ U \\ V \end{pmatrix}, \quad t = \theta,$$

$$F_0(\mathbf{x}, \theta) = \begin{pmatrix} 0 \\ \lambda Z + U \\ \lambda U + V \\ \lambda V \end{pmatrix}, \quad (123)$$

$$F_1(\mathbf{x}, \theta) = \begin{pmatrix} -\sin \theta G(r, \theta, Z, U, V) \\ \left( \frac{\lambda Z + U}{r} \cos \theta \right) G(r, \theta, Z, U, V) \\ \left( \frac{\lambda U + V}{r} \cos \theta \right) G(r, \theta, Z, U, V) \\ \left( 1 - \frac{\lambda V}{r} \cos \theta \right) G(r, \theta, Z, U, V) \end{pmatrix}.$$

We shall apply Theorem 6 to system (122). System (122) with  $\varepsilon = 0$  has the  $2\pi$ -periodic solutions

$$\begin{pmatrix} r(\theta) \\ Z(\theta) \\ U(\theta) \\ V(\theta) \end{pmatrix} = \begin{pmatrix} r_0 \\ 0 \\ 0 \\ 0 \end{pmatrix}, \quad \forall r_0 > 0. \quad (124)$$

By the notations of Theorem 6, we have that  $k = 1$  and  $n = 4$ . Let  $r_1 > 0$  and  $r_2 > 0$ ; we take  $\mathbb{V} = ]r_1, r_2[ \subset \mathbb{R}$ ,  $\alpha = r_0 \in [r_1, r_2]$ , and

$$\begin{aligned} \beta_0: [r_1, r_2] &\longrightarrow \mathbb{R}^3, \\ r_0 &\longmapsto \beta_0(r_0) = (0, 0, 0). \end{aligned} \quad (125)$$

We also take

$$\mathcal{X} = \{z_\alpha = (r_0, 0, 0, 0), \quad r_0 \in [r_1, r_2]\}. \tag{126}$$

The fundamental matrix  $M_{z_\alpha}(\theta)$  of the linear system (122) with  $\varepsilon = 0$  with respect to the periodic solution  $z_\alpha = (r_0, 0, 0, 0)$  satisfying that  $M_{z_\alpha}(0)$  is the identity matrix is

$$M_{z_\alpha}(\theta) = \begin{pmatrix} 1 & 0 & 0 & 0 \\ 0 & e^{\lambda\theta} & \theta e^{\lambda\theta} & \frac{\theta^2}{2} e^{\lambda\theta} \\ 0 & 0 & e^{\lambda\theta} & \theta e^{\lambda\theta} \\ 0 & 0 & 0 & e^{\lambda\theta} \end{pmatrix}. \tag{127}$$

We have

$$M_{z_\alpha}^{-1}(0) - M_{z_\alpha}^{-1}(2\pi) = \begin{pmatrix} 0 & 0 & 0 & 0 \\ 0 & 1 - e^{-2\pi\lambda} & 2\pi e^{-2\pi\lambda} & -2\pi^2 e^{-2\pi\lambda} \\ 0 & 0 & 1 - e^{-2\pi\lambda} & 2\pi e^{-2\pi\lambda} \\ 0 & 0 & 0 & 1 - e^{-2\pi\lambda} \end{pmatrix}, \tag{128}$$

which satisfy the assumption (ii) of Theorem 6. Taking

$$\begin{aligned} \xi: \mathbb{R} \times \mathbb{R}^3 &\longrightarrow \mathbb{R}, \\ (r, Z, U, V) &\mapsto \xi(r, Z, U, V) = r, \end{aligned} \tag{129}$$

we must compute the function  $\mathcal{F}(\alpha)$  given by (36), and we obtain

$$\mathcal{F}(r_0) = \frac{1}{2\pi_0} \int_0^{2\pi} \sin \theta G(r_0, \theta, 0, 0, 0) d\theta, \tag{130}$$

$$\mathcal{F}(\alpha) = \frac{1}{2\pi_0} \int_0^{2\pi} \sin \theta F(E_1, E_2, E_3, E_4, E_5) d\theta,$$

and  $E_1, E_2, E_3, E_4,$  and  $E_5$  are given by (29). Then, by Theorem 6, for every simple zero  $r_0^*$  of the function  $\mathcal{F}(r_0)$ , there exists a limit cycle  $(r, Z, U, V)(\theta, \varepsilon)$  of system (122) such that

$$(r, Z, U, V)(0, \varepsilon) \longrightarrow (r_0^*, 0, 0, 0), \text{ when } \varepsilon \longrightarrow 0. \tag{131}$$

Going back through the change of coordinates, we obtain a limit cycle  $(r, \theta, Z, U, V)(t, \varepsilon)$  of system (121) such that

$$(r, \theta, Z, U, V)(0, \varepsilon) \longrightarrow (r_0^*, 0, 0, 0, 0), \text{ when } \varepsilon \longrightarrow 0. \tag{132}$$

We have a limit cycle  $(X, Y, Z, U, V)(t, \varepsilon)$  of system (119) such that

$$(X, Y, Z, U, V)(0, \varepsilon) \longrightarrow (r_0^*, 0, 0, 0, 0), \text{ when } \varepsilon \longrightarrow 0. \tag{133}$$

Finally, we obtain a limit cycle  $x(t, \varepsilon)$  of equation (3) tending to the periodic solution (30) of equation (31) when  $\varepsilon \longrightarrow 0$ .

Theorem 5 is proved.

3.5.2. Proof of Corollary 5. If  $F(x, \dot{x}, \ddot{x}, \dot{x}, \ddot{x}) = -\ddot{x}^2 x + x^3 + x^2 - \dot{x}\ddot{x} + \dot{x} - 1$ , then we have

$$\mathcal{F}(r_0) = \frac{r_0 \left( 3r_0^2(3\lambda^2 - 1) - 4\lambda(\lambda^2 - 3)(1 + \lambda^2)^3 \right)}{8(1 + \lambda^2)^6}, \tag{134}$$

which have the real positive simple zero  $r_0^* = 2\sqrt{3}/3(\sqrt{\lambda(3\lambda^2 - 1)((\lambda^2 - 3))(1 + \lambda^2)}(1 + \lambda^2)/3\lambda^2 - 1)$  with

$$\frac{df}{dr_0}(r_0^*) = \frac{\lambda(\lambda^2 - 3)}{(1 + \lambda^2)^3} \neq 0. \tag{135}$$

The proof of Corollary 5 follows directly by applying Theorem 5 and (32) is obtained by substituting  $r_0^*$  in (30).

### 4. Conclusion

There are several theories and methods for the study of the existence, uniqueness, or number and stability of limit cycles of differential equations which have been developed in trying to answer Hilbert’s sixteenth problem posed in 1900 (see reference [1]) about the maximum number of limit cycles that a planar polynomial differential system can obtain. In this work, we study the limit cycles of the fifth-order differential equation by using the averaging theory of first order [6, 7], and we provide sufficient conditions for the existence of limit cycles of equation (12); in the next work, we will try to apply the same method on higher order differential equations.

### Data Availability

No data were used to support the study.

### Conflicts of Interest

The authors declare that they have no conflicts of interest.

### Acknowledgments

The authors extend their appreciation to the Deanship of Scientific Research at King Khalid University for funding this work through Research Group Project under Grant no. (R.G.P-2/53/42).

### References

- [1] D. Hilbert, “Nachr. Ges. Wiss. Goett. Math.-Phys. Kl,” *Bulletin of the American Mathematical Society*, vol. 8, pp. 437–479, 1900, English transl.
- [2] A. Menaceur and S. Boulaaras, “A number of limit cycle of sextic polynomial differential systems via the averaging theory,” *Boletim da Sociedade Paranaense de Matemática*, vol. 39, no. 4, pp. 181–197, 2021.

- [3] J. Llibre and P. C. Ernesto, "Limit cycles of a class of perturbed differential systems via the first-order averaging method," *Complexity*, vol. 2021, Article ID 5581423, 6 pages, 2021.
- [4] A. Menaceur, S. Boulaaras, A. Makhlouf, K. Rajagopal, and M. Abdalla, "Limit cycles for fourth-order autonomous differential equations," *Electronic Journal of Differential Equations*, vol. 2012, no. 22, pp. 1–17, 2012.
- [5] J. Llibre and L. Roberto, "On the periodic orbits of the third-order differential equation  $x''' - \mu x'' + x' - \mu x = \varepsilon F(x, x', x'')$ ," *Applied Mathematics Letters*, vol. 26, no. 4, pp. 425–430, 2013.
- [6] A. Menaceur, S. Boulaaras, and S. Alkhalaf, "Jain limit cycles of a class of polynomial differential systems bifurcating from the periodic orbits of a linear center," *Symmetry*, vol. 12, no. 8, p. 1346, 2020.
- [7] J. Llibre, J. Yu, and X. Zhang, "Limit cycles for a class of third order differential equations," *Rocky Mountain Journal of Mathematics*, vol. 40, pp. 581–594, 2010.
- [8] N. Sellami and A. Makhlouf, "Limit cycles for a class of fifth-order differential equations," *Annals of Differential Equations*, vol. 28, no. 2, pp. 202–219, 2012.
- [9] J. A. Sanders and F. Verhulst, *Averaging Methods in Nonlinear Dynamical Systems*, Vol. 59, Springer, New York, NY, USA, 1985.
- [10] I. G. Malkin, *Some Problems of the Theory of Nonlinear Oscillations*, Gostexizdat, Moscow, Russia, 1956.
- [11] M. Roseau, *Vibrations Non-linéaires et Théorie de la Stabilité*, vol. 8, Springer-Verlag, Berlin, Germany, 1966, French.
- [12] A. Buica, J. P. Francoise, and J. Llibre, "Periodic solutions of nonlinear periodic differential systems with a small parameter," *Communications on Pure and Applied Analysis*, vol. 6, pp. 103–111, 2007.

## Research Article

# Fifteen Limit Cycles Bifurcating from a Perturbed Cubic Center

Amor Menaceur,<sup>1</sup> Mufda Alrawashdeh,<sup>2</sup> Sahar Ahmed Idris ,<sup>3,4</sup> and Hala Abd-Elmageed<sup>5</sup>

<sup>1</sup>Laboratory of Analysis and Control of Differential Equations ACED, Department of Mathematics, University of Guelma, P.O. Box 401, Guelma 24000, Algeria

<sup>2</sup>Department of Mathematics, College of Sciences and Arts, ArRas, Qassim University, Buraydah, Saudi Arabia

<sup>3</sup>College of Industrial Engineering, King Khalid University, Abha, Saudi Arabia

<sup>4</sup>Department of Mathematics, College of Sciences, Juba University, Juba, Sudan

<sup>5</sup>Department of Mathematics, Faculty of Science, SVU, Qena 83523, Egypt

Correspondence should be addressed to Sahar Ahmed Idris; sa6044690@gmail.com

Received 19 October 2021; Accepted 12 November 2021; Published 1 December 2021

Academic Editor: Sundarapandian Vaidyanathan

Copyright © 2021 Amor Menaceur et al. This is an open access article distributed under the Creative Commons Attribution License, which permits unrestricted use, distribution, and reproduction in any medium, provided the original work is properly cited.

In this work, we study the bifurcation of limit cycles from the period annulus surrounding the origin of a class of cubic polynomial differential systems; when they are perturbed inside the class of all polynomial differential systems of degree six, we obtain at most fifteenth limit cycles by using the averaging theory of first order.

## 1. Introduction and Statement of the Main Result

Hilbert in 1900 was interested in the maximum number of the limit cycles that a polynomial differential system of a given degree can have. This problem is the well-known 16th Hilbert problem, which together with the Riemann conjecture are the two problems of the famous list of 23 problems of Hilbert which remain open. See for more details [1, 2].

A classical way to produce limit cycles is by perturbing a system which has a center, in such a way that limit cycles bifurcate in the perturbed system from some of the periodic orbits of the period annulus of the center of the unperturbed system [3–7].

In [8], the authors improved the result of the maximum number of limit cycles for a class of polynomial differential systems which bifurcate from the period annulus surrounding the origin of the system:

$$\begin{cases} \dot{u} = v - v(u - y + a)(u + v + a), \\ \dot{v} = -u + u(u - v + a)(u + v + a), \end{cases} \quad (1)$$

where  $(u - y + a)(u + v + a) = 1$  is a conic,  $a^2 \neq 1$ , and  $|a| \leq \sqrt{2}$  by using the first order of the averaging theory method.

In [9], the authors improved the result of the maximum number of limit cycles of sixth polynomial differential systems which bifurcate from the period annulus surrounding the origin of the system:

$$\begin{cases} \dot{u} = -v(u - v^2 - a)^2, \\ \dot{v} = u(u - v^2 - a)^2, \end{cases} \quad (2)$$

where  $u - v^2 - a = 0$  is a conic and  $a \neq 0$ , by using the first order of the averaging theory method.

In this work, we perturb the cubic systems equation (1). Thus, we consider these classes of all polynomial differential systems of degree  $n$ , i.e.,

$$\begin{cases} \dot{u} = v - v(u - y + a)(u + v + a) + \varepsilon P(u, v), \\ \dot{v} = -u + u(u - v + a)(u + v + a) + \varepsilon Q(u, v), \end{cases} \quad (3)$$

where  $(u - v + a)(u + v + a) = 1$  is a conic,  $|a| > \sqrt{2}$ ,  $P(u, v)$  and  $Q(u, v)$  are the real polynomials of degree  $n \geq 3$ , and  $\varepsilon$  is

a small parameter. Main result of this study is the following Theorem 1.

**Theorem 1.** For the sufficiently small  $|\varepsilon|$  and the polynomials  $P(u, v)$  and  $Q(u, v)$  having degree 6, suppose that  $|a| > \sqrt{2}$ , system equation (3) has at most 15 limit cycles bifurcating from the period annulus surrounding the origin of cubic polynomial differential system equation (1) using averaging theory of first order (Figures 1 and 2).

### 2. The Averaging Theory of First Order

**Theorem 2.** Consider the following two initial value problems:

$$\dot{x} = \varepsilon R(t, x) + \varepsilon^2 G(t, x, \varepsilon), \quad x(0) = x_0, \quad (4)$$

and

$$\dot{y} = \varepsilon f^0(y), \quad y(0) = x_0, \quad (5)$$

where  $x, y$ , and  $x_0 \in D$  is an open domain of  $\mathbb{R}$ ,  $t \in [0, \infty)$ ,  $\varepsilon \in (0, \varepsilon_0]$ ,  $R$  and  $G$  are the periodic functions with their period  $T$  with its variable  $t$ , and  $f^0(y)$  is the average function of  $R(t, y)$  with respect to  $t$ , i.e.,

$$f^0(y) = \frac{1}{T} \int_0^T F(t, y) dt. \quad (6)$$

Assume that

- (i)  $R, \partial R/\partial x, \partial^2 R/\partial x^2, G$ , and  $\partial G/\partial x$  are well defined, continuous, and bounded by a constant independent by  $\varepsilon \in (0, \varepsilon_0]$  in  $[0, \infty) \times D$
- (ii)  $T$  is a constant independent of  $\varepsilon$
- (iii)  $y(t)$  belongs to  $D$  on the time scale  $1/\varepsilon$ . Then, the following statements hold.

- (a) On the time scale  $1/\varepsilon$ , we have

$$x(t) - y(t) = O(\varepsilon), \text{ as } \varepsilon \rightarrow 0. \quad (7)$$

- (b) If  $p$  is an equilibrium point of the averaged system equation (5), such that

$$\left. \frac{\partial f^0}{\partial y} \right|_{y=p} \neq 0. \quad (8)$$

Then, system equation (4) has a  $T$ -periodic solution  $\phi(t, \varepsilon) \rightarrow p$  as  $\varepsilon \rightarrow 0$ .

- (c) If equation (8) is a negative, the corresponding periodic solution  $\phi(t, \varepsilon)$  of equation (4) according to  $(t, x)$  is asymptotically stable for all  $\varepsilon$  sufficiently small, and if equation (8) is a positive, then it is unstable.

For more details on the averaging method, see [10, 11].

### 3. Proof of Theorem 1

For  $|a| > 2$ , the cubic system equation (1) has a unique period annulus:

$$A = \left\{ (u, v) : 0 < u^2 + v^2 < \frac{a^2 - 2}{2} \right\}. \quad (9)$$

According to Figures 1 and 2, this proof is based on the first order of the averaging theory method, in polar coordinates  $(r, \theta)$ , where  $u = r \cos \theta, v = r \sin \theta$ , and  $r > 0$ . We take

$$P(u, v) = \sum_{k=1}^n \sum_{i+j=k} p_{ij} u^i v^j, \quad Q(u, v) = \sum_{k=1}^n \sum_{i+j=k} q_{ij} u^i v^j. \quad (10)$$

Equation (3) can be written as follows:

$$\begin{cases} \dot{r} = \varepsilon \sum_{k=1}^n (\cos \theta M_k(\cos \theta, \sin \theta) + \sin \theta N_k(\cos \theta, \sin \theta)) r^k, \\ \dot{\theta} = S(r, \theta) + \varepsilon \sum_{k=1}^n (\cos \theta N_k(\cos \theta, \sin \theta) - \sin \theta M_k(\cos \theta, \sin \theta)) r^{k-1}, \end{cases} \quad (11)$$

where

$$\begin{aligned} M_k(\cos \theta, \sin \theta) &= \sum_{i+j=k} p_{ij} \cos^i \theta \sin^j \theta, \\ N_k(\cos \theta, \sin \theta) &= \sum_{i+j=k} q_{ij} \cos^i \theta \sin^j \theta, \end{aligned} \quad (12)$$

and

$$S(r, \theta) = (r(\cos \theta - \sin \theta) + a)(r(\cos \theta + \sin \theta) + a) - 1. \quad (13)$$

Therefore, we have

$$\frac{dr}{d\theta} = \varepsilon \sum_{k=1}^n \cos \theta M_k(\cos \theta, \sin \theta) + \sin \theta N_k(\cos \theta, \sin \theta) \quad (14)$$

$$\cdot \frac{r^k}{S(r, \theta)} + \varepsilon^2 R(r, \theta, \varepsilon).$$

The averaged function of equation (14) is

$$\begin{aligned} f^0(r) &= \frac{1}{2\pi} \sum_{k=1}^n r^k \\ &\cdot \int_0^{2\pi} \frac{\cos \theta M_k(\cos \theta, \sin \theta) + \sin \theta N_k(\cos \theta, \sin \theta)}{S(r, \theta)} d\theta. \end{aligned} \quad (15)$$

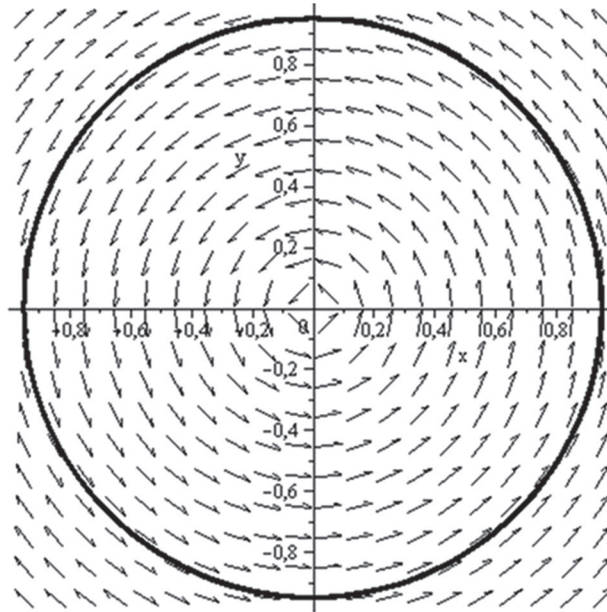


FIGURE 1: Phase portrait of the cubic system equation (1) with  $a = 2$ .

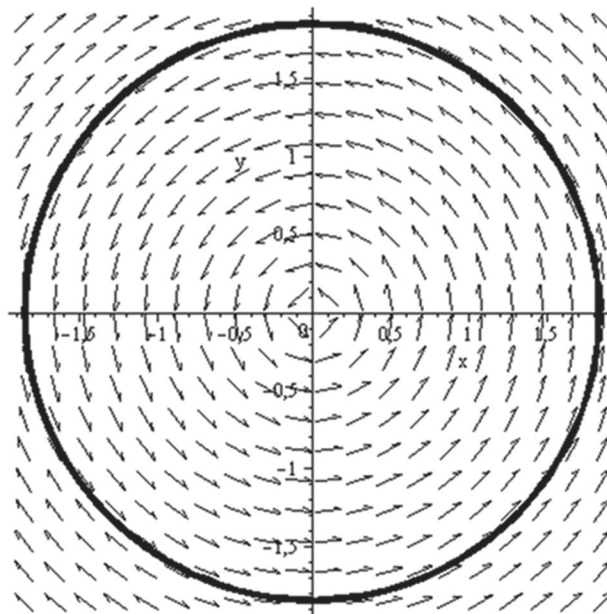


FIGURE 2: Phase portrait of the cubic system equation (1) with  $a = 2$ .

For  $n = 6$ , we get

$$f^0(r) = \sum_{k=1}^6 \sum_{i+j=k} (p_{ij}A_{i+1,j}(r) + q_{ij}A_{i,j+1}(r))r^k, \quad (16)$$

where

$$A_{p,q} = \frac{1}{2\pi} \int_0^{2\pi} \frac{\cos^p \theta \sin^q \theta}{S(r, \theta)} d\theta. \quad (17)$$

According to Theorem 2, every simple zero of the average function  $f^0(r)$  provides a limit cycle of system

equation (3). Now, we prove Theorem 1; in the first step, we compute the integral  $f^0(r)$ , and in the second step, the number of its simple zeros is studied.

**Lemma 1.** *From the above, we have*

$$A_{0,0} = -\frac{G_1 - G_2}{2SH_1H_2} \text{ and } A_{1,0} = \frac{a(G_1 - G_2)}{4rSH_1H_2} + \frac{G_1 + G_2}{4rH_1H_2}, \quad (18)$$

where



$$\begin{aligned}
H_1 &= \sqrt{(a-1)^2 - r^2}, \\
H_2 &= \sqrt{(a+1)^2 - r^2}, \\
G_1 &= \sqrt{-2r^2 - 2aS + 2}, \\
G_2 &= \sqrt{-2r^2 + 2aS + 2},
\end{aligned} \tag{19}$$

with

$$S = \sqrt{2r^2 - a^2 + 2} \neq 0. \tag{20}$$

$$\frac{2\pi}{0} \frac{\cos \theta d\theta}{S(r, \theta)} \equiv \frac{1}{ir^2 C} \frac{z^2 + 1}{(z - z_1)(z - z_2)(z - z_3)(z - z_4)} dz, \tag{21}$$

whose poles are

$$\begin{aligned}
z_{1,2} &= \frac{-a - \sqrt{2r^2 - a^2 + 2} \pm \sqrt{-2r^2 + 2 + 2a\sqrt{2r^2 - a^2 + 2}}}{2r}, \\
z_{3,4} &= \frac{-a + \sqrt{2r^2 - a^2 + 2} \pm \sqrt{-2r^2 + 2 - 2a\sqrt{2r^2 - a^2 + 2}}}{2r}.
\end{aligned} \tag{22}$$

*Proof.* Assume that  $z = e^{i\theta}$  and  $C$  is the circle  $|z| = 1$ ; we get

$$\frac{2\pi}{0} \frac{d\theta}{S(r, \theta)} \equiv \frac{2}{ir^2 C} \frac{z}{(z - z_1)(z - z_2)(z - z_3)(z - z_4)} dz,$$

By applying the residue theorem, for  $|a| > \sqrt{2}$ , we obtain  $|z_1| < 1$ ,  $|z_3| < 1$ ,  $C$  encloses the two singular points of the integrand, so

$$\begin{aligned}
A_{0,0} &= \frac{1}{2\pi} \frac{2\pi}{0} \frac{d\theta}{S(r, \theta)}, \\
&= \frac{1}{\pi ir^2} \frac{z}{(z - z_1)(z - z_2)(z - z_3)(z - z_4)} dz, \\
&= \frac{2}{r^2} \left( \frac{z_1}{(z_1 - z_2)(z_1 - z_3)(z_1 - z_4)} + \frac{z_3}{(z_3 - z_1)(z_3 - z_2)(z_3 - z_4)} \right).
\end{aligned} \tag{23}$$

Therefore, we have

$$\begin{aligned}
A_{0,0} &= -\frac{\sqrt{-2r^2 - 2a\sqrt{2r^2 - a^2 + 2} + 2} - \sqrt{-2r^2 + 2a\sqrt{2r^2 - a^2 + 2} + 2}}{2\sqrt{2r^2 - a^2 + 2}\sqrt{(a-1)^2 - r^2}\sqrt{(a+1)^2 - r^2}}, \\
A_{1,0} &= \frac{1}{2\pi} \frac{2\pi \cos \theta d\theta}{S(r, \theta)}, \\
&= \frac{1}{2\pi ir^2} \frac{z^2 + 1}{(z - z_1)(z - z_2)(z - z_3)(z - z_4)} dz, \\
&= \frac{1}{r^2} \left( \frac{z_1^2 + 1}{(z_1 - z_2)(z_1 - z_3)(z_1 - z_4)} + \frac{z_3^2 + 1}{(z_3 - z_1)(z_3 - z_2)(z_3 - z_4)} \right).
\end{aligned} \tag{24}$$

Therefore, we get

$$A_{1,0} = \frac{a \left( \sqrt{-2r^2 - 2a\sqrt{2r^2 - a^2 + 2} + 2} - \sqrt{-2r^2 + 2a\sqrt{2r^2 - a^2 + 2} + 2} \right)}{4r\sqrt{2r^2 + 2 - a^2}\sqrt{(a-1)^2 - r^2}\sqrt{(a+1)^2 - r^2}} + \frac{\sqrt{-2r^2 - 2a\sqrt{2r^2 - a^2 + 2} + 2} + \sqrt{-2r^2 + 2a\sqrt{2r^2 - a^2 + 2} + 2}}{4r\sqrt{(a-1)^2 - r^2}\sqrt{(a+1)^2 - r^2}}. \tag{25}$$

This completes the proof.  $\square$

where  $\lambda_{k-1} = 3.5 \dots (2k-3), \lambda_k = (2k-1)\lambda_{k-1}$  ([12]). Thus,

**Lemma 2.** Under the previous notations, we have

$$A_{2k,0} = -\frac{a}{r}A_{2k-1,0} + \frac{r^2 + 1 - a^2}{2r^2}A_{2k-2,0} + \frac{\lambda_{k-1}}{2^k(k-1)!r^2}, \tag{30}$$

(a)  $A_{2k+1,0} = -(a/r)A_{2k,0} + (r^2 + 1 - a^2/2r^2)A_{2k-1,0}$

(b)  $A_{2k,0} = -(a/r)A_{2k-1,0} + (r^2 + 1 - a^2/2r^2)A_{2k-2,0} + (\lambda_{k-1}/2^k(k-1)!r^2),$

Where  $\lambda_{k-1} = 3.5 \dots (2k-3)$

(c)  $A_{0,2k} = \sum_{i=0}^k (-1)^i C_k^i A_{2i,0}$

(d)  $A_{n-2m+1,2m} = \sum_{i=0}^m (-1)^i C_m^i A_{n-2m+2i+1,0}, \quad m = 1, \dots, [n + 1/2].$

(c) 
$$\frac{\sin^{2k} \theta}{S(r, \theta)} = \frac{(1 - \cos^2 \theta)^k}{S(r, \theta)} = \sum_{i=0}^k (-1)^i C_k^i \frac{\cos^{2i} \theta}{S(r, \theta)}, \tag{31}$$

then

$$A_{0,2k} = \sum_{i=0}^k (-1)^i C_k^i A_{2i,0}, \tag{32}$$

*Proof.* Putting  $u = r \cos \theta, v = r \sin \theta$ , we get for (a) and (b)

$$\begin{aligned} \frac{\cos^n \theta}{S(r, \theta)} &= \frac{\cos^n \theta}{(a^2 - 2r^2 - 2/2) + 2(r \cos \theta + (a/2))^2} \\ &= \frac{-2ar \cos^{n-1} \theta + (r^2 + 1 - a^2)\cos^{n-2} \theta + S(r, \theta)\cos^{n-2} \theta}{2r^2 S(r, \theta)}, \\ &= -\frac{a \cos^{n-1} \theta}{r S(r, \theta)} + \frac{r^2 + 1 - a^2 \cos^{n-2} \theta}{2r^2 S(r, \theta)} + \frac{1}{2r^2} \cos^{n-2} \theta. \end{aligned} \tag{26}$$

Thus,

$$\begin{aligned} A_{n,0} &= -\frac{a}{2\pi r} \int_0^{2\pi} \frac{\cos^{n-1} \theta}{S(r, \theta)} d\theta + \frac{r^2 + 1 - a^2}{4\pi r^2} \int_0^{2\pi} \frac{\cos^{n-2} \theta}{S(r, \theta)} d\theta \\ &\quad + \frac{1}{4\pi r^2} \int_0^{2\pi} \cos^{n-2} \theta d\theta. \end{aligned} \tag{27}$$

Therefore,

$$\begin{aligned} A_{2k+1,0} &= -\frac{a}{r}A_{2k,0} + \frac{r^2 + 1 - a^2}{2r^2}A_{2k-1,0}, \\ A_{2k,0} &= -\frac{a}{r}A_{2k-1,0} + \frac{r^2 + 1 - a^2}{2r^2}A_{2k-2,0} + \frac{1}{4\pi r^2} \int_0^{2\pi} \cos^{2k-2} \theta d\theta, \end{aligned} \tag{28}$$

and

$$\int_0^{2\pi} \cos^{2(k-1)} \theta d\theta = \frac{\pi \lambda_{k-1}}{2^{k-2} (k-1)!}, \tag{29}$$

(d) 
$$\frac{\cos^{n-2m+1} \theta \sin^{2m} \theta}{S(r, \theta)} = \frac{\cos^{n-2m+1} \theta (1 - \cos^2 \theta)^m}{S(r, \theta)} = \sum_{i=0}^m (-1)^i C_m^i \frac{\cos^{n-2m+2i+1} \theta}{S(r, \theta)}, \tag{33}$$

$m = 1, \dots, \left[ \frac{n+1}{2} \right].$

Thus,

$$A_{n-2m+1,2m} = \sum_{i=0}^m (-1)^i C_m^i A_{n-2m+2i+1,0}, \quad m = 1, \dots, \left[ \frac{n+1}{2} \right]. \tag{34}$$

This completes the proof.  $\square$

*Remark 1.*  $A_{p,2k+1} = 0.$

By Lemmas 1 and 2, we have

$$\begin{aligned} A_{2,0} &= \frac{1}{4\pi r^2} \int_0^{2\pi} d\theta - \frac{a}{r}A_{1,0} + \frac{r^2 + 1 - a^2}{2r^2}A_{0,0} \\ &= \frac{1}{2r^2} - \frac{a}{r} \left( \frac{a(G_1 - G_2)}{4rSH_1H_2} + \frac{G_1 + G_2}{4rH_1H_2} \right) \\ &\quad + \frac{r^2 + 1 - a^2}{2r^2} \left( \frac{G_1 - G_2}{2SH_1H_2} \right) \\ &= -\frac{1}{4SH_1H_2r^2} (-2SH_1H_2 + aS(G_1 + G_2) \\ &\quad + (r^2 + 1)(G_1 - G_2)). \end{aligned} \tag{35}$$

Then,

$$\begin{aligned}
 A_{0,2} &= A_{0,0} - A_{2,0} \\
 &= \frac{G_1 - G_2}{2SH_1H_2} - \left( \frac{1}{4SH_1H_2r^2} (-2SH_1H_2 + aS(G_1 + G_2) + (r^2 + 1)(G_1 - G_2)) \right) \\
 &= \frac{-2SH_1H_2 + aS(G_1 + G_2) - (r^2 - 1)(G_1 - G_2)}{4SH_1H_2r^2},
 \end{aligned} \tag{36}$$

and we also have

$$\begin{aligned}
 A_{3,0} &= \frac{-4aS H_1H_2 + (r^2 + a^2 + 1)S(G_1 + G_2) + a(3r^2 - a^2 + 3)(G_1 - G_2)}{8SH_1H_2r^3}, \\
 A_{1,2} &= -\frac{(-4aS H_1H_2 + (-r^2 + a^2 + 1)S(G_1 + G_2) + a(r^2 - a^2 + 3)(G_1 - G_2))}{8SH_1H_2r^3}, \\
 A_{4,0} &= -\frac{1}{8SH_1H_2r^4} \left[ (-4r^2 - 2(a^2 + 1))SH_1H_2 + 2a(r^2 + 1)S(G_1 + G_2) \right. \\
 &\quad \left. + (r^4 + 2(a^2 + 1)r^2 + (-a^4 + 2a^2 + 1))(G_1 - G_2) \right], \\
 A_{2,2} &= \frac{1}{8SH_1H_2r^4} \left[ 2(-a^2 - 1)SH_1H_2 + 2aS(G_1 + G_2) \right. \\
 &\quad \left. + (-r^4 + 2a^2r^2 + (-a^4 + 2a^2 + 1))(G_1 - G_2) \right],
 \end{aligned} \tag{37}$$

and

$$\begin{aligned}
 A_{0,4} &= -\frac{1}{8SH_1H_2r^4} \left[ 2(2r^2 - a^2 - 1)SH_1H_2 + 2a(-r^2 + 1)S(G_1 + G_2) \right. \\
 &\quad \left. + (r^4 + 2(a^2 - 1)r^2 + (-a^4 + 2a^2 + 1))(G_1 - G_2) \right], \\
 A_{5,0} &= \frac{1}{16SH_1H_2r^5} \left[ 4a(-3r^2 - 2)SH_1H_2 + (r^4 + 2(2a^2 + 1)r^2 + (-a^4 + 4a^2 + 1))S(G_1 + G_2) \right. \\
 &\quad \left. + a(5r^4 + 10r^2 - a^4 + 5)(G_1 - G_2) \right], \\
 A_{3,2} &= -\frac{1}{16SH_1H_2r^5} \left[ 4a(-r^2 - 2)SH_1H_2 + (-r^4 + 2a^2r^2 + (-a^4 + 4a^2 + 1))S(G_1 + G_2) \right. \\
 &\quad \left. + (-ar^4 + 2a(a^2 + 2)r^2 + a(-a^4 + 5))(G_1 - G_2) \right], \\
 A_{1,4} &= \frac{1}{16SH_1H_2r^5} \left[ 4a(r^2 - 2)SH_1H_2 + (r^4 - 2r^2 + (-a^4 + 4a^2 + 1))S(G_1 + G_2) \right. \\
 &\quad \left. + (-3ar^4 + 2a(2a^2 - 1)r^2 + a(5 - a^4))(G_1 - G_2) \right],
 \end{aligned}$$

$$\begin{aligned}
A_{6,0} &= \frac{1}{16SH_1H_2r^6} \left[ (-7r^4 + 2(-5a^2 - 3)r^2 + 2(a^4 - 4a^2 - 1))SH_1H_2 \right. \\
&\quad + a(3r^4 + 2(a^2 + 3)r^2 + (-a^4 + 2a^2 + 3))S(G_1 + G_2) \\
&\quad \left. + (r^6 + 3(2a^2 + 1)r^4 + 3(4a^2 - a^4 + 1)r^2 + (6a^2 - 3a^4 + 1))(G_1 - G_2) \right], \\
A_{4,2} &= \frac{1}{16SH_1H_2r^6} \left[ (r^4 + (-6a^2 - 2)r^2 + (2a^4 - 8a^2 - 2))SH_1H_2 \right. \\
&\quad + ((-a)r^4 + (2a^3 + 2a)r^2 + (2a^3 - a^5 + 3a))S(G_1 + G_2) \\
&\quad \left. + (-r^6 + (2a^2 - 1)r^4 + (8a^2 - a^4 + 1)r^2 + (6a^2 - 3a^4 + 1))(G_1 - G_2) \right].
\end{aligned} \tag{38}$$

In addition, we have

$$\begin{aligned}
A_{2,4} &= \frac{1}{16SH_1H_2r^6} \left[ (r^4 + 2(1 - a^2)r^2 + 2(a^4 - 4a^2 - 1))SH_1H_2 \right. \\
&\quad + (-ar^4 + 2a(a^2 - 1)r^2 + a(-a^4 + 2a^2 + 3))S(G_1 + G_2) \\
&\quad \left. + (r^6 + (-2a^2 - 1)r^4 + (a^4 + 4a^2 - 1)r^2 + (6a^2 - 3a^4 + 1))(G_1 - G_2) \right], \\
A_{0,6} &= \frac{1}{16SH_1H_2r^6} \left[ (-7r^4 + 2(a^2 + 3)r^2 + 2(a^4 - 4a^2 - 1))SH_1H_2 \right. \\
&\quad + (3ar^4 + 2a(a^2 - 3)r^2 + a(-a^4 + 2a^2 + 3))S(G_1 + G_2) \\
&\quad \left. + (-r^6 + 3(-2a^2 + 1)r^4 + 3(a^4 - 1)r^2 + (-3a^4 + 6a^2 + 1))(G_1 - G_2) \right], \\
A_{7,0} &= \frac{1}{32SH_1H_2r^7} \left[ (4(-3a - 7)r^4 + 4(7a - 10a^2 - 8)r^2 + 8(a^4 - 4a^2 + 3a - 1))SH_1H_2 \right. \\
&\quad + (r^6 + (4a^2 + 12a - 1)r^4 + (-a^4 + 8a^3 - 8a^2 + 24a - 5)r^2 \\
&\quad + (-4a^5 + 3a^4 + 8a^3 - 12a^2 + 12a - 3))S(G_1 + G_2) \\
&\quad + ((5a + 4)r^6 + (24a^2 - 5a + 12)r^4 + (-a^5 - 12a^4 + 48a^2 - 25a + 12)r^2 \\
&\quad \left. + (3a^5 - 12a^4 + 24a^2 - 15a + 4))(G_1 - G_2) \right], \\
A_{5,2} &= \frac{1}{32SH_1H_2r^7} \left[ (4(3a - 7)r^4 + 4(11a - 10a^2 - 8)r^2 + 8(a^4 - 4a^2 + 3a - 1))SH_1H_2 \right. \\
&\quad + (-r^6 + (-4a^2 + 12a - 5)r^4 + (a^4 + 8a^3 - 16a^2 + 24a - 7)r^2 \\
&\quad + (-4a^5 + 3a^4 + 8a^3 - 12a^2 + 12a - 3))S(G_1 + G_2) \\
&\quad + ((-5a + 4)r^6 + (24a^2 - 25a + 12)r^4 + (a^5 - 12a^4 + 48a^2 - 35a + 12)r^2 \\
&\quad \left. + (3a^5 - 12a^4 + 24a^2 - 15a + 4))(G_1 - G_2) \right],
\end{aligned}$$

$$\begin{aligned}
 A_{3,4} = & \frac{1}{32SH_1H_2r^7} \left[ (4(5a-7)r^4 + 4(15a-10a^2-7)r^2 + 8(a^4-4a^2+3a-1))SH_1H_2 \right. \\
 & + (r^6 + (-8a^2+12a-5)r^4 + (3a^4+8a^3-24a^2+24a-9)r^2 \\
 & + (-4a^5+3a^4+8a^3-12a^2+12a-3))S(G_1+G_2) \\
 & + ((-3a+4)r^6 + (-4a^3+24a^2-33a+12)r^4 \\
 & + (3a^5-12a^4+48a^2-45a+12)r^2 \\
 & \left. + (3a^5-12a^4+24a^2-15a+4))(G_1-G_2) \right], \tag{39}
 \end{aligned}$$

$$\begin{aligned}
 A_{1,6} = & \frac{1}{32SH_1H_2r^7} \left[ (4(3a-7)r^4 + 4(19a-10a^2-7)r^2 + 8(a^4-4a^2+3a-1))SH_1H_2 \right. \\
 & + (-r^6 + (-8a^2+12a-1)r^4 + (5a^4+8a^3-32a^2+24a-11)r^2 \\
 & + (-4a^5+3a^4+8a^3-12a^2+12a-3))S(G_1+G_2) \\
 & + ((3a+4)r^6 + (-12a^3+24a^2-29a+12)r^4 \\
 & + (5a^5-12a^4+48a^2-55a+12)r^2 \\
 & \left. + (3a^5-12a^4+24a^2-15a+4))(G_1-G_2) \right].
 \end{aligned}$$

Using equation (15), we get

$$f^0(r) = \frac{1}{rSH_1H_2} (XSH_1H_2 + YS(G_1+G_2) + Z(G_1-G_2)), \tag{40}$$

where

$$X = (x_4r^4 + x_2r^2 + x_0), Y = (y_6r^6 + y_4r^4 + y_2r^2 + y_0), \tag{41}$$

and

$$Z = \left( z_6r^6 + z_4r^4 + z_2r^2 + \frac{(a^2-1)x_0 + 2ay_0}{2} \right), \tag{42}$$

with the coefficients  $x_i, y_i,$  and  $z_i$  the polynomials in the coefficients of  $a, p_{i,j},$  and  $q_{i,j}.$

In fact, there are only ten independent parameters between  $x_i, y_i,$  and  $z_i$  with respect to  $p_{ij}, q_{ij},$  and  $a.$  In order to bound the zeros number of numerator of  $f^0(r),$  it is sufficient to bound the zeros number of

$$K(r) = X^2S^2H_1^2H_2^2 - [YS(G_1+G_2) + Z(G_1-G_2)]^2. \tag{43}$$

Since

$$\begin{aligned}
 (G_1+G_2)(G_1-G_2) &= -4aS, \\
 (G_1+G_2)^2 &= 4(1-r^2) + 2G_1G_2, \tag{44}
 \end{aligned}$$

and

$$(G_1-G_2)^2 = 4(1-r^2) - 2G_1G_2, \tag{45}$$

we have

$$\begin{aligned}
 K(r) = & X^2S^2H_1^2H_2^2 - 4Y^2S^2(1-r^2) - 4Z^2(1-r^2) \\
 & + 8aYZS^2 - 2(Y^2S^2 - Z^2)G_1G_2. \tag{46}
 \end{aligned}$$

Finally, in order to bound the zeros number of the above expression, we should bound the zeros of the following polynomial:

$$\begin{aligned}
 H(r) = & [X^2S^2H_1^2H_2^2 - 4Y^2S^2(1-r^2) - 4Z^2(1-r^2) + 8aYZS^2]^2 \\
 & - 4(Y^2S^2 - Z^2)^2G_1^2G_2^2. \tag{47}
 \end{aligned}$$

We have

$$\begin{aligned}
H(r) = & S^2 \left[ (16Y^4 a^2) S^4 \right. \\
& + \left( (4Y^2(r^2 - 1) + 8YZa + X^2((a-1)^2 - r^2))((a+1)^2 - r^2) \right)^2 \\
& - 4Y^4(2r^2 - 2)^2 - 32Y^2 Z^2 a^2 \left. \right] S^2 \\
& + (16Z^4 a^2 + 8Z^2(r^2 - 1))(4Y^2(r^2 - 1) + 8YZa + X^2((a-1)^2 - r^2))((a+1)^2 - r^2) \\
& + 8Y^2 Z^2 (2r^2 - 2)^2 \left. \right]. \tag{48}
\end{aligned}$$

Therefore, we get

$$H(r) = S^2(d_{30}r^{30} + \dots + d_2r^2 + d_0), \tag{49}$$

where  $d_i$  are the polynomials in  $a, x_i, y_i,$  and  $z_i$ . We conclude that  $f^0(r)$  has at most 15 simple zeros. Hence, Theorem 1 is proved.

#### 4. Conclusion

As we know, the limit cycles and a polynomial differential system is the well-known 16th Hilbert problem, which together with the Riemann conjecture are the two problems of the famous list of 23 problems of Hilbert which remain open. In addition, a classical way to produce limit cycles is by perturbing a system which has a center, in such a way that limit cycles bifurcate in the perturbed system from some of the periodic orbits of the period annulus of the center of the unperturbed system; in this work, by using the averaging theory of first order, we study the bifurcation of limit cycles from the period annulus surrounding the origin of a class of cubic polynomial differential systems; when they are perturbed inside the class of all polynomial differential systems of degree six, we have obtained at most 15th limit cycles for this kind of the problem; in the next study, we will try to extend the same tools but for higher degrees.

#### Data Availability

No data were used to support the study.

#### Conflicts of Interest

The authors declare that they have no conflicts of interest.

#### Acknowledgments

The authors extend their appreciation to the Deanship of Scientific Research at King Khalid University for funding this work through Research Group Project (R.G.P-2/53/42).

#### References

- [1] L. Hongwei, "Limit cycles in a sextic lyapunov system," *Nonlinear Dynamics*, vol. 72, pp. 555–559, 2013.
- [2] C. Hilbert, "Mathematische probleme, lecture, second internat," *Nachrichten von der Gesellschaft der Wissenschaften zu Göttingen, Mathematisch-Physikalische Klasse*, pp. 253–297, American Mathematical Society, Providence, RI, USA, 1900.
- [3] L. Feng and W. Miao, "Bifurcation of limit cycles in a quintic system with ten parameters," *Nonlinear Dynamics*, vol. 71, pp. 213–222, 2013.
- [4] H. Giacomini, J. Llibre, and M. Viano, "On the nonexistence, existence and uniqueness of limit cycles," *Nonlinearity*, vol. 9, no. 2, pp. 501–516, 1996.
- [5] J. Giné and J. Llibre, "Limit cycles of cubic polynomial vector fields via the averaging theory," *Nonlinear Analysis: Theory, Methods & Applications*, vol. 66, no. 8, pp. 1707–1721, 2007.
- [6] A. Menaceur, S. Boulaaras, S. Alkhalaf, and S. Jain, "Limit cycles of a class of polynomial differential systems bifurcating from the periodic orbits of a linear center," *Symmetry*, vol. 12, no. 8, p. 15, 2020.
- [7] A. Menaceur, S. Boulaaras, A. Makhlof, K. Rajagobal, and M. Abdalla, "Limit cycles of a class of perturbed differential systems via the first-order averaging method," *Complexity*, vol. 2021, Article ID 5581423, 6 pages, 2021.
- [8] S. Li, Y. Zhao, and J. Li, "On the number of limit cycles of a perturbed cubic polynomial differential center," *Journal of Mathematical Analysis and Applications*, vol. 404, no. 2, pp. 212–220, 2013.
- [9] A. Menaceur and S. Boulaaras, "A number of limit cycle of sextic polynomial differential systems via the averaging theory," *Boletim da Sociedade Paranaense de Matemática*, vol. 39, no. 4, pp. 181–197, 2021.
- [10] B. Coll, A. Gasull, and R. Prohens, "Bifurcation of limit cycles from two families of centers," *Dynamics of Continuous, Discrete and Impulsive Systems*, vol. 12, pp. 275–288, 2005.
- [11] J. Murdock, A. Sanders, and F. Verhulst, "Averaging methods in nonlinear dynamical systems," *Applied Mathematical Sciences*, vol. 59, 2007.
- [12] M. Abramowitz and I. Stegun, "Handbook of mathematical functions with formulas, graphs, and mathematical tables," *National Bureau of Standards Applied Mathematics Series*, US Government Printing Office, Washington, DC, USA, 1964.

## Research Article

# Modeling and Dynamical Analysis of Multi-Area Network with a Third-Order Chaotic Power System

Lixin Yang , Jie Gao, and Jie Ma

*School of Arts and Sciences, Shaanxi University of Science and Technology, Xi'an 710021, China*

Correspondence should be addressed to Lixin Yang; [yanglixin@sust.edu.cn](mailto:yanglixin@sust.edu.cn)

Received 16 September 2021; Revised 8 October 2021; Accepted 12 October 2021; Published 28 October 2021

Academic Editor: Sundarapandian Vaidyanathan

Copyright © 2021 Lixin Yang et al. This is an open access article distributed under the Creative Commons Attribution License, which permits unrestricted use, distribution, and reproduction in any medium, provided the original work is properly cited.

The synchronization of states is important to sustain the energy of consumers at any given time for power networks. This paper focuses on the multi-area power network model and then analyzes the cluster synchronization of this kind of network comprised of a third-order chaotic power system. Specifically, we investigate the rich dynamic properties of the single third-order power system. Furthermore, the multi-area network model with the chaotic power system is proposed and the adaptive controller is designed to achieve cluster synchronization. Combining analytical considerations with numerical simulations on a small-scale network, we address the cluster synchronous performance in the multi-area power network. Therefore, our results can provide a basic physical picture for power system dynamics and enable us to further understand the complex dynamical behavior in the multi-area power network.

## 1. Introduction

As we know, modern power networks play a crucial role in our modern society today. Power networks refer to complex interconnected systems for routing power via transmission lines [1–3].

Generally, they consist of a large number of heterogeneous elements that operate interlinked, creating a multiplex network. In this multiplex network, the interlinked nodes either play the role of an energy generator or an energy consumer. Furthermore, it operates normally only if the total demand power matches the total supply from all the generators [4]. Meanwhile, its dynamical behavior is extremely important for stable operation of the power network. One of the most common and useful models for studying power systems is the canonical single machine infinite bus system, which takes into account its electrobehavior [5]. Furthermore, the single machine infinite bus system refers to a power network that corresponds to an oscillatory power-grid node and a connected system as an environment. In addition, the Kuramoto-like model is a standard mathematical model to investigate the dynamics of the power network [6–9]. However, the Kuramoto-like model

does not take into account the physical characteristics of the power grid. Therefore, most of the existing works have missed a detailed analysis of the nonlinear dynamic behaviors for the third-order power system.

Due to the increasing of renewable energy sources on power production, questions concerning the limits, quantification, and control of power grid stability face new challenges. Therefore, the power system represents a distributed network carrying many small units of energy to the consumers instead of large units of energy coming from a few power plants. This implies that the power system will undergo a lot of challenges concerning grid topology [10–12]. As a consequence, the power network will be divided into small areas. As a matter of fact, the real power network usually has a multi-area structure. However, in many recent studies on power system dynamics, this special topology structure is neglected.

Based on the above discussion, in the present paper, we focus on a more realistic third-order system model to describe the multi-area power network. The investigation of power systems has been recently addressed from a nonlinear dynamics point of view. Meanwhile, synchronization is vital for the stable operation and control of the power network,



and it is necessary to ensure appropriate operation of power generation [13–16]. From the dynamics viewpoint, synchronization is essential for the proper functioning of the power network. Its loss can lead to cascading failure [17–19]. In virtue of multi-area structures, new patterns of synchronization are relevant [15]. In particular, cluster synchronization plays a crucial role on keeping the power balance [20–24]. This synchronous pattern implies that nodes in different areas can achieve different synchronous states to cope with energy imbalance. Thus, we are going to address the cluster synchronization in the multi-area network.

This paper is organized as follows. First, we present a third-order power system model in Section 2. Afterwards, the characteristics of dynamic behavior for a single power system are investigated in Section 3. We propose the multi-area power network model and analyze the cluster synchronization in Section 4. Finally, we present our results, followed by a summary in Section 5.

## 2. Analysis of Dynamics of the Third-Order Power System

**2.1. The Third-Order Power System Model.** The simple third-order power model is illustrated in Figure 1, which can be viewed as a generalized case. In terms of the power system,  $V_t$  denotes generator,  $x_t$  represents transformer reactance,  $x_L$  is the transmission line reactance, and  $V_s$  and  $V_t$  denote infinite bus voltage and synchronous generator terminal voltage, respectively.

In what follows, we will focus on the third-order single machine infinite bus system with the excitation mechanism model, which is given by

$$\begin{cases} \dot{\delta} = \omega_0 \omega, \\ \dot{\omega} = \frac{1}{H} \left( P_m - D\omega - \frac{EV_s}{x_{d\Sigma}} \sin \delta \right), \\ \dot{E} = \frac{1}{T'_{d0}} \left[ -\frac{x_{d\Sigma}}{x'_d} E + \frac{x_d - x'_d}{x'_d} V_s \cos \delta + E_f \right], \end{cases} \quad (1)$$

where  $\delta$  denotes the generator rotor angle,  $\omega$  represents the deviation of rotor angular velocity from synchronous angular velocity,  $E$  is the transient voltage,  $\omega_0$ ,  $D$ ,  $H$  denote synchronous angular velocity, damping coefficient, and inertia constant, respectively,  $E_f$  is the excitation voltage, and  $P_m$  represents the mechanical power of generator.

Without loss of generality, the third-order single machine infinite bus system can be cast into a simplified model, namely,

$$\begin{cases} \dot{\delta} = \omega_0 \omega, \\ H\dot{\omega} = -\gamma\omega + P_m - BV_s E \sin \delta, \\ \alpha\dot{E} = -(1 + XB)E + XB V_s \cos \delta + E_f. \end{cases} \quad (2)$$

For convenience, we set  $B = 1/x'_{d\Sigma}$ ,  $X = x_d - x'_d$ ,  $D = \gamma$ ,  $T'_{d0} = \alpha$ ,  $x_{d\Sigma}/x'_d = 1 + XB$ .

Moreover, we select the parameters  $B = 1$ ,  $X = 1$ ,  $\alpha = 2$ ,  $E_f = 1$ ,  $V_s = 1$ . Thus, we can obtain the third-order single machine infinite bus system from equation (2):

$$\begin{cases} \dot{x} = dy, \\ \dot{y} = -ay + b - cz \sin x, \\ \dot{z} = -z + 0.5 \cos x + 0.5, \end{cases} \quad (3)$$

where  $x$  denotes the generator rotor angle,  $y$  represents the transient voltage, and  $z$  is the relative speed. In what follows, we aim to study the rich dynamic behavior of system (3).

**2.2. Basic Properties of the System.** In this section, the chaotic dynamics of the third-order power system are analyzed. According to the Wolff algorithm, the largest Lyapunov exponents of the system are  $\lambda_1 = 0.1599$ ,  $\lambda_2 = -0.0264$ ,  $\lambda_3 = -0.9935$ , and the system displays chaotic state. We consider the vector field divergence of the system, and one can obtain

$$\nabla \mathbf{V} = \frac{\partial \dot{x}}{\partial x} + \frac{\partial \dot{y}}{\partial y} + \frac{\partial \dot{z}}{\partial z} = 0 - a - 1 = -a - 1. \quad (4)$$

Thus, we can get

$$\sum_{i=1}^3 \lambda_i = \text{Tr}(J) = \text{div} \mathbf{V}. \quad (5)$$

Then,

$$\begin{aligned} \text{div} \mathbf{V} = \nabla \mathbf{V} &= \frac{\partial \dot{x}}{\partial x} + \frac{\partial \dot{y}}{\partial y} + \frac{\partial \dot{z}}{\partial z} = \text{Tr}(J) \\ &= -a - 1 = \lambda_1 + \lambda_2 + \lambda_3 = -0.86. \end{aligned} \quad (6)$$

In particular,  $dV/dt = e^{-(a+1)t} = e^{-0.86t}$ . If  $a + 1 > 0$ , system (3) will be a dissipative system.

Furthermore, we can calculate the Kaplan–Yorke dimension for chaotic system (3):

$$D = j + \frac{1}{|\lambda_{j+1}|} \sum_{i=1}^j \lambda_i = 2 + \frac{0.1599 - 0.0264}{0.9935} = 2.134. \quad (7)$$

That is, system (3) displays chaotic behavior.

In order to better understand the dynamic behavior of the third-order power system, we show the phase diagrams and the evolution of variables of the system under different parameters.

Firstly, we take the parameter  $(a, b, c, d) = (0.5, -0.08, 1, 1)$  and the initial values  $(x, y, z) = (1, 0.1, 1)$ , and the system is in periodic state, as shown in Figures 2(a) and 2(b).

In what follows, we select the parameter  $(a, b, c, d) = (0.5, 0.12, 1, 1)$  and the initial value  $(x, y, z) = (1, 0.1, 1)$ ; as can be seen from Figures 3(a) and 3(b), one can find that the system converges to a fixed point. That is, the values of parameters play an important role on the dynamics for the power system.

2.3. *Analysis of Bifurcation Condition for the Power System.* In this section, we focus on investigating the bifurcation behavior of the third-order chaotic power system. Firstly, according to equation.(3), the Jacobian matrix can be calculated as follows:

$$J = \begin{bmatrix} 0 & \omega_0 & 0 \\ -\frac{BV_s E_0 \cos \delta_0}{H} & \frac{-\gamma}{H} & -\frac{BV_s \sin \delta_0}{H} \\ \frac{XBV_s \sin \delta_0}{\alpha} & 0 & \frac{1 + XB}{\alpha} \end{bmatrix}, \quad (8)$$

where  $(\delta_0, 0, E_0)$  denotes the equilibrium point of system (3), and from equation (8), we get

$$|\lambda E - J| = \begin{vmatrix} \lambda & -\omega_0 & 0 \\ \frac{-BV_s E_0 \cos \delta_0}{H} & \lambda + \frac{\gamma}{H} & \frac{BV_s \sin \delta_0}{H} \\ \frac{XBV_s \sin \delta_0}{\alpha} & 0 & \lambda + \frac{1 + XB}{\alpha} \end{vmatrix} = 0. \quad (9) \quad \text{where}$$

Based on the above algebraic equation, we can obtain that

$$\lambda^3 + \left( \frac{H(1 + XB) + \gamma\alpha}{H\alpha} \right) \lambda^2 + \frac{\gamma(1 + XB) + \alpha\omega_0 BV_s E_0 \cos \delta_0}{H\alpha} \lambda + \frac{\omega_0 BV_s (1 + XB) E_0 \cos \delta_0 - XBV_s \sin^2 \delta_0}{H\alpha} = 0. \quad (10)$$

In the following, we suppose that

$$\lambda^3 + \left( \frac{H(1 + XB) + \gamma\alpha}{H\alpha} \right) \lambda^2 + \frac{\gamma(1 + XB) + \alpha\omega_0 BV_s E_0 \cos \delta_0}{H\alpha} \lambda + \frac{\omega_0 BV_s (1 + XB) E_0 \cos \delta_0 - XBV_s \sin^2 \delta_0}{H\alpha} = \lambda^3 + p\lambda^2 + q^2\lambda + pq^2, \quad (11)$$

$$p = \frac{H(1 + XB) + \gamma\alpha}{H\alpha},$$

$$q^2 = \frac{\gamma(1 + XB) + \alpha\omega_0 BV_s E_0 \cos \delta_0}{H\alpha},$$

$$pq^2 = \frac{\omega_0 BV_s (1 + XB) + \gamma\alpha}{H\alpha} \cdot \frac{\gamma(1 + XB) + \alpha\omega_0 BV_s E_0 \cos \delta_0}{H\alpha} = \frac{\omega_0 BV_s (1 + XB) E_0 \cos \delta_0 - XBV_s \sin^2 \delta_0}{H\alpha} \quad (12)$$

$$(1 + XB)H\gamma^2 + \left( \alpha H \omega_0 BV_s E_0 \cos \delta_0 + \frac{H^2 (1 + XB)^2}{\alpha} \right) \gamma + \omega_0 XB^2 V_s^2 \sin^2 \delta_0 = 0.$$

Thus, the equation of bifurcation curve can be described by the following equations:

$$\begin{cases} P_m = BV_s E_0 \sin \delta_0, \\ (1 + XB)E_0 = E_f + XBV_s \cos \delta_0, \\ (1 + XB)H\gamma^2 + \left( \alpha H \omega_0 BV_s E_0 \cos \delta_0 + \frac{H^2 (1 + XB)^2}{\alpha} \right) \gamma + \omega_0 XB^2 V_s^2 \sin^2 \delta_0 = 0. \end{cases} \quad (13)$$

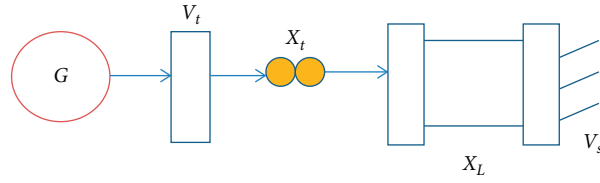


FIGURE 1: Schematic diagram of the single machine infinite bus system.

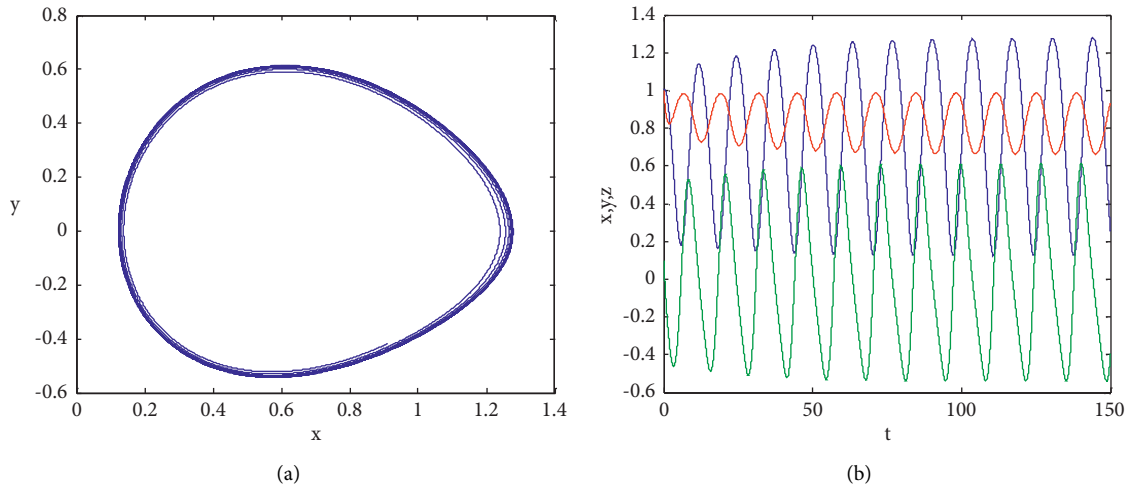


FIGURE 2: (a) Phase diagram of system (3). (b) The evolution of the state variables with time.

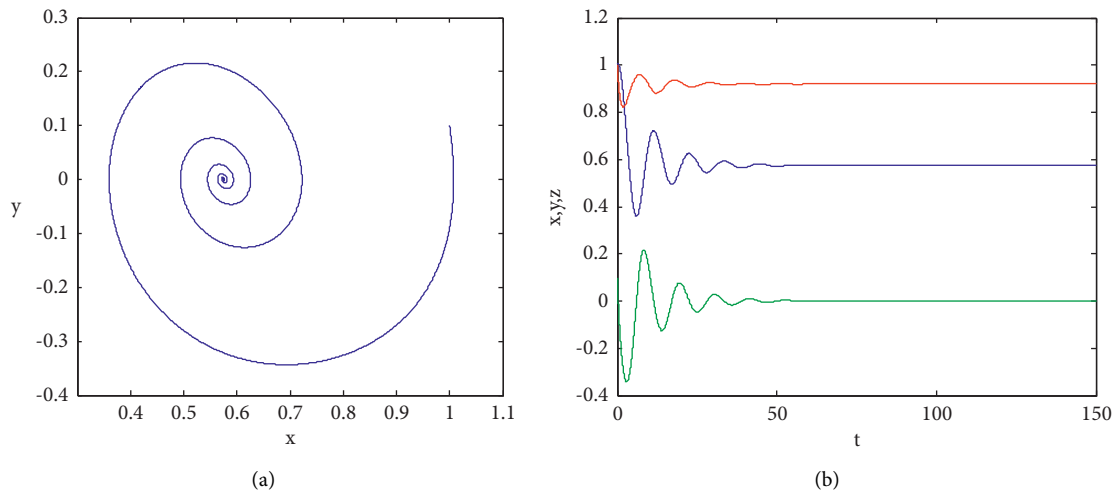


FIGURE 3: (a) Phase diagram of system (3). (b) The evolution of the state variables with time.

By means of bifurcation diagram, dynamic behaviors with varying system parameter  $a$  are investigated. Let the system parameter  $a$  vary from  $-0.2$  to  $1$  with the step size of  $0.001$ , and the other parameters are taken as  $b = 0.5, c = 1, d = 1$ ; the bifurcation diagram can provide an overall perspective of the dynamics of the system, which is depicted in Figure 4.

From the bifurcation diagram, it can be observed that with the increase of  $a$  from  $-0.2$ , system (3) is chaotic over

most of the scope  $a \in [-0.2, -0.1]$ , and when  $a \in [0.2, 1]$ , the system converges to a fixed point. With the value of  $a$  increasing from  $-0.1$ , system (3) presents Hopf bifurcation.

### 3. Analysis of Multi-Area Network Coupled with Chaotic Power System

We are witnessing a time of drastic changes in the operation of power grids caused by the necessity to reduce global

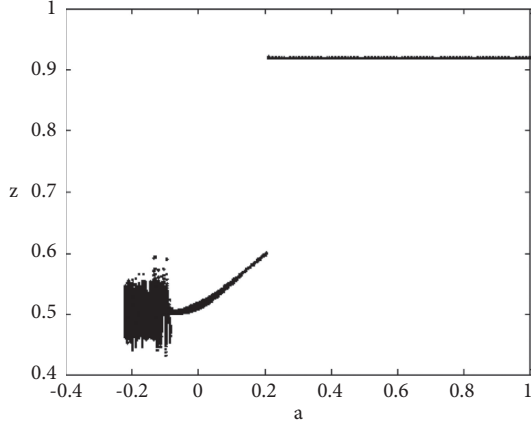


FIGURE 4: Dynamic behaviors of the chaotic third-order power system with  $a$ .

warming caused by large emission of carbon dioxide gases. Thus, more and more decentralized renewable energy sources are replacing centralized power generation. The strategy can change the effective grid structure from a fully connected to a locally connected one. Hence, large-scale real power networks will be divided into many areas. This implies that the power network usually has multi-area structure.

$$\begin{cases} \dot{x}_i(t) = F_k(\dot{x}_i(t)) + \sum_{j=1, j \neq i}^{N_k} a_{ij} c_{ij}^{kk} (x_j(t) - x_i(t)) + \sum_{l=1, l \neq k}^M \sum_{j=1}^{N_l} a_{ij}(t) (c_{ij}^{kl} x_j(t) - c_{ij}^l x_i(t)) \\ i = 1, 2, \dots, N_k, k = 1, 2, \dots, M, \end{cases} \quad (14)$$

where  $x_i^k = (x_{i1}^k, x_{i2}^k, \dots, x_{in_k}^k)^T \in R^{n_k}$  denotes the state vector of the  $i$ th node in the  $k$ th area.  $F_k$  describes the node's dynamics of the  $k$ th area. The matrix  $C_{kk} = \text{diag}(c_{kk}^1, c_{kk}^2, \dots, c_{kk}^{n_k})$  is the inner coupling matrix which denotes the internal connection in  $k$ th area, and  $C_{kl} = (c_{kl}^{rs}) \in R^{n_k \times n_l}$  and  $C_{kl}^l = \text{diag}(c_{kk}^{l(1)}, c_{kk}^{l(2)}, \dots, c_{kk}^{l(n_k)})$  are the inner coupling matrices between the  $k$ th and  $l$ th areas; if the  $r$ th element of  $x_i(t)$  in the  $k$ th area is influenced by the  $l$ th element of  $x_j(t)$  in the  $l$ th, then  $c_{kk}^{l(r)} \neq 0, c_{kl}^{rs} \neq 0$ ; otherwise,  $c_{kk}^{l(r)} = 0, c_{kl}^{rs} = 0$ . Also, matrix  $A = (a_{ij})_{N \times N}$  denotes the topology structure of the entire multi-area power network, which is described as follows: if there exists a connection between node  $i$  and  $j$ , then  $a_{ij} = a_{ji} > 0 (i \neq j)$ ; otherwise,  $a_{ij} = a_{ji} = 0 (i \neq j)$ .

Suppose that the sets of subscripts of these areas are  $G_1 = \{1, 2, \dots, N_1\}, G_2 = \{N_1 + 1, N_1 + 2, \dots, N_1 + N_2\}, \dots, G_M = \{N_1 + \dots + N_{M-1} + 1, \dots, N\}$ , where  $N_1 + N_2$

Generally, the interactions between nodes (generators and consumers) in the same area are identical and those in different areas are nonidentical. Hence, there exist diverse coupling forms in the multi-area power network. For better describing this kind of phenomenon, the multi-area power network model is presented. Also, the schematic diagram of the multi-area power network is shown in Figure 5. Here, we suppose that the node's dynamics in different areas are identical, which is described as system (3).

Furthermore, alternating voltage of the power plants is required to be synchronized around a certain specific frequency; otherwise, severe problems like large blackouts may be occur in a large area. Thus, cluster synchronization is essential for the proper functioning of the multi-area power network. In the following, we will investigate the multi-area power network model and its cluster synchronization.

**3.1. The Multi-Area Power Network Model.** In this section, we consider a complex multi-area power network with  $M$  areas and each node is a third-order power system. Suppose that the  $k$ th area is composed of  $N_k$  nodes. Then, the general multi-area power network can be described as

$+ \dots + N_M = N$ . The coupling matrix  $A$  can be written in the following form:

$$A = \begin{bmatrix} A_{11} & A_{12} & \dots & A_{1M} \\ A_{21} & A_{22} & \dots & A_{2M} \\ \vdots & \ddots & \ddots & \vdots \\ A_{M1} & & & A_{MM} \end{bmatrix}, \quad (15)$$

where  $A_{pp} \in R^{r_p \times r_p} (p = 1, 2, \dots, M)$  show the coupling pattern in the same area and  $A_{pq} \in R^{r_p \times r_q} (p = 1, 2, \dots, M, q = 1, 2, \dots, M, p \neq q)$  are the coupling schemes among different areas.

In order to achieve cluster synchronization of the multi-area power network, the control inputs  $u_i(t) \in R^n$  are added and the controlled multi-area power network can be characterized by the following equation:

$$\begin{cases} \dot{x}_i(t) = F_k(\dot{x}_i(t)) + \sum_{j=1, j \neq i}^{N_k} a_{ij}(t) c_{ij}^{kk} (x_j(t) - x_i(t)) + \sum_{l=1, l \neq k}^M \sum_{j=1}^{N_l} a_{ij}(t) (c_{ij}^{kl} x_j(t) - c_{ij}^{kl} x_i(t) - c_{ij}^l x_i(t)) + u_i(t) \\ i = 1, 2, \dots, N_k, k = 1, 2, \dots, M. \end{cases} \quad (16)$$

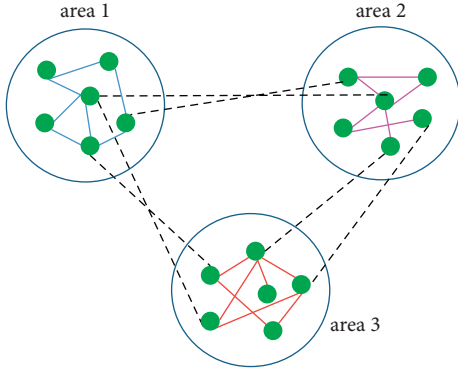


FIGURE 5: The multi-area power network topology structure.

Define the synchronous errors

$$e_i(t) = x_i(t) - s_k(t) \quad (i = 1, 2, \dots, N_k), \quad (17)$$

where  $s_k(t)$  is a solution of an isolated node in the  $k$ th hand satisfies  $\dot{s}_k(t) = F_k(s_k(t))$ . The network can realize the cluster synchronization, if  $\lim_{t \rightarrow \infty} \|e_i(t)\| = 0, i = 1, 2, \dots, N$ .

### 3.2. Cluster Synchronization of Multi-Area Power Network.

For simplicity, we suppose that all the inner coupling patterns between different areas are identical, and equation (14) can be derived as

$$\begin{cases} u_i(t) = -\sum_{j=1}^N a_{ij} c_{ij}^{kk} s_j(t) - q_i(t) c_{ij}^{kk} (x_i(t) - s_k(t)), & i \in \tilde{\phi}_k, k = 1, 2, \dots, M \\ 0, & \text{otherwise,} \end{cases} \quad (21)$$

where the coupling strength  $a_{ij}(t) = (a_{ij}^1(t), a_{ij}^2(t), \dots, a_{ij}^n(t))^T$  between the nodes and the feedback gains adopts the following adaptive strategy:

$$\begin{cases} \dot{a}_{ij}(t) = \beta \|(x_j(t) - s_j(t)) - (x_i(t) - s_i(t))\|, & i \in \tilde{\phi}_k, k = 1, 2, \dots, M, \\ \dot{q}_i = \alpha \|e_i(t)\|_2^2, \end{cases} \quad (22)$$

where  $\alpha > 0, \beta > 0$  are the adaptive gains.

**Theorem 1.** For multi-area power network (18), cluster synchronization can be achieved under designed controllers (21) and (22).

$$V(t) = \frac{1}{2} \sum_{i=1}^N e_i(t)^T e_i(t) + \frac{1}{2\alpha} \sum_{i=1}^N (q_i(t) - q_i^*)^2 + \frac{1}{2\beta} \sum_{\epsilon} (b_{ij} - a_{ij})^T (b_{ij} - a_{ij}). \quad (23)$$

$$\begin{cases} \dot{x}_i(t) = F_k(x_i(t)) + \sum_{j=1, j \neq i}^{N_k} a_{ij}(t) c_{ij}^{kk} (x_j(t) - x_i(t)) + u_i(t) \\ i = 1, 2, \dots, N_k, k = 1, 2, \dots, M. \end{cases} \quad (18)$$

According to the above definition of the error variables, we can get the error dynamical system as follows:

$$\begin{aligned} \dot{e}_i(t) &= F_k(x_i(t)) - F_k(s_i(t)) \\ &+ \sum_{j=1}^{N_k} a_{ij} c_{ij}^{kk} e_j(t) + \sum_{j=1}^N a_{ij} c_{ij}^{kk} s_j(t) + u_i(t). \end{aligned} \quad (19)$$

Since the above coupling condition holds, one can obtain

$$\sum_{j=1}^N a_{ij} c_{ij}^{kk} s_j(t) = 0, \quad i \in G_{\phi_i} - \bar{G}_{\phi_i}, \quad (20)$$

where  $G_{\phi_i}$  represents all the nodes in the area and  $\bar{G}_{\phi_i}$  represents the nodes in other areas.

Subsequently, the control scheme is given via adaptive pinning control idea. The adaptive controller is designed as follows:

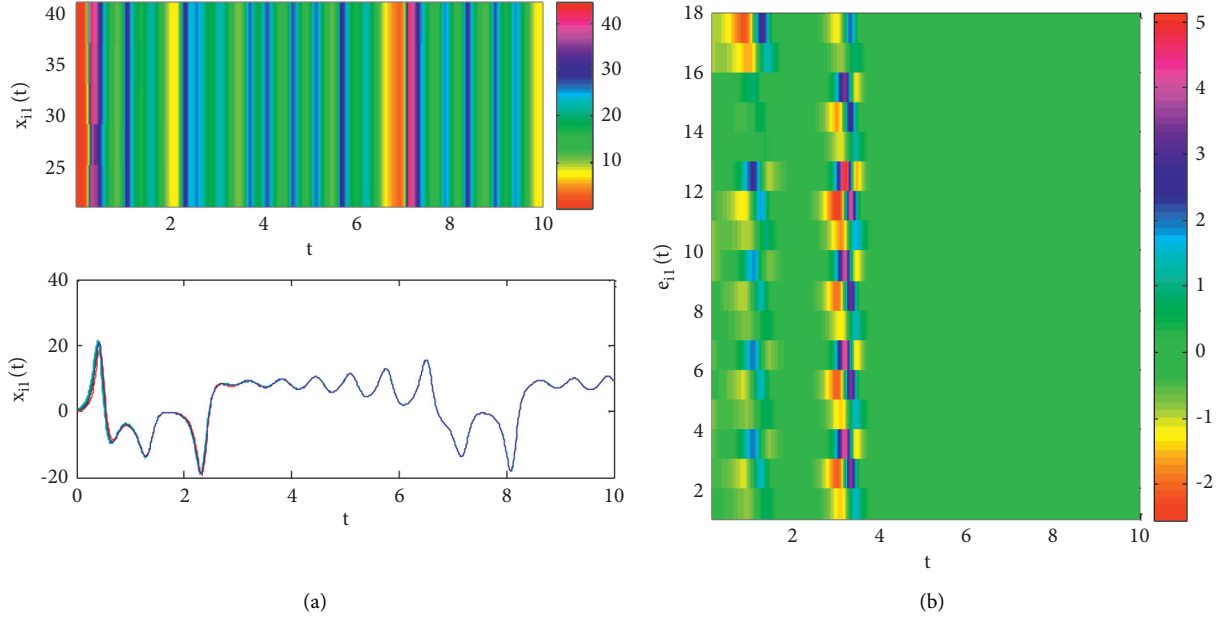


FIGURE 6: The evolution of state variables in the first area and the synchronization error.

Then, the derivative of  $V(t)$  can be calculated as follows:

$$\begin{aligned}
 \dot{V} &= \sum_{i=1}^N e_i(t)^T \dot{e}_i(t) + \frac{1}{\alpha} \sum_{i=1}^N (q_i(t) - q_i^*) \dot{q}_i(t) + \frac{1}{\beta} \sum_{\xi}^N (b_{ij} - a_{ij})^T \dot{a}_{ij}, \\
 &= \sum_{k=1}^M \sum_{i=1}^{N_k} e_i^T(t) \left[ F_k(x_i(t)) - F_k(s_i(t)) + \sum_{j=1}^N a_{ij} c_{ij}^{kk} e_j(t) - q_i c_{ij}^{kk} (x_i - s_k(t)) \right] \\
 &\quad + \sum_{i=1}^N (q_i(t) - q_i^*) e_i^T(t) e_i(t) - \sum_{\xi} (b_{ij} - a_{ij})^T \left\| (x_j(t) - s_j(t)) - (x_i(t) - s_i(t)) \right\| \\
 &\leq \omega_k \sum_{k=1}^M \sum_{i=1}^{N_k} e_i^T(t) e_i(t) + \sum_{k=1}^M \sum_{i=1}^{N_k} e_i^T(t) \left[ \sum_{j=1}^N a_{ij} C_{kk} e_j(t) - q_i^* C_{kk} e_i(t) \right] \\
 &\quad - \sum_{\xi} (b_{ij} - a_{ij})^T \left\| (x_j(t) - s_j(t)) - (x_i(t) - s_i(t)) \right\| \\
 &= \sum_{k=1}^M \sum_{i=1}^{N_k} \omega_k e_i^T(t) e_i(t) + \sum_{j=1}^n \gamma_j \tilde{e}_j^T(t) P \tilde{e}_j(t) - \sum_{j=1}^n \gamma_j \tilde{e}_j^T(t) Q \tilde{e}_j(t) \\
 &\quad - \sum_{\xi} (b_{ij} - a_{ij})^T \left\| (x_j(t) - s_j(t)) - (x_i(t) - s_i(t)) \right\| \\
 &\leq \sum_{i=1}^n \tilde{e}_j^T(t) (w_i I_N + \gamma_j (P - Q)) \tilde{e}_j(t) - \sum_{\xi} (b_{ij} - a_{ij})^T \left\| (x_j(t) - s_j(t)) - (x_i(t) - s_i(t)) \right\|,
 \end{aligned} \tag{24}$$

where  $P = A \otimes C_{kk}$ ,  $Q = q_i^* C_{kk}$ .

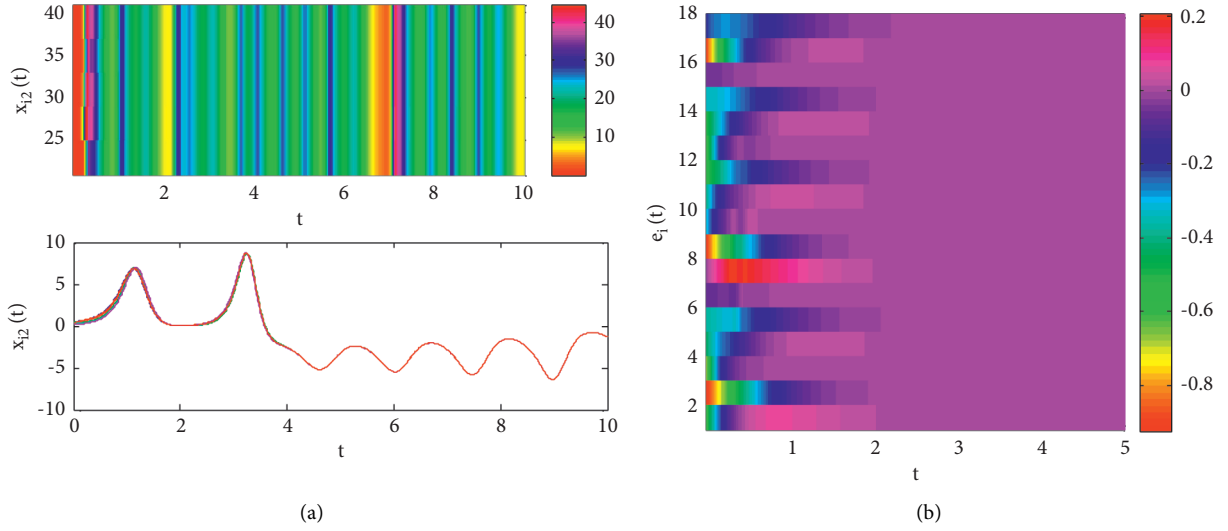


FIGURE 7: The evolution of state variables and the synchronization error in the second area.

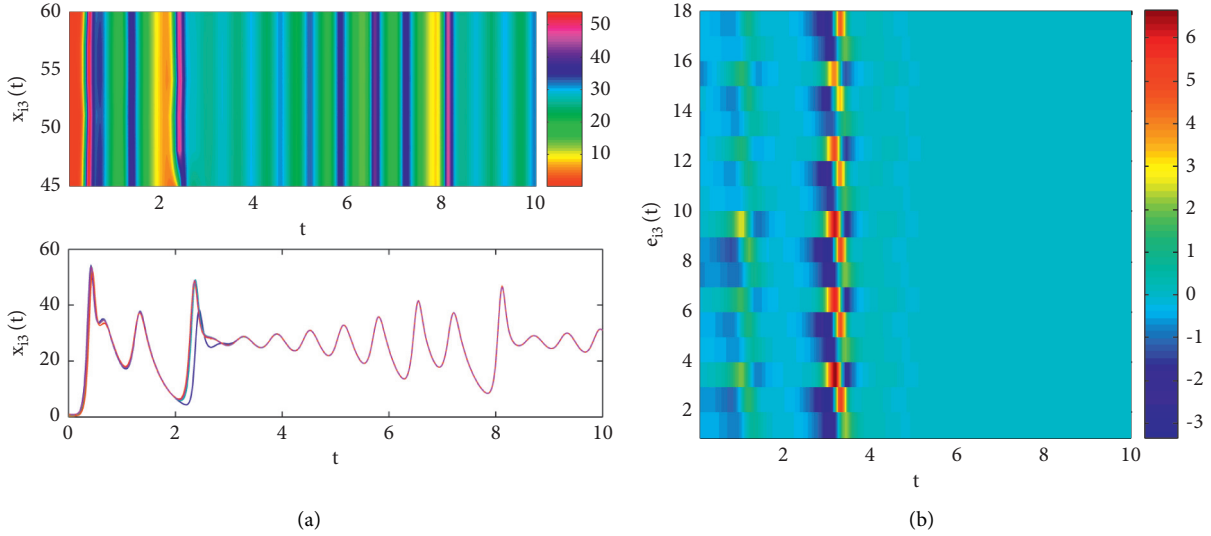


FIGURE 8: The evolution of state variables and the synchronization error in the third area.

Thus, there exists a positive constant  $b_{ij}$  larger than the corresponding coupling strength  $a_{ij}$ , i.e.,

$$\sum_{\xi} (b_{ij} - a_{ij})^T \|e_j(t) - e_i(t)\| \geq 0. \quad (25)$$

Therefore, one can take sufficiently large positive constants  $q_i^*$ , i.e.,  $\dot{V} < 0$ . That is, cluster synchronization can be achieved via designed adaptive controllers (21) and (22).

#### 4. Numerical Simulations

In this section, several numerical examples are presented to verify the theoretical results about cluster synchronization in the multi-area power network. In the following simulations, we take the network topology structure shown in Figure 1 as example. Moreover, we select the

node dynamics of the different area as the third-order power system:

$$\begin{cases} \dot{x}_{i1} = dx_{i2}, \\ \dot{x}_{i2} = -ax_{i2} + b - cz \sin x_{i1}, \\ \dot{x}_{i3} = -x_{i3} + 0.5 \cos x_{i1} + 0.5, \end{cases} \quad (26)$$

with  $i = 1, 2, \dots, 18$ .

Figures 6–8 show the evolution of state variables and the error time of each area; from these figures, one can observe that the different areas synchronize to different chaotic orbits and errors evolve toward zero. An intuitive representation of the evolution of the components of the state variables of the multi-area network can be found in Figures 6(a)–8(a). In these figures, the top subfigures show the amplitudes of state variables in different areas and the bottom subfigures represent the corresponding evolution of



state variables. In addition, Figures 6–8 show the state trajectories of the nodes in different areas with different initial conditions. As can be seen from these figures, state variables evolve in the same direction and get closer with time and finally coincide under the designed controller. It implies that cluster synchronization can be realized for the multi-area power network.

## 5. Conclusions

As we know, real power networks have complex structures. This paper investigated the multi-area power network to model the network topology underlying high-voltage transmission grids, while the single node dynamics are described by the third-order chaotic power system. We studied the rich dynamics of the single third-order system via theoretical analysis and numerical simulations. The dynamic behaviors of the system are depicted by means of the phase portrait and Hopf bifurcation analysis. In addition, it is noted that real power networks usually have multi-area structure. Therefore, we analyze the cluster synchronization behavior of the multi-area power network. Furthermore, we presented an adaptive feedback control scheme for achieving cluster synchronization.

Even though we investigated these phenomena in a small-scale multi-area power network, we would like to emphasize that small-scale power network structure is indeed in reality.

## Data Availability

The data used to support the findings of this study are included within the article.

## Conflicts of Interest

The authors declare that they have no conflicts of interest.

## Acknowledgments

This study was supported by the National Natural Science Foundation of China (NSFC) under grant no. 11702195.

## References

- [1] C. Wang, C. Grebogi, and M. S. Baptista, "Control and prediction for blackouts caused by frequency collapse in smart grids," *Chaos: An Interdisciplinary Journal of Nonlinear Science*, vol. 26, no. 9, Article ID 093119, 2016.
- [2] P. D. Hines, I. Dobson, and P. Rezaei, "Cascading power outages propagate locally in an influence graph that is not the actual grid topology," *IEEE Transactions on Power Systems*, vol. 32, pp. 958–967, 2017.
- [3] P. Crucitti, V. Latora, and M. Marchiori, "A topological analysis of the Italian electric power grid," *Physica A: Statistical Mechanics and Its Applications*, vol. 338, no. 1-2, pp. 92–97, 2004.
- [4] P. Pourbeik, P. S. Kundur, and C. W. Taylor, "The anatomy of a power grid blackout-root causes and dynamics of recent major blackouts," *Power and Energy Magazine*, vol. 4, pp. 22–29, 2006.
- [5] J. Peter, J. H. Menck, J. Kurths, and H. J. Schellnhuber, "How dead ends undermine power grid stability," *Nature Communications*, vol. 5, p. 3969, 2014.
- [6] L. O. Chua, "A unified approach for teaching basic nonlinear electronic circuits to sophomores," *Proceedings of the IEEE*, vol. 59, no. 6, pp. 880–886, 1971.
- [7] R. Carareto, M. S. Baptista, and C. Grebogi, "Natural synchronization in power-grids with anti-correlated units," *Communications in Nonlinear Science and Numerical Simulation*, vol. 18, no. 4, pp. 1035–1046, 2013.
- [8] D. Florian, C. Michael, and B. Francesco, "Synchronization in complex oscillator networks and smart grids," *Proceedings of the National Academy of Sciences*, vol. 110, no. 6, pp. 2005–2010, 2013.
- [9] M. L. Ma and F. H. Min, "Bifurcation behavior an coexisting motions in a time-delayed power system," *Chinese Physics B*, vol. 24, no. 3, Article ID 030501, 2005.
- [10] Z. Chen, J. Wu, Y. Xia, and X. Zhang, "Robustness of interdependent power grids and communication networks: a complex network perspective," *IEEE Transactions on Circuits and Systems II: Express Briefs*, vol. 65, no. 1, pp. 115–119, 2018.
- [11] T. Tian, S. Roy, and S. Baldi, "Stable adaption in multi-area load frequency control under dynamically-changing topologies," *IEEE Transactions on Power Systems*, vol. 99, Article ID 3044436, 2020.
- [12] S. Boccaletti, G. Bianconi, R. Criado et al., "The structure and dynamics of multilayer networks," *Physics Reports*, vol. 544, no. 1, pp. 1–122, 2014.
- [13] F. Dorfler, M. Chertkov, and F. Bullo, "Synchronization in complex oscillator networks and smart grids," *Proceedings of the National Academy of Sciences*, vol. 110, no. 6, pp. 2005–2010, 2013.
- [14] D. Witthaut and M. Timme, "Braess's paradox in oscillator networks, desynchronization and power outage," *New Journal of Physics*, vol. 14, no. 8, Article ID 083036, 2012.
- [15] J. W. Wu, W. You, T. C. Wu, and Y. X. Xia, "Abnormal phenomenon in robustness of complex networks with heterogeneous node functions," *Physica A: Statistical Mechanics and Its Applications*, vol. 506, pp. 451–461, 2018.
- [16] J. Aguirre, R. Sevilla-Escoboza, R. Gutiérrez, D. Papo, and J. M. Buldú, "Synchronization of inter-connected networks: the role of connector nodes," *Physical Review Letters*, vol. 112, no. 24, Article ID 248701, 2014.
- [17] L. K. Tang, J. A. Lu, J. H. Lu, and X. Wu, "Bifurcation Analysis of synchronized regions in complex dynamical networks with coupling delay," *International Journal of Bifurcation and Chaos in Applied Sciences and Engineering*, vol. 24, no. 1, Article ID 1450011, 2014.
- [18] A. Patel, S. Roy, and S. Baldi, "Wide-area damping control resilience towards cyber-attacks: a dynamic loop approach," *IEEE Transactions on Smart Grid*, vol. 12, no. 4, pp. 3438–3447, Article ID 3055222, 2021.
- [19] E. Mallada, C. Zhao, and S. Low, "Optimal load-side control for frequency regulation in smart grids," *IEEE Transactions on Automatic Control*, vol. 62, no. 12, pp. 6294–6309, 2017.
- [20] I. V. Belykh, B. N. Barrett, and V. N. Vladimír, "Bistability of patterns of synchrony in Kuramoto oscillators with inertia," *Chaos: An Interdisciplinary Journal of Nonlinear Science*, vol. 26, no. 9, Article ID 094822, 2016.
- [21] T. Coletta and P. Jacquod, "Linear stability and the Braess paradox in coupled-oscillator networks and electric power grids," *Physical Review E*, vol. 93, no. 3, Article ID 032222, 2016.

- [22] M. S. Baptista<sup>1</sup>, R. M. Szmowski, and R. F. Pereira, "Chaotic, informational and synchronous behavior of multiplex networks," *Scientific Reports*, vol. 6, Article ID 22617, 2016.
- [23] R. Sevilla-Escoboza, I. Sendina-Nadal, I. Leyva, R. Gutiérrez, J. M. Buldú, and S. Boccaletti, "Inter-layer synchronization in multiplex networks of identical layers," *Chaos: An Interdisciplinary Journal of Nonlinear Science*, vol. 26, no. 6, Article ID 065304, 2016.
- [24] Z. Y. Wu and X. C. Fu, "Cluster mixed synchronization via pinning control and adaptive coupling strength in community networks with nonidentical nodes," *Communications in Nonlinear Science and Numerical Simulation*, vol. 17, no. 4, pp. 1628–1636, 2012.